JOURNAL OF POWDER MATERIALS

Volume 31, Number 6 December 2024

Critical Reviews

Research Articles

kpmi
Korean Powder Metallurgy & Materials Institute

사단법인 한국분말재료학회
Unit 706, (635-4, Yeoksam-Dong)22, 7Gil, Teheran-Ro, Gangnam-Gu, 06130, Seoul, Korea
TEL + 82-2-539-4603 FAX + 82-0303-0947-4603
Homepage : http://www.kpmi.or.kr e-mail :kpmi@kpmi.or.kr

9 772799 852009 02
ISSN 2799-8525

Journal of Powder Materials
VOL. 31 NO. 6 / December 2024
Page 365-576
kpmi

ISSN 2799-8525 (Print)
ISSN 2799-8681 (Online)

한국분말재료학회지
Journal of Powder Materials

VOL. 31 NO. 6 / December 2024 Page 465-576

kpmi
Korean Powder Metallurgy & Materials Institute

Journal of
Powder Materials

ISSN 2799-8525 (Print)
ISSN 2799-8681 (Online)

VOL. 31 NO. 6 (Total 167) / December 2024

Aims and Scope

The Journal of Powder Materials (JPM) aims to share advanced technologies and the latest research findings in the fields in powder metallurgy and powder-related materials science and engineering with researchers and industry professionals worldwide. Furthermore, JPM aims to provide a valuable resource for material scientists, technologists, engineers, designers and manufacturers by bridging the gap between pure research and the more practical aspects of production and properties.

JPM covers the whole fields of powder materials and processes, which includes powder production (including their precursor materials), milling, granulation, cold and hot compaction, sintering, cold and hot isostatic pressing, pulsed and other assisted consolidation, additive manufacturing, injection molding, as well as coating technology using powders. The journal also encompasses research in characterization, testing, quality assurance, and applications. The scope of topics covered by JPM can be categorized into two main areas which are powder materials and powder technology, as outlined below.

Powder materials: advanced structural materials, environmental/energy materials, functional materials, high-temperature materials
Powder technology: additive manufacturing, computational and data-driven sciences/artificial intelligence (A.I.), chemical and physical analysis, general technologies, and powder theory

JPM primarily focuses on Korean researchers due to global powder metallurgy industry in Korea; however, we welcome research contributions from international researchers and industry without imposing any restrictions on manuscript types.

ISO abbreviation of journal title

✓ Topic

Powder Materials
- Fe-based powders
- Non-ferrous powders
- Ceramic powders
- Particulate Composite
- Tool/Cemented Carbides
- Porous powders
- Electric/Electronic powders
- Bio materials
- Magnetic powders
- Energy conversion/storage powders
- Multi-functional powders
- Organic/inorganic powders

Powder Technology
- Powder synthesis
- Powder characterization/analysis
- Powder compaction
- Powder pretreatment
- Sintering
- Densification process
- PIM
- Post-treatment
- Novel powder technology
- Nanostructured powders
- Simulation of powder/process
- Powder test
- Powder business/industry

The official title of the journal is 'Journal of Powder Materials' and the abbreviated title is 'J. Powder Mater.'

Year of launching (history)

Journal of Powder Materials was launched in 1993.

The frequency of publication

Journal of Powder Materials is published bi-monthly in February, April, June, August, October, and December. Supplementary issues are also published at times.

Availability of the full-text in the web, URL address

The published articles from the initial to the present issue are available free of charge at http://ejournal.kpmi.or.kr.

Index in database

The articles published in Journal of Powder Materials are indexed and/or abstracted in Google Scholar, KISTI, and KCI.

Fund support

"본 사업은 기획재정부의 복권기금 및 과학기술정보통신부의 과학기술진흥기금으로 추진하여 사회적 가치 실현과 국가 과학기술 발전에 기여합니다."
"This work was supported by the Korean Federation of Science and Technology Societies(KOFST) grant funded by the Korean government."

kpmi
Korean Powder Metallurgy
& Materials Institute

Subscription info
The annual subscription fee for this journal is Korean Won ₩50,000 (US$ 50.00 or equivalent). Back issues are available on request. The number of circulated print copies is 600. Full published papers from the initial to the present issue are available free of charge at http://ejournal.kpmi.or.kr. Correspondence concerning business matters should be addressed to Ms. Youn-Ho Kim, Manager, The Korean Powder Metallurgy & Materials Institute, Unit 706, (635-4, Yeoksam-Dong) 22, 7Gil, Teheran-Ro, Gangnam-Gu, Seoul 06130, Korea (Tel: +82-2-539-4603, Fax: +82-0303-0947-4603, e-mail: kpmi@kpmi.or.kr).

Submission
Manuscripts should be submitted via the online Manuscript Central website (https://submit.powdermat.org). Other correspondence can be sent by e-mail (ktkim@kims.re.kr or kpmi@kpmi.or.kr) to the Editor-in-Chief, Dr. Kyung Tae Kim, Korea Institute of Materials Science, Changwon, Gyeongnam 51508, Korea. All manuscripts are peer-reviewed.

Contact info (Editorial office)
The Korean Powder Metallurgy & Materials Institute Unit 706, 22, 7Gil, Teheran-Ro, Gangnam-Gu, Seoul 06130, Korea
Tel: +82-2-539-4603, Fax: +82-0303-0947-4603, E-mail: kpmi@kpmi.or.kr

Printed by M2PI
#805, 26 Sangwon 1-gil, Seongdong-gu, Seoul 04779, Korea
Tel: +82-2-6966-4930, Fax: +82-2-6966-4945, E-mail: support@m2-pi.com, Homepage: http://m2-pi.com

Editorial Board

Journal of Powder Materials

Contents

Journal of Powder Materials

VOL. 31 NO.6 / December 2024

Critical Reviews

Research Articles

Contents

Journal of Powder Materials

VOL. 31 NO.6 / December 2024

Critical Reviews

Research Articles

Critical Review

pISSN 2799-8525 · eISSN 2799-8681
J Powder Mater 2024;31(6):465-479

Journal of Powder Materials

Epsilon Iron Oxide (ε-Fe_2O_3) as an Electromagnetic Functional Material: Properties, Synthesis, and Applications

Ji Hyeong Jeong, Hwan Hee Kim, Jung-Goo Lee, Youn-Kyoung Baek*

Nano Materials Research Division, Korea Institute of Materials Science, 797 Changwondaero, Changwon 51508, Republic of Korea

Iron oxide (ε-Fe_2O_3) is emerging as a promising electromagnetic material due to its unique magnetic and electronic properties. This review focuses on the intrinsic properties of ε-Fe_2O_3, particularly its high coercivity, comparable to that of rare-earth magnets, which is attributed to its significant magnetic anisotropy. These properties render it highly suitable for applications in millimeter wave absorption and high-density magnetic storage media. Furthermore, its semiconducting behavior offers potential applications in photocatalytic hydrogen production. The review also explores various synthesis methods for fabricating ε-Fe_2O_3 as nanoparticles or thin films, emphasizing the optimization of purity and stability. By exploring and harnessing the properties of ε-Fe_2O_3, this study aims to contribute to the advancement of next-generation electromagnetic materials with potential applications in 6G wireless telecommunications, spintronics, high-density data storage, and energy technologies.

Keywords: Epsilon iron oxide; Permanent magnet; Millimeter wave absorption; Magnetic recording; Photocatalyst

Received: September 19, 2024
Revised: November 20, 2024
Accepted: December 5, 2024

***Corresponding author:**
Youn-Kyoung Baek
TEL: +82-55-280-3605
FAX: +82-55-280-3391
E-mail: ykbaek@kims.re.kr

1. Introduction

Iron oxide (Fe_2O_3) exists in a variety of structural polymorphs, each of which is utilized in a wide range of applications due to its distinct physical and chemical properties[1–6]. Representative polymorphs of Fe_2O_3, include the alpha (α), beta (β), gamma (γ), and epsilon (ε) phases, with their distinctive properties summarized in Table 1 [4, 5, 7–10]. α-Fe_2O_3 (hematite), the most thermodynamically stable phase, has a corundum structure (space group = $R\bar{3}c$) and is widely utilized in pigments and photocatalysts. β-Fe_2O_3, a metastable phase with a bixbyite structure (space group = $Ia\bar{3}$), has potential applications in advanced energy materials [11, 12] and environmental technologies[13, 14]. γ-Fe_2O_3 (maghemite), which adopts a spinel structure (space group = $P4_12_12_1$), is primarily utilized in the form of nanoparticles as a soft magnetic material for magnetic recording media and biomedical applications. Among the polymorphs, epsilon iron oxide (ε-Fe_2O_3) is distinguished by its orthorhombic structure (space group = $Pna2_1$) and its entirely unique electromagnetic properties, which recently garnered significant attention as a potential electromagnetic functional material (Fig. 1) [3, 5].

ε-Fe_2O_3 exhibits unique magnetic and electronic properties including extremely high magnetic anisotropy and coercivity (H_c) comparable to or exceeding rare earth-based magnets [6, 15]. These properties enable the utilization of ε-Fe_2O_3 in advanced magnetic applications such as millimeter-wave absorbers, high-density magnetic recording media, and spintronics [3, 16, 17]. Additionally, ε-Fe_2O_3 also exhibits semiconductor properties with a bandgap that allows it to absorb visible light, suggesting its potential as a photocatalyst for hydrogen production [9]. These characteristics suggest that ε-Fe_2O_3 is a versatile material capable of performing various functions beyond simple magnetic materials. However, to maximize the electromagnetic functionality of the iron oxides, it is essential to it is essential to synthesize high purity ε phase. As ε-Fe_2O_3 is an intermediate phase between α-Fe_2O_3 and γ-Fe_2O_3, it is only appears in the form of nanoparticles with diameters ranging from 8 to 50 nm, which requires more demanding synthesis conditions than other polymorphs [6]. Recent advances in wet/dry powder preparation and advanced deposition techniques have enabled

https://doi.org/10.4150/jpm.2024.00290

Table 1. Physical and magnetic properties of various polymorphs of iron oxide [4,5,7-10]

Properties	Iron Oxide Molecular Formula			
	α-Fe_2O_3	β-Fe_2O_3	γ-Fe_2O_3	ε-Fe_2O_3
Structural type	Corundum structure	Bixbyite structure	Spinel structure	Orthorhombic structure
Space group	$R\bar{3}c$	$Ia\bar{3}$	$P4_332$ (cubic), $P4_12_12_1$ (tetragonal)	$Pna2_1$
Transition temperature	T_C = 956 K	T_N = 119 K	T_C = 820-986 K	T_C = 495 K
Type of magnetism	Weak ferromagnetic or antiferromagnetic	Antiferromagnetic	Ferrimagnetic	Ferrimagnetic
Density (g/cm^3)	5.26	-	4.87	4.78
Crystallographic system	Rhombohedral, hexagonal	Cubic	Cubic or tetrahedral	Orthorhombic
Lattice parameter (Å)	a_{Rh} = 5.427, a_{Hex} = 5.034, c_{Hex} = 13.75	a = 9.393	a_{Cubic} = 8.3474, a_{Tetra} = 8.347, c_{Tetra} = 25.01	a = 5.095, b = 8.789, c = 7.437
Fe site	-	Fe_A site, Fe_B site	Fe_A site, Fe_B site	Fe_A site, Fe_B site, Fe_C site, Fe_D site
Particle size	≥ 50 nm	≤ 50nm	≤ 8nm	≤ 50nm
Band gap	2.0 – 2.2 eV	1.7 – 1.9 eV	2.3 eV	1.6 – 1.9 eV

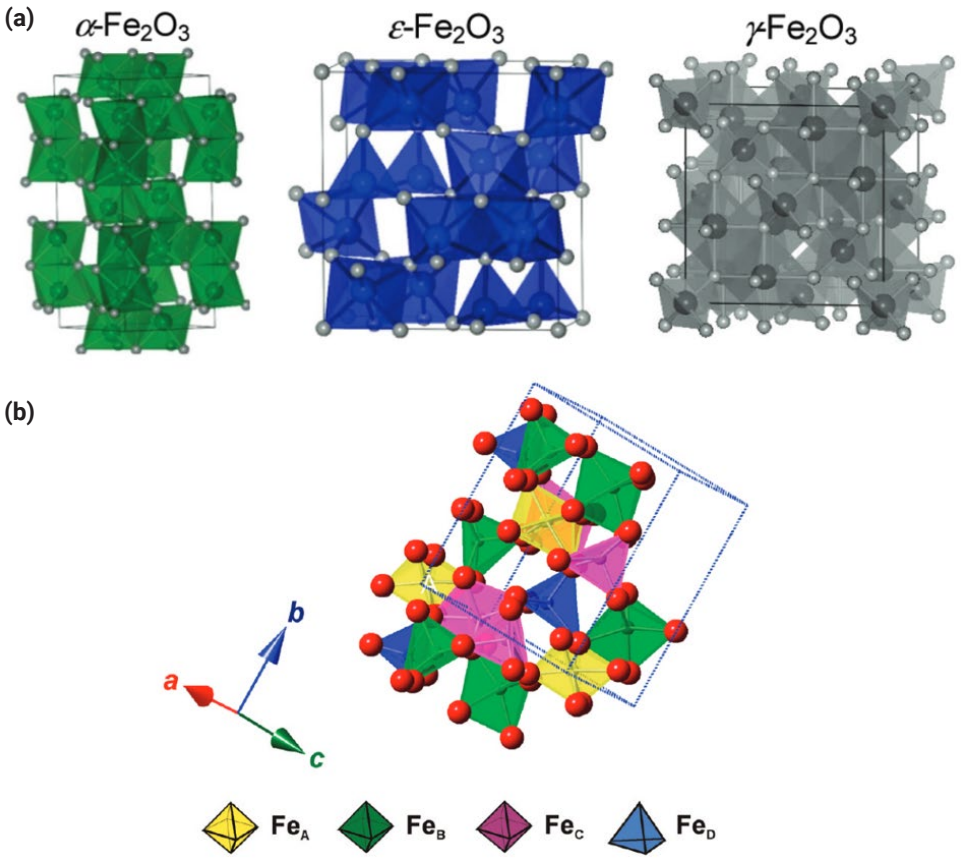

Fig. 1. (a) Graphical representations of the crystal structures of α-Fe_2O_3, ε-Fe_2O_3, and γ-Fe_2O_3. Adapted with permission from [5] Copyright 2009 American Chemical Society. (b) Crystallographic structure of the ε-Fe_2O_3 phase represented by the cation polyhedral. Adapted with permission from [3] Copyright 2010 American Chemical Society.

ε-Fe_2O_3 materials to be stably prepared not only as nanoparticles but also as nanofilms, greatly expanding their potential for electromagnetic applications [18, 19].

In this paper, we will discuss the electromagnetic properties of ε-Fe_2O_3 among the many polymorphs of Fe_2O_3, and review the latest synthesis methods and applications to fully utilize its properties. Through this, we will revisit the scientific and technological significance of ε-Fe_2O_3 and investigate its potential as a next-generation electromagnetic functional material.

2. Properties and Synthesis of ε-Fe_2O_3

2.1. Structure and Properties of ε-Fe_2O_3

Among the polymorphs of iron oxide, ε-Fe_2O_3 exhibits distinct structural and magnetic properties that set it apart as a promising material for advanced applications. Notably, ε-Fe_2O_3 is characterized by its unique orthorhombic crystal structure, where Fe ions have four sites: three octahedral sites (Fe_AO_6, Fe_BO_6, Fe_CO_6) and one tetrahedral site (Fe_DO_4) located at the center of the crystal, with a spin of S = 5/2 [5].

Molecular-field theory calculations suggest that the magnetism of ε-Fe_2O_3 at room temperature arises from super-exchange interactions between Fe ions mediated by O. The spins of Fe_B and Fe_C are aligned upward along the a-axis, while Fe_A and Fe_D exhibit Neel P-type ferrimagnetism, with their spins aligned downward along the a-axis [3, 20]. ε-Fe_2O_3 exhibits a coercivity (H_c) of over 2 T at room temperature[6], which is fourfold greater than of conventional M-type ferrites and nearly twice that of NdFeB. This ultra-high coercivity can be explained by two factors. First, ε-Fe_2O_3 is only formed in a specific range of particle size conditions (8 nm to 50 nm), which corresponds to the single magnetic domain particle size that exhibits the maximum coercivity [5]. The actual iron oxide crystal phase undergoes a phase transition in the sequence of γ → ε → β → α phase depending on the size of the powder. This transition is driven by the relationship of the free energies of the nanopowders as shown in (Eq. 1).

$$G(i)=G_B(i)+\left(\frac{6V_m}{d}\right)G_s(i) \quad (1)$$

Where $G(i)$ is the free energy of the nanopowder, $G_B(i)$ is the free energy of the bulk state, V_m is the molar volume, d is the diameter of the nanopowder, $G_S(i)$ is the surface free energy, and i represents the phase type. Since the magnitudes of bulk and surface free energies vary across different crystalline phases ($G_B(\gamma) > G_B(\varepsilon) > G_B(\beta) > G_B(\alpha)$, $G_S(\gamma) < G_S(\varepsilon) < G_S(\beta) < G_S(\alpha)$, the relationship between the free energy $G(i)$ of the nanopowder and the diameter (d) of the powder is given by (Fig. 2) [3]. Specifically, within a certain particle size range, the free energy $G(\varepsilon)$ of the ε crystalline phase is the lowest, indicating that the ε-phase forms with high purity in the single magnetic domain particle size range (8 nm to 50 nm). Furthermore, the high coercivity of ε-Fe_2O_3 is attributed to its magnetic anisotropy fields (H_a). H_a is proportional to the crystal magnetic anisotropy constant (K_1) and inversely proportional to the saturation magnetization (M_s) value as expressed in (Eq. 2).

$$H_a=\frac{2K_1}{4\pi M_s} \quad (2)$$

The crystal magnetic anisotropy constant is a physical parameter that quantifies the anisotropy of energy in the magnetization direction, which depends on the crystal structure of the material. A higher value indicates greater stability of the magnetization direction. The crystal magnetic anisotropy constant (K_1) of epsilon iron oxide is calculated to be 2×10^6 erg/cm^3, which is significantly larger than the K_1 value of γ-Fe_2O_3 (~ 10^4 erg/cm^3) and the K_1 value of α-Fe_2O_3 (~ 10^5 erg/cm^3) [5]. This large K_1 of ε-Fe_2O_3 has been reported to be due to the strong orbital hybridization of Fe and O [20]. Generally, Fe^{3+} has a d^5 electron configuration, resulting in zero orbital angular momentum (L). However, in the case of ε-Fe_2O_3, the orbital hy-

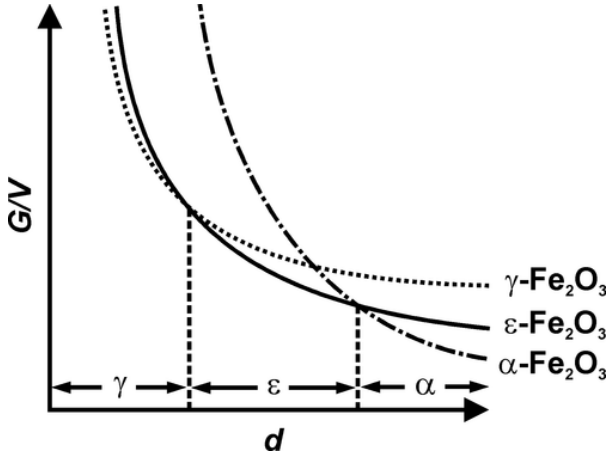

Fig. 2. Stability of individual polymorphs of Fe_2O_3 based on the calculated dependence of the free energy per volume (i.e., G/V) on the size (d) of the iron(III) oxide nanoparticles of a particular polymorph. Reproduced with permission from [3] Copyright 2010 American Chemical Society.

bridization of Fe and O alters the Fe ion's electron configuration to d^{5+q}, instead of the standard d^5 electron configuration. This increases the orbital angular momentum of Fe, leading to stronger spin-orbit coupling and consequently, a high coercive force [21].

Similar to other iron oxide polymorphs ε-Fe_2O_3 exhibits distinct band gap characteristics and semiconductor properties. The valence band in ε-Fe_2O_3 primarily consists of O2p orbitals, while the conduction band is dominated by Fe3d orbitals. Density of states (DOS) analysis from previous studies[21] shows that in ε-Fe_2O_3, the occupied Fe3d band located between -8.3 and -6.6 eV, the O2p band spans from -6.3 to -0.8 eV, and the unoccupied Fe3d band extends from +0.7 to +3.2 eV relative to the Fermi level (Fig. 3(a)) [21]. The resulting band gap is estimated to be 1.6-1.9 eV for ε-Fe_2O_3, compared to the 2.0 to 2.2 eV band gap of α-Fe_2O_3, as shown in Table 1. This band structure characterizes ε-Fe_2O_3 as a charge-transfer insulator, where electronic transitions involve electron transfer from O2p to Fe3d states [21, 22]. Such charge-transfer transitions enable efficient electron excitation under visible light, making ε-Fe_2O_3 suitable for photocatalytic applications. Density functional theory (DFT) calculations further reveal that the heterostructure of ε-Fe_2O_3 and α-Fe_2O_3 forms a type-III broken band-gap alignment, with the band edges of α-Fe_2O_3 positioned higher in energy than those of ε-Fe_2O_3 [22]. This alignment facilitates spontaneous spatial separation of photogenerated charge carriers, with electrons transferring from α-Fe_2O_3 to ε-Fe_2O_3 and holes moving in the opposite direction (Fig. 3(b)) [22]. Such charge separation reduces electron-hole recombination, enhancing photocatalytic efficiency compared to using a single material. These electronic and magnetic properties highlight the potential of ε-Fe_2O_3 as a multifunctional material. Its tunable electromagnetic properties enable diverse applications, as explored in subsequent sections.

2.2. Fabrication Methods for ε-Fe_2O_3

The unique crystal structure and excellent electromagnetic properties of ε-Fe_2O_3 show that it has significant potential as an electromagnetic functional material. However, unlike α-Fe_2O_3, which is abundant in nature, and γ-Fe_2O_3, which is easily synthesized, ε-Fe_2O_3 is strongly influenced by the surface free energy, and the ε crystalline phase is only forms under conditions that maintain a particle morphology with diameters in tens of nanometers. In 2004, high purity epsilon iron oxide was artificially synthesized by the Ohkoshi group using the reverse micelle sol-gel method [6]. In this process, surfactants such as cetyltrimethylammonium bromide (CTAB) and cetyltrimethylammonium chloride (CTAC) were used above the critical micelle concentration to create reverse micelles in oil. Then, a water-soluble iron salt solution was added to trap Fe ions in the micelles and disperse them in a lipophilic solvent, followed by the addition of silica precursors to initiate a sol-gel reaction [17, 23, 24]. This process involved emulsifying Fe ions with surfactants, trapping them in a silica matrix, which restricted the growth of iron oxide particles during subsequent heat treatment, leading to the formation of nanometer-sized ε crystalline

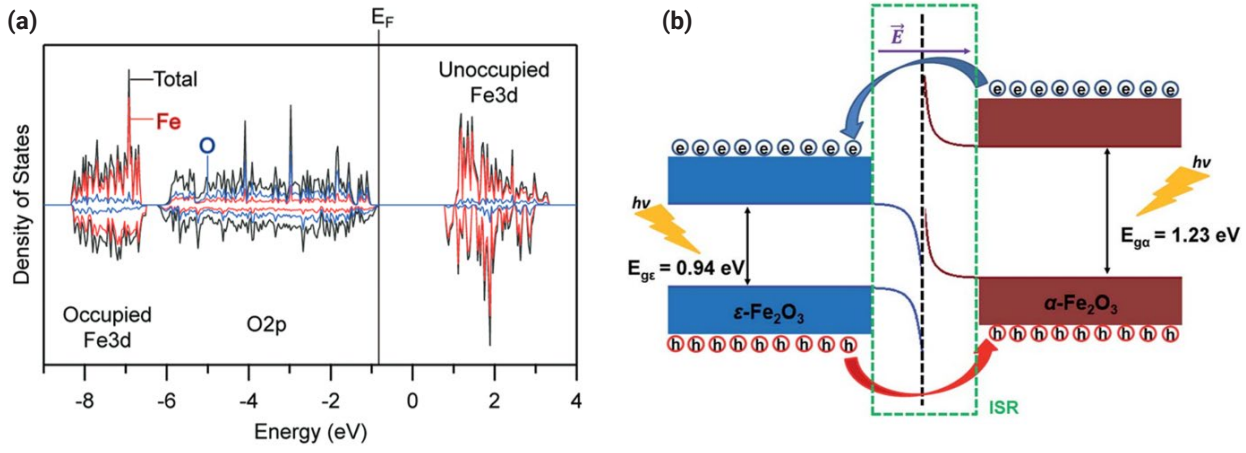

Fig. 3. (a) Density of states (DOS) of ε-Fe_2O_3, with the total DOS (black), iron DOS (red), and oxygen DOS (blue). Adapted with permission from [21] Copyright 2012 American Chemical Society, (b) Schematic diagram of band bending and the charge flow at the interface of ε-Fe_2O_3 and α-Fe_2O_3 heterostructure after connection. Adapted with permission from [22] Copyright 2020 Royal Society of Chemistry.

phases. However, the use of surfactants and oils to create reverse micelle, combined with 12-hour sol-gel reaction is inefficient in terms of yield and cost. Accordingly, efforts have been made to reduce the overall reaction time of the silica sol-gel reaction to 2 hours, though a multi-step batch process [15]. Additionally, studies have been conducted on synthesizing ε-Fe_2O_3 using cost-effective raw materials and scalable production methods. The clay mineral nontronite, an iron-rich silicate, is inexpensive, readily available, and requires no additional pretreatment, facilitating its use in low-cost synthesis [25]. Similarly, the ball milling process, a scalable mechanochemical technique for producing fine powders, has been utilized to synthesize ε-Fe_2O_3 [26]. While both methods effectively produce the ε-Fe_2O_3, they may have limitations related to secondary phase formation and elemental substitution for Fe.

Recently, a study reported the continuous preparation of ε-Fe_2O_3 nanoparticles using a spray-drying method although this method only produced micrometer-sized powders (Fig. 4)

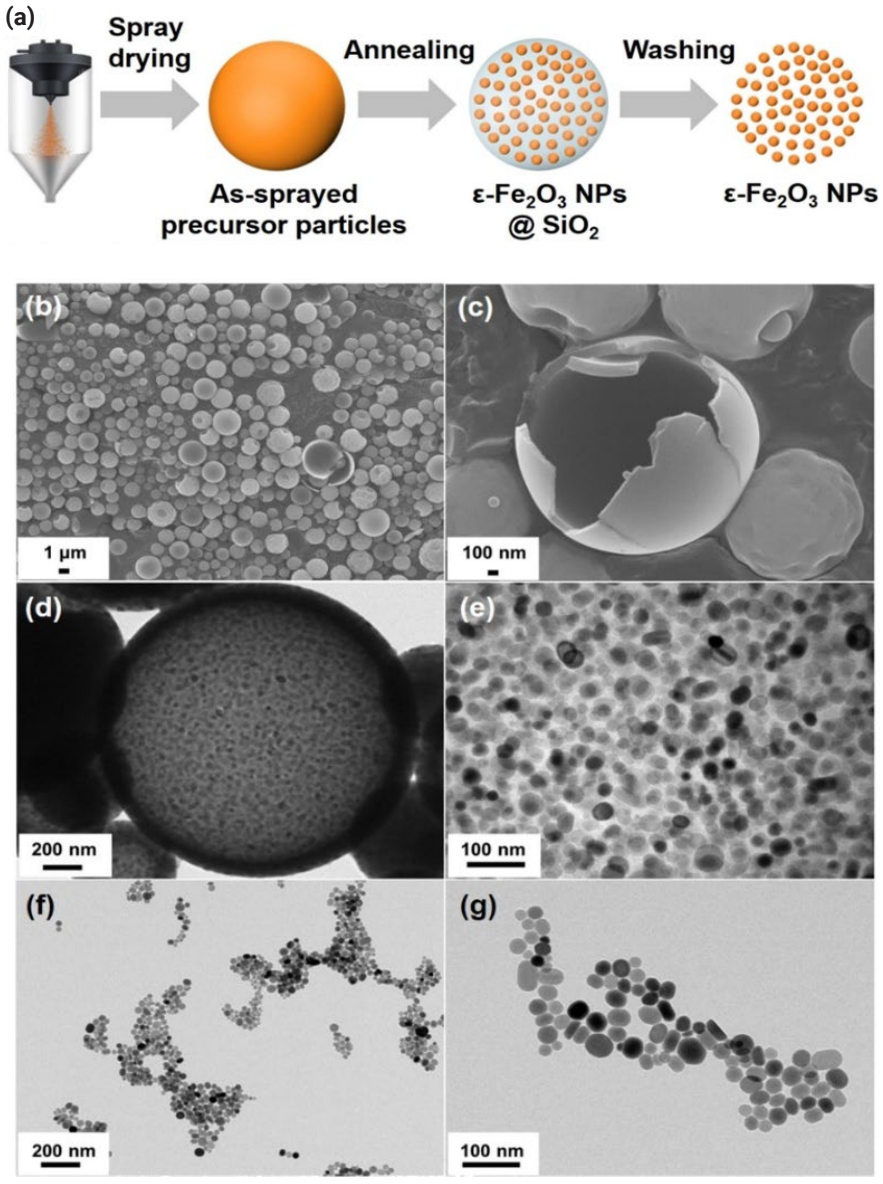

Fig. 4. (a) Schematic illustration of the preparation of ε-Fe_2O_3 nanoparticles via spray drying. (b) and (c) Scanning electron microscopy (SEM) images of as-spray-dried precursor particles with a precursor molar ratio (Fe/Si) of 0.4:1. (d) and (e) Field-emission transmission electron microscopy (FE-TEM) images of ε-Fe_2O_3 nanoparticles embedded in SiO_2 particles after annealing at 1180°C for 4 h. (f) and (g) TEM images of the corresponding ε-Fe_2O_3 NPs after SiO_2 removal. Reproduced with permission from [27] Copyright 2022 Royal Society of Chemistry.

[27]. In this approach, a water-soluble iron salt and silica precursor are homogeneously mixed to form a clear solution, which is continuously injected through a nozzle, and atomized in a high-temperature reactor. As the solution dries instantaneously, the silica forms a micrometer-sized xerogels, within which the Fe precursor is trapped, resulting in a composite powder. During subsequent heat treatment, when Fe ions inside the silica xerogel combine with oxygen to transition to the iron oxide crystalline phase. The silica matrix restricts particle growth, allowing the final particle size to be reduced 50 nm or less, leading to high purity (92.7%) formation of the ε crystalline phase. The aerosol method has been a widely used continuous manufacturing process that has been widely used in the industrial preparation of fine powders for pharmaceuticals, food, and chemicals, can produce powders in a single step without additional washing. Moreover, the method is versatile in combining different compounds into particles and allows the synthesis of composites containing dispersed Fe and Si elements without the use of surfactants. Therefore, it is expected that a commercialized technology capable of producing pure ε-phase at high yields will soon be realized. These advancements in cost-effective and scalable synthesis methods for ε-Fe_2O_3 hold significant potential for applications requiring ferromagnetic nanoparticles with high magnetic anisotropy. In particular, these nanoparticles are anticipated to find extensive use in fields such as magnetic recording media and electromagnetic wave absorbers, as further detailed in the following sections.

The ε-Fe_2O_3 crystalline phase, which occurs on the scale of a few to several tens of nanometers, has recently actively researched for the fabrication of thin films and their application in spintronic devices [28]. Spintronics devices, such as spin valves, magnetic tunnel junctions, and spin current devices, are integral to magnetoresistive random access memory (MRAM), a spintronic memory based on these devices, has been utilized as a non-volatile memory [29–32]. The operation principle of MRAMs is based on the tunnel magnetoresistance (TMR) effect, where the spin of electrons tunnels through an insulating layer located between two ferromagnetic layers, causing a change in electrical resistance depending on magnetization direction of the two layers. The change in resistance is used to store data as 0 and 1, and the magnetization direction is retained even when the power is turned off, ensuring non-volatility. One of the ferromagnetic layers has a fixed magnetization direction, requiring an anisotropic material, while the other is composed of a soft magnetic material to allow its magnetization direction to change in response to an external magnetic field or current[30]. In addition, to improve data stability and the efficiency of reading and writing, thin film fabricated in the form of single crystal rather than polycrystals, where magnetization directions may be distributed in multiple directions are more suitable for application in magnetic recording device.

Although ε-Fe_2O_3 exhibits high magnetic anisotropy, its crystalline phase, which only appears in nanoparticle form, has not been suitable for application in substrate-based devices. In previous studies, researchers attempted to immobilize a mixture of ε-Fe_2O_3 nanorods composites onto wafers using chemical vapor deposition (CVD) [33], but a significant reduction in magnetic properties was observed compared to the nanoparticle form. This reduction was speculated to result from decreased ordering of the crystal structure [18]. Therefore, it is crucial to study the preparation of ε-Fe_2O_3 in thin film form while preserving its unique magnetic properties, and various preparation methods have been tried. Gich group used pulsed laser deposition (PLD) to form single crystal thin films, stabilizing the ε crystalline phase through epitaxial modification on $SrTiO_3$ single crystal substrates, or by using a $GaFeO_3$ buffer layer with the same structure as ε-Fe_2O_3 to promote the growth of ε-Fe_2O_3 thin films. These thin film exhibited a coercivity of about 8 kOe [34]. Also, in 2017, Corbellini group successfully achieved the growth of (001)-oriented ε-Fe_2O_3 epitaxial thin films on single crystal zirconia (YSZ) (100) substrates using PLD (Fig. 5) [18]. This study is the result of growing ε-Fe_2O_3 thin films directly on the YSZ substrate, which are commonly used to grow oxides on silicon wafers in the (100) orientation. This suggests the potential for directly growth of ε-Fe_2O_3 thin films on silicon wafers, an important milestone for expanding applications to large-area devices. The Curie temperature of the prepared thin film was 460 K, showed a similar level to the Curie temperature observed in the nanoparticle form (approximately 490 K). However, the PLD has limitations, including the needs for high deposition temperature (700-900 K) and lattice-matched substrate. For the practical application of ε-Fe_2O_3 thin films, it is essential to develop methods that can form thin films at lower temperatures or to explore new fabrication technique compatible with a wider range of substrates.

Recently, a method for fabricating high-purity ε-Fe_2O_3 thin films without a lattice-matched substrate at a low temperature of 280°C using the atomic layer deposition (ALD) has been devised [19]. ALD is a chemical vapor deposition method that uses chemical precursors under relatively low vacuum (10^{-2} to 10 mbar) and low temperature (< 400 °C), enabling atomically

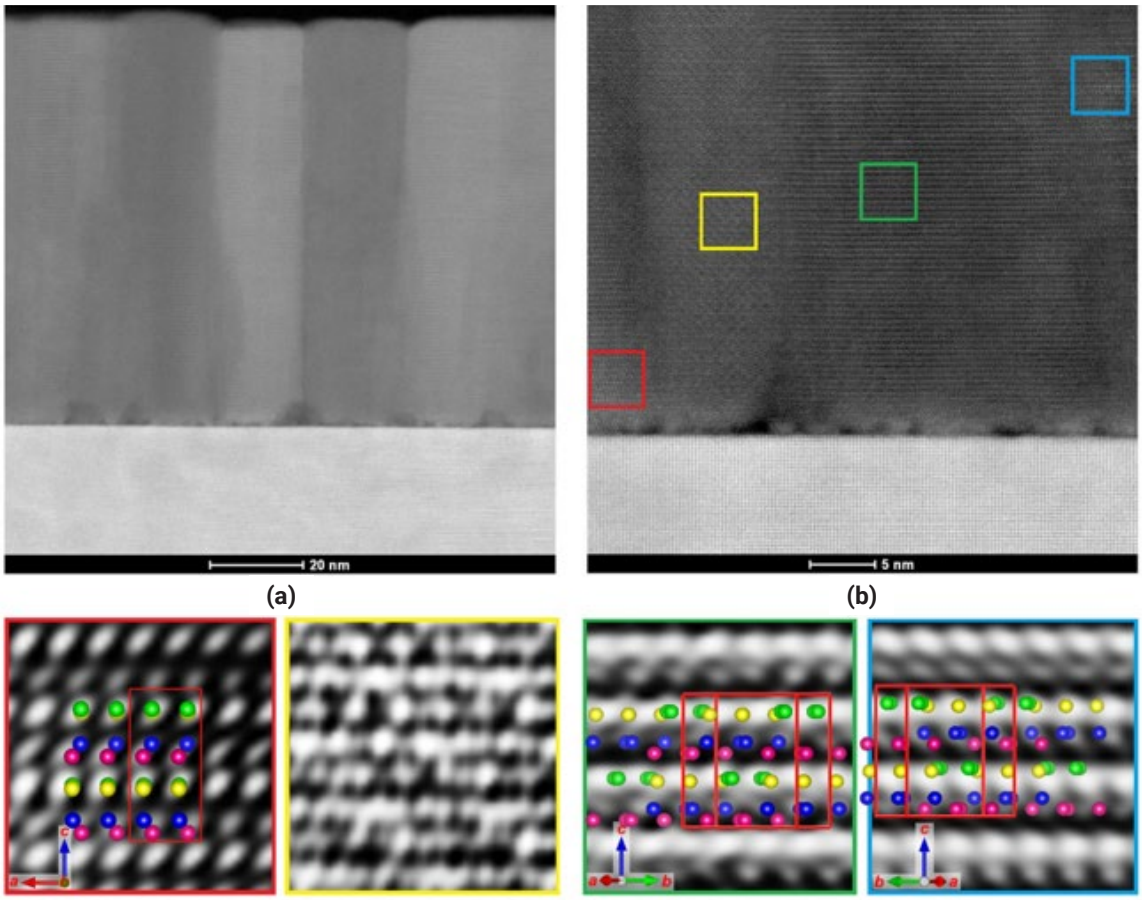

Fig. 5. (a) STEM image of an approximately 100-nm-thick film of ε-Fe_2O_3 on YSZ (100) highlighting the formation of pillar-like twins, (b) details of the interface between the substrate and the film, evidencing the formation of "bubbles" of a foreign phase (most likely Fe_3O_4) at the interface. Reproduced with permission from [18] Copyright 2017 Nature.

precise thickness control and fine composition control. The iron oxide thin films prepared by ALD are ε crystalline phase, with only 2.5% α crystalline phase impurities. As shown in the M-H curve (Fig. 6) [35], there was no kink resulting from soft magnetic phase (typically γ-Fe_2O_3) admixture, confirming the formation of high-purity ε-Fe_2O_3 thin films. Furthermore, ^{57}Fe Mössbauer measurements identified the four distinct Fe sites inherent to the ε crystalline phase. While the low-temperature transition observed in nanoparticles between 110 K and 150 K was shifted to the higher temperature range in the thin film, the transition was still present. This shift in transition temperature, characteristic of the thin film, was attributed to grain boundaries and substrate-induced strain. The use of ALD for ε-Fe_2O_3 thin film holds significant potential for broader applications, as it does not require a lattice-matched substrate. The development represents an advancement in expanding the application range of ε-Fe_2O_3. Furthermore, it is expected to play a critical role in advanced technological applications, such as photocatalytic devices that require its semiconducting properties and efficient charge carrier transport, as discussed in subsequent sections.

3. Applications of ε-Fe_2O_3

3.1. Millimeter-Wave Absorption Applications

The high magnetic anisotropy of ε-Fe_2O_3 has attracted attention for its potential application as a millimeter wave (30-300 GHz) absorber and is currently under active investigation. Electromagnetic wave absorbers are classified into conduction loss, dielectric loss, and magnetic loss materials, which attenuate the incident electromagnetic waves. Among these, magnetic loss materials offer the advantage of more effective electromagnetic wave absorption in high frequency bands, due to magnetic loss caused by the imaginary component of permeability, al-

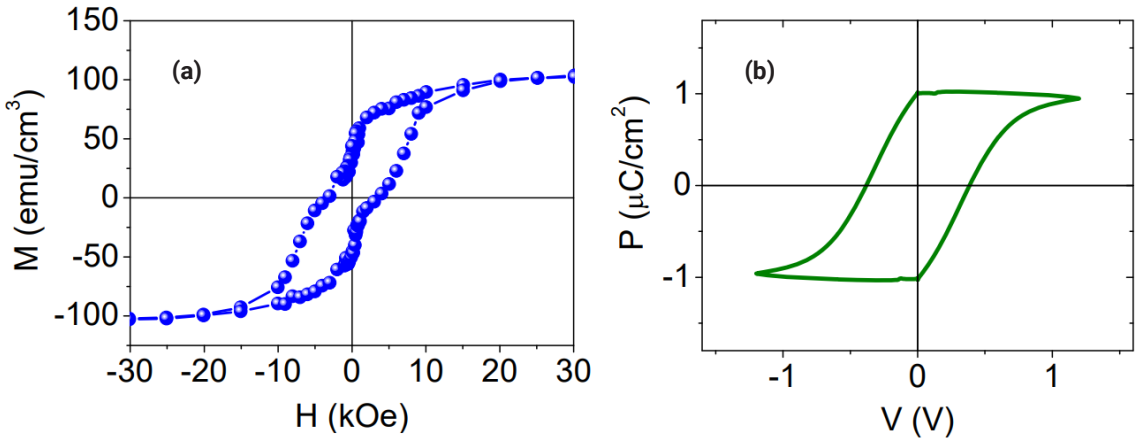

Fig. 6. (a) Magnetization hysteresis loop at 300 K of ε-Fe_2O_3/$AlFeO_3$//Nb:STO(111). (b) Ferroelectric hysteresis loop measured at 300 K and 10 Hz with 100 ms of delay time. Reproduced with permission from [34] Copyright 2014 Wiley-VCH.

lowing them to selectively absorb electromagnetic signals in specific frequency bands. This phenomenon is attributed to the ferromagnetic resonance of magnetic materials, where ferromagnetic materials in a magnetic field selectively absorb specific frequencies. When a ferromagnet is exposed to electromagnetic waves, its spins precess around the magnetization axis, absorbing electromagnetic waves at a frequency that matches the precession. The natural resonance frequency (f_r) is proportional to the anisotropic field (H_a) as shown in the equation (3) below [35], where v is the gyromagnetic constant.

$$f_r = \left(\frac{v}{2\pi}\right) \times H_a \quad (3)$$

Therefore, to adjust the frequency band to be absorbed, the magnetic anisotropy of the magnetic material must be adjusted, which can be achieved through control of the material composition. ε-Fe_2O_3 has been reported to exhibit ferromagnetic resonance absorption at approximately 180 GHz due to its high H_a [17]. The crystalline magnetic anisotropy of ε-Fe_2O_3 can also be controlled by substituting transition metal element at the Fe sites, and studies have been conducted to adjust the absorption band accordingly (Fig. 7(a)-(b)) [17, 36]. It has been reported that substitution Fe^{3+} (S = 5/2) with non-magnetic ion such as Ga^{3+} and Al^{3+} (S = 0) can modulate f_r over a wide range by substituting Fe_D or Fe_A sites. When substituted with Ga (ε-$Ga_xFe_{2-x}O_3$) and Al (ε-$Al_xFe_{2-x}O_3$), it has been reported that f_r can be adjusted from 35 GHz (x = 0.67) to 147 GHz (x = 0.10)[17] and from 182 GHz (x = 0.04) to 112 GHz (x = 0.4), respectively, depending on the content (x = 0.10 ~ 0.67) and (x = 0.04 ~ 0.4)[36]. Conversely, f_r was found to increase when the spin-orbit interaction was enhanced by substituting Rh^{3+}, which has a larger orbital angular momentum than Fe^{3+} [37]. With Rh substitution, H_c increased up to 3.5 T [16], and for ε-$Rh_{0.14}Fe_{1.86}O_3$, a H_c of 2.7 T and f_r of 209 GHz were observed (Fig. 7(c)) [37].

In addition, complex substitution of various elements on ε-Fe_2O_3 is also being actively studied. A representative example is the co-substitution of Co^{2+}(S = 3/2), Ti^{4+} and Ga^{3+} (ε-$Ga_xTi_yCo_yFe_{2-x-y}O_3$). This combination is notable because the large magnetic anisotropy in the a-axis direction, caused by the orbital angular momentum of Fe^{3+} at the Fe_B site, is counteracted by the magnetic anisotropy of Co^{2+}, which substitutes for Fe_D along the c-axis direction (Fig. 7(d)-(e)) [38]. As a result, the crystalline magnetic anisotropy is significantly reduced, lowering the coercivity to below 3 kOe [38]. In addition, to utilize this material as a more efficient millimeter-wave absorber, a study was conducted in which ceramic nanopowders with high conductivity (Ti_4O_7) were applied to achieve both dielectric loss and magnetic loss effect [16, 38]. This resulted in a high dielectric constant, as electron transfer on the Ti_4O_7 surface was blocked at the iron oxide nanoparticle interface, inhibiting the current flow. When prepared as a thin film (216 μm), it exhibited 99.8% absorption capacity (RL = -27.2 dB) at 80 GHz with a broadband width of 16.2 GHz (Fig. 8) [39]. ε-Fe_2O_3 can serve as an effective absorber in the millimeter-wave band due to a large magnetic anisotropy, and the absorption band can be tuned by controlling the substitutional composition. This demonstrates its potential as a multifunctional absorber capable of responding to wide band of electromagnetic waves, making it suitable for 6G mobile communication applications.

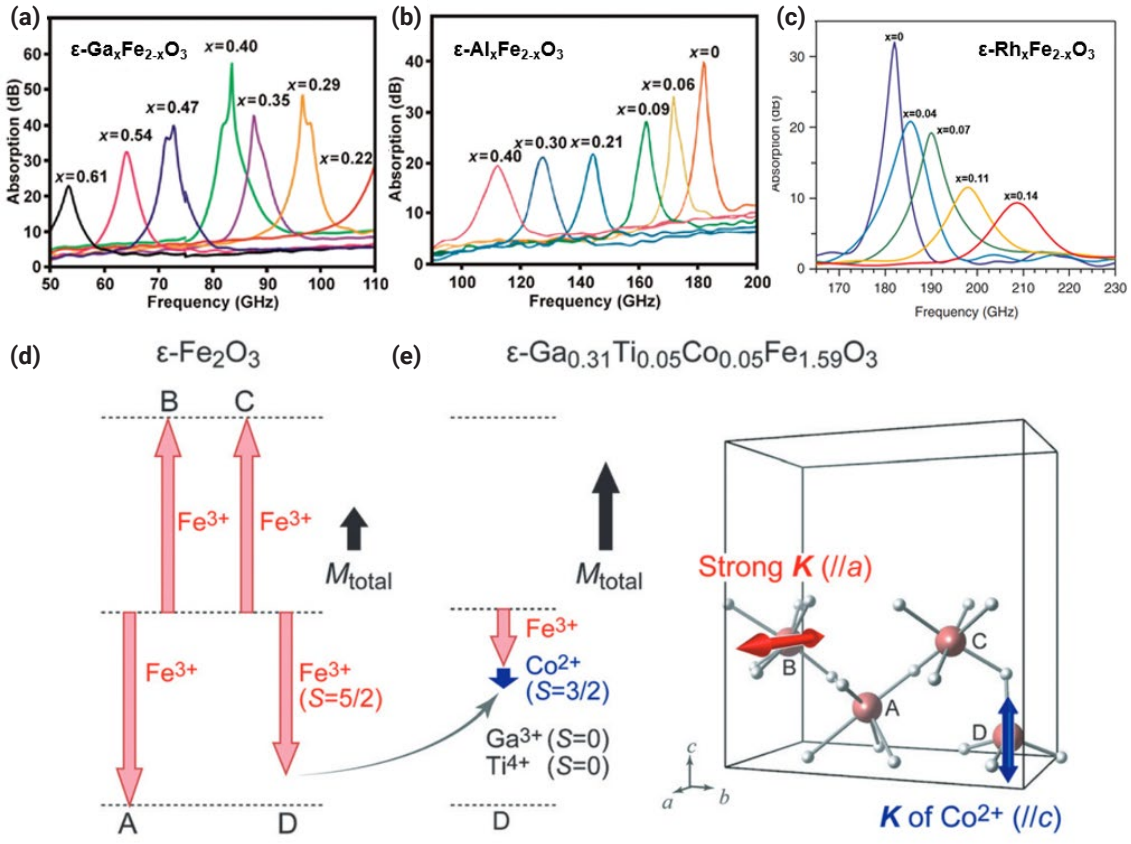

Fig. 7. Absorption spectra of Absorption spectra of (a) ε-GaxFe$_{2-x}$O$_3$. Adapted with permission from [17]. Copyright 2007 Wiley-VCH. (b) ε-AlxFe$_{2-x}$O$_3$. Adapted with permission from [36]. Copyright 2008 American Chemical Society. (c) ε-RhxFe$_{2-x}$O$_3$. Adapted with permission from [37]. Copyright 2012 Nature. Magnetic structure of (d) ε-Fe$_2$O$_3$ and (e, left) ε -Ga$_{0.31}$Ti$_{0.05}$Co$_{0.05}$Fe$_{1.59}$O$_3$. Red and blue arrows denote the sublattice magnetizations of Fe^{3+} and Co^{2+}, respectively. Black arrows show the total magnetization. (e, Right) The direction of the single-ion anisotropies (*K*, red and blue arrows) for Fe^{3+} at the B site along *a*-axis and Co^{2+} at the D site along *c*-axis. Adapted with permission from [38] Copyright 2016 Wiley-VCH.

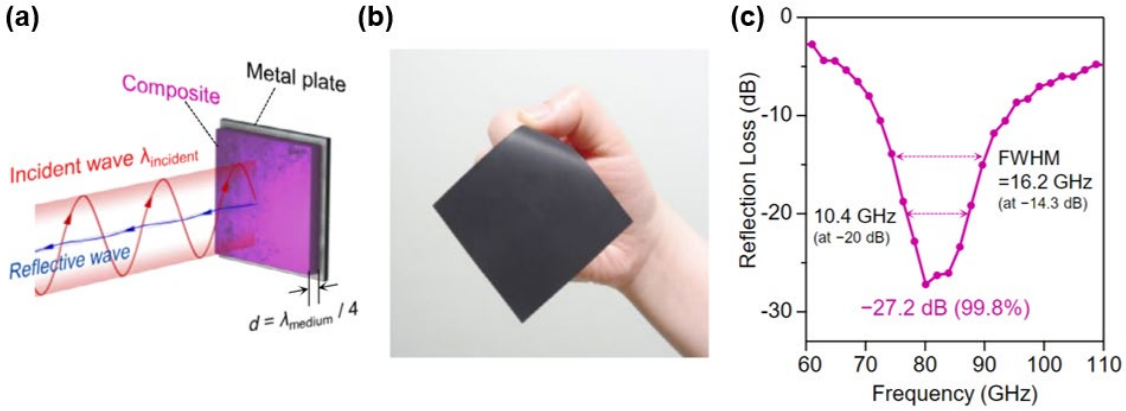

Fig. 8. (a) Schematic illustration of phase matching for absorption, (b) photograph, and (c) observed RL spectrum of the flexible millimeter-wave–absorbing ultrathin film composed of the Ti$_4$O$_7$@ε-Ga$_{0.21}$Ti$_{0.05}$Co$_{0.05}$Fe$_{1.69}$O$_3$ composite and acrylic acid ester polymer on a copper foil. Adapted with permission from [39] Copyright 2021 Wiley-VCH.

3.2. High-Density Magnetic Recording Media Applications

In the era of big data, the need for high-density magnetic recording media capable of reliably storing and managing large amounts of data over long periods become increasingly important [40–43]. Currently, magnetic recording tapes are mainly composed of magnetic materials such as spindle Co-Fe alloy nanoparticles or barium ferrite, which play an crucial role in long-term data storage across various fields such as insurance, finance, broadcasting, and web services [44–47]. To achieve high-density recording, it is essential to reduce the size of the magnetic filler particles used in these tapes. However, the reduction in size lead to several side effects. In the case of metallic alloys, a decrease in particle size increases the surface area, which raises the potential for oxidation and can result in pyrophoric character. On the other hand, iron oxides such as barium ferrite and magnetite do not exhibit pyrophoric character, but as their particle size decreases, they may lose magnetic ordering, potentially leading to a transition to superparamagnetism. As a solution to this issue, ε-Fe_2O_3 particles have been found to have a superparamagnetic limit at a particle size of 7.5 nm, allowing them to maintain a smaller size compared to barium ferrite (20-25 nm) [48]. This indicates that ε-Fe_2O_3 has significant potential as an ultra-high-density magnetic recording media.

Furthermore, magnetic particles in the form of multiple magnetic domains, rather than single magnetic domain are likely to have their spins only partially aligned due to their magnetic anisotropy. While this partial alignment does not affect data playback but it raises concerns about potential noise generation. Therefore, ε-Fe_2O_3 with its low superparamagnetic limit, well-maintained magnetic arrangement can be synthesized with single magnetic domain sphere sizes ranging from 8 to 30 nm, making it a suitable candidate for ultra-high-density magnetic recording media. However, ε-Fe_2O_3 exhibits a high coercivity of more than 20 kOe at room temperature, which can decrease the efficiency of information storage if used in its original form. To address this issue, research has been conducted to adjust the coercivity by substituting Fe with transition metal elements. Since magnetic fillers suitable for magnetic recording media typically require a coercivity of around 3 kOe, the Ohkoshi group has worked on modifying the coercivity by substituting element such as Ga, Ti and Co [16, 38, 49, 50].

In particular, the $Ga_{0.31}Ti_{0.05}Co_{0.05}Fe_{1.59}O_3$ case exhibits a magnetization value of 23.4 emu/g at 7 T, which represents a 44% increase from the original ε-Fe_2O_3 value of 16.2 emu/g. This increase is attributed to the substitution of Fe^{3+} ions (S = 5/2) with Ga^{3+} (S = 0), Ti^{4+} (S = 0), and Co^{2+} (S = 3/2) at rates of 48%, 10%, and 10%, respectively. The total magnetization of ε-Fe_2O_3 is determined by the sum of the positive sublattice magnetization (M_B, M_C > 0) at the Fe_B and Fe_C sites and the negative sublattice magnetization (M_A, M_D < 0) at the Fe_A and Fe_D sites. Ga substitution reduces the negative sublattice magnetization at Fe_D, thereby increasing the overall magnetization value. Furthermore, the coercivity (H_c) was adjusted to below 2.69 kOe through element substitution. This reduction in H_c is attributed to the compensating effect of the single-ion magnetic anisotropy of Fe^{3+} and Co^{2+}. First-principles calculations indicate the ε-Fe_2O_3 crystal phase originally exhibits a strong magnetic anisotropy along the a-axis, which arises from the orbital angular momentum resulting from the hybridization between Fe^{3+} and O^{2-}ions at the Fe_B site. However, the substitution of Co^{2+} ions at Fe_D sites introduces magnetic anisotropy along the c-axis, which appears to offset the magnetic anisotropy along the a-axis, thereby reducing the coercivity to below 3 kOe [38]. The resulting ε-Fe_2O_3 nanoparticles were dispersed in a urethane resin and vinyl chloride polymer and then coated on a non-magnetic polyethylene (PE) film while an external magnetic field was applied (Fig. 9) [38]. During this process, the ε-Fe_2O_3 nanoparticles were oriented vertically, forming a coated magnetic tape. Compared to commercial CoFe alloys from Dowa Electric Materials, the magnetic recording tape produced exhibited a sharper power spectrum and a higher signal-to-noise ratio (S/N) than existing commercial products. This indicates the high potential of ε-Fe_2O_3 nanoparticles as a magnetic recording media. This study demonstrates that magnetic recording media utilizing the properties of ε-Fe_2O_3 can outperform current commercial materials, highlighting its potential application as a next-generation high-density magnetic recording media.

3.3. Visible light catalytic Applications

Solar hydrogen production is an environmentally friendly method to produce hydrogen by utilizing clean, renewable energy sources. It has gained significant attention as a key technology for building a sustainable hydrogen economy. The main approaches include photoelectrochemical (PEC) water splitting, photocatalytic water splitting, and photo-reforming using oxygenated organic compounds (OOCs), all of which aim to minimize greenhouse gas emissions and maximize energy efficiency. Recently, research has focused on the potential of ε-Fe_2O_3, which can absorb visible light.

Currently, PEC water splitting has attracted considerable at-

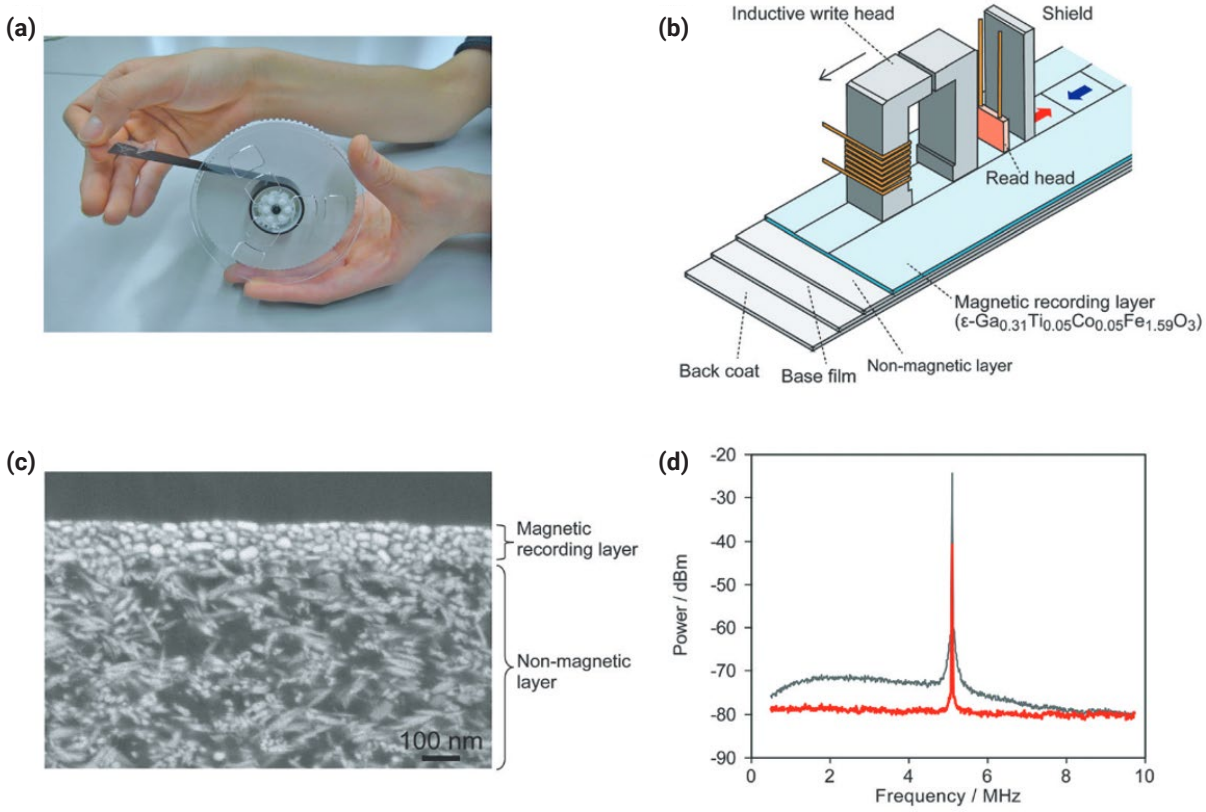

Fig. 9. (a) Photograph of the manufactured magnetic recording tape composed of ε-$Ga_{0.31}Ti_{0.05}Co_{0.05}Fe_{1.59}O_3$. (b) Schematic illustration of the LTO-3 AMR head. (c) Cross-section SEM image of the manufactured magnetic tape. (d) Power spectrum of the signal of the ε-$Ga_{0.31}Ti_{0.05}Co_{0.05}Fe_{1.59}O_3$ tape (red line) and cobalt–iron alloy tape (gray line) measured with the LTO-3 AMR head. Reproduced with permission from [38] Copyright 2016 Wiley-VCH.

tention from researchers, and it has been found that ferroelectric materials can play an important role as PEC catalysts. This is due to the internal electric field induced by their spontaneous electric polarization, which can enhance the separation of electron-hole pairs generated by sunlight[51-53]. Conventional ferroelectrics such as $BaTiO_3$ and $Pb(Zr_x,Ti_{1-x})O_3$ have bandgaps greater than 3 eV, making them unsuitable for use in the visible light range. In contrast, $BiFeO_3$ possesses a relatively narrow bandgap (≈2.2–2.8 eV) and exhibits the largest spontaneous polarization (100 μC cm^{-2}) [54]. However, the solar energy conversion efficiency of $BiFeO_3$ remains limited due to the rapid recombination rate of photoexcited charge carriers[50]. On the other hand, Fe_2O_3 is a well-known photocatalyst for solar hydrogen production due to its visible light absorption (bandgap ≈ 2.1 eV), non-toxicity, and low cost [55-58]. However, its primary drawbacks low electrical conductivity, hole diffusion length of 2-4 nm, and low absorption coefficient have resulted in solar-to-hydrogen conversion values that are lower than theoretically predicted, with photocurrent reaching up to 12 mA cm^{-2} [59, 60]. To overcome the limitations of these single photocatalysts and enhance solar energy conversion efficiency, a study on nanocomposite photocatalysts based on heterojunction of ε-Fe_2O_3 and $BiFeO_3$ was published[61]. In this study, a photoelectrode for solar water splitting was fabricated based on a heterostructure in which $BiFeO_3$ nanopillars were vertically embedded into an ε-Fe_2O_3 matrix thin film using the PLD (Fig. 10) [61]. By optimizing the photodegradation performance through the adjustment of the ratio between the two materials, the $BiFeO_3$-ε-Fe_2O_3 photoelectrode containing 9% ε-Fe_2O_3 exhibited more than double the photocurrent (0.19 mA cm^{-2}) compared to the single-material sample. Additionally, it maintained high stability under continuous light irradiation for 25 hours. This result can be explained by the charge separation effect caused by band-bending between the two materials. When the two materials are contacted, free charge carriers are redistributed across the interface until equilibrium is achieved, leading to the realignment of the Fermi (Fig. 10(g)-(h)) [61]. Since the work function of $BiFeO_3$ (approximately 4.95 eV) is smaller

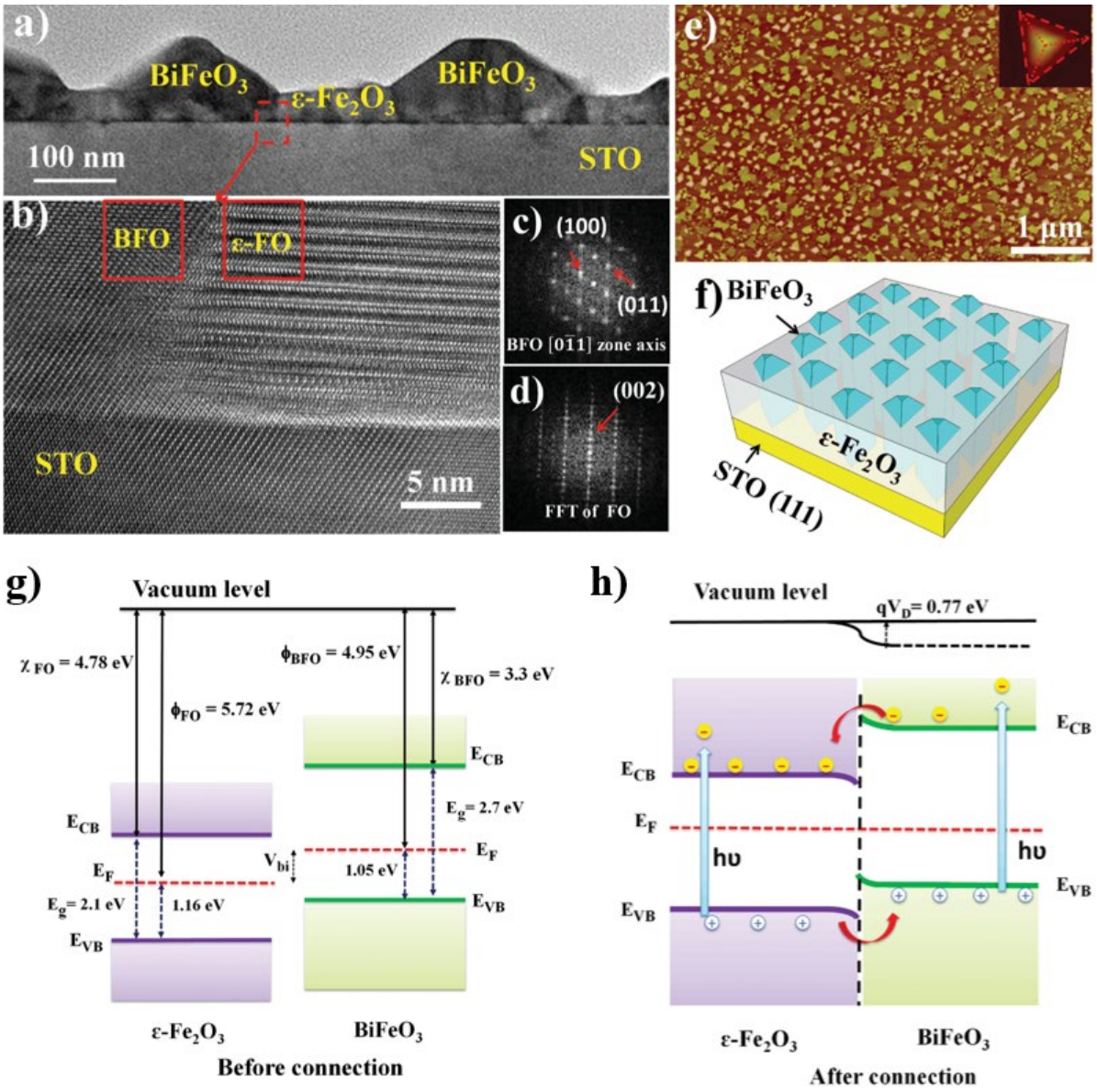

Fig. 10. (a) Cross-sectional TEM image of BFO-FO heterostructures on STO substrate. (b) High-resolution TEM image showing the interfaces between films and STO substrates. The corresponding FFT patterns of (c) BFO and (d) ε-FO. (e) Top view. (f) Schematic of the self-assembled BFO-FO vertical heterostructures with BFO pillars embedded in the ε-FO matrix. (g), (h) Schematic diagrams illustrating the energy band alignment and the expected charge flow at the BFO-FO heterojunction under light excitation. Adapted with permission from [61] Copyright 2016 Wiley-VCH.

than that of ε-Fe_2O_3 (approximately 5.72 eV) [61-63], electrons migrate from $BiFeO_3$ to ε-Fe_2O_3. This migration forms a charge region at the heterointerface and induces band-bending, which results in hole accumulation (electron deficiency) at the $BiFeO_3$ interface. Due to this band-bending, photoexcited electrons can easily migrate from $BiFeO_3$ to ε-Fe_2O_3, while holes can migrate from ε-Fe_2O_3 to $BiFeO_3$, significantly inhibiting electron-hole recombination. In other words, ε-Fe_2O_3, with a bandgap corresponding to visible light, can be utilized as a photocatalytic material. Furthermore, it is a promising material for enhancing photocurrent by inducing charge separation when combined with existing materials.

ε-Fe_2O_3 has also been actively studied as a photocatalyst for the photoreforming of oxygen-containing organic compounds such as ethanol, glycerol, and glucose [9]. This approach to hydrogen production via biomass photoreforming offers signifi-

cant environmental benefits by simultaneously removing pollutants and processing waste from the biomass industry [64-66]. Although α-Fe_2O_3 has traditionally been used as visible light catalyst due to its low fabrication cost and ease of processing into various nanostructures, its performance has been constrained by factors such as a low absorption coefficient, high recombination losses of charge carriers, and a short diffusion length of charge carriers [2, 67]. To retain the advantages of α-Fe_2O_3 while overcoming its disadvantages, ε-Fe_2O_3 and β-Fe_2O_3 polymorphs of Fe_2O_3 were prepared by chemical vapor deposition (CVD) and their performance was compared in this study. The catalytic activity of the Fe_2O_3 polymorphs increased in the order of α-Fe_2O_3 < ε-Fe_2O_3 < β-Fe_2O_3 with the average hydrogen production rate of ε-Fe_2O_3 reaching 125 mmol h^{-1} m^{-2}, which was significantly higher than that of α-Fe_2O_3 [9]. Additionally, ε-Fe_2O_3 demonstrated better photocorrosion resistance than α-Fe_2O_3, indicating its ability to maintain photocatalytic activity over an extended period. Stable hydrogen generation was observed for at least 20 hours of continuous irradiation, demonstrating the robustness and reliability of ε-Fe_2O_3 as a photocatalyst. This study shows that ε-Fe_2O_3 is a promising alternative material that can overcome the limitations of α-Fe_2O_3 and make an important contribution to the development of high-performance photocatalysts.

4. Summary

Epsilon iron oxide (ε-Fe_2O_3) has attracted attention for various advanced applications, including millimeter-wave absorbers, high-density magnetic storage media, and photocatalysis, due to its unique magnetic and electronic properties. Specifically, its high magnetic anisotropy and coercivity set ε-Fe_2O_3 apart from conventional magnetic materials, enhancing its potential as an electromagnetic wave absorber in the millimeter-wave band and as a high-density magnetic storage media. In addition, its semiconducting property of visible light absorption suggests potential applications as a catalyst for solar hydrogen production. To maximize the electromagnetic functionality of ε-Fe_2O_3, it is crucial to synthesize it in high purity and stable form. Various synthesis methods have been developed, successfully yielding nanoparticles and thin films. Advances in the continuous manufacturing process of ε phase nanoparticles, which are particularly challenging to prepare, are expected to further promote the practical applications of ε-Fe_2O_3 across various applications.

Future research will need to focus on optimizing the properties of ε-Fe_2O_3 for each application and developing structural design and fabrication techniques to enhance performance. For example, magnetic property optimization and composite structuring to enhance absorption in high-frequency band, control of thin film structure for spintronics device applications, and design of heterostructure to improve efficiency as photocatalysts will become a key area of research. With continued research, ε-Fe_2O_3 is expected to become a core material in various industries including 6G wireless communication, spintronic devices, high-density magnetic storage, and hydrogen production, serving as a next-generation electromagnetic functional material.

Funding

This research was supported by the Basic Research Program (PNK9960) of Korea Institute of Materials Science.

Conflict of Interest

The authors declare no relevant conflicts of interest.

Author Information and Contribution

Jihyeong Jeong : Writing a manuscript and researching previous studies, Hwanhee Kim and Jung-Goo Lee: data organization and researching previous studies, Youn-Kyoung Baek: Supervision, reviewing and editing.

Acknowledgement

None.

References

[1] S. Piraman, S. Sundar, R. Mariappan, Y. Y. Kim and K. Min: Sens. Actuators, B Chem., **234** (2016) 386.
[2] K. Sivula, F. Le Formal and M. Grätzel: ChemSusChem, **4** (2011) 432.
[3] J. Tuček, R. Zbořil, A. Namai and S. I. Ohkoshi: Chem. Mater., **22** (2010) 6483.
[4] L. MacHala, J. Tuček and R. Zbořil: Chem. Mater., **23** (2011) 3255.
[5] S. Sakurai, A. Namai, K. Hashimoto and S. I. Ohkoshi: J. Am. Chem. Soc., **131** (2009) 18299.
[6] J. Jin, S. I. Ohkoshi and K. Hashimoto: Adv. Mater., **16**

(2004) 48.
[7] A. S. Teja and P. Y. Koh: Prog. Cryst. Growth Charact. Mater., **55** (2009) 22.
[8] I. Ahamed, R. Pathak, R. Skomski and A. Kashyap: AIP Adv., **8** (2018) 148.
[9] G. Carraro, C. MacCato, A. Gasparotto, T. Montini, S. Turner, O. I. Lebedev, V. Gombac, G. Adami, G. Van Tendeloo, D. Barreca and P. Fornasiero: Adv. Funct. Mater., **24** (2014) 372.
[10] O. Malina, J. Tuček, P. Jakubec, J. Kašlík, I. Medřík, H. Tokoro, M. Yoshikiyo, A. Namai, S. I. Ohkoshi and R. Zbořil: RSC Adv., **5** (2015) 49719.
[11] C. Liu, N. Zhang, Y. Li, R. Fan, W. Wang, J. Feng, C. Liu, J. Wang, W. Hao, Z. Li and Z. Zou: Nat. Commun., **14** (2023) 1.
[12] G. Carraro, D. Barreca, M. Cruz-Yusta, A. Gasparotto, C. MacCato, J. Morales, C. Sada and L. Sánchez: ChemPhysChem, **13** (2012) 3798.
[13] M. M. Rahman, A. Jamal, S. B. Khan and M. Faisal: Superlattices Microstruct., **50** (2011) 369.
[14] M. Li, J. Wu and G. Shen: Catal. Sci. Technol., **12** (2022) 2659.
[15] E. Gorbachev, M. Soshnikov, M. Wu, L. Alyabyeva, D. Myakishev, E. Kozlyakova, V. Lebedev, E. Anokhin, B. Gorshunov, O. Brylev, P. Kazin and L. Trusov: J. Mater. Chem. C, **9** (2021) 6173.
[16] H. Tokoro, A. Namai and S. I. Ohkoshi: Dalt. Trans., **50** (2021) 452.
[17] S. Ohkoshi, S. Kuroki, S. Sakurai, K. Matsumoto, K. Sato and S. Sasaki: Angew. Chem., **119** (2007) 8544.
[18] L. Corbellini, C. Lacroix, C. Harnagea, A. Korinek, G. A. Botton, D. Ménard and A. Pignolet: Sci. Rep., **7** (2017) 3712.
[19] T. Jussila, A. Philip, J. Lindén and M. Karppinen: Adv. Eng. Mater., **25** (2023) 2201262.
[20] S. I. Ohkoshi, A. Namai and S. Sakurai: J. Phys. Chem. C, **113** (2009) 11235.
[21] M. Yoshikiyo, K. Yamada, A. Namai and S. I. Ohkoshi: J. Phys. Chem. C, **116** (2012) 8688.
[22] I. Ahamed, N. Seriani, R. Gebauer and A. Kashyap: RSC Adv., **10** (2020) 27474.
[23] S. Sakurai, K. Tomita, K. Hashimoto, H. Yashiro and S. I. Ohkoshi: J. Phys. Chem. C, **112** (2008) 20212.
[24] S. Sakurai, J. I. Shimoyama, K. Hashimoto and S. I. Ohkoshi: Chem. Phys. Lett., **458** (2008) 333.
[25] K. Kelm and W. Mader: Z. Anorg. Allg. Chem., **631** (2005) 2383.
[26] Y. Zhao and G. Wen: J. Magn. Magn. Mater., **512** (2020) 167039.
[27] G. R. Jo, M. B. Yun, Y. Hun Son, B. Park, J. G. Lee, Y. G. Kim, Y. G. Son and Y. K. Baek: Chem. Commun., **58** (2022) 11442.
[28] S. M. Suturin, A. M. Korovin, S. V. Gastev, M. P. Volkov, A. A. Sitnikova, D. A. Kirilenko, M. Tabuchi and N. S. Sokolov: Phys. Rev. Mater., **2** (2018) 1.
[29] S. Bhatti, R. Sbiaa, A. Hirohata, H. Ohno, S. Fukami and S. N. Piramanayagam: Mater. Today, **20** (2017) 530.
[30] S. A. Wolf, D. D. Awschalom, R. A. Buhrman, J. M. Daughton, S. Von Molnár, M. L. Roukes, A. Y. Chtchelkanova and D. M. Treger: Science, **294** (2001) 1488.
[31] S. A. Wolf, J. Lu, M. R. Stan, E. Chen and D. M. Treger: IEEE, **98** (2010) 2155.
[32] A. Fert: Rev. Mod. Phys., **80** (2008) 1517.
[33] D. Barreca, G. Carraro, D. Peeters, A. Gasparotto, C. Maccato, W. M. M. Kessels, V. Longo, F. Rossi, E. Bontempi, C. Sada and A. Devi: Chem. Vap. Depos., **20** (2014) 313.
[34] M. Gich, I. Fina, A. Morelli, F. Sánchez, M. Alexe, J. Gàzquez, J. Fontcuberta and A. Roig: Adv. Mater., **26** (2014) 4645.
[35] C. Kittel: Phys. Rev., **71** (1947) 270.
[36] A. Namai, S. Sakurai, M. Nakajima, T. Suemoto, K. Matsumoto, M. Goto, S. Sasaki and S. I. Ohkoshi: J. Am. Chem. Soc., **131** (2008) 1170.
[37] A. Namai, M. Yoshikiyo, K. Yamada, S. Sakurai, T. Goto, T. Yoshida, T. Miyazaki, M. Nakajima, T. Suemoto, H. Tokoro and S. I. Ohkoshi: Nat. Commun., **3** (2012) 1035.
[38] S. ichi Ohkoshi, A. Namai, M. Yoshikiyo, K. Imoto, K. Tamazaki, K. Matsuno, O. Inoue, T. Ide, K. Masada, M. Goto, T. Goto, T. Yoshida and T. Miyazaki: Angew. Chem. Int. Ed., **55** (2016) 11403.
[39] R. Kinugawa, K. Imoto, Y. Futakawa, S. Shimizu, R. Fujiwara, M. Yoshikiyo, A. Namai and S. I. Ohkoshi: Adv. Eng. Mater., **23** (2021) 2001473.
[40] G. Cherubini, C. C. Chung, W. C. Messner and S. O. R. Moheimani: IEEE Trans. Control Syst. Technol., **20** (2012) 296.
[41] H. Nishio and H. Yamamoto: IEEE Trans. Magn., **46** (2010) 3747.
[42] S. I. Ohkoshi, K. Imoto, A. Namai, M. Yoshikiyo, S. Miyashita, H. Qiu, S. Kimoto, K. Kato and M. Nakajima: J. Am. Chem. Soc., **141** (2019) 1775.
[43] S. ichi Ohkoshi, M. Yoshikiyo, K. Imoto, K. Nakagawa, A. Namai, H. Tokoro, Y. Yahagi, K. Takeuchi, F. Jia, S. Miyashita, M. Nakajima, H. Qiu, K. Kato, T. Yamaoka, M. Shirata, K.

Naoi, K. Yagishita and H. Doshita: Adv. Mater., **32** (2020) 139821.
[44] I. Tudosa, C. Stamm, A. B. Kashuba, F. King, H. C. Siegmann, J. Stöhr, G. Ju, B. Lu and D. Weeler: Nature, **428** (2004) 831.
[45] D. Alloyeau, C. Ricolleau, C. Mottet, T. Oikawa, C. Langlois, Y. Le Bouar, N. Braidy and A. Loiseau: Nat. Mater., **8** (2009) 940.
[46] M.L. Plumer, J. van Ek and D. Weller, The Physics of Ultra-High-Density Magnetic Recording, Springer Science and Business Media, 41 (2001)
[47] S. U. T Hayashi, S. Hirono and M. Tomita: Nature, **381** (1996) 772.
[48] S. I. Ohkoshi, A. Namai, K. Imoto, M. Yoshikiyo, W. Tarora, K. Nakagawa, M. Komine, Y. Miyamoto, T. Nasu, S. Oka and H. Tokoro: Sci. Rep., **5** (2015) 14414.
[49] M. Yoshikiyo, A. Namai, K. Imoto, H. Tokoro and S. I. Ohkoshi: Eur. J. Inorg. Chem., **2018** (2018) 847.
[50] M. Yoshikiyo, Y. Futakawa, R. Shimoharai, Y. Ikeda, J. MacDougall, A. Namai and S. Ohkoshi: Chem. Phys. Lett., **803** (2022) 139821.
[51] W. Yang, Y. Yu, M. B. Starr, X. Yin, Z. Li, A. Kvit, S. Wang, P. Zhao and X. Wang: Nano Lett., **15** (2015) 7574.
[52] D. Cao, Z. Wang, L. Wen, Y. Mi and Y. Lei: Angew. Chem., **126** (2014) 11207.
[53] W. Ji, K. Yao, Y. F. Lim, Y. C. Liang and A. Suwardi: Appl. Phys. Lett., **103** (2013) 103.
[54] C. B. E., R. R. T. Zhao, A. Scholl, F. Zavaliche, K. Lee, M. Barry, A. Doran, M. P. Cruz, Y. H. Chu, C. Ederer, N. A. Spaldin, R. R. Das, D. M. Kim and S. H. Baek: Nat. Mater., **5** (2006) 823.
[55] Y. Ling, G. Wang, D. A. Wheeler, J. Z. Zhang and Y. Li: Nano Lett., **11** (2011) 2119.
[56] G. Wang, Y. Ling, D. A. Wheeler, K. E. N. George, K. Horsley, C. Heske, J. Z. Zhang and Y. Li: Nano Lett., **11** (2011) 3503.
[57] D. A. Wheeler, G. Wang, Y. Ling, Y. Li and J. Z. Zhang: Energy Environ. Sci., **5** (2012) 6682.
[58] A. R. H. Dotan, O. Kfir, E. Sharlin, O. Blank, M. Gross, I. Dumchin and G. Ankonina: Nat. Mater., **12** (2013) 158.
[59] M. S. Prévot and K. Sivula: J. Phys. Chem. C, **117** (2013) 17879.
[60] K. Sivula, R. Zboril, F. Le Formal, R. Robert, A. Weidenkaff, J. Tucek, J. Frydrych and M. Grätzel: J. Am. Chem. Soc., **132** (2010) 7436.
[61] L. T. Quynh, C. N. Van, Y. Bitla, J. W. Chen, T. H. Do, W. Y. Tzeng, S. C. Liao, K. A. Tsai, Y. C. Chen, C. L. Wu, C. H. Lai, C. W. Luo, Y. J. Hsu and Y. H. Chu: Adv. Energy Mater., **6** (2016) 1600686.
[62] S.J. Clark and J. Robertson: Appl. Phys. Lett., **90** (2007) 132903.
[63] Y. Xu and M. A. A. Schoonen: Am. Mineral., **85** (2000) 543.
[64] M. Cargnello, A. Gasparotto, V. Gombac, T. Montini, D. Barreca and P. Fornasiero: Eur. J. Inorg. Chem., **28** (2011) 4309.
[65] D. I. Kondarides, V. M. Daskalaki, A. Patsoura and X. E. Verykios: Catal. Letters, **122** (2008) 26.
[66] A. Patsoura, D. I. Kondarides and X. E. Verykios: Catal. Today, **124** (2007) 94.
[67] M. J. Katz, S. C. Riha, N. C. Jeong, A. B. F. Martinson, O. K. Farha and J. T. Hupp: Coord. Chem. Rev, **256** (2012) 2521.

Critical Review

pISSN 2799-8525 · eISSN 2799-8681
J Powder Mater 2024;31(6):480-492

Journal of Powder Materials

Advances in Powder Metallurgy for High-Entropy Alloys

Sheetal Kumar Dewangan[1], Cheenepalli Nagarjuna[1], Hansung Lee[1], K. Raja Rao[2], Man Mohan[1,3], Reliance Jain[1], Byungmin Ahn[1,4,*]

[1]Department of Materials Science and Engineering, Ajou University, Suwon, 16499, Republic of Korea
[2]Department of Mechanical Engineering, Mandsaur University, Mandsaur, 458002, India
[3]Department of Mechanical Engineering, Rungta College of Engineering and Technology, Bhilai, 490024, India
[4]Department of Energy Systems Research, Ajou University, Suwon, 16499, Republic of Korea

High-entropy alloys (HEAs) represent a revolutionary class of materials characterized by their multi-principal element compositions and exceptional mechanical properties. Powder metallurgy, a versatile and cost-effective manufacturing process, offers significant advantages for the development of HEAs, including precise control over their composition, microstructure, and mechanical properties. This review explores innovative approaches integrating powder metallurgy techniques in the synthesis and optimization of HEAs. Key advances in powder production, sintering methods, and additive manufacturing are examined, highlighting their roles in improving the performance, advancement, and applicability of HEAs. The review also discusses the mechanical properties, potential industrial applications, and future trends in the field, providing a comprehensive overview of the current state and future prospects of HEA development using powder metallurgy.

Keywords: Powder metallurgy; High entropy alloys; Sintering

Received: September 19, 2024
Revised: November 19, 2024
Accepted: November 24, 2024

***Corresponding author:**
Byungmin Ahn
TEL: +82-31-219-3531
FAX: +82-31-219-1613
E-mail: byungmin@ajou.ac.kr

1. Introduction

High-entropy alloys (HEAs) have emerged as a groundbreaking class of materials with unique properties and diverse potential applications. Unlike traditional alloys, which typically consist of one or two principal elements, HEAs are composed of multiple principal elements (usually five or more) in near-equiatomic ratios [1–4]. This complex composition results in a high configurational entropy, which stabilizes the formation of simple solid solution phases and imparts exceptional mechanical and physical properties. HEAs are known for their superior strength [5], excellent wear [6] and corrosion resistance [7], and remarkable high-temperature stability [8], making them highly attractive for advanced engineering applications in industries such as aerospace, automotive, and energy [9, 10].

Despite their promising attributes, the development and commercialization of HEAs face significant challenges, primarily due to the difficulties associated with their fabrication. Conventional manufacturing techniques often fall short in producing HEAs with consistent quality and desirable properties. This is where powder metallurgy (PM) techniques come into play. PM offers a versatile and cost-effective approach to producing HEAs, allowing for precise control over composition and microstructure. The inherent advantages of PM, such as the ability to produce fine and uniform powders, complex shapes, and high-performance materials, make it an ideal method for HEA fabrication [11–13]. In addition, HEAs typically consist of multiple elements in near-equiatomic proportions, leading to a high degree of atomic mixing. This randomness in atomic arrangement increases configurational entropy, which stabilizes the solid solution phase because the system prefers higher entropy for thermodynamic stability.

Configurational entropy discourages the formation of intermetallic compounds because these ordered structures have lower entropy. Intermetallic compounds are more rigid, with specific atomic arrangements, which reduce the system's overall entropy. In contrast, solid solutions allow for more

https://doi.org/10.4150/jpm.2024.00297

atomic disorder, leading to higher entropy and thus more stability at elevated temperatures. This stabilization mechanism contributes to the unique properties of HEAs, such as improved mechanical strength, corrosion resistance, and thermal stability, making them superior for various high-performance applications.

When comparing PM with conventional alloy production methods, several distinct differences and advantages emerge. Conventional methods typically involve significant material waste due to machining and cutting processes, whereas PM offers near-net shape capabilities, resulting in minimal material waste. Conventional methods often require multiple steps and extensive machining to achieve complex geometries, while PM can produce intricate shapes directly from the powder, reducing the need for additional machining [14, 15]. Microstructural control is another area where PM excels; conventional methods may result in inhomogeneous microstructures due to the melting and solidification processes, whereas PM provides better control and uniformity through controlled powder production and sintering processes. In terms of processing temperature and energy consumption, conventional methods typically involve high temperatures for melting and casting, leading to higher energy consumption, whereas PM often operates at lower temperatures, particularly in sintering and consolidation steps, resulting in energy savings [16]. Mechanical properties are also enhanced in PM, which can achieve superior properties through uniform microstructures, enhanced diffusion bonding, and advanced consolidation techniques like hot isostatic pressing (HIP) and spark plasma sintering (SPS) [15, 17–19]. PM offers greater flexibility in alloy design, enabling the development of novel alloys, including HEAs, with unique properties, whereas conventional methods are limited in the range of compositions that can be processed due to melting point differences and segregation issues. While conventional methods are generally more cost-effective for high-volume production of standard alloys, PM can be more cost-effective for producing specialized, high-performance alloys and components, especially in lower volumes or for complex shapes. In conclusion, powder metallurgy provides a versatile and efficient approach to alloy development, offering significant advantages in terms of material utilization, complexity of shapes, microstructural control, and energy consumption. These benefits make PM an attractive option for developing advanced materials like high-entropy alloys, which require precise control over composition and properties [11, 12, 20, 21].

In advancement, machine learning (ML) is transforming powder metallurgy in the production of HEAs by accelerating the discovery, optimization, and processing of these complex materials with improved material efficiency. In HEAs, where numerous elements combine in near-equiatomic proportions, the vast design space makes traditional trial-and-error approaches time-consuming and cost-prohibitive. ML algorithms can efficiently analyze and predict optimal compositions, powder processing parameters, and sintering conditions by learning from extensive datasets on composition, microstructure, and performance metrics. For instance, ML models can predict how variations in milling speed, time, or temperature will influence microstructure homogeneity, grain size, and phase stability. Additionally, ML can aid in identifying ideal parameters for high-energy ball milling and sintering to maximize chemical uniformity and mechanical properties. By enhancing process control and material characterization, ML in powder metallurgy improves the efficiency and precision of HEA development, leading to faster innovations and superior performance of these advanced alloys [22, 23].

Here, presenting a comprehensive overview of advancements in powder production, sintering methods, and additive manufacturing. Unlike previous reviews, it emphasizes PM's unique ability to finely control HEA composition and microstructure, which is essential for tailoring mechanical properties and enhancing performance. Additionally, this review extends beyond technical discussions to address current and emerging industrial applications for PM-processed HEAs, providing valuable insights into future trends and the evolving landscape of HEA research. By integrating detailed analyses of PM process innovations and their impact on HEA mechanical properties, this review serves as a critical resource for researchers and industry professionals seeking to leverage PM techniques for specific HEA applications. Thus, this paper aims to explore the revolutionary impact of powder metallurgy techniques on the development of high-entropy alloys. It will discuss the various PM processes, including atomization, mechanical alloying, and advanced sintering techniques, and how they contribute to the optimization of HEAs. Furthermore, the paper will delve into the applications of HEAs produced through PM, highlighting their superior properties and potential industrial uses. By examining the latest advancements and future trends in this field, this review seeks to provide a comprehensive understanding of how PM is transforming the landscape of high-entropy alloy development and paving the way for next-generation materials.

2. Fundamentals and background of High-Entropy Alloys

HEAs represent a novel class of materials characterized by their unique composition and exceptional properties. Unlike traditional alloys, which typically consist of one or two principal elements, HEAs are composed of five or more elements in near-equiatomic proportions [24–26]. This unconventional approach to alloy design leads to a variety of beneficial characteristics, making HEAs a subject of intense research and interest in materials science. A brief fundamental has been present in Fig. 1.

HEAs were first introduced in the early 2000s as researchers sought to explore the untapped potential of multi-component systems. Unlike traditional alloy design, which focuses on a principal element with minor additions. Initial studies revealed that HEAs could form stable, single-phase structures despite their complex compositions, attributed to the high entropy of mixing, which stabilizes disordered solid solutions over intermetallic compounds. The field of HEAs has rapidly expanded, with ongoing research into various element combinations to tailor properties for specific applications. Advances in computational methods and high-throughput experimental techniques have accelerated HEA development, promising significant impacts across industries such as aerospace, automotive, biomedical, and energy. Despite developmental challenges, the unique properties of HEAs continue to drive innovation and interest in this groundbreaking field of alloy design [28–30].

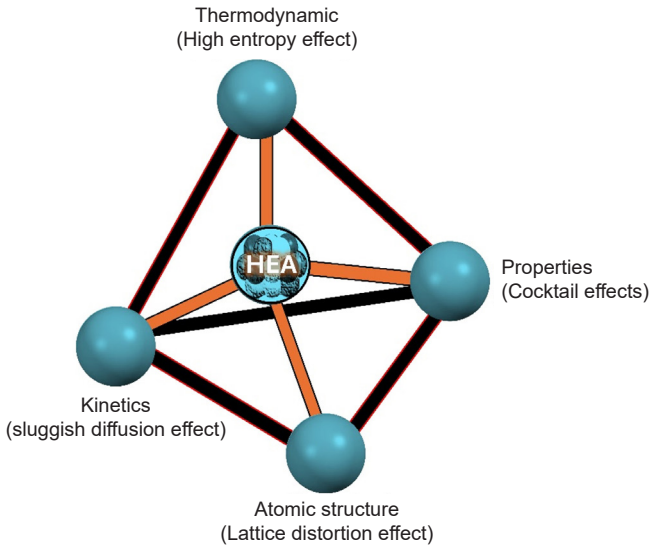

Fig. 1. Fundamental aspects of high-entropy alloys (permission will be obtained after acceptance) [27].

2.1. Constituents of Elements and Structure

HEAs are a novel class of materials defined by their unique compositional complexity. Unlike conventional alloys, which typically consist of one or two primary elements with minor additions, HEAs are composed of five or more principal elements in near-equiatomic ratios. This high configurational entropy leads to the stabilization of simple solid solution phases rather than complex intermetallic compounds.

I. Multi-Principal Element Composition: HEAs are designed with multiple elements, each contributing significantly to the overall composition. This multi-element approach increases the entropy of mixing, which promotes the formation of simple structures like face-centered cubic (FCC), body-centered cubic (BCC), or hexagonal close-packed (HCP) phases, rather than multiple complex phases [31].

II. Solid Solution Phases: The high entropy effect favors the formation of solid solutions where different atoms are randomly distributed on the lattice sites. This random mixing can occur in FCC, BCC, or HCP structures, resulting in high configurational entropy that stabilizes these phases at high temperatures.[32, 33].

III. Microstructure: The microstructure of HEAs can be highly varied and is influenced by the specific elemental composition and processing conditions. Typically, HEAs exhibit a single-phase or dual-phase microstructure with a mix of FCC and BCC phases. The presence of multiple principal elements can lead to lattice distortion, which plays a significant role in the mechanical properties of HEAs [34].

2.2. Exceptional Properties of HEAs

The distinctive composition and structure of HEAs impart several unique properties that distinguish them from traditional alloys.

I. Mechanical Strength: HEAs exhibit remarkable mechanical strength due to the combined effects of solid solution strengthening, lattice distortion, and the presence of multiple phases. These factors contribute to high yield strength and tensile strength [14].

II. Wear and Corrosion Resistance: The random distribution of different atoms can lead to enhanced wear and corrosion resistance. The multiple elements can form a passive oxide layer that protects the alloy from aggressive environments [35, 36].

III. High-Temperature Stability: HEAs maintain their structural integrity and mechanical properties at high temperatures. The high entropy stabilizes simple solid solution phases

even at elevated temperatures, making them suitable for high-temperature applications.

IV. Thermal Stability and Creep Resistance: HEAs exhibit excellent thermal stability and resistance to creep deformation, which is critical for applications in harsh thermal environments [37, 38].

V. Magnetic and Electrical Properties: Depending on the constituent elements, HEAs can exhibit a range of magnetic and electrical properties, making them versatile for various applications, from structural components to functional materials [39].

Thus, high-entropy alloys represent a paradigm shift in alloy design, offering a range of exceptional properties due to their unique compositional and structural characteristics. However, their development is hindered by several challenges that need to be addressed through continued research and innovation in materials science and engineering.

3. Powder Metallurgy Processes

Powder metallurgy (PM) is a manufacturing process that involves producing components from powdered materials through compaction and sintering. It offers a high degree of control over the final material properties and allows for the creation of complex shapes and unique material compositions. Fundamental steps are shown in Fig. 2.

3.1. Powder Production

Atomization: Atomization is the most common method for producing metal powders, where molten metal is dispersed into fine droplets and solidified rapidly. Techniques include gas atomization, water atomization, and centrifugal atomization [40, 41].

Mechanical Alloying: This process involves repeated fracturing, welding, and re-welding of a blend of powders to create alloy powders. It is particularly useful for creating composite powders and nanostructured materials. A detailed illustration of the material synthesized through the mechanical alloying is presented in Fig. 3.

Chemical Methods: These include reduction of metal oxides, electrolysis, and chemical vapor deposition (CVD). These methods can produce high-purity powders with controlled particle sizes.

Atomization: Atomization is a primary method for producing metal powders in powder metallurgy (PM). It involves disintegrating molten metal into fine droplets, which then solidify into powder particles. This technique is crucial for creating powders with controlled particle sizes and shapes, essential for high-quality PM processes. The main atomization methods are gas atomization, water atomization, and plasma atomization, each with unique characteristics and applications. Different types of atomization methods are widely used for the production of alloy powder, some important methods are described in Table 1.

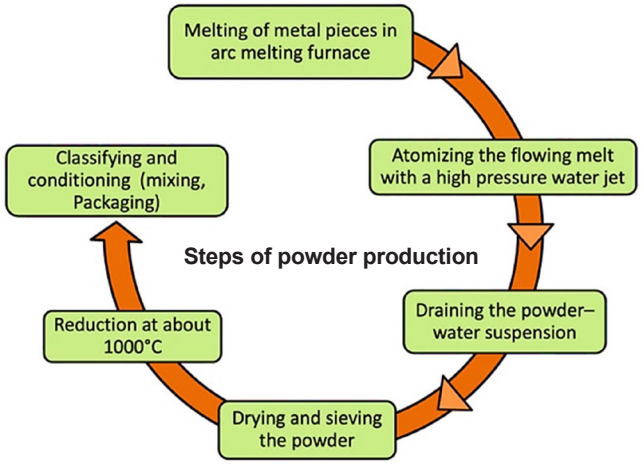

Fig. 2. Basic steps of powder production.

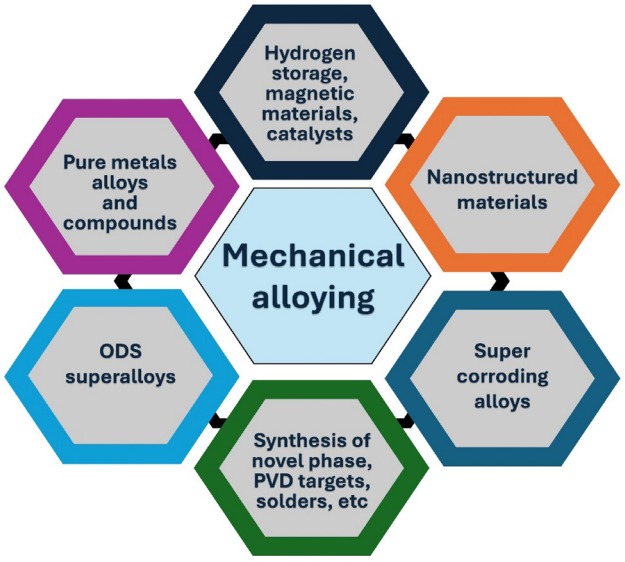

Fig. 3. Different materials synthesized through mechanical alloying (permission will be obtained after acceptance) [27].

Table 1. Different atomization methods and respective advantages and applications [11–13, 42, 43]

Methods	Process	Description	Advantages	Applications
Gas atomization	Molten metal stream	Melted in crucible and poured through nozzle	Spherical particles Controlled particle size High purity	Aerospace and automotive Additive manufacturing
	Gas stream	High-pressure gas jets break molten stream into droplets		
	Cooling and solidification	Droplets rapidly solidify in atomization chamber, forming fine powder.		
Water atomization	Molten metal Stream	Metal is melted and poured through a tundish into water-cooled chamber.	Cost-effective High production rates Diverse particle shapes	Structural components Hard materials
	Water jets	High-pressure water jets break molten stream into droplets.		
	Cooling and solidification	Droplets solidify quickly due to high cooling rate from water.		
Plasma atomization	Plasma torch	Plasma torch melts metal feedstock (wire or rod) at high temperatures.	High-purity spherical particles Fine powders	Aerospace and biomedical Additive manufacturing
	Inert gas stream	Inert gas (argon) atomizes molten metal into fine droplets.		
	Cooling and solidification	Droplets solidify in atomization chamber, forming fine powder particles.		

3.2. Sintering and Consolidation Methods in Powder Metallurgy

Sintering and consolidation are critical processes in PM that transform compacted metal powders into solid, dense materials with enhanced mechanical properties. These processes involve heating the powder compact to promote bonding between particles, eliminate porosity, and achieve the desired microstructure and properties [44, 45]. Various sintering and consolidation methods are employed, each offering distinct advantages for different applications. Various types of processes have been used to consolidate the powder which are described in Table 2.

3.3. Advantages of PM in Alloy Development

Powder metallurgy (PM) offers several significant advantages over traditional metallurgical processes, particularly in the development of advanced alloys such as HEAs. One of the most notable benefits is material efficiency. PM minimizes waste, as nearly all the powder can be utilized in the final product, making the process highly efficient in terms of material usage. This contrasts with conventional methods, which often involve substantial material loss due to machining and cutting [50].

The ability to produce complex shapes and near-net shapes is another key advantage of PM. This capability reduces the need for extensive machining and post-processing, saving both time and resources. PM processes can create intricate geometries directly from the powder, allowing for greater design flexibility and the production of components that would be challenging or impossible to achieve with traditional methods. In addition, Uniform microstructure is a critical factor in determining the mechanical properties and performance of an alloy. PM excels in this area by producing materials with highly uniform microstructures. This uniformity enhances the mechanical properties, such as strength and durability, leading to superior performance in the final product. In addition, PM allows for precise control over the alloy composition, enabling the development of new alloys with tailored properties. This level of control is particularly beneficial for creating HEAs, which require specific elemental combinations to achieve their unique characteristics [11, 13, 51, 52]. In addition, chemical homogeneity is crucial for HEAs as it ensures uniform mechanical properties, corrosion resistance, and thermal stability by preventing localized weaknesses from elemental segregation. Powder metallurgy techniques like high-energy ball milling and homogeneous sintering are particularly effective in achieving this uniformity. High-energy ball milling breaks down segregated phases by repeatedly fracturing and cold-welding particles, promoting atomic-level mixing of elements. Homogeneous sintering then densifies the milled powders without melting, allowing controlled atomic diffusion for even elemental distribution. Together, these methods create a chemically homogeneous alloy microstructure, which significantly enhances HEA performance.

Enhanced properties are another major advantage of PM. Processes such as mechanical alloying and SPS can significantly improve the mechanical properties of the material, including hardness, strength, and wear resistance. These enhancements are crucial for applications that demand high-performance materials capable of withstanding extreme conditions. Further, scalability is also a strength of PM. The process is suitable for both small-scale production of specialized components and

Table 2. Different atomization methods and respective advantages and applications

Methods	Process	Description	Advantages	Applications
Conventional sintering	Heating	Green compact is gradually heated to sintering temperature.	Simplicity	Structural components,
	Soaking	Held at sintering temperature for a specific duration to enable diffusion and bonding.	Cost-effectiveness	Hard materials
	Cooling	Material is cooled at controlled rate to prevent thermal stresses.		
Hot isostatic pressing (HIP)	Encapsulation	Powder compact is encapsulated in a gas-tight container.	High density	Aerospace components
	Pressurization and heating	Encapsulated compact is subjected to high pressure and temperature in an autoclave using inert gas.	Isotropic properties	Biomedical implants
	Densification	Pressure and heat induce particle bonding and densification.		
Spark plasma sintering (SPS)	Electric pulses	Pulsed electric current generates internal heat in the compact.	Fast processing	Nanomaterials
	Pressure application	Uniaxial pressure applied simultaneously to promote densification.	Fine microstructures	Functionally graded materials
	Rapid sintering	Process is rapid, often completed in minutes.		
Microwave sintering [46, 47]	Microwave energy	Microwaves generate heat, ensuring uniform temperature distribution.	Energy efficiency	Ceramics and composites
	Sintering	Material is sintered via dielectric heating	Uniform heating	Low-temperature sintering
Hot pressing [48, 49]	Compaction and heating	Powder is compacted and heated simultaneously in a die	High density and strength	Tool materials
	Densification	Pressure and heat promote densification and grain growth.	Dimensional control	Refractory metals
Cold isostatic pressing (CIP)	Encapsulation	Powder compact is placed in a flexible mold.	Uniform pressure	Preforms for sintering
	Pressure application	Mold is placed in a pressure vessel; uniform pressure is applied using a liquid medium.	Shape flexibility	Large components
	Pre-sintering densification	Compact is densified before sintering process		

large-scale industrial manufacturing, providing versatility in production volumes. This scalability makes PM an attractive option for various industries, from aerospace to biomedical, where both precision and volume production are required [11, 20].

3.4. Comparison with Other Processing Routes

In comparison with conventional alloy production methods, PM stands out for its ability to efficiently utilize materials, produce complex shapes, ensure uniform microstructures, offer alloy design flexibility, enhance material properties, and scale production to meet diverse needs. These advantages make powder metallurgy a powerful and versatile tool in the development of advanced materials like high-entropy alloys, driving innovation and performance across multiple fields. Thus, a comparison has been made in Table 3.

High-entropy alloys prepared by powder metallurgy exhibit outstanding mechanical and thermal properties, including high strength, hardness, toughness, wear resistance, and thermal stability. The PM process offers superior control over microstructure and composition compared to traditional casting and additive manufacturing. This results in materials with enhanced performance, particularly in high-temperature and demanding environments. As research and technology in powder metallurgy advance, the potential for HEAs in various high-performance applications continues to grow, highlighting the significance of this fabrication method in the development of advanced materials.

Table 3. Comparison of different processing routes with powder metallurgy process

	Casting [53]	Powder metallurgy [11, 12]	Additive manufacturing [54]
Microstructural control	Produces larger grain sizes and may lead to segregation of elements due to the slow cooling rates, resulting in inhomogeneous microstructures.	Achieves finer grain sizes and more uniform element distribution due to controlled powder production and sintering. Produces uniform and isotropic properties with better control over porosity and grain size.	Can achieve complex geometries and near-net shapes with fine microstructures, but may suffer from anisotropy and residual stresses.
Mechanical properties	Typically yields materials with lower strength and hardness compared to powder metallurgy due to the presence of casting defects such as porosity and segregation.	Produces materials with higher strength, hardness, and improved toughness due to better microstructural control. Delivers consistent mechanical properties due to uniform microstructure and controlled processing conditions.	Offers high strength and hardness, but properties can vary depending on the build direction and process parameters.
Thermal properties	Can result in lower thermal stability due to the potential for coarse intermetallic phases.	Provides higher thermal stability and oxidation resistance due to the homogeneous microstructure.	Exhibits good thermal properties, but residual stresses and anisotropy can affect performance at high temperatures.

4. Mechanical and Thermal Properties of HEAs

HEAs synthesized by PM followed by milling and sintering exhibit remarkable mechanical properties due to their unique multi-component composition and refined microstructure. The PM process, particularly through high-energy ball milling, ensures a homogeneous distribution of elements at the atomic level, resulting in a fine and uniform microstructure. This leads to high strength and hardness as the multiple principal elements create lattice distortions that impede dislocation movement. Thus, in Fig. 4 and Fig. 5 (a & b), the mechanical properties of some reported HEAs have been compared and presented as a bar chart.

Additionally, the enhanced toughness is attributed to the effective energy dissipation facilitated by the high-entropy effect, reducing the risk of brittle fracture. The superior hardness and toughness also translate into excellent wear resistance, making these HEAs suitable for abrasive environments. Furthermore, the uniform and fine-grained microstructure enhances fatigue resistance, enabling the alloys to endure cyclic loading conditions without premature failure. Overall, the mechanical properties of HEAs synthesized by PM followed by milling and sintering make them highly suitable for demanding applications that require a combination of high strength, toughness, and durability. In addition, Fig. 6 (a & b) presents the thermal properties of different high-entropy alloys.

HEAs are distinguished by their unique multi-element composition, which imparts exceptional thermal properties. These alloys exhibit remarkable thermal stability, maintaining phase integrity and resisting phase transformations at elevated temperatures due to high configurational entropy. Their thermal conductivity is generally moderate to low, a result of phonon scattering by diverse atomic sizes and mass differences. This property, along with a reduced coefficient of thermal expansion, helps mitigate thermal stress and reduces thermal distortion. HEAs also demonstrate excellent thermal shock resistance, distributing thermal stress evenly and enhancing durability in environments with rapid temperature changes. Their high melting points extend their operational range in extreme thermal conditions, while superior oxidation resistance, facilitated by the formation of stable protective oxide layers, and good corrosion resistance at high temperatures ensure robust performance in harsh chemical environments. Furthermore, HEAs exhibit significant resistance to thermal fatigue, maintaining their properties through repeated heating and cooling cycles, which enhances the lifespan and reliability of components made from these materials. In addition, Table 4 and 5 shows the microstructure and their properties of different high entropy alloys.

5. Applications of HEAs Produced by Powder Metallurgy

HEAs produced by powder metallurgy have diverse and promising applications due to their unique properties, such as high thermal stability, mechanical strength, and corrosion resistance. The versatility and enhanced properties of HEAs pro-

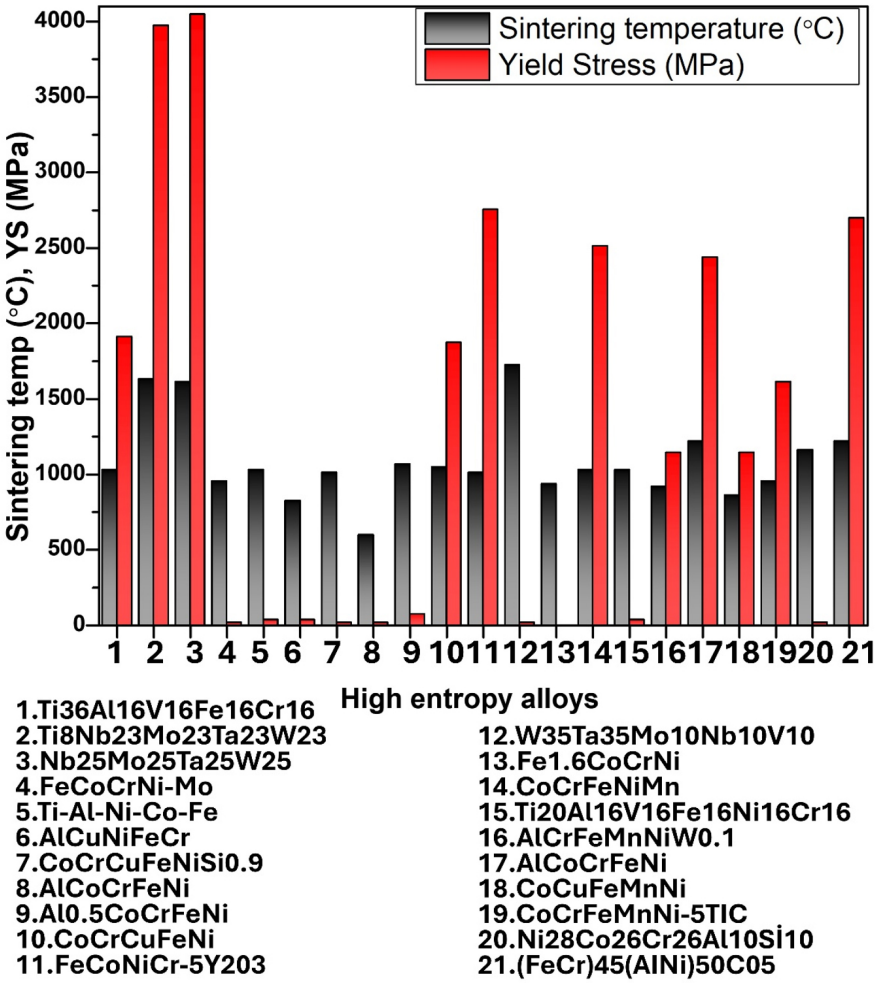

Fig. 4. Mechanical properties of some reported high-entropy alloys for sintering temperature and yield stress [55]. (permission will be obtained after acceptance).

duced by powder metallurgy make them suitable for a wide range of advanced engineering applications. A schematic presentation has been shown in Fig. 7.

Aerospace industry: The aerospace industry has traditionally relied on superalloys and single-crystal alloys for components. However, the discovery of HEAs is shifting this narrative. HEAs offer high thermal stability and strength at elevated temperatures, making them ideal replacements for conventional alloys in jet engine components such as turbine blades, compressors, and combustors. For instance, GE Aviation has developed a NbMoTaW HEA to replace ferritic steel in rotors, offering superior properties like temperature resistance above 800°C, high strength, corrosion resistance, and sound creep resistance. Additionally, HEAs in other jet engine parts exhibit enhanced resistance to wear, corrosion, oxidation, fatigue, and creep compared to traditional superalloys and single-crystal alloys [55, 57].

Automotive industry: HEAs are emerging as novel materials for the automotive industry due to their high strength and ductility. These properties make HEAs ideal for robust automotive components such as engine valves, gears, brake calipers, shafts, connecting rods, engine pistons, and ball joints. HEAs also offer resistance to fatigue, corrosion, wear, and impact loads, which are essential for automotive applications. For example, the AlCoCrFeNi HEA is lightweight, with a high yield strength of 1263 MPa at 773 K, ultimate compressive strength (UCS) of 1702 MPa, and plasticity of 19.9% up to 773 K. These characteristics make it suitable for structural and high-temperature applications like gears, engine pistons, and valves [58, 59].

Marine industry: HEAs are becoming valuable in the nautical and maritime industry due to their high strength-to-weight ratio and excellent corrosion resistance. These properties are crucial for submarine machines and other maritime devices

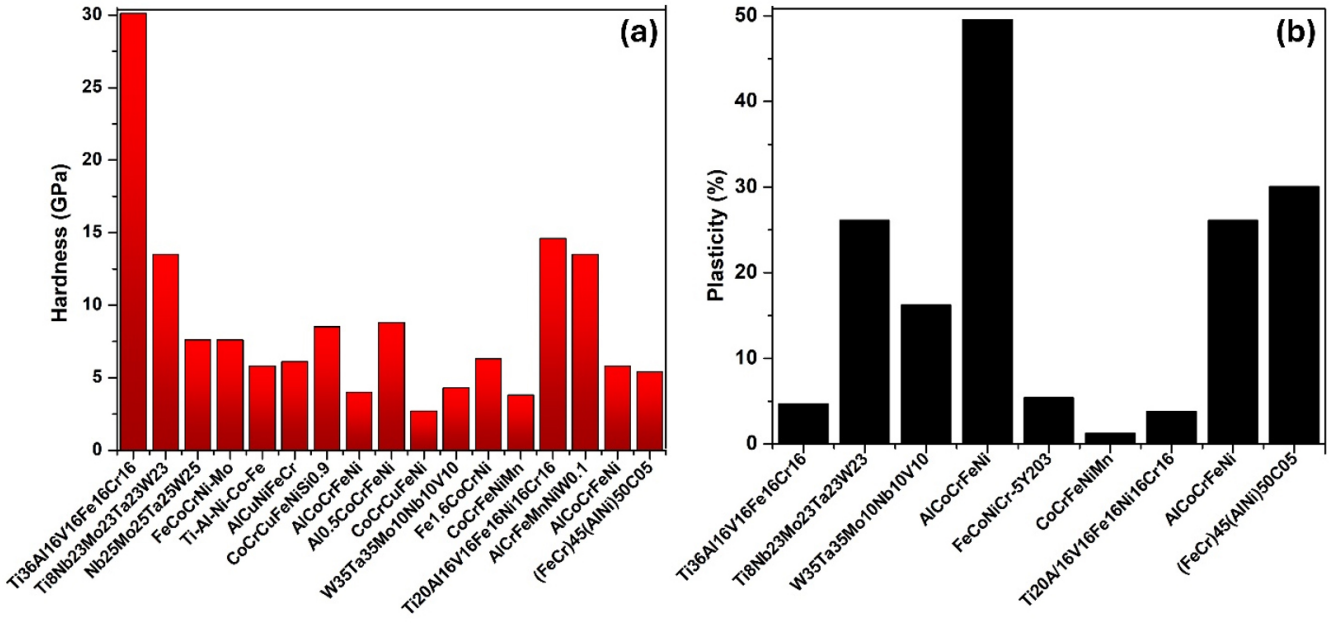

Fig. 5. Mechanical properties of some reported high-entropy alloys (HEAs). (a) Hardness; (b) plasticity of HEAs [55]. (permission will be obtained after acceptance).

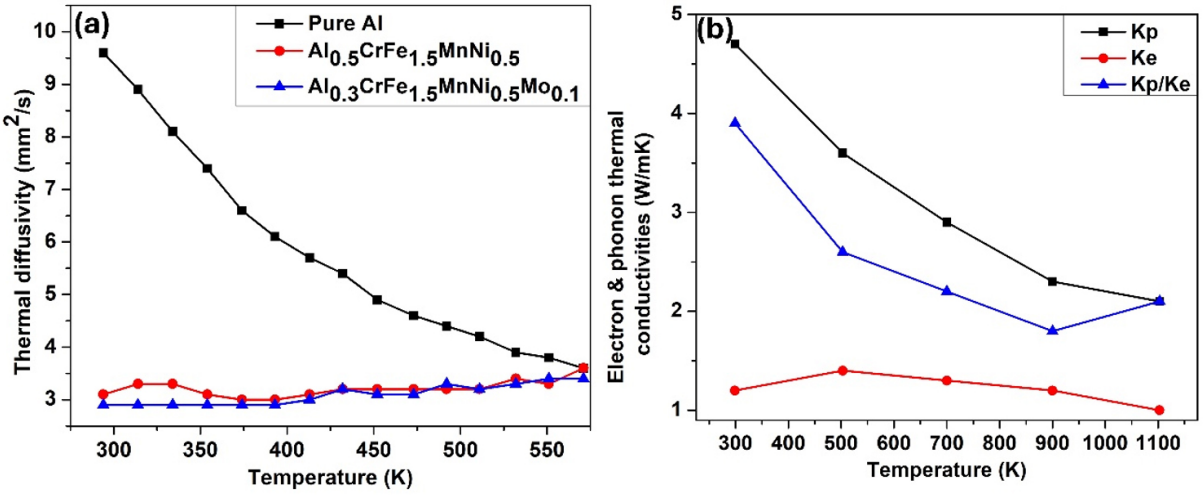

Fig. 6. Properties of some reported high-entropy alloys. (a) Plot of thermal diffusivity of pure Al, Al0.5CrFe1.5MnNi0.5 and Al0.3CrFe1.5MnNi0.5Mo0.1 alloys; (b) Variation of electron thermal conductivity (Ke) and phonon thermal conductivity (Kp) of Al0.3CoCrFeNi with temperature and their ratio [55]. (Permission will be obtained after acceptance).

that are in constant contact with salt water, which is highly corrosive. Components for these applications require superior corrosion resistance and low density. One such HEA, MAR-M247 (NiCr16Co11Mo4), is a nickel-based alloy recognized for its effectiveness in constructing maritime ships and boats, offering enhanced durability and performance in harsh marine environments [60, 61].

Biomedical industries: HEAs show great promise in biomedical applications, particularly for implants. Popescu et al. developed TiZrNbTaFe HEA, which exhibits superior corrosion resistance compared to the conventional Ti6Al4V alloy due to its single β phase and the presence of Ta, which forms a protective Ta2O5 film. This HEA has proven to be more biocompatible than Ti6Al4V, making it suitable for orthopedic implants like

Table 4. Microstructures and their effects on different high-entropy alloys

HEA	Observed phase(s) through different processing route(s)			Effects on mechanical properties		
Composition	Melting and casting	MA SPS	AM	Melting and casting	MA SPS	AM
CoCrFeNiMn	FCC	FCC	FCC + BCC		Compressive strength: 1987 MPa Hardness: 646 HV	Tensile strength: 601 MPa
CoCrFeNiAl03	FCC	FCC + BCC	FCC	UTS: 528 MPa YTS: 275 MPa	Compressive strength: 1907 MPa Hardness: 625 HV	YS: 730 MPa UTS: 896 MPa
CoCrFeNi		FCC + Cr7C3	FCC		Hardness: 580 HV	
AICoCrCuFeNi	FCC + BCC	FCC + BCC	BCC	Hardness: 515.5 HV (5.056 GPa) Compressive strength: 1.82 GPa	Hardness: 8.13 GPa Elastic modulus: 172 GPa	
TiZrNbMon3 V0.3	BCC		FCC BCC	Yield strength: 1312 MPa and 50% increase in plastic strain		
Ni155015CrFeT105	FCC	FCC		YS: 896 MPa Compressive strength:1502 MPa Hardness: 515 HV	Hardness: 442 $HV_{0.3}$ Tensile strength: 1384 MPa Elastic modulus:216 GPa	

hip and knee replacements, as well as dental implants. CoCrFeMnNi HEA has shown superior performance in hip and knee replacements, while CoCrFeNiMnMo HEA has excelled in dental applications due to its corrosion resistance, biocompatibility, and strength. Additionally, HEAs are being explored as substitutes for conventional synthetic drugs [62–66].

Energy industries: HEAs are emerging as superior materials for hydrogen energy storage, surpassing traditional metal hydrides like MgH2 and NaAlH4, which have a maximum hydrogen-to-metal (H/M) ratio of 2. Research indicates that HEAs can achieve an H/M ratio of 2.5 or more [67]. For instance, TiVZrNbHf HEA can store more hydrogen than its individual elements due to the large lattice strain in the alloy. This strain creates an environment conducive to absorbing hydrogen in both tetrahedral and octahedral interstitial sites, enhancing its storage capacity [68, 69].

Defense Industries: HEAs are crucial in the military sector, particularly for military vehicles, protective shields, and armories. Their high strength, hardness, corrosion and wear resistance, impact strength, and fatigue resistance make them ideal for these applications. For instance, AerMet 100 (NiCoFeVMo) is used in ammunition casings due to its excellent wear and impact resistance. Research by Tang and Li using molecular dynamics simulations revealed that the ballistic performance of CrMnFeCoNi and CrFeCoNi HEAs is influenced by their dislocation dynamics under strain. CrFeCoNi HEA, with stronger atomic bonds and higher dislocation densities, exhibits superior strain-hardening and toughness, while CrMnFeCoNi, with weaker bonds and lower dislocation densities, is more susceptible to failure under ballistic impact. Thus, the presence of Mn reduces the impact energy of ballistic-resistant HEAs [70, 71].

6. Conclusions and Challenges in HEA Development

Despite their promising properties, the development and commercialization of HEAs face several significant challenges.

(1) Complexity in Alloy Design: Designing HEAs involves selecting appropriate combinations of elements from a vast compositional space. The interactions between multiple elements are complex and not fully understood, making it challenging to predict the resulting phases and properties.

(2) Manufacturing Difficulties: Traditional casting and processing methods may not be suitable for HEAs due to their compositional complexity. Achieving a homogeneous distribution of elements and preventing segregation during solidification are major challenges.

(3) Characterization and Testing: The characterization of HEAs requires advanced techniques to accurately determine their phase composition, microstructure, and properties. High-throughput experimental methods and computational modeling are often necessary to understand the behavior of HEAs.

(4) Cost and Scalability: The high cost of raw materials and the complexity of processing can make HEAs expensive to pro-

Table 5. Microstructure, process and properties of various high-entropy alloys [56]

Alloys	Processing	Density (g/cm^3)	Phases	Yield strength
Ti0.5VNbMoTa	MA+SPS	9.99	BCC	2563
Ti1VNbMoTa	MA+SPS	9.45	BCC	2208
Ti1.5VNbMoTa	MA+SPS	9.08	BCC+FCC	2696
Ti2VNbMoTa	MA+SPS	8.75	BCC+FCC	2824
NbMoTaWVCr	MA+SPS	11.06	BCC+Laves+Oxide	3410
NbMoTaWVCr	MA+SPS	11.16	BCC+Laves+Oxide	3416
MoNbTaTiV	MA+SPS	9.45	BCC	2208
NbMoTaWVTi	MA+SPS	10.6	BCC+TiO	2709
CrNbVMo	MA+SPS	8.03	BCC+NbO0.7	2743
Al0.5CrNbVMo	MA+SPS	7.53	BCC+Al2O3	2497
Al1CrNbVMo	MA+SPS	7.05	BCC+Al2O3	2326
(W35Ta35Mo15Nb15)95Ni5	MA+SPS	14.55	BCC+Nb5.7Ni4Ta2.3O2	2128
NbTaWMo	MA+SPS	13.44	BCC+Silicide	1217
NbTaWMoSi0.25	MA+SPS	12.92	BCC+Silicide	1826
NbTaWMoSi0.5	MA+SPS	12.65	BCC+Silicide	1883
NbTaWMoSi0.75	MA+SPS	12.23	BCC+Silicide	2483
Al0.1CrMoNbV	MA+SPS	7.97	BCC+Al2O3	2544
Al0.1CrMoNbVB0.015	MA+SPS	7.97	BCC+Al2O3	2933
TiNbTa0.5Zr	Sintering	7.6	BCC	1310
TiNbTa0.5ZrAl0.2	Sintering	–	BCC	1500
TiNbTa0.5ZrAl0.5	Sintering	7.3	BCC	1740
W0.3(TaTiCrV)0.7	SPS	13.4	BCC	2265
W0.4(TaTiCrV)0.6	SPS	13.6	BCC	2314
W0.5(TaTiCrV)0.5	SPS	14.5	BCC	2144
W0.6(TaTiCrV)0.4	SPS	14.9	BCC	2187
W0.7(TaTiCrV)0.3	SPS	15.7	BCC	1473
W0.8(TaTiCrV)0.2	SPS	16.5	BCC	1208
W0.9(TaTiCrV)0.1	SPS	16.5	BCC	1206
V0.5Nb0.5ZrTi	SLM	6.5	BCC	1450

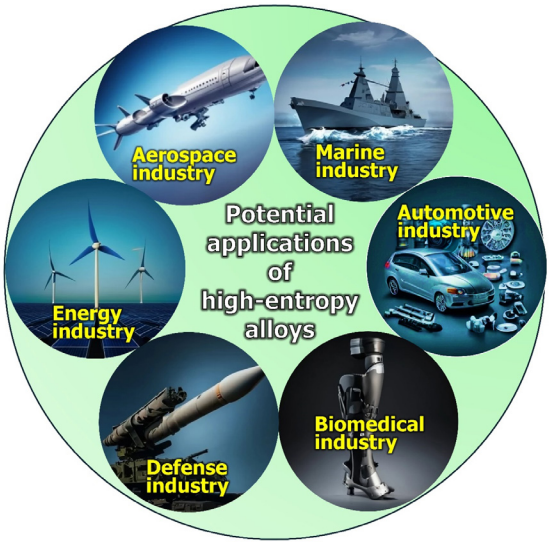

Fig. 7. Potential applications of high-entropy alloys.

duce. Developing cost-effective and scalable manufacturing processes is crucial for their widespread adoption.

(5) Limited Understanding of Properties: While HEAs exhibit unique properties, there is still limited understanding of how these properties change with different compositions and processing conditions. More research is needed to fully exploit the potential of HEAs.

(6) In conclusion, the advancement of HEAs through powder metallurgy techniques marks a significant breakthrough in materials science. Powder metallurgy allows for precise control over composition and microstructure, leading to HEAs with superior mechanical properties, thermal stability, and corrosion resistance. This innovative approach not only enhances the performance and durability of HEAs but also broadens their application range across industries such as

aerospace, automotive, medical, and energy. The synergy between HEA development and powder metallurgy techniques paves the way for the creation of next-generation materials that meet the stringent demands of modern engineering challenges. As research and technology continue to evolve, the potential of HEAs produced via powder metallurgy promises to revolutionize material design and application, driving forward industrial innovation and efficiency.

Funding

This work was supported by the National Research Foundation of Korea (NRF) grant funded by the Korea government (MSIT) (No. 2021R1A2C1005478).

Conflict of Interest

The authors declare no competing financial interests or personal relationships.

Data Availability Statement

All data generated or analyzed during this study are included in this published article

Author Information and Contribution

Sheetal Kumar Dewangan: Postdoctoral researcher, conceptualization, formal analysis, investigation, writing - original draft, writing - review & editing. Cheenepalli Nagarjuna: Postdoctoral researcher, formal analysis, investigation. Hansung Lee: Postdoctoral researcher, formal analysis, investigation. K. Raja Rao: Postdoctoral researcher, formal analysis, investigation. Man Mohan: Postdoctoral researcher, formal analysis, investigation. Reliance Jain: Professor, formal analysis, investigation. Byungmin Ahn: Professor, conceptualization, funding acquisition, supervision, writing - review & editing.

Acknowledgement

None.

References

[1] B. S. Murty, J. W. Yeh, S. Ranganathan and P. P. Bhattacharjee, In : B. S. Murty, J. W. Yeh, S. Ranganathan, P. P. Bhattacharjee, editors. High-Entropy Alloys, Second EdiElsevier, (2019) 13.

[2] B. S. Murty, J. W. Yeh, S. Ranganathan and P. P. Bhattacharjee, In : B. S. Murty, J. W. Yeh, S. Ranganathan, editors. High-Entropy Alloys, Second EdiElsevier, Boston (2019) 1.

[3] J. W. Yeh: JOM, **65** (2013) 1759.

[4] M. H. Tsai and J. W. Yeh: Mat. Res. Lett., **2** (2014) 107.

[5] M. J. Chae, A. Sharma, M. C. Oh and B. Ahn: Met. Mater. Int., **27** (2021) 629.

[6] T. Zirari and V. Trabadelo: Heliyon, **10** (2024) e25867.

[7] R. B. Nair, H. S. Arora, S. Mukherjee, S. Singh, H. Singh and H. S. Grewal: Ultrason. Sonochem., **41** (2018) 252.

[8] L. Han, X. Xu, L. Wang, F. Pyczak, R. Zhou and Y. Liu: Mater. Res. Lett., **7** (2019) 3831.

[9] M. Yue, H. Lambert, E. Pahon, R. Roche and S. Jemei: Renewable Sustainable Energy Rev., **146** (2021) 11118.

[10] N. Kaushik, A. Meena and H. S. Mali: Mater. Manuf. Processes, **37** (2021) 1085.

[11] G. S. Upadhyaya, Powder Metallurgy Technology, Cambridge International Science Pub, Cambridge (2002)

[12] J. M. Torralba, Improvement of Mechanical and Physical Properties in Powder Metallurgy, Elsevier, (2014)

[13] L. Moravcikova-Gouvea, I. Moravcik, V. Pouchly, Z. Kovacova, M. Kitzmantel, E. Neubauer and I. Dlouhy: Materials, **14** (2021) 5796.

[14] L. Moravcikova-Gouvea, I. Moravcik, M. Omasta, J. Veselý, J. Cizek, P. Minárik, J. Cupera, A. Záděra, V. Jan and I. Dlouhy: Mater. Charact., **159** (2020) 110046.

[15] V. Kruzhanov and V. Arnhold: Powder Metall., **55** (2012) 14.

[16] T. DebRoy and J. W. Elmer: Mater. Today, **80** (2024) 737.

[17] B. Ren, R. F. Zhao, A. Y. Jiang and Y. Yu: Micron, **158** (2022) 103291.

[18] R. F. Zhao, B. Ren, B. Cai, Z. X. Liu, G. P. Zhang and J. J. Zhang: Results Phys., **15** (2019) 102667.

[19] K. R. Rao, S. K. Dewangan, A. H. Seikh, S. K. Sinha and B. Ahn: Met. Mater. Int., **30** (2024) 726.

[20] S. H. Huo, M. Qian, G. B. Schaffer and E. Crossin: Fundamentals of Aluminium Metallurgy: Production, Processing and Applications, (2010) 655.

[21] A. R. E. Singer: Powder Metall., **19** (1976) 4.

[22] R. Jain, S. Jain, S. K. Dewangan, L. K. Boriwal and S. Samal: Journal of Alloys and Metallurgical Systems, **8** (2024) 100110.

[23] S. K. Dewangan, S. Samal and V. Kumar: Mater. Today Commun., **27** (2021) 102356.

[24] B. Cantor, I. T. H. Chang, P. Knight and A. J. B. Vincent: Mater. Sci. Eng., A, **375–377** (2004) 213.
[25] K. H. Huang and J. W. Yeh, A Study on Multicomponent Alloy Systems Containing Equal-Mole Elements. National Tsing Hua University, M. S. thesis (1996).
[26] M. H. Tsai and J. W. Yeh: Mater. Res. Lett., **2** (2014) 107.
[27] S.K. Dewangan, A. Mangish, S. Kumar, A. Sharma, B. Ahn and V. Kumar: Eng. Sci. Technol. Int. J., **35** (2022) 101211.
[28] J.-W. Yeh: Ann. Chim. Sci. Mat., **31** (2006) 633.
[29] J. Li, Y. Huang, X. Meng and Y. Xie: Adv. Eng. Mater., **21** (2019) 1900343.
[30] P.-K. Huang, J.-W. Yeh, T.-T. Shun and S.-K. Chen: Adv. Eng. Mater., **6** (2004) 74.
[31] B. Chanda and J. Das: Adv. Eng. Mater., **20** (2017) 1700908.
[32] X. Yang and Y. Zhang: Mater. Chem. Phys., **132** (2012) 233
[33] F. Tian: Front. Mater., **4** (2017) 1.
[34] Y. Zhang, T. T. Zuo, Z. Tang, M. C. Gao, K. A. Dahmen, P. K. Liaw and Z. P. Lu: Prog. Mater. Sci., **61** (2014) 1.
[35] Y. Ren, Q. Zhou, D. Hua, Z. Huang, Y. Li, Q. Jia, P. Gumbsch, C. Greiner, H. Wang and W. Liu: Sci. Bull., **69** (2024) 227.
[36] D. Banik, S. Mukherjee, H. Fujiwara, K. Ameyama and K. Mondal: Wear, **534–535** (2023) 205125.
[37] A. Karati, K. Guruvidyathri, V. S. Hariharan and B. S. Murty: Scr. Mater., **162** (2019) 465.
[38] Z. Xu, H. Zhang, W. Li, A. Mao, L. Wang, G. Song and Y. He: Addit. Manuf., **28** (2019) 766.
[39] Y. F. Kao, S. K. Chen, T. J. Chen, P. C. Chu, J. W. Yeh and S. J. Lin: J. Alloys Compd., **509** (2011) 1607.
[40] D. J. Hodkin, J. S. Pollock and P. W. Sutcliffe: Powder Metall., **19** (1976) 12.
[41] D. Yim, P. Sathiyamoorthi, S. J. Hong and H. S. Kim: J. Alloys Compd., **781** (2019) 389.
[42] B. S. Murty, J. W. Yeh, S. Ranganathan, P. P. Bhattacharjee: B. S. Murty, J. W. Yeh, S. Ranganathan, P. P. Bhattacharjee (Eds.), High-Entropy Alloys (Second Edition), Second Edi, Elsevier, (2019) 103.
[43] A. Kumar, S. Kumar Dewangan, S. Singh, M. Chopkar and R. B. Sreesha: High-Entropy Alloys, (2023) 31.
[44] S. K. Dewangan: Indian Institute of Technology Indore, (2021).
[45] S. K. Dewangan, D. Kumar, S. Samal and V. Kumar: J. Mater. Eng. Perform., **30** (2021) 4421.
[46] P. Veronesi, R. Rosa, E. Colombini and C. Leonelli: Technologies, Basel, **3** (2015) 182.
[47] W. Wong and M. Gupta: Technologies Basel, **3** (2015) 1.
[48] C. Nagarjuna, S.K. Dewangan, H. Lee and B. Ahn: Mater. Sci. Eng., A, **886** (2023) 145680.
[49] X. Liu, H. Cheng, Z. Li, H. Wang, F. Chang, W. Wang, Q. Tang and P. Dai: Vacuum, **165** (2019) 297.
[50] S. K. Dewangan, C. Nagarjuna, H. Lee, A. Sharma and B. Ahn: Powder Metall., **66** (2023) 650.
[51] A. N. Klein, R. P. Cardoso, H. C. Pavanati, C. Binder, A. M. Maliska, G. Hammes, D. Fusao, A. Seeber, S. F. Brunatto and J. L. R. Muzart: Plasma Sci. Technol., **15** (2013) 70.
[52] E. Colombini, R. Rosa, L. Trombi, M. Zadra, A. Casagrande and P. Veronesi: Mater. Chem. Phys., **210** (2018) 78.
[53] M. E. Glicksman, Principals of Solidification An Introduction to Modern Casting and Crystal Growth Concepts, Springer, (2011).
[54] S. Chen, Y. Tong and P. Liaw: Entropy, **20** (2018) 937.
[55] C. O. Ujah, D. V. V. Kallon and V. S. Aigbodion: Mater. Today Sustainability, **25** (2024) 100639.
[56] B. Zhang, Y. Huang, Z. Dou, J. Wang and Z. Huang: Adv. Mater. Devices, **9** (2024) 100688.
[57] D.O. Svensson: High Entropy Alloys: Breakthrough Materials for Aero Engine Applications, (2015).
[58] M. G. Perspectives and G. Mazzolai: Recent Patents on Materials Science, **5** (2012) 137.
[59] Q. Tian, G. Zhang, K. Yin, W. Wang, W. Cheng and Y. Wang: Mater. Charact., **151** (2019) 302.
[60] M. N. Rao: Trans. Indian Inst. Met., **61** (2008) 87.
[61] X. Gong, Y. Yu, T. Wang, Y. Liu, L. Zhang, Z. Gao, H. Ziyong, X. Chen, S. He and X. Qu: Met. Mater. Int., **29** (2023) 3286.
[62] Y. Guo, X. Li and Q. Liu: Mater. Des., **196** (2020) 109085.
[63] O. Bazaka, K. Bazaka, P. Kingshott, R. J. Crawford and E. P. Ivanova: The Chemistry of Inorganic Biomaterials, (2021) 1.
[64] W. Y. Ching, S. San, J. Brechtl, R. Sakidja, M. Zhang and P. K. Liaw: NPJ Comput. Mater., **6** (2020) 45.
[65] G. Shibo, Q. Xuanhui, H. Xinbo, Z. Ting and D. Bohua: J. Mater. Process Technol., **173** (2006) 310.
[66] A. T. Sidambe: Materials, **7** (2014) 8168.
[67] M. Sahlberg, D. Karlsson, C. Zlotea and U. Jansson: Sci Rep, **6** (2016) 36770.
[68] M. Fu, X. Ma, K. Zhao, X. Li and D. Su: iScience, **24** (2021) 102177.
[69] Office-of-Energy-Efficiency-&-Renewable-Energy, Materials-Based Hydrogen Storage | Department of Energy (2015).
[70] S. Siengchin: Def. Techno., **24** (2023) 1.
[71] J. L. Dong, F. C. Li, Z. P. Gu, M. Q. Jiang, Y. H. Liu, G. J. Wang and X. Q. Wu: Int. J. Plast., **171** (2023) 103801.

Research Article

pISSN 2799-8525 · eISSN 2799-8681
J Powder Mater 2024;31(6):493-499

Journal of Powder Materials

Effect of Calcium Addition on the High-Temperature Recovery of Nd and Dy from Nd-Fe-B Scrap Using Mg-Based Extractants

Hyoseop Kim*

Korea Institute of Industrial Technology, 156, Gaetbeol-ro, Yeonsu-gu, Incheon, 22099, Republic of Korea

This study investigated whether calcium (Ca) addition improved the recovery of neodymium (Nd) and dysprosium (Dy) from Nd-Fe-B magnet scrap using magnesium (Mg)-based liquid metal extraction (LME). Traditional LME processes are limited to temperatures up to 850 °C due to oxidation issues, reducing the efficiency of rare earth element (REE) recovery, especially for Dy. By adding 10 wt.% Ca to Mg and increasing the processing temperature to 1,000 °C, we achieved nearly 100% Nd and approximately 38% Dy recovery, compared to 91% and 28%, respectively, with pure Mg at 850 °C. However, excessive Ca addition (20 wt.%) decreased the recovery efficiency due to the formation of stable intermetallic compounds. These results highlight the critical role of Ca in optimizing REE recycling from Nd-Fe-B magnet scrap.

Keywords: Rare Earth Elements (REEs); Neodymium (Nd); Dysprosium (Dy); Liquid Metal Extraction (LME); Calcium (Ca) Addition; Nd-Fe-B Magnet Scrap; Mg-Ca Alloys; High-Temperature Processing

Received: September 9, 2024
Revised: November 4, 2024
Accepted: November 5, 2024

***Corresponding author:**
Hyoseop Kim
TEL: +82-10-9477-6914
E-mail: hyoseop1231@kitech.re.kr

1. Introduction

Rare earth elements (REEs), particularly neodymium (Nd) and dysprosium (Dy), are essential components in Nd-Fe-B permanent magnets due to their exceptional magnetic properties [1–4]. These magnets are crucial in technologies such as electric vehicles, wind turbines, medical devices, and electronic equipment [5]. The global demand for Nd-Fe-B magnets is increasing rapidly, with an estimated annual growth rate of 8–12%, driven by clean energy initiatives and the proliferation of high-tech devices [6, 7]. This surge intensifies pressure on REE supply chains, which are vulnerable due to geopolitical factors and the environmental impact of primary mining operations.

Recycling Nd-Fe-B magnet scrap offers a sustainable alternative to primary mining, providing a secondary source of REEs while mitigating environmental degradation. However, efficient REE recovery from scrap poses significant challenges. Recycling methods are mainly hydrometallurgical or pyrometallurgical [8-11]. Hydrometallurgical techniques like acid leaching [9] and solvent extraction [11] are effective but involve complex processing steps, high operational costs, and generate hazardous waste requiring careful disposal. Pyrometallurgical approaches such as molten salt electrolysis [12, 13] and gas-phase extraction [14, 15] offer faster processing and simpler operation but are energy-intensive and may face scalability issues due to equipment and energy requirements.

Liquid metal extraction (LME) has emerged as a promising pyrometallurgical method for recycling Nd-Fe-B scrap [16, 17]. In LME, molten metals like magnesium (Mg) selectively extract REEs based on their solubility and affinity compared to other elements like iron (Fe) and boron (B). This method benefits from operational simplicity and potential for continuous processing, making it attractive for industrial applications. However, while Mg effectively extracts light REEs (LREEs) like Nd, extraction of heavy REEs (HREEs) such as Dy remains inefficient due to Dy's lower solubility and tendency to form stable oxides, which hinder its recovery during the LME process [18-22].

Enhancing Dy extraction is challenged by the formation of thermodynamically stable oxides like Dy_2O_3 at elevated temperatures [23], acting as diffusion barriers and impeding Dy dissolution into molten Mg. To mitigate oxidation, traditional

https://doi.org/10.4150/jpm.2024.00283

LME operates below 850 °C, which is suboptimal for REE diffusion kinetics [24]. Recent studies have explored adding calcium (Ca) to molten Mg to address this issue [25, 26]. Ca can reduce REE oxides to their metallic forms, forming CaO as a byproduct that does not hinder the extraction process. This approach enables higher-temperature operations, improving the kinetics of REE extraction, particularly for HREEs like Dy. However, optimal conditions for Ca-assisted LME, including precise Ca content and the effects of high-temperature processing on Nd and Dy recovery, are not fully understood. Additionally, the impact of intermetallic compounds formed at higher Ca concentrations on REE solubility and extraction efficiency requires thorough investigation.

This study aims to address these challenges by systematically investigating the effect of Ca addition and high-temperature processing on the extraction efficiencies of Nd and Dy from Nd-Fe-B magnet scrap using Mg-based extractants. By varying Ca content (0 wt.%, 10 wt.%, and 20 wt.%), processing temperatures (850 °C and 1,000 °C), and holding times (1 to 3 hours), we seek to determine the optimal conditions that maximize REE recovery without adverse effects from intermetallic compound formation. Understanding the thermodynamic and kinetic mechanisms by which Ca enhances the reduction of REE oxides and facilitates their diffusion into the molten alloy will contribute to optimizing the LME process for efficient recycling of Nd-Fe-B magnet scrap. Improving the recovery of HREEs like Dy is crucial due to their limited availability and significant role in enhancing the performance of Nd-Fe-B magnets, thereby supporting the advancement of clean energy technologies and electronic devices.

2. Experimental Procedure

2.1. Materials

The Nd-Fe-B magnet scrap used in this study was sourced from industrial waste generated during the production of permanent magnets. The chemical composition of the scrap was determined using micro–X-ray fluorescence (μ-XRF) analysis, revealing approximately 23.84 wt.% neodymium (Nd), 8.57 wt.% dysprosium (Dy), 64.60 wt.% iron (Fe), 0.89 wt.% boron (B), along with minor amounts of cobalt (Co), aluminum (Al), and copper (Cu). The detailed composition is presented in Table 1.

High-purity magnesium (Mg, ≥99.9%) and calcium (Ca, ≥99.9%) were used as extractant materials. Mg–Ca alloys were prepared with Ca concentrations of 0 wt.%, 10 wt.%, and 20 wt.% to evaluate the effect of Ca addition on REE extraction efficiency.

2.2. Sample Preparation

The Nd-Fe-B magnet scrap was mechanically crushed using a jaw crusher to reduce the particle size, enhancing reaction kinetics during extraction. The crushed material was then sieved to obtain particles ranging from 1 mm to 2 mm. Approximately 200 g of the sieved magnet scrap was used for each experimental run.

The prepared magnet scrap was placed into a stainless steel (SS) mesh container with a mesh size of 0.8 mm to retain the particles during the extraction process and allow efficient contact with the molten extractant.

2.3. Liquid Metal Extraction

Extraction experiments were conducted using an induction furnace capable of reaching 1,100 °C. A crucible with an inner diameter of 100 mm and a height of 150 mm, featuring a sealed 10 mm bottom orifice, was used to hold the extractant metal. For each experiment, 200 g of Mg or Mg–Ca alloy (0 wt.%, 10 wt.%, or 20 wt.% Ca) was placed into the crucible. The magnet scrap, contained in a stainless steel (SS) mesh container, was positioned above the extractant metal within the crucible.

Prior to heating, the assembly was placed inside a quartz chamber, evacuated to approximately 1×10^{-2} Pa to remove air and moisture, and purged with high-purity argon gas. This vacuum-purge cycle was repeated three times to minimize oxygen presence and reduce oxidation risk during heating.

The furnace heated the crucible to target temperatures of 850 °C or 1,000 °C at a controlled rate of 10 °C/min. Temperature was monitored using a calibrated Type-K thermocouple near the crucible bottom. Once the target temperature was reached, the system was held isothermally for 1 to 3 hours, depending on the experimental conditions in Table 2.

After the holding time, the system was cooled to approximately 800 °C to reduce the vapor pressures of Mg and Ca. The stopper rod sealing the crucible's bottom orifice was removed, allowing the molten alloy to flow into a preheated graphite

Table 1. Detailed chemical composition of the Nd-Fe-B magnet scrap used in this study (wt.%)

Elements	Nd	Dy	Fe	B	Co	Al	Cu
Concentration (wt.%)	23.84	8.57	64.60	0.89	1.92	0.06	0.12

Table 2. Experimental conditions for liquid metal extraction, including temperature, holding time, Nd-Fe-B scrap mass, and extractant composition

Experiment Number	Temperature (°C)	Holding Time (h)	NdFeB Scrap (g)	Extractant	
				Mg (g)	Ca (g)
Exp. 1	850	1	200	200	-
Exp. 2	850	1	200	180	20
Exp. 3	850	1	200	160	40
Exp. 4	850	3	200	180	20
Exp. 5	1,000	1	200	180	20
Exp. 6	1,000	3	200	180	20

Table 3. Chemical compositions (wt.%) of alloys obtained after liquid metal extraction under various experimental conditions

Experiment Number	Chemical composition (wt.%)					Mg to Ca Ratio
	Nd	Dy	Mg	Ca	Fe	
Exp. 1	16.05	1.84	82.09	-	0.02	-
Exp. 2	17.95	1.88	70.16	10.00	0.00	7.02
Exp. 3	10.11	1.15	66.56	22.16	0.03	3.00
Exp. 4	20.08	1.98	67.44	10.51	0.00	6.42
Exp. 5	21.11	2.45	64.52	11.73	0.19	5.50
Exp. 6	24.28	2.22	60.11	13.21	0.18	4.55

mold beneath the crucible, which minimized thermal shock and facilitated alloy removal. During pouring, the stainless-steel mesh container holding the residual magnet scrap was gently agitated to ensure maximum drainage of the molten alloy and prevent entrapment of liquid metal among the scrap particles. The entire operation was conducted under continuous argon gas flow to maintain an inert atmosphere and prevent oxidation. After solidification in the mold under argon atmosphere, the alloy ingot and residual magnet scrap were cooled to room temperature and collected separately for analysis.

2.4. Sample Analysis

The collected alloy ingots were sectioned using a diamond saw to obtain representative samples for analysis. The chemical compositions of both the alloy and the residual magnet scrap were determined using micro–X-ray fluorescence (μ-XRF).

The extraction efficiency of Nd and Dy was calculated using the following equation:

$$R_{REE} = \left(1 - \frac{wREE_{\text{residue}}}{wREE_{scrap}}\right) \times 100\,\% \quad (1)$$

Where R_{REE} is the extraction efficiency of the REE (Nd or Dy), $wREE_{residue}$ is the mass fraction (wt.%) of the REE remaining in the residual magnet scrap after extraction, and $wREE_{scrap}$ is the mass fraction (wt.%) of the REE in the original magnet scrap before extraction.

3. Results and Discussion

3.1. REE Extraction with Mg and Mg-Ca Alloys

The chemical compositions of the alloys obtained from the liquid metal extraction (LME) experiments at 850 °C are summarized in Table 3.

Fig. 1 illustrates the extraction efficiencies of Nd and Dy as a function of Ca addition at 850 °C. When pure magnesium (Mg) was used as the extractant (Exp. 1), the extraction efficiencies for Nd and Dy were approximately 91% and 28%, respectively. The high recovery of Nd aligns with Mg's known effectiveness in extracting light rare earth elements (LREEs) due to favorable thermodynamics and kinetics [18-22]. The lower recovery of Dy, a heavy rare earth element (HREE), is attributed to its higher thermodynamic stability in oxide form and lower diffusion rate in molten Mg [27].

Adding 10 wt.% Ca to Mg (Exp. 2) significantly improved the extraction efficiency of Nd to nearly 100% and modestly increased Dy recovery to approximately 30%. This enhancement is primarily due to Ca's higher affinity for oxygen, enabling it to

reduce stable REE oxides like Nd_2O_3 and Dy_2O_3 more effectively than Mg alone.

The thermodynamic favorability of the reduction reactions can be quantified by the standard Gibbs free energy changes (ΔG°). At 850 °C, the reduction of Nd_2O_3 and Dy_2O_3 by Ca has ΔG° values of approximately –370 kJ/mol and –360 kJ/mol, respectively [18, 19]. These highly negative values indicate spontaneous reactions. In contrast, the corresponding reductions by Mg have less negative ΔG° values (approximately –180 kJ/mol for Nd_2O_3 and –170 kJ/mol for Dy_2O_3) [20], making them less favorable. The ability of Ca to reduce these oxides enhances the availability of metallic REEs for dissolution into the molten alloy.

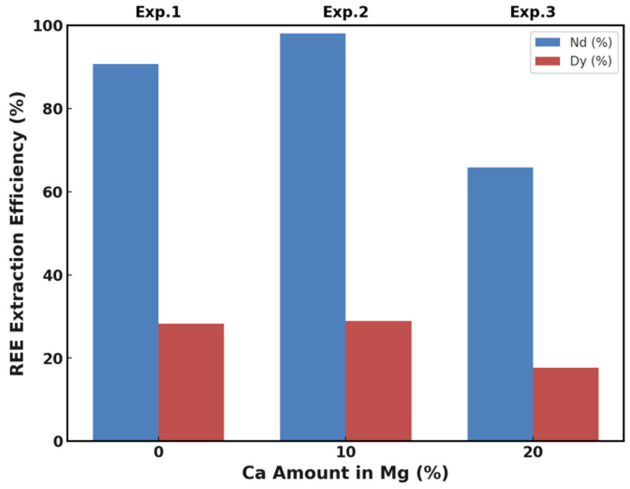

Fig. 1. Effect of calcium addition on the efficiency of Nd and Dy extraction at 850 °C.

However, increasing the Ca content to 20 wt.% (Exp. 3) resulted in decreased extraction efficiencies for both Nd (approximately 66%) and Dy (approximately 18%). This decrease can be attributed to the formation of stable intermetallic compounds at higher Ca concentrations, such as Ca_3Nd and Ca_5Dy_3, which have been reported in the literature [23, 25]. These compounds have low solubility in the Mg–Ca melt and tend to precipitate out, reducing the concentration of free REEs available for extraction.

The formation of intermetallic phases not only consumes REEs but also alters the melt's properties, hindering mass transfer and diffusion processes. Previous studies have indicated that excessive Ca can lead to the formation of such intermetallic compounds, negatively impacting the extraction process [26]. These findings highlight the importance of optimizing Ca content to balance the benefits of oxide reduction against the drawbacks of intermetallic compound formation.

3.2. Effect of Temperature and Holding Time

The impact of temperature and holding time on the extraction efficiencies of Nd and Dy was evaluated using Mg–10 wt.% Ca alloy. The results are presented in Fig. 2. At 850 °C with a holding time of 1 hour (Exp. 2), Nd extraction efficiency was nearly 100%, while Dy recovery was approximately 30%. Extending the holding time to 3 hours at the same temperature

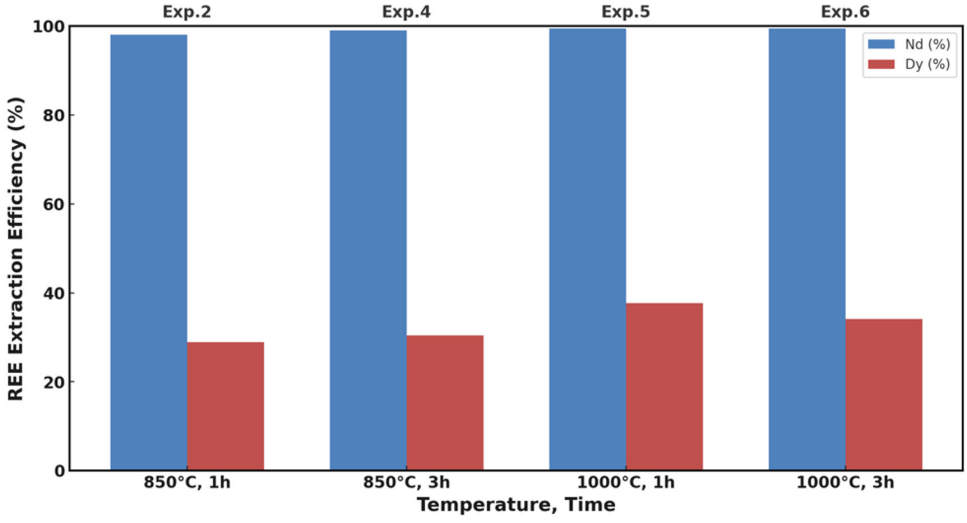

Fig. 2. Efficiency of Nd and Dy extraction as a function of temperature and holding time using Mg–10 wt.% Ca alloy.

(Exp. 4) had a minimal effect on Nd recovery but slightly improved Dy extraction to about 32%. This suggests that Nd extraction is kinetically fast once the oxide barrier is reduced, whereas Dy extraction is diffusion-limited.

Raising the temperature to 1,000 °C significantly enhanced Dy extraction efficiency to approximately 38% after 1 hour (Exp. 5). However, extending the holding time to 3 hours at 1,000 °C (Exp. 6) resulted in a decrease in Dy recovery to about 35%, indicating that prolonged exposure at high temperatures may adversely affect Dy extraction.

The decrease in Dy recovery with extended holding time can be attributed to several factors. One possible explanation is the formation of stable intermetallic compounds between Dy and Ca or Mg, such as Ca_5Dy_3 or Mg_3Dy, which have low solubility in the molten alloy and tend to precipitate out, reducing the amount of free Dy available for extraction [23, 25]. Additionally, prolonged high-temperature exposure can increase the vaporization of Mg and Ca due to their high vapor pressures, altering the composition of the extractant and reducing its effectiveness [26]. Despite maintaining an inert atmosphere, trace amounts of oxygen could lead to re-oxidation of Dy over extended periods, forming Dy_2O_3 and diminishing extraction efficiency.

Despite the thermodynamic favorability of Dy reduction at higher temperatures, these factors can counteract the benefits, leading to decreased Dy extraction with prolonged holding times. Dy extraction remains lower than Nd due to kinetic limitations and its higher tendency to form stable compounds. Dy has a higher melting point (1,412 °C) and a smaller atomic radius, contributing to slower diffusion rates in the molten alloy [27]. Additionally, Dy_2O_3 is more thermodynamically stable than Nd_2O_3, requiring higher activation energy for reduction.

3.3. Mechanism of REE Oxide Reduction by Calcium

Ellingham diagrams (Fig. 3) were used to compare the stability of oxides and the tendency of different elements to form oxides. Ca has a more negative standard free energy of formation for its oxide (CaO) compared to Nd_2O_3 and Dy_2O_3, indicating that Ca can effectively reduce these REE oxides. The reduction reactions are thermodynamically favorable across the temperature range studied, with the driving force increasing at higher temperatures.

The reduction reactions can be represented as:

$$Nd_2O_3 + 3Ca \rightarrow 2Nd + 3CaO \ (\Delta G° = -370\,kJ/mol \text{ at } 850^{\circ}C) \quad (2)$$

$$Dy_2O_3 + 3Ca \rightarrow 2Dy + 3CaO \ (\Delta G° = -360\,kJ/mol \text{ at } 850^{\circ}C) \quad (3)$$

The Ca–Nd–O ternary phase diagrams at 1,000 °C (Fig. 4) illustrate the phase equilibria and confirm the formation of CaO and metallic REEs upon reduction of REE oxides by Ca. These diagrams also show that excessive Ca can lead to the formation of intermetallic compounds (e.g., Ca_3Nd, CaNd, Ca_5Dy_3), which correspond with the decreased extraction efficiencies observed at higher Ca concentrations.

The mechanism of REE oxide reduction by Ca involves the following steps:

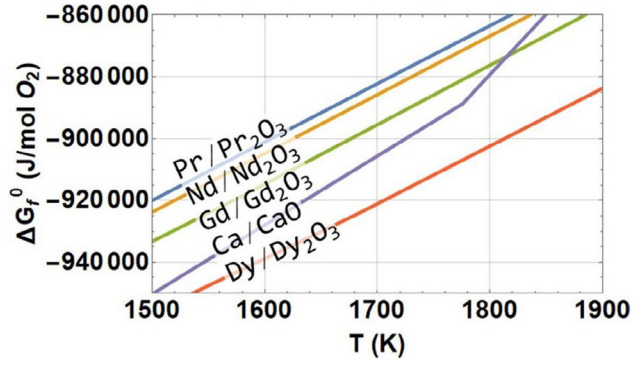

Fig. 3. Ellingham diagram illustrating the thermodynamic favorability of calcium reducing Nd_2O_3 and Dy_2O_3 compared to CaO formation [18, 19].

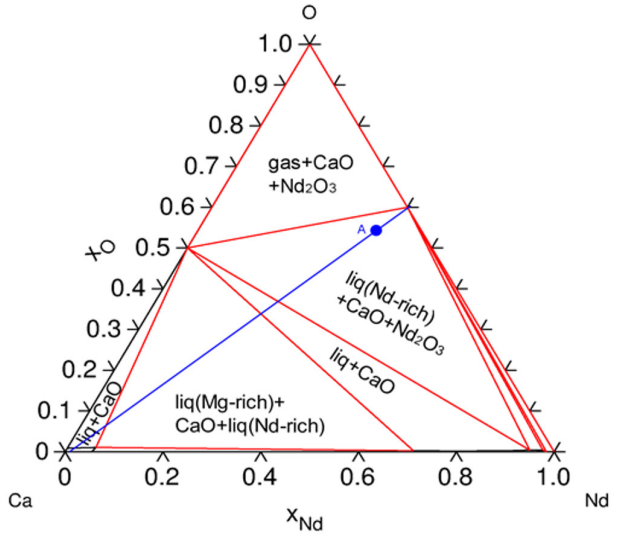

Fig. 4. Calculated Ca–Nd–O ternary phase diagram at 1,000 °C, illustrating the formation of intermetallic compounds affecting REE extraction efficiency.

(1) Reduction of REE Oxides: Calcium reduces Nd_2O_3 and Dy_2O_3 to metals, forming CaO.
(2) Dissolution into Molten Alloy: The reduced REEs dissolve into the molten Mg–Ca alloy.
(3) Formation of CaO: CaO forms and may precipitate from the melt due to its high melting point.

The overall reaction can be simplified as:

$$REE_2O_3 + 3Ca \rightarrow 2REE \text{ (in Mg–Ca alloy)} + 3CaO \quad (4)$$

Where REE represents Nd or Dy.

The removal of oxygen enhances the solubility of REEs in the molten alloy. However, Dy's propensity to form stable intermetallic compounds at higher Ca concentrations limits its solubility. This underscores the necessity of optimizing Ca content to prevent excessive formation of such compounds.

3.4. Comparison with Previous Studies

The findings of this study demonstrate an improved Dy extraction efficiency (~38%) compared to previous reports, which typically achieved Dy recoveries of 20–30% using pure Mg at lower temperatures. The use of Ca as a reducing agent and the increase in processing temperature to 1,000 °C effectively enhanced the reduction of Dy_2O_3, facilitating greater Dy recovery. Furthermore, identifying an optimal Ca content (~10 wt.%) aligns with the need to balance oxide reduction benefits against the formation of undesirable intermetallic compounds. This balance was not thoroughly explored in prior studies, highlighting the contribution of this research to advancing the understanding of Ca-assisted LME processes.

Incorporating Ca into the LME process at controlled concentrations can significantly enhance REE recovery from Nd-Fe-B magnet scrap, particularly for HREEs like Dy. Operating at higher temperatures (up to 1,000 °C) is feasible with Ca addition, as it mitigates oxidation concerns. However, careful control of Ca content is essential to prevent the formation of intermetallic compounds that reduce extraction efficiency.

3.5. Implications and Future Work

This study highlights the pivotal role of Ca in overcoming oxidation barriers and optimizing the LME process for REE recycling. The optimized addition of Ca at around 10 wt.% to Mg-based extractants, combined with high-temperature processing at 1,000 °C, significantly enhances the recovery of both Nd and Dy from Nd-Fe-B magnet scrap. These findings provide valuable insights into the thermodynamic and kinetic factors governing the LME process and emphasize the importance of precise Ca content control.

Future research should focus on further improving Dy recovery by exploring alternative reducing agents or alloying elements that facilitate Dy extraction without forming undesirable intermetallic compounds. Additionally, optimizing process parameters such as holding time, temperature profiles, and atmosphere control could lead to even more efficient extraction processes. Assessing the scalability of this method for industrial applications is also crucial for advancing sustainable recycling practices for critical rare earth elements.

4. Conclusion

Adding 10 wt.% calcium (Ca) to magnesium (Mg)-based extractants significantly enhanced the extraction of neodymium (Nd) and dysprosium (Dy) from Nd-Fe-B magnet scrap at elevated temperatures. At 1,000 °C, Nd extraction efficiency reached nearly 100%, and Dy recovery improved to approximately 38%. This improvement is due to Ca's strong affinity for oxygen, effectively reducing stable REE oxides like Nd_2O_3 and Dy_2O_3, which facilitates the release and diffusion of metallic REEs into the molten Mg–Ca alloy.

However, increasing Ca content to 20 wt.% decreased extraction efficiencies for both Nd and Dy because of the formation of stable intermetallic compounds like Ca_3Nd and Ca_5Dy_3. These compounds have low solubility in the Mg–Ca melt, reducing the availability of free REEs. Optimizing Ca content is therefore crucial to balance oxide reduction benefits against intermetallic compound formation.

Operating at higher temperatures enhanced reaction kinetics and thermodynamic favorability, further improving Dy recovery. However, prolonged holding times at high temperatures slightly decreased Dy extraction efficiency, likely due to additional intermetallic formation, increased vaporization losses of Mg and Ca, and potential re-oxidation of Dy.

This research advances the understanding of Ca-assisted liquid metal extraction (LME) for REE recycling. By optimizing Ca content and processing conditions, oxidation barriers can be overcome, enhancing the recovery of both light and heavy REEs from Nd-Fe-B scrap. These findings have significant implications for developing efficient, scalable recycling methods, reducing reliance on primary REE mining, and supporting sustainable supply chains.

Future work should focus on further enhancing Dy recovery by exploring alternative reducing agents or alloying elements

that prevent undesirable intermetallic compounds while maintaining effective oxide reduction. Refining process parameters and assessing the scalability and economic feasibility of this method are essential for potential industrial application.

Funding

This work was supported by grants from the Korea Institute of Industrial Technology (KITECH) under the "Manufacturing Innovation Support Program" (KITECH JH-24-0008, KITECH JH-24-0013).

Conflict of Interest

The authors have no conflicts of interest to declare.

Data Availability Statement

All dataset files used in this study are already provided in the manuscript.

Author Information and Contribution

Hyoseop Kim: Researcher; conceptualization, writing–original draft, writing–review & editing, funding acquisition, supervision.

Acknowledgement

None.

References

[1] Z. Hua, J. Wang, L. Wang, Z. Zhao, X. Li and Y. Xiao: ACS Sustainable Chem. Eng., **2** (2014) 2536.
[2] M. Sagawa, S. Fujimura, N. Togawa, H. Yamamoto and Y. Matsuura: J. Appl. Phys., **55** (1984) 2083.
[3] K. Binnemans, P. T. Jones, B. Blanpain and T. V. Gerven: J. Cleaner Prod., **51** (2014) 1.
[4] J. J. Croat, J. F. Herbst, R. W. Lee and F. E. Pinkerton: J. Appl. Phys., **55** (1984) 2078.
[5] H.-S. Yoon, C.-J. Kim, K. W. Chung, S.-J. Lee and A.-R. Joe: Korean J. Chem. Eng., **31** (2014) 706.
[6] D. Dupont and K. Binnemans: Green Chem., **17** (2015) 2150.
[7] O. Takeda, T. H. Okabe and Y. Umetsu: J. Alloys Compd., **392** (2005) 206.
[8] J. W. Lyman and G. R. Palmer: High Temp Mater Process, **11** (1993) 175.
[9] X. Sun and K. E. Waters: ACS Sustainable Chem. Eng., **2** (2014) 1910.
[10] M.-S. Lee, J.-Y. Lee, J.-S. Kim and G.-S. Lee: Sep. Purif. Technol., **46** (2005) 72.
[11] T. Itakura, R. Sasai and H. Itoh: J. Alloys Compd., **408-412** (2006) 1382.
[12] M. Itoh, K. Miura and K.-I. Machida: Chem. Lett., **37** (2008) 372.
[13] T. Uda: Mater. Trans., **43** (2002) 55.
[14] K. Murase, K. Machida and G. Adachi: J. Alloys Compd., **217** (1995) 218.
[15] Y. Mochizuki, N. Tsubouchi and K. Sugawara: ACS Sustainable Chem. Eng., **1** (2013) 655.
[16] T. W. Ellis and F. A. Schmidt: Ames, Iowa, US Patent, 5,437,709, (1995).
[17] Y. Xu, L. Chumbley and F. Laabs: J. Mater. Res., **15** (2000) 2296.
[18] T. H. Okabe, O. Takeda, K. Fukuda and Y. Umetsu: Mater. Trans., **44** (2003) 798.
[19] O. Takeda, T. H. Okabe and Y. Umetsu: J. Alloys Compd., **408-412** (2006) 387.
[20] H. J. Chae, Y. D. Kim, B. S. Kim, J. G. Kim and T.-S. Kim: J. Alloys Compd., **586** (2014) S143.
[21] H. W. Na, Y. H. Kim, H. T. Son, I. H. Jung, H. S. Choi and T. B. Kim: Curr. Nanosci., **10** (2014) 128.
[22] M. Sun, X. Hu, L. Peng, P. Fu, W. Ding and Y. Peng: J. Mater. Process. Technol., **218** (2015) 57.
[23] S.-W. Nam, S.-M. Park, D.-H. Kim and T.-S. Kim: Metals and Materials International, **27** (2020) 538.
[24] S.-W. Nam, S.-M. Park, M. Z. Rasheed, M.-S. Song, D.-H. Kim and T.-S. Kim: Metals, **11** (2021) 1345.
[25] R. Schmid-Fetzer, A. Kozlov, B. Wiese, C. L. Mendis, D. Tolnai, K. U. Kainer and N. Hort, Magnesium Technology, 2016, Springer, Cham (2016) 67.
[26] S.-H. Ha, J.-K. Lee and S. K. Kim: Mater. Trans., **49** (2008) 1081.
[27] M. Firdaus, M. A. Rhamdhani, Y. Durandet, W. J. Rankin and K. McGregor: J. Sustain. Metall., **2** (2016) 276.

Research Article

pISSN 2799-8525 · eISSN 2799-8681
J Powder Mater 2024;31(6):500-507

Journal of Powder Materials

Design of Conductive Inks Containing Carbon Black and Silver Nanowires for Patternable Screen-Printing on Fabrics

Seokhwan Kim[1,2,3], Geumseong Lee[1,2,3], Jinwoo Park[4], Dahye Shin[4], Ki-Il Park[1,2,3], Kyoung Jin Jung[4,*], Yuho Min[1,2,3,*]

[1]Department of Materials Science and Metallurgical Engineering, Kyungpook National University, Daegu, 41566, Republic of Korea
[2]Innovative Semiconductor Education and Research Center for Future Mobility, Kyungpook National University, Daegu, 41566, Republic of Korea
[3]Research Institute of Automotive Parts and Materials, Kyungpook National University, Daegu, 41566, Republic of Korea
[4]Defense Materials & Energy Technology Center Team 1, Agency for Defense Development, Daejeon, 34186, Republic of Korea

This study developed conductive inks composed of carbon black (CB) and silver nanowires (Ag NWs) for cost-effective screen-printing on fabrics. The Ag NW density within the CB matrix was precisely controlled, achieving tunable electrical conductivity with minimal Ag NW usage. The resulting inks were successfully patterned into shapes such as square grids and circles on textile surfaces, demonstrating excellent conductivity and fidelity. Adding 19.9 wt% Ag NWs reduced sheet resistance by ~92% compared to CB-only inks, highlighting the effectiveness and potential of this hybrid approach for cost-effective, high-performance textile-based electronics. The one-dimensional morphology of Ag NWs facilitated the formation of conductive percolation networks, creating efficient electron pathways within the CB matrix even at low loadings. This work advances the field of CB-based conductive inks and provides a scalable and practical method for producing functional, patterned electronic textiles.

Keywords: Conductive inks; Carbon black; Silver nanowires; Screen-printing; Textile electronics

Received: November 21, 2024
Revised: December 8, 2024
Accepted: December 11, 2024

***Corresponding author:**
Kyoung Jin Jung
E-mail: charley@add.re.kr

Yuho Min
E-mail: yuhomin@knu.ac.kr

1. Introduction

The development of flexible, fabric-based electronics has attracted significant interest due to their potential applications in wearable technology, smart textiles, and integrated sensors [1]. Solution-based conductive inks play a crucial role in realizing these applications, enabling direct circuit printing onto fabric substrates with advantages such as low cost, ease of patterning, and compatibility with existing manufacturing processes for flexible electronics [2]. Printing techniques like screen printing, inkjet, and gravure are essential for efficiently depositing conductive materials onto textiles, each offering unique benefits [3]. Screen printing, in particular, is well-suited for fabric-based electronics due to its adaptability, cost-effectiveness, and suitability for large-scale production with precise control over ink thickness and pattern [4].

Conductive inks typically contain conductive filers, solvents, binders, dispersants, and additives. The formulation of these inks significantly influences their electrical conductivity, mechanical durability, chemical stability, patterning precision, and compatibility with coating methods [5]. A primary challenge in the field is the high cost of conductive inks, largely driven by the cost of conductive fillers, typically including materials like CNT, graphene, and metals (Ag, Au, etc.) [6]. Carbon-based conductive fillers, such as graphene and CNT, exhibit high carrier mobility, thermal conductivity, tensile strength, and resistance to electromigration, making them suitable for flexible electronics [7]. However, their high cost and dispersion issues remain unresolved [8]. Metal-based fillers, such as Ag nanoparticles, offer high conductivity and stability but are relatively expensive, which limits their use in large-scale or disposable applications. More affordable alternatives, like Cu nanoparticles, are susceptible to oxidation, requiring protective measures such as inert processing conditions and surface coatings [9]. Conductive polymers, including polyaniline (PANI), polypyrrole

https://doi.org/10.4150/jpm.2024.00409

(PPy), poly(3,4-ethylenedioxythiophene) (PEDOT), and poly (3,4-ethylenedioxythiophene)/poly (styrene sulfonate) (PEDPT/PSS), have also been explored. Still, their environmental sensitivity, lower conductivity, and complex synthesis processes limit their broader application in durable electronics [10].

Given these cost constraints, carbon black (CB) serves as an effective, low-cost, and environmentally stable conductive filler with a high surface area [11]. However, its relatively lower conductivity and higher loading requirements in ink formulations remain challenging [12]. The use of hybrid ink formulations to enhance conductivity has been consistently proposed [13]. To address these issues, this study develops a cost-effective CB-based conductive ink incorporating a small amount of Ag nanowires (Ag NWs). By carefully controlling the density of Ag NWs within the CB matrix, we achieve stable, tunable conductivity at a fraction of the cost of pure silver inks. The one-dimensional (1D), high-aspect-ratio structure of Ag NWs facilitates electron flow, enhancing conductivity at low loadings. Screen printing enables precise pattering of these inks on fabric, offering a promising approach for high-resolution, scalable textile-based electronics. This research advances CB-based conductive inks as a cost-effective, scalable, and high-performance solution for fabric-compatible electronics. Additionally, comparing the prices of conductive materials, which constitute the majority of conductive inks, highlights the economic advantages of the ink proposed in this study. Traditional silver nanoparticle-based inks typically contain 10–90% silver nanoparticles, whereas our developed carbon black-based ink contains approximately 15%. According to market data, silver nanoparticles are priced at approximately $1,000 per kg (based on LT-Metal, South Korea), while the carbon black powder we used is priced at $140 per kg. Even at the same weight percentage, this results in a cost difference of over seven times, demonstrating that carbon black-based inks can provide significant economic advantages. This cost-efficiency further underscores the potential of our ink formulation for practical applications.

2. Experimental Section

2.1. Materials

The chemicals used in this study included carbon black (Dae Myung Chemical), $AgNO_3$ (Sigma Aldrich, 99.0%), poly(vinylpyrrolidone) (PVP, Sigma Aldrich, Mw = 55000 g/mol), propylene glycol (PG, Dae Jung, 99%), 1-butyl-3-methylimidazolium chloride (BMIM-Cl, Sigma-Aldrich), polymeric binder (BNMR-215-40, BN Chemical), dimethyl glutarate (DG, Sigma Aldrich), and ethyl carbitol acetate (ECA, Dae Jung). DI-water was obtained using an 18-MQ (SHRO-plus DI) system. Polyurethane-coated fabrics were provided by INNO CHEM.

2.2. Preparation of Carbon Black-Based Ink

Carbon black-based conductive inks were prepared by ball-milling a mixture of DG (10 mL), ECA (10 mL), polymeric binder (10 mL), and carbon black at different weight percentages (15 wt%, 20 wt%, and 25 wt%). The specific amounts of carbon black used for each formulation were 5.3 g, 7.5 g, and 10 g, respectively. The prepared CB-based inks were denoted as CB15, CB20, and CB25, corresponding to their respective CB weight percentages.

2.3. Synthesis of Ag Nanowires

Ag nanowires were synthesized by modifying the method reported previously [14]. A solution of PVP (4.17 g) and BMIM-Cl (0.13 g) was dissolved in 440 mL of PG and heated to 90 °C under magnetic stirring. Separately, a solution of $AgNO_3$ (3.56 g) in 21 mL of PG was prepared. Once the PVP/BMIM-Cl solution reached a stable temperature, the $AgNO_3$ solution was rapidly injected, resulting in a color change from transparent to yellow, orange, and finally gray-green. The reaction proceeded at 90 °C for 24 h, followed by cooling to 25 °C. Ag nanowires were collected by centrifugation at 4000 rpm for 10 min and washed twice with ethyl alcohol and acetone to remove unreacted chemicals.

2.4. Preparation of Inks with Carbon Black and Ag Nanowires

CB15 inks were mixed with Ag nanowires at varying weight percentages (7.7, 14.2, and 19.9 wt%) using an overhead stirrer at 250 rpm for 4 h. The resulting mixture inks were labeled CB92.3Ag7.7, CB85.8Ag14.2, and CB80.1Ag19.9, corresponding to the weight percentages of Ag nanowires.

2.5. Screen Printing of Conductive Inks on Fabrics

Polyurethane-coated fabrics (50 denier) were cut into 10 cm x 10 cm squares. The as-prepared CB-based and mixed CB/Ag NWs inks were screen-printed onto fabric surfaces using a stainless steel screen with a mech density of 325. After printing, the fabrics were dried at 150 °C for 10 min. Two pattern types were printed: grids with a line width of 0.5 mm and 9 mm spacing, and circles with a diameter of 10 mm.

2.6. Characterization

The morphologies of carbon black powders, Ag nanowires, and films were investigated using a JSM-IT700HR (JEOL) scanning electron microscope (SEM). Energy-dispersive X-ray spectroscopy (EDS) elemental mapping images were acquired using an EDS spectrometer attached to the SEM. X-ray diffraction (XRD) analysis was performed using a Rigaku MiniFlex 600 instrument with Cu Kα radiation (λ = 0.1542 nm) to examine the crystal structures. The sheet resistances of the printed patterns were measured using a four-point probe method with an ARMS 200C sheet resistance measurement system (DASOLENG Co., Korea). Ink viscosities were measured with an MCR702 rheometer (Anton Paar).

3. Results and Discussion

Fig. 1 illustrates the experimental procedure, detailing the steps from preparing conductive inks to screen-printing them onto fabric substrates. Carbon black (CB)-based inks were prepared by ball-milling a mixture of solvents, polymer binders, and CB powders at weight percentages of 15 wt%, 20 wt%, and 25 wt%. To enhance conductivity, Ag NWs, synthesized via the polyol method, were incorporated into the CB-based inks at weight percentages of 7.7 wt%, 14.2 wt%, and 19.9 wt% and thoroughly mixed by overhead stirring. The CB-based and mixed CB/Ag NW inks were then screen-printed onto fabrics using grid and circular pattern masks (see Experimental Section). Ball-milling was essential for achieving a homogeneous dispersion of CB powders within the ink and high CB loadings. However, ball-milling is unsuitable for mixing CB-based inks with Ag NWs, as it can damage the one-dimensional structures of the nanowires, leading to short nanorods or particles. The mixing methods adopted in this study offer a simple, scalable approach for the large-scale production of conductive inks. However, maintaining uniform dispersion of carbon black and Ag NWs in large-scale production is crucial to preserve the ink's conductivity and performance. Therefore, advanced dispersion technologies will be required to address this challenge, especially for scaled-up production effectively.

To determine the optimal loading conditions for carbon black, ink stability and the sheet resistance of films were evaluated across various CB concentrations. Fig. 2(a) presents digital

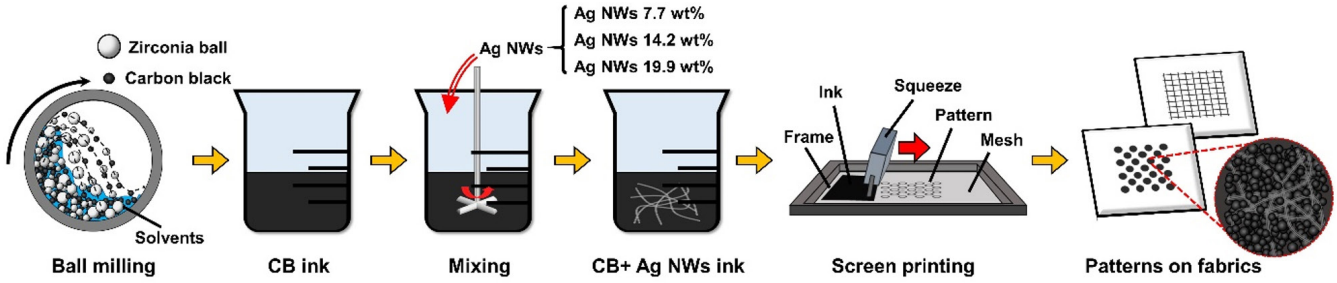

Fig. 1. Schematic illustration of the experimental procedure from conductive ink formulation to screen printing on fabrics.

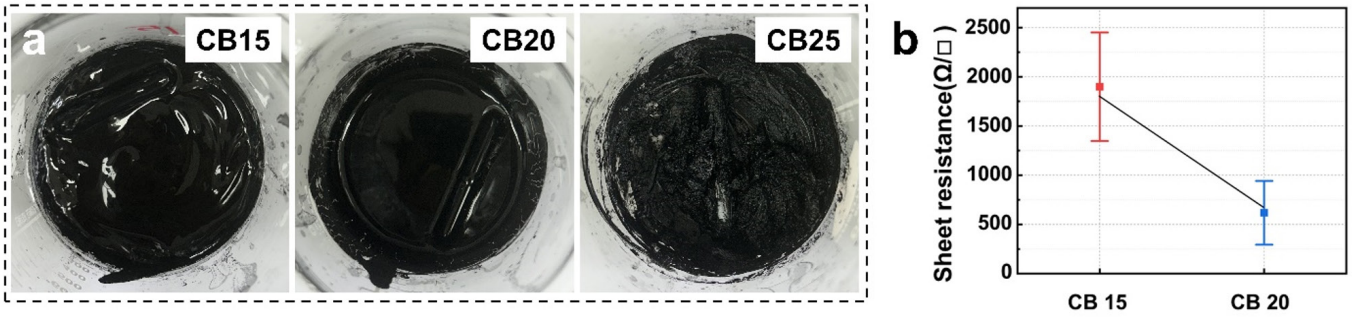

Fig. 2. (a) Digital photo images of CB-based inks prepared at different CB loadings (15, 20, and 25 wt%) and (b) their corresponding sheet resistance values. The sheet resistance of CB25 ink could not be measured due to its high agglomeration and viscous properties. CB, carbon black.

photo images of as-prepared CB inks with different CB loadings: CB15, CB20, and CB25. The CB25 ink exhibited highly viscous, slurry-like behavior with visible CB agglomerates, rendering it unsuitable for screen printing. Consequently, the sheet resistance of films prepared with CB25 ink could not be measured. Although CB20 ink exhibited lower sheet resistance compared to the other formulations, it failed to produce uniform patterns when combined with Ag NWs, resulting in cracking through the printed patterns on fabrics (not shown here). In contrast, CB15 ink demonstrated uniform dispersion and moderate sheet resistance (~1900 Ω/□), as illustrated in Fig. 2(b). Based on these observations, CB15 ink was selected for further formulation with Ag NWs, as its sheet resistance remains too high for practical applications, requiring further enhancement in electrical conductivity.

To address this issue, Ag NWs were incorporated as a co-conductive filler, contributing to conductivity improvement through their unique one-dimensional morphology and conductive percolation network formation, even at low concentrations. Fig. 3 exhibits the as-synthesized Ag NWs with average dimensions of 29.7 μm in length and 65 nm in diameter. The inset of Fig. 3(a) highlights the pentagonal edge structure, which serves as a seed for the growth of 1D Ag NW as reported in previous studies [15]. The high-aspect-ratio structure of Ag NWs promotes efficient electron pathways within the ink matrix, reducing resistance within the conductive network. Even in small amounts, Ag NWs in the CB matrix establish a conductive percolation network, significantly enhancing conductivity with minimal NW content.

The crystal structures of CB powders, Ag NWs, and their mixtures in the CB80.1Ag19.9 ink were analyzed by XRD (Fig. 4 (a)). The XRD pattern of CB powders (black pattern) exhibits two broad peaks at around 24° and 44° of 2θ, corresponding to the (002) and (100) Bragg peaks, which signify an amorphous nature or the presence of randomly oriented small graphitic zones [16] On the other hand, Ag NWs showed strong, narrow peaks (red pattern) at around 36.5°, 42.3°, 63.7°, 76.6°, and 82° of 2θ, corresponding to the (111), (200), (220), (311), and (222)

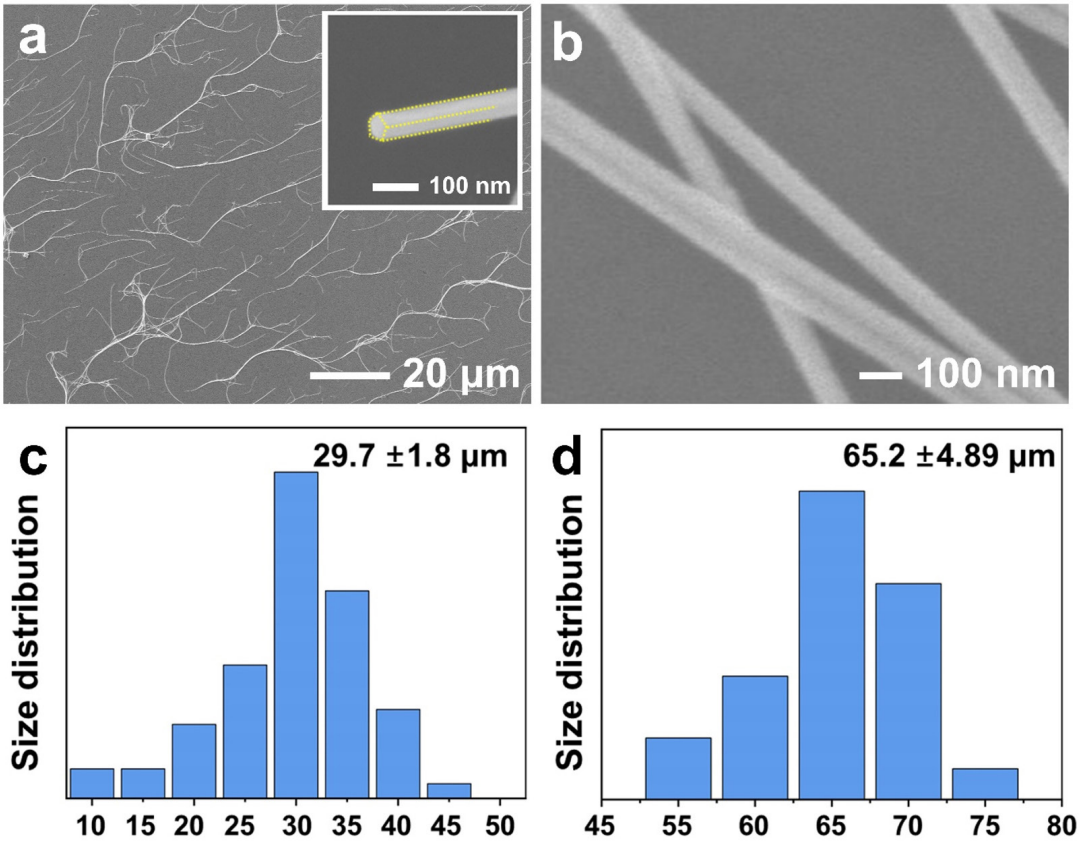

Fig. 3. (a) Low-magnification and (b) high-magnification scanning electron microscopy (SEM) images of as-synthesized Ag nanowires along with (c) their average length and (d) diameter measured by analyzing 100 nanowires. The inset in (a) shows a high-resolution SEM image highlighting the pentagonal edge of an Ag nanowire.

planes of metallic Ag with an FCC structure [17]. In CB80.1Ag19.9 (blue pattern) as a representative mixed ink, the amorphous nature of CB powders and the FCC structure of Ag NWs were evident, although Ag NW peaks had lower relative intensities due to their smaller loading. SEM images and corresponding EDS mappings for elemental C and Ag (Fig. 4 (b)-(c)), confirmed the spherical shape of CB powders, the 1D morphology of Ag NWs, and the spatial elemental distribution of both within the nanostructures.

Three different formulations of mixed CB/Ag NW inks were prepared by adding various Ag NW percentages to the CB15 inks such as CB100Ag0 (no Ag NWs), CB92.3Ag7.7, CB85.8Ag14.2, and CB80.1Ag19.9. These mixed inks were screen-printed onto fabric squares (15 cm × 15 cm) in grid patterns (0.5 mm line width, 9 mm spacing) and circular patterns (10 mm diameter, 10 mm spacing) (Fig. 5). All patterns

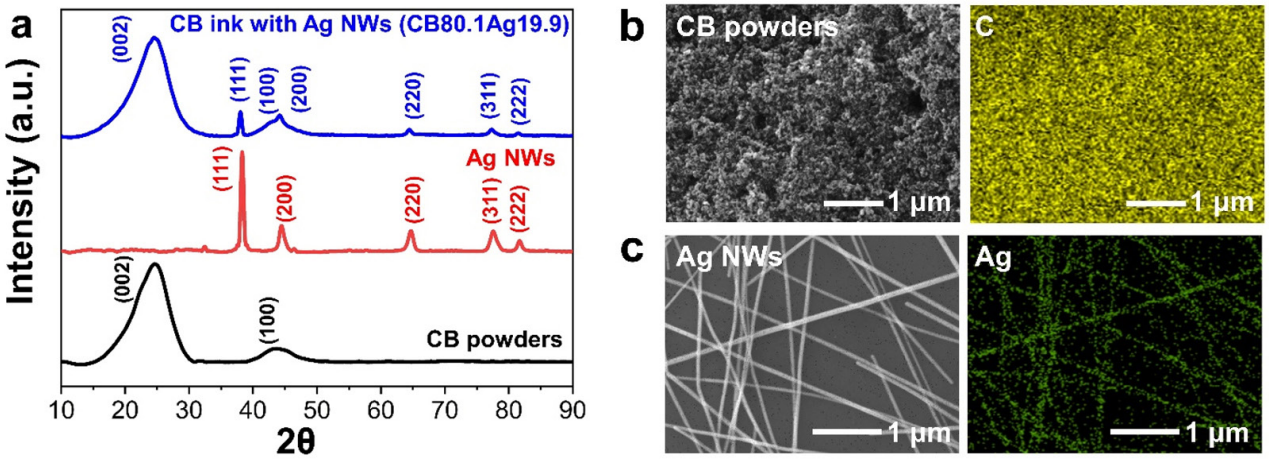

Fig. 4. (a) X-ray diffraction patterns of CB powders (black), Ag NWs (red), and CB80.1Ag19.9 mixed powders (blue). (b,c) Scanning electron microscopy image and corresponding energy-dispersive X-ray spectroscopy elemental mapping image of (b) CB powders and (c) Ag NWs. CB, carbon black; NWs, nanowires.

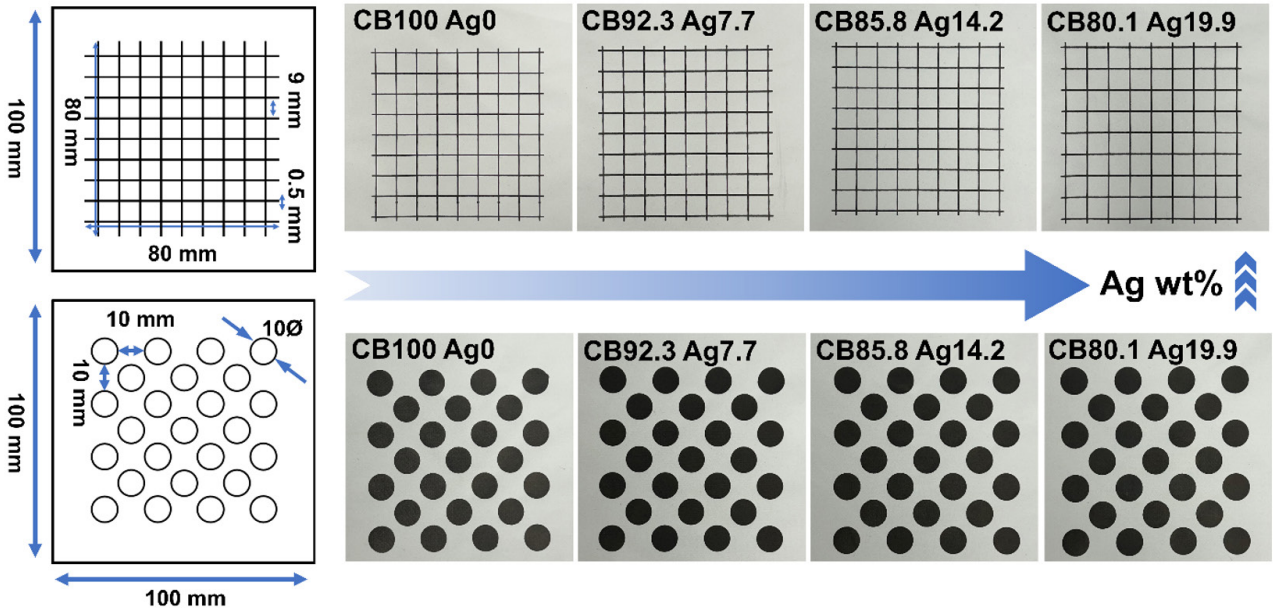

Fig. 5. (a) Schematic illustrations depicting the size, dimensions, and shapes of square grid and circular patterns. (b,c) Digital photo images of screen-printed (b) square grid and (c) circular patterns on fabrics using different conductive inks.

showed dense coverage, with grid patterns exhibiting clear connections, demonstrating the suitability of mixed inks for forming various screen-printed patterns. Top-view SEM images of circular patterns reveal increased Ag NW density and connectivity with higher Ag NW content (Fig. 6). In particular, the Ag NWs were uniformly dispersed and embedded in the CB80.1Ag19.9 sample, leading to a continuous conducting network, which potentially reduces the sheet resistance.

The resulting sheet resistance (R_s) of four patterns was measured using a four-point probe method as shown in Fig. 7 (a). As expected, the R_s values dramatically decreased with increasing Ag NW content in the mixed inks. Notably, the R_s of CB80.1Ag19.9 samples decreased by approximately 92%, 86%, and 78% compared to those of CB100Ag0, CB92.3Ag07.7, and CB85.8Ag14.2 samples, respectively. The dramatic decrease in R_s can be understood by a percolation model for randomly distributed nanowires. The R_s of a nanowire film has the following relation to the nanowire density (N):

$$R_s \sim (N - N_c)^{-\alpha}$$

Where N_c is the critical nanowire density required for conduction, and α is a critical exponent, with values of 1.33 for 2D networks and 1.94 for 3D networks [18-21] Based on this relationship, R_s decreases significantly with increasing nanowires density. The quantities of Ag NW were estimated by dividing the total Ag weight in each ink by each nanowire's weight (Fig. 7 (b)). The weight of each nanowire was calculated using the density and volume of each nanowire based on the measured average diameter and length. Although the effect of the CB matrix is not directly included in this percolation model, it likely has minimal impact due to its spherical shape and lower conductivity. The N_c of nanowires with a length of l can be estimated as follows [21]:

$$N_c l^2 = 5.71$$

Using the equation and the average length of 29.7 μm, the value of N_c was determined to be approximately 0.0065/μm^2. Based on the circular pattern area and the concentration of Ag NWs in each ink, the calculated N values increased from 0.068, 0.15, and 0.22/μm^2 for CB92.3Ag7.7, CB85.8Ag14.2, and CB80.1Ag19.9 samples, respectively. Consequently, the sheet resistance decreased as the conductive percolation networks expanded with higher Ag loading. The Ag NWs network forms as the NWs overlap and connect, creating continuous conductive paths across the printed ink layer (Fig. 7 (c)). In particular, this percolation effect reduces the need for high Ag NWs content while achieving significant conductivity enhancement of the CB matrix. The result is a stable, low-resistance network that effectively bridges gaps within the CB matrix. It should be noted that increasing the amounts of Ag nanowires can further reduce the R_s values, but it also increases the viscosity of the inks, as observed with the CB-based ink at higher CB loadings (CB25). This can lead to difficulties in

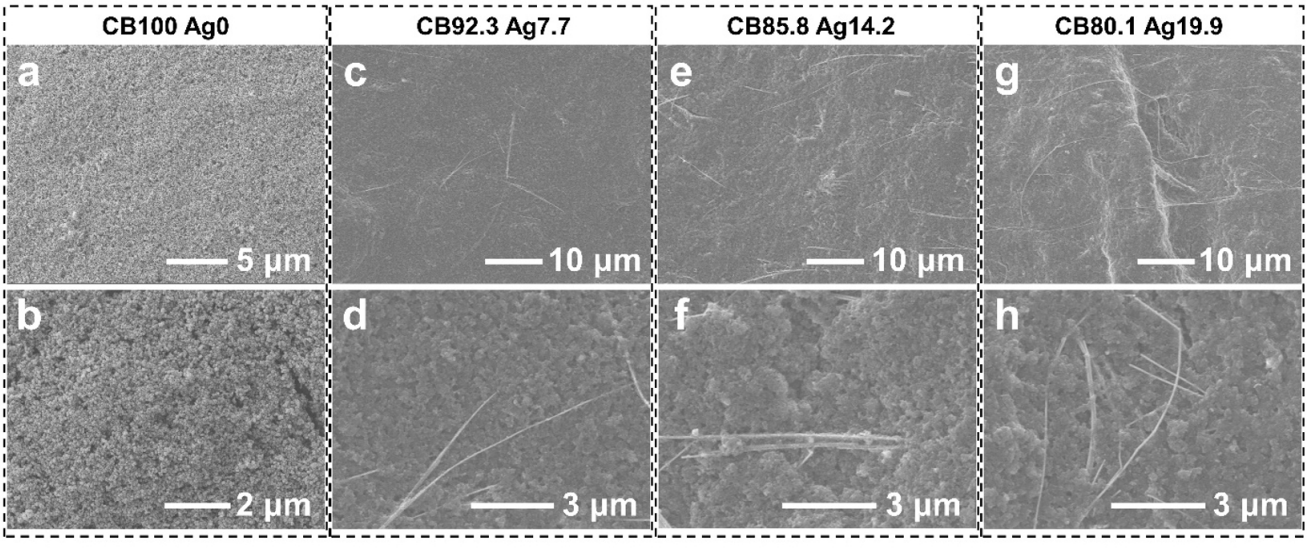

Fig. 6. (a-h) Top-view low-magnification (first line) and high-magnification (second line) scanning electron microscopy images of circular patterns on fabric fabricated with different ink formulations: (a,b): CB100Ag0, (c,d): CB92.3Ag7.7, (e,f) CB85.8Ag14.2, and (g,h) CB80.1Ag19.9. CB, carbon black.

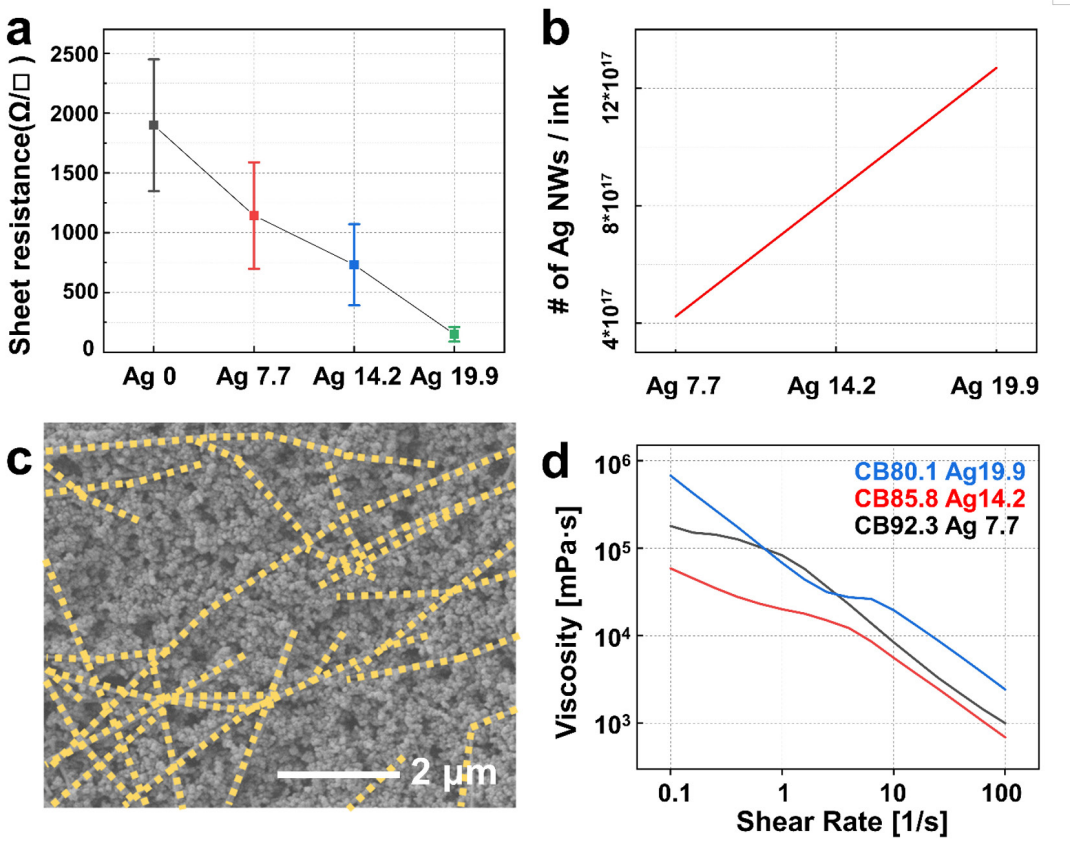

Fig. 7. (a) Variations in sheet resistance values measured from the circular patterns prepared with different conductive inks. (b) Estimated quantities of Ag NWs in each mixed ink depending on the Ag NW weight percentage. (c) SEM image showing the conductive percolation network of Ag NWs within the CB matrix. (d) Change in ink viscosity as a function of shear rates. CB, carbon black; NW, nanowire.

screen printing and non-uniform film formation. Fig. 7(d) shows the viscosity increase in mixed inks as Ag NW content rises. Therefore, a balance between conductivity and printability must be carefully controlled, along with considerations such as cost and scalability.

4. Conclusion

This study presents the development of cost-effective, CB-based conductive inks incorporating small amounts of Ag nanowires (Ag NWs) for patternable screen-printing on fabrics. The CB matrix provides a stable, low-cost conductive base, while the addition of Ag NWs significantly enhances conductivity due to their one-dimensional morphology and high aspect ratio, which facilitate effective electron pathways through percolation. By controlling Ag NW content, the inks achieve tunable conductivity without compromising cost-efficiency. Screen printing enabled precise patterning of these inks into grid and circular forms on polyurethane-coated fabric, demonstrating high-resolution, scalable applications for flexible and wearable electronics. The CB80.1Ag19.9 ink formulation, with optimal Ag NW loading, achieved a dramatic reduction in sheet resistance, establishing continuous conductive networks within the CB matrix. This conductive percolation network efficiently bridges gaps in the CB structure, resulting in low-resistance, durable patterns suitable for practical applications. While increasing Ag NW content can further reduce sheet resistance, it also raises ink viscosity, potentially impacting print quality. This balance between conductivity and printability underscores the utility of CB/Ag NW inks for flexible electronics. Overall, this work advances the potential of CB-based inks for fabric-compatible electronics by addressing key challenges of cost, conductivity, and scalability, offering a promising pathway for the large-scale production of conductive fabrics for wearable technologies and smart textiles.

Funding

This study was supported by a grant from the Agency for Defense Development of Korea (project No. 915050201).

Conflict of Interest

K.-I Park serves as an editor of the Journal of Powder Materials editing but has no role in publishing this article. Except for that, the authors declare no competing financial interests or personal relationships.

Author Information and Contribution

S. Kim: M.S. student; Conceptualization, Methodology, Investigation, Data curation, Visualization, Writing–original draft

G. Lee: Undergraduate; Formal analysis, Investigation

J. Park: Senior Researcher; Resources, Validation

D. Shin: Senior Researcher; Methodology, Validation

K. I. Park: Professor; Conceptualization, Validation

K. J. Jung: Principal Researcher; Conceptualization, Writing–review & editing, Supervision, Resources

Y. Min: Professor; Conceptualization, Validation, Writing–review & editing, Supervision, Resources

Acknowledgement

None.

References

[1] K. Dong, X. Peng and Z. L. Wang: Adv. Mater., **32** (2020) 1902549.

[2] D. S. Saidina, N. Eawwiboonthanakit, M. Mariatti, S. Fontana and C. Hérold: J. Electron. Mater., **48** (2019) 3428.

[3] A. Carlson, A. M. Bowen, Y. Huang, R. G. Nuzzo and J. A. Rogers: Adv. Mater., **24** (2012) 5284.

[4] Y. Kim, H. Kim and H.-J. Yoo: IEEE Trans. Adv. Packag., **33** (2009) 196.

[5] E. Dimitriou and N. Michailidis: Nanotechnology, **32** (2021) 502009.

[6] L. Li, M. Gao, Y. Guo, J. Sun, Y. Li, F. Li, Y. Song and Y. Li: J. Mater. Chem. C, **5** (2017) 2800.

[7] P. S. Karthik and S. P. Singh: RSC Adv., **5** (2015) 77760.

[8] W. Yang and C. Wang: J. Mater. Chem. C, **4** (2016) 7193.

[9] W. Li, Q. Sun, L. Li, J. Jiu, X.-Y. Liu, M. Kanehara, T. Minari and K. Suganuma: Appl. Mater. Today, **18** (2020) 100451.

[10] H. Yuk, B. Lu, S. Lin, K. Qu, J. Xu, J. Luo and X. Zhao: Nat. Commun., **11** (2020) 1604.

[11] R. Islam, N. Khair, D. M. Ahmed and H. Shahariar: Mater. Today Commun., **19** (2019) 32.

[12] J. Zhang, M. Ahmadi, G. Fargas, N. Perinka, J. Reguera, S. Lanceros-Méndez, L. Llanes and E. Jiménez-Piqué: Metals, **12** (2022) 234.

[13] Y. Z. N. Htwe and M. Mariatti: J. Sci.: Adv. Mater. Devices, **7** (2022) 100435.

[14] T. Y. Kim, Y. W. Kim, H. S. Lee, H. Kim, W. S. Yang and K. S. Suh: Adv. Funct. Mater., **23** (2013) 1250.

[15] S.-H. Zhang, Z.-Y. Jiang, Z.-X. Xie, X. Xu, R.-B. Huang and L.-S. Zheng: J. Phys. Chem. B, **109** (2005) 9416.

[16] P. Barpanda, G. Fanchini and G. G. Amatucci: Carbon, **49** (2011) 2538.

[17] Y. Li, S. Guo, H. Yang, Y. Chao, S. Jiang and C. Wang: RSC Adv., **8** (2018) 8057.

[18] A. R. Madaria, A. Kumar, F. N. Ishikawa and C. Zhou: Nano Res., **3** (2010) 564.

[19] G. E. Pike and C. H. Seager: Phys. Rev. B, **10** (1974) 1421.

[20] J. Li and S.-L. Zhang: Phys. Rev. E, **80** (2009) 040104.

[21] H. S. Lee, Y. W. Kim, J. E. Kim, S. W. Yoon, T. Y. Kim, J.-S. Noh and K. S. Suh: Acta Mater., **83** (2015) 84.

Research Article

pISSN 2799-8525 · eISSN 2799-8681
J Powder Mater 2024;31(6):508-512

Journal of Powder Materials

콜로이드 ITO 나노입자를 활용한 고투명 열 차단 유연 필름개발

배효인[1], 정혜연[1], 이주나[1], 신다혜[2,*], 허성연[1,*]

[1]서울과학기술대학교 화공생명공학과
[2]국방과학연구소 국방소재/에너지 센터

Development of Highly Transparent and Thermo-Shielding Flexible Film via Colloidal ITO Nanocrystals

Hyoin Bae[1], Hyeyeon Jung[1], Juna Lee[1], Dahye Shin[2,*], Sungyeon Heo[1,*]

[1]Department of Chemical and Biomolecular Engineering, Seoul National University of Science & Technology, Seoul 01811, Republic of Korea
[2]Defense Materials & Energy Technology Center Team 1, Agency for Defense Development, Daejeon, 34186, Republic of Korea

Infrared radiation accounts for approximately 50% of the solar spectrum. Specifically, the near-infrared (NIR) spectrum, ranging from 760 nm to 2500 nm, is primarily responsible for solar heat gain, increasing indoor temperatures and reducing heating and cooling efficiency. To address this issue, we developed a highly transparent thermo-shielding flexible film that maintains a high transmittance of the visible region (T = 80%) while reducing the transmittance of the NIR region (T ≈ 0%). NIR-absorbing indium tin oxide (ITO) nanocrystals were coated onto polyethylene terephthalate (PET) films, and both films were sandwiched to improve the NIR absorption properties and protect the nanocrystal film layer. The fabricated films were applied to a model house and decreased the indoor temperature by approximately 8°C. Our study demonstrates that energy consumption can be reduced by ITO nanocrystal-coated flexible films, with potential implications for the smart window and mobility markets.

Keywords: Tin-doped Indium Oxide; Nanocrystals; Highly-transparent; Thermo-shielding; Flexible film

Received: November 25, 2024
Revised: December 10, 2024
Accepted: December 11, 2024

***Corresponding author:**
Sungyeon Heo, Dahye Shin
E-mail: sungyeonh@seoultech.ac.kr, sth528@add.re.kr

1. Introduction

오늘날 많은 건물들은 유리창을 도입하고 있으며, 이를 통해 날씨와 계절의 변화와는 큰 관계없이 가시광선과 적외선이 지속적으로 유입되고 있다. 특히, 지구온난화로 인하여 여름철이 길어지고 있는 현 시점에서 쾌적한 실내 온도를 유지하기 위해 냉난방 시스템의 사용 증가로 전 세계 에너지 소비량의 약 50 %는 건물에서 소모되고 있다[1, 2]. 이러한 냉난방에 관련된 에너지 소비를 최소화하고자 하는 연구가 지속되고 있다. 예로써, 가시광선 영역 (Vis, 400-760 nm)의 투과율은 높이고 실내로 들어오는 열 복사와 연관된 근적외선 영역 (NIR, 760-2500 nm)의 투과율은 낮추는 것은 자연 채광의 효과를 높이고, 열 차단 효과를 갖게 됨으로써 그 적용 분야가 크다고 할 수 있다. 이를 통해 조명 및 냉난방 에너지 시스템에 대한 의존도를 줄일 수 있을 것이라 기대한다[3]. 미래의 건축물 및 모빌리티의 경우, 투명 창의 사용량이 증가할 것으로 예측되며, 따라서 관련 분야의 연구가 필요하다.

최근 연구에서 근적외선을 흡수할 수 있는 콜로이드 반도체 나노입자를 이용한 기술들이 주목받고 있다[4, 5]. 나노미터 크기의 금속 산화물 콜로이드 반도체 나노입자는 원자 단위의 도핑 조절을 통하여 국소적으로 빛과 강하게 상호작용함으로써 국소 표면 플라즈몬 공명(LSPR, Localized Surface Plasmon Resonance)을 일으킨다[6, 7]. 이는 특정 파장 영역에서 빛에 의해 자유 전자가 집단적으로 진동하여 가시광선 및 근적외선 영역에서 흡수 및 산란이 극대화된다[8-10]. LSPR에 의한 흡수 파장 및 세기는 반도체 나노입자의 크기, 형태, 물질 조성 및 주변 환경을 통해 조절할 수 있다[11].

콜로이드 반도체 나노입자 중 ITO (tin-doped indium oxide)

https://doi.org/10.4150/jpm.2024.00423

의 LSPR 흡수는 약 1600 nm부터 2200 nm까지의 근적외선 영역에서 tin의 도핑 농도에 따라 조절될 수 있어 적외선의 투과도를 낮추어 차열을 하는 데에 유리하다[12, 13]. 또한, 콜로이드 ITO 나노입자는 가시광선 영역에서 우수한 광학적 투명도를 가짐과 동시에 높은 결정성, 형태적 균일함, 고분산성을 가져 넓은 면적에 투명 박막으로 적용할 수 있다[14].

기존의 콜로이드 나노입자 필름 제작에서는 주로 스핀 코팅 기술이 사용되었으나, 이 기술은 일괄 처리 공정으로 연속 공정을 필요로 하는 대규모 생산에는 한계가 있다[15]. 이러한 문제를 해결하기 위해 blade coating 방법을 도입하면 큰 면적의 유연 필름에 입자의 균일한 코팅과 연속 공정이 동시에 가능해져 산업적 응용에 실용적인 방안을 제시할 수 있다[16, 17].

본 연구에서는 blade coating 방법을 이용하여 콜로이드 ITO 반도체 나노입자를 비교적 큰 면적의 PET (polyethyleneterephthalate) 유연 필름에 코팅하였고, 이를 통해 가시광선에서는 투과율이 높고 근적외선을 효과적으로 차단할 수 있음을 확인하였다. 또한, 열차단의 기능을 모델 하우스에 적용하여 온도 저감의 효과를 확인하였고, 이러한 본 연구는 추후 다양한 분야에 적용 가능성이 높을 것으로 예상된다.

2. Experimental

콜로이드 ITO 반도체 나노입자는 보고된 연구를 따라 Schlenk 라인을 사용하여 질소 분위기에서 합성하였다[6, 18]. Tin이 1% 도핑된 ITO를 합성하기 위해, 0.061 g의 tin(Ⅱ) acetate와 7.5 g의 indium(Ⅲ) acetate를 60 ml의 oleylamine 에 혼합하고, 120 ˚C에서 진공 상태로 1시간 동안 degassing한 후 나노입자의 형성과 성장을 위해 질소 환경에서 230 ˚C로 가열하여 1시간 동안 유지하였다. 반응이 끝난 후 각 튜브의 용액에 5 ml의 hexane으로 희석하고 2 ml의 oleic acid를 넣어 분산시킨 후, 알코올을 사용한 침전, 원심분리, hexane 재분산의 과정을 다섯 번 반복하여 회수하고 정제하였다. 본 합성법을 활용하여, tin의 도핑 비율을 1 %, 3 %, 5 %, 7 %, 10 %로 다양하게 조절하여 용액을 각각 합성했다.

얻어진 나노입자가 분산된 용액을 blade coater를 사용하여 10 × 10 cm 크기의 PET기판에 도포하였다[16]. 용액의 도포 두께는 35 μm로 설정하였으며, 도포 전에 PET 기판은 acetone, isopropyl alcohol, hexane을 이용하여 순차적으로 세척하였다. 인도어 테스트는 20 × 25 × 30 cm 크기의 스티로폼에서 진행하였다. Sample 이외의 공간에서의 효과를 모두 제거하기 위해 외벽은 알루미늄 호일로 둘러쌌으며, 적외선 램프는 모델 하우스와 20 cm 떨어진 거리에서 실험을 수행하였다. 총 측정 시간은 40분이며 30초 간격으로 온도를 확인하였다[19].

콜로이드 ITO 반도체 나노입자의 형태는 투과 전자 현미경(Transmission Electron Microscopy, TEM, JEOL JEM-2010)을 이용하여 분석하였다. ITO 나노입자의 용액과 필름의 흡광도 및 투과도 데이터는 UV-Vis-NIR 분광기(UV-Vis-NIR spectrometer, JASCO V-770)를 이용하여 분석하였다.

3. Results and Discussion

3.1. Tin 도핑 농도에 따른 콜로이드 ITO 반도체 나노입자의 특성

그림 1(a)와 같이 합성된 ITO 나노입자는 모든 도핑 농도에서 콜로이드 형태로 톨루엔, 헥산 등 유기용매에 고분산성을 보여주었고, 이는 합성 나노입자 잉크가 용액 공정을 통해 기판에 박막 형태로 균일하게 코팅이 될 수 있음을 시사한다. 그림 1(b)는 합성한 콜로이드 ITO 반도체 나노입자 (7%-doped)의 TEM 분석 결과를 보여준다. 고분산성의 콜로이드 용액은 TEM 분석으로도 확인할 수 있는데, 나노입자가 뭉침이 없이 고르게 분산된 형태로 이미지를 확인할 수 있음으로써 콜로이드 용액의 고분산성을 간접적으로 확인할 수 있었다. 이미지 분석 결과 ITO 나노입자들의 평균 입자 크기는 약 6.3 nm, 입자 직경은 주로 4 nm에서 8 nm 사이에 분포하는 것으로 확인되었다. 이는 합성된 ITO 나노입자들이 비교적 균일한 크기를 가지고 있음을 나타내며, 이전 연구에서 보고된 결과와 일치한다[18].

그림 1(c)는 tin 도핑 농도에 따른 ITO 나노입자의 광 흡수 특성을 UV-Vis-NIR 분광기로 분석한 결과를 보여준다. 도핑 농도가 증가함에 따라 LSPR 흡수 피크가 근적외선(NIR) 영역으로 blue-shift되는 경향을 보였다[20]. 이는 tin이 도핑되면서 ITO 나노입자의 자유 전자 농도의 증가로 플라즈몬 공명 주파수를 더 높은 에너지 영역으로 이동시키는 것에 대한 결과이다[5, 15, 21]. 그러나 도핑 농도가 7%를 초과하면 LSPR 흡수 피크가 red-shift되는 현상이 나타났다. 그 원인 7% 이상에서는 tin이 산소와 결합하여 tin 복합체가 형성되는데, 이 복합체는 전자 농도의 증가를 억제하여 플라즈몬 공명 주파수가 다시 낮은 에너지로 이동하기 때문이다[20]. 이러한 결과로 도핑 농도가 7%일 때 전자 농도가 최대치에 도달하고 LSPR 특성이 뚜렷하게 관찰되어 7%가 ITO 나노입자의 최적의 도핑 농도임을 확인할 수 있었다.

이와 같이 ITO 나노입자의 도핑 농도가 광학적 특성에 미치는 영향을 확인한 후, 이를 유연 기판 PET에 코팅하여 필름 상태에서의 특성을 분석하였다(그림 1(d)). 필름은 가시광선 영역에서 약 95 %의 매우 높은 투과도를 보였고 적외선 차단 성능은 7% 도핑 농도에서 최적의 효과를 나타내어 근적외선 영역에서 약 20%의 낮은 투과도를 보였다. 이러한 결과는 필름에서 가시광 영역에서 투명도를 유지하면서 근적외선 차단 성능을 극대화할 수 있음을 보여준다.

3.2. 콜로이드 ITO 반도체 나노입자가 코팅된 단일 및 이중 필름 비교

ITO 나노입자가 PET 기판에 코팅되었을 때, 20%의 낮은 투과도를 보였음에도 불구하고, 다음과 같은 사항을 고려해야할 것이다. 먼저, 코팅된 나노입자 층이 외부 환경에 노출된다면, 나노입자 층의 박리 및 손상이 야기될 가능성이 있다. 또한, 20% 보다 더 낮은 투과도를 달성한다면 더욱 효과적으로 열을 차단시킬 수 있을

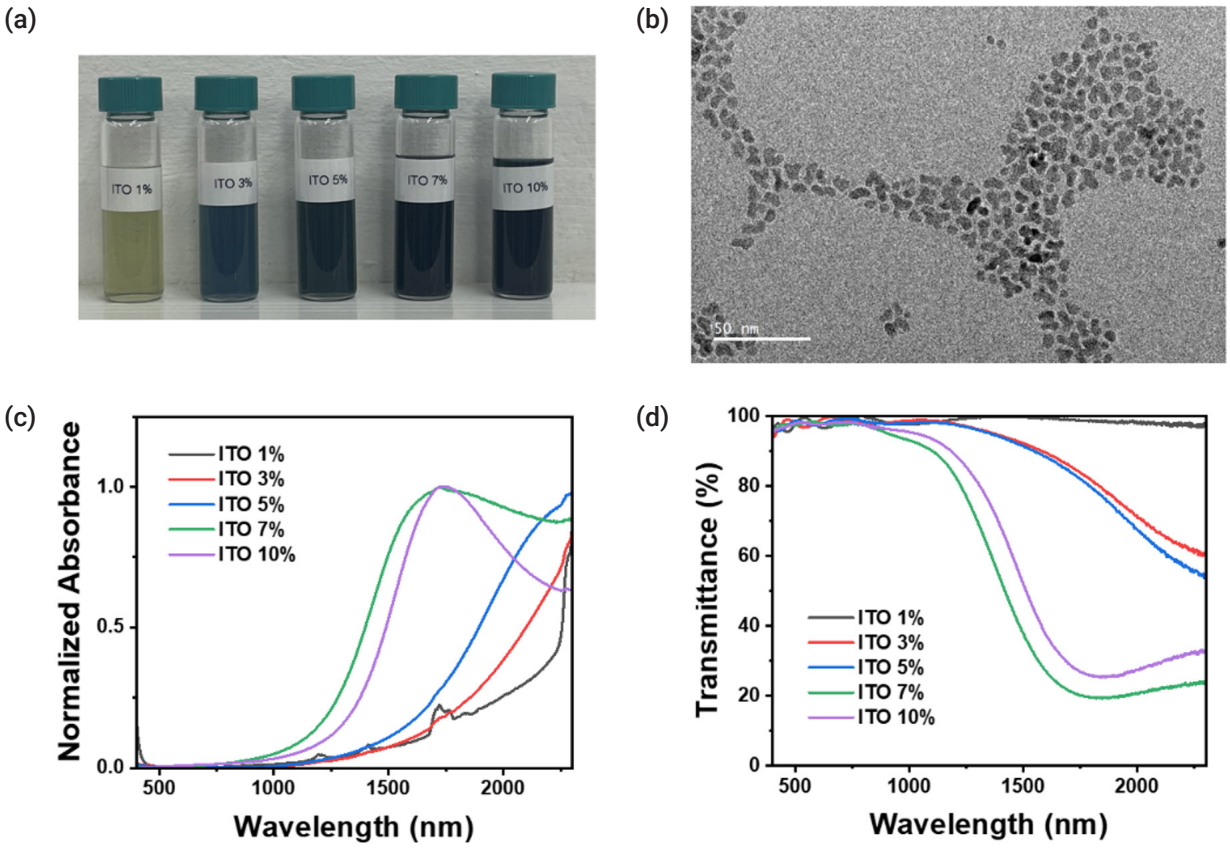

Fig. 1. Colloidal indium tin oxide (ITO) semiconductor nanocrystals. (a) Optical images of 1%, 3%, 5%, 7%, and 10%-doped ITO nanocrystal solution dispersed in hexane. (b) Transmission electron microscopy image of 7% doped ITO nanocrystals. (c) Normalized absorbance of ITO nanocrystal solution dispersed in tetrachloroethylene with varying tin concentration. (d) Transmittance spectra of ITO nanocrystals coated on PET films.

것이다. 하지만, 더 낮은 투과도를 달성하기 위해서는 나노입자 박막의 두께를 더 두껍게 코팅해야하고, 이에 따라 나노 입자 층의 박리 등의 문제가 야기될 가능성이 있다.

이러한 문제를 해결하기 위해 tin이 7% 도핑된 ITO 나노입자를 PET 기판에 코팅한 후, 나노입자의 박리, 이중층 구조의 단열 효과, 외부 환경으로부터의 보호를 고려하여 코팅된 두 개의 단일 필름을 마주 보도록 겹쳐 이중 필름을 제작했다(그림 2(a))[16]. 완성한 이중 필름을 UV-Vis-NIR 분광기로 측정한 결과, 가시광선 투과율을 약 80%로 유지하는 동시에 1750 nm 이상의 근적외선 투과율은 거의 0%에 수렴하는 것을 확인할 수 있었다 (그림 2(b)). 이는 단일 필름보다 더 우수한 근적외선 차단 특성을 보이며, 또한, 이중 필름으로 제작 시 비록 가시광선의 투과도가 80%까지 내려가긴 했지만, 제작된 이중 필름은 그림 2(c)에서처럼, 필름 뒷면의 마크를 확인할 수 있음을 통해서 가시광선 영역에서 투명함을 유지함을 확인할 수 있었다. ITO 나노입자가 코팅된 이중 필름이 투명도를 유지하면서 단일 필름보다 근적외선을 효과적으로 차단하는 것을 통해 이중으로 제작하는 것이 열 차단의 효과를 극대화 할 수 있을 것이라고 예상하였다.

3.3. 모델 하우스 적용을 통한 나노입자 유연 필름 열 차단 성능 평가

ITO 나노입자가 코팅된 이중 필름의 열 차단 효과를 확인하기 위해, 모델 하우스를 제작하여 모델 하우스 내부의 온도 변화 테스트를 진행하였다 (그림 3(a)). PET 단일 필름은 시간이 지남에 따라 빠르게 온도가 상승해 최대 38 ˚C까지 도달한 반면, ITO 나노입자가 코팅된 이중 필름은 온도 상승 속도가 상대적으로 느리며 최대 30 ℃까지 상승하는 것을 확인할 수 있었다 (그림 3(b)). 이는 필름에 코팅된 ITO 나노입자가 근적외선 범위의 빛을 흡수하여 실내로 전달되는 열을 효과적으로 차단했기 때문이며, 그 결과 나노입자가 코팅되지 않은 PET 단일 필름과 나노입자가 코팅된 이중 필름 간의 온도 차이는 최대 8 ˚C에 이르렀다. 이는 ITO 나노입자가 코팅된 단일 필름의 경우 약 35 ˚C까지 상승한 점을 고려할 때, 이중 필름의 경우 단일 필름보다 약 5 ˚C의 저감 효과를 기록하였다. 이를 통해 이중 필름 구조의 효용성을 확인할 수 있었다.

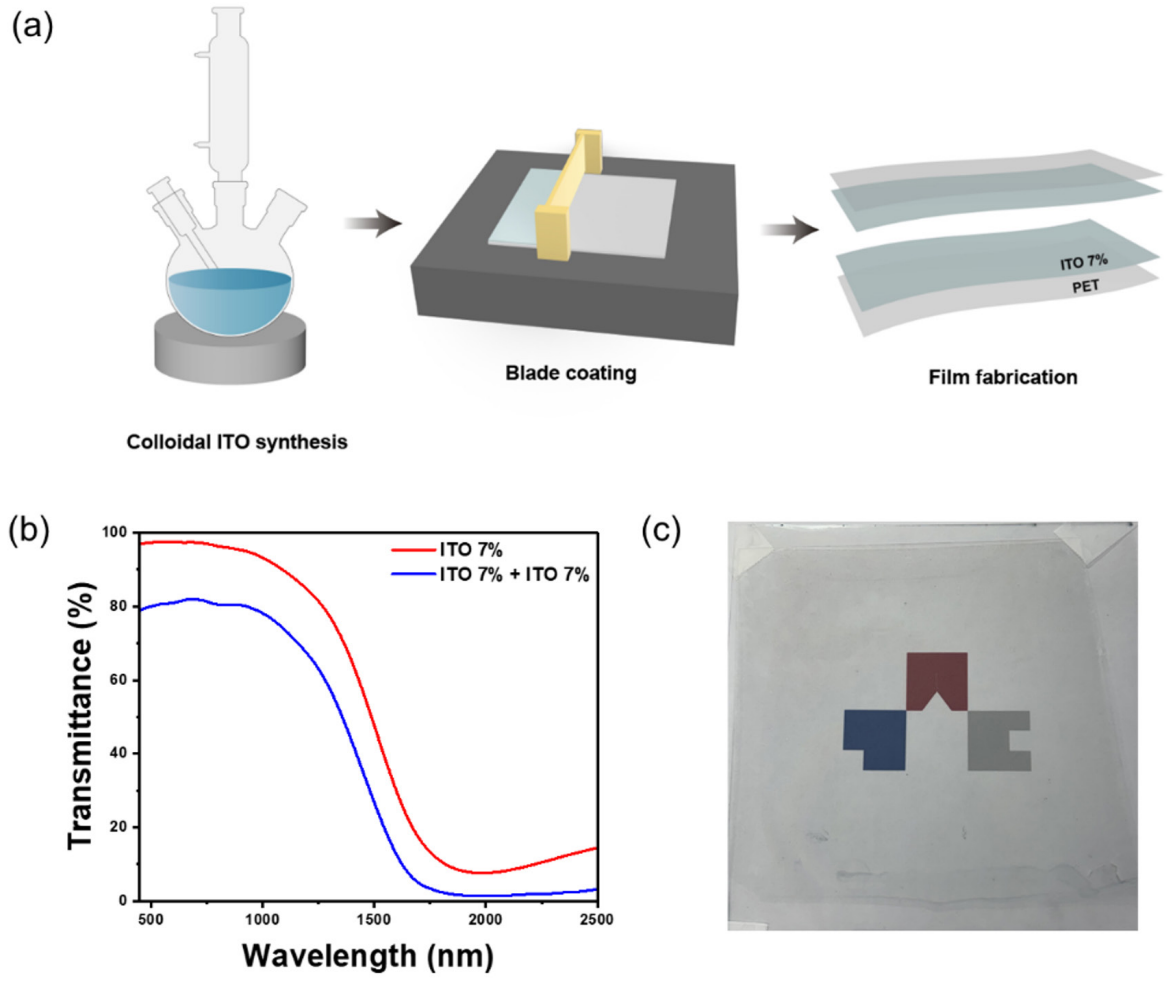

Fig. 2. Single and sandwiched films coated with colloidal indium tin oxide (ITO) semiconductor nanocrystals. (a) Schematic of sandwiched film fabrication. (b) UV-Vis-NIR spectra of single and sandwiched film coated with 7% ITO nanocrystals. (c) An optical image of sandwiched film coated with 7% ITO nanocrystals. UV, ultraviolet; Vis, visible; NIR, near-infrared.

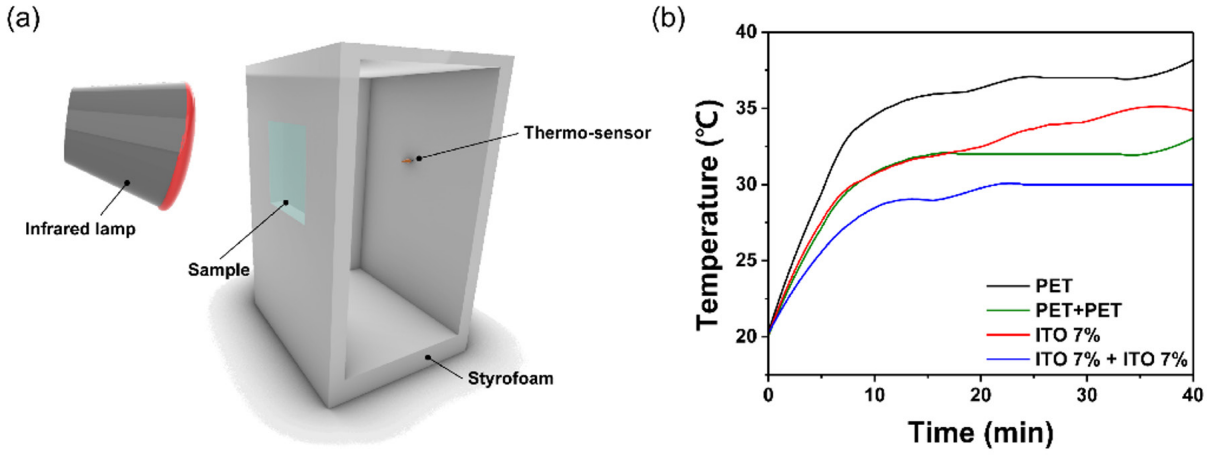

Fig. 3. Model house experiment. (a) Schematic of the thermo-shielding effect experiment using a model house. (b) Temperature versus time curves in the model house for different films.

4. Conclusion

본 연구에서는 PET 유연 기판에 콜로이드 ITO 반도체 나노입자를 용액 공정인 블레이드 코터로 코팅하고, 이를 이중 필름으로 제작하여 높은 투명도를 유지하면서도 외부로부터 유입되는 빛에 의한 실내 온도 상승을 효과적으로 억제할 수 있음을 입증하였다. 모델 하우스에 이중 필름을 부착하여 테스트를 진행함으로써 ITO 나노입자가 코팅된 이중 필름이 나노입자가 코팅되지 않은 단일 필름보다 실내 온도 상승 속도가 낮으며 8℃의 차이가 난다는 것으로 근적외선 영역에서 태양빛의 유입을 차단하여 실내 온도가 낮게 유지됨을 보였다. 또한 가시광선 영역에서 약 80%의 높은 투과도를 기록하여, 고투명성을 가진 열 차단이 가능한 기능성 윈도우로 적용 가능함을 확인하였다. 이러한 연구 결과는 미래에 투명 창문의 비율이 증가할 것으로 예상되는 건축 및 모빌리티 시장에 중요한 기여를 할 수 있을 것으로 기대된다.

Funding

This study was supported by a grant from the Agency for Defense Development of Korea (project No. 915050201).

Conflict of Interest

저자들은 이해상충관련 해당사항 없음을 선언합니다.

Author Information and Contribution

배효인: 학사과정 학생/합성 및 논문 초안 작성, 정혜연: 학사과정 학생/합성 및 물성 평가, 이주나: 학사과정 학생/합성 및 인도어 테스트 평가, 신다혜: 박사/실험디자인, 논문작성 및 연구책임자, 허성연: 교수/실험디자인, 논문작성 및 연구책임자

Acknowledgement

None.

References

[1] Q. Wang, Y.-J. Hu, J. Hao, N. Lv, T.-Y. Li and B.-J. Tang: J. Clean. Prod., **231** (2019) 370.
[2] Y. Wang, Y. Zhao, Z. Yan, T. Li, S. Wang and W. Dong: ACS Appl. Mater. Interfaces, **15** (2023) 43038.
[3] S.-Z. Sheng, J.-L. Wang, B. Zhao, Z. He, X.-F. Feng, Q.-G. Shang, C. Chen, G. Pei, J. Zhou, J.-W. Liu and S.-H. Yu: Nat. Commun., **14** (2023) 3231.
[4] J. Kim, G. K. Ong, Y. Wang, G. LeBlanc, T. E. Williams, T. M. Mattox, B. A. Helms and D. J. Milliron: Nano Lett., **15** (2015) 5574.
[5] G. Garcia, R. Buonsanti, E. L. Runnerstrom, R. J. Mendelsberg, A. Llordes, A. Anders, T. J. Richardson and D. J. Milliron: Nano Lett., **11** (2011) 4415.
[6] R. Buonsanti and D. J. Milliron: Chem. Mater., **25** (2013) 1305.
[7] A. Comin and L. Manna: Chem. Soc. Rev., **43** (2014) 3957.
[8] E. Hutter and J. H. Fendler: Adv. Mater., **16** (2004) 1685.
[9] A. Agrawal, R.W. Johns and D. J. Milliron: Annu. Rev. Mater. Res., **47** (2017) 1.
[10] I. Kriegel, F. Scotognella and L. Manna: Phys. Rep., **674** (2017) 1.
[11] H. Yin, Y. Kuwahara, K. Mori, C. Louis and H. Yamashita: Catal. Sci. Technol., **10** (2020) 4141.
[12] S.-I. Choi, K. M. Nam, B. K. Park, W. S. Seo and J. T. Park: Chem. Mater., **20** (2008) 2609.
[13] M. Kanehara, H. Koike, T. Yoshinaga and T. Teranishi: J. Am. Chem. Soc., **131** (2009) 17736.
[14] R. A. Gilstrap, C. J. Capozzi, C. G. Carson, R. A. Gerhardt and C. J. Summers: Adv. Mater., **20** (2008) 4163.
[15] E. L. Runnerstrom, A. Llordés, S. D. Lounis and D. J. Milliron: Chem. Commun., **50** (2014) 10555.
[16] H. Yang and P. Jiang: Langmuir, **26** (2010) 13173.
[17] N. Sukharevska, D. Bederak, V. M. Goossens, J. Momand, H. Duim, D. N. Dirin, M. V. Kovalenko, B. J. Kooi and M. A. Loi: ACS Appl. Mater. Interfaces, **13** (2021) 5195.
[18] C. A. Saez Cabezas, G. K. Ong, R. B. Jadrich, B. A. Lindquist, A. Agrawal, T. M. Truskett and D. J. Milliron: Proc. Natl. Acad. Sci. U.S.A, **115** (2018) 8925.
[19] L. Hu, C. Wang, H. Zhu, Y. Zhou, H. Li, L. Liu and L. Ma: Small, **20** (2024) 2306823.
[20] S. D. Lounis, E. L. Runnerstrom, A. Bergerud, D. Nordlund and D. J. Milliron: J. Am. Chem. Soc., **136** (2014) 7110.
[21] A. Agrawal, S. H. Cho, O. Zandi, S. Ghosh, R. W. Johns and D. J. Milliron: Chem. Rev., **118** (2018) 3121.

Research Article

pISSN 2799-8525 · eISSN 2799-8681
J Powder Mater 2024;31(6):513-520

Journal of Powder Materials

B_2O_3 입자 크기 및 분포 제어를 통한 향상된 유동성을 갖는 $Al_{18}B_4O_{33}$ 구형 분말 제작

송기호†, 이상인†, 송현승, 안창의*

한국세라믹기술원 엔지니어링소재센터

Fabrication of $Al_{18}B_4O_{33}$ Spherical Powder with Increased Fluidity via Control of B_2O_3 Particle Size and Distribution

Kiho Song†, Sang in Lee†, Hyunseung Song, Changui Ahn*

Engineering Ceramic Center, Korea Institute of Ceramic Engineering & Technology (KICET), Icheon 17303, Republic of Korea

Ceramic materials have become essential due to their high durability, chemical stability, and excellent thermal stability in various advanced industries such as aerospace, automotive, and semiconductor. However, high-performance ceramic materials face limitations in commercialization due to the high cost of raw materials and complex manufacturing processes. Aluminum borate ($Al_{18}B_4O_{33}$) has emerged as a promising alternative due to its superior mechanical strength and thermal stability, despite its simple manufacturing process and low production cost. In this study, we propose a method for producing $Al_{18}B_4O_{33}$ spherical powder with increased uniformity and high flowability by controlling the particle size of B_2O_3. The content ratio of the manufactured $Al_{18}B_4O_{33}$ spherical powder was Al_2O_3: B_2O_3 = 87:13, and it exhibited a 17% reduction in the Hausner ratio (1.04) and a 29% decrease in the angle of repose (23.9°) compared to pre-milling conditions, demonstrating excellent flowability.

Keywords: Aluminum borate; 3D mixer; Spray-dry; Spherical powder; Flowability

Received: September 13, 2024
Revised: October 25, 2024
Accepted: October 25, 2024

***Corresponding author:**
Author: Changui Ahn
TEL: +82-31-645-1459
FAX: +82-31-645-1492
E-mail: acu2001@kicet.re.kr

†These authors contributed equally to this work.

1. Introduction

최근 항공 우주, 자동차, 반도체 등의 첨단 산업들이 발전함에 따라 우수한 내구성과 열 안정성을 가지는 소재에 대한 개발 요구가 급격히 증가하고 있다[1, 2]. 세라믹 소재는 높은 내구성과 화학적 안정성 및 열 안정성이라는 우수한 특성으로 인해 위 첨단 산업 분야에 필수적으로 사용된다[3, 4]. 항공 우주 산업에서 초음속 항공기 및 고압의 터빈 블레이드 개발로 높은 내구성과 고온 안정성이 요구되는 핵심 부품에 Si_3N_4 와 SiC 등이 활용되며, 더 높은 종횡비와 초미세 공정을 요구하는 반도체 식각 공정에서 플라즈마에 의한 식각을 방지하고 교체 주기를 향상시키기 위해 Y_2O_3와 YF_3 등 이 활용된다[5-8]. 이러한 우수한 특성의 세라믹 소재를 활용해 기계적, 열적, 화학적 손상을 방지하여 내구성을 향상시키고 있지만, 고물성의 세라믹 소재들은 높은 원재료 단가와 더불어 높은 공정 단가라는 단점으로 상용화에 한계가 있다. 알루미늄 보레이트 ($Al_{18}B_4O_{33}$)는 쉬운 제조 공정과 낮은 제조 단가에 비해 기계적 강도 (8,000 GPa) 및 열 안정성 (4.5 ppm/℃)이 우수하므로 미래 산업에서 기존 고가 세라믹 소재를 대체할 훌륭한 대안 중 하나로 부각되고 있다[9-11]. 현재까지 $Al_{18}B_4O_{33}$는 금속 복합재료의 강화제로 주로 주목받아 왔으며 세라믹 단일재료로서는 많이 연구되지 않은 상황이다[12].

$Al_{18}B_4O_{33}$ 소재를 포함한 세라믹 소재를 이용하여 고부가가치 세라믹 제품을 구현하기 위해서는 고유동도 구형 분말화 기술이 가장 핵심이다. 예를 들어 구형 세라믹 분말은 입자간 충진도를 높일 수 있으므로 고밀도 세라믹 성형체를 제작할 수 있으며 높은 유동도에 따라 균일한 피딩 (Feeding) 속도를 보장하여 균일한 세라믹 용사 코팅을 가능하게 한다[13-17]. 졸 겔 공정 (Sol gel), 열 플라즈

https://doi.org/10.4150/jpm.2024.00304

마 구형화 공정 (Thermal plasma spraying), 제트밀 공정 (Jet mill), 등 구형 분말을 제작하는 다양한 기술들이 제시되었지만 제작 공정이 복잡하고 비싸며 많은 시간이 소요되어 대량 생산의 제한으로 실제 양산에 접목이 어렵다는 한계를 나타낸다[18-20]. 이에 반해 분무건조 공정 (Spray drying)은 상대적으로 제작 공정이 쉬우며 일정하고 균일한 형태의 구형 분말을 대량으로 제작 가능하다는 장점이 있다[21]. 특히, 분무건조 공정은$Al_{18}B_4O_{33}$와 같이 이종 원료 분말의 혼합을 통한 다양한 조성의 분말 제작에 가장 적합한 구형화 기술이다[22]. 이종 분말의 구형화는 각 분말의 입자, 형태, 분포 및 슬러리 내 분산도에 따라 생성되는 구형 분말의 상 균일도, 구형화율, 유동도에 큰 영향을 받으므로 정밀한 분말 제어 기술이 필요하다[23, 24]. 본 연구에서 B_2O_3 입자의 크기 및 분포 제어를 통한 향상된 균일성과 유동성을 가지는 $Al_{18}B_4O_{33}$ 구형 분말 제조 방법을 제시한다. B_2O_3 원료 분말은 3D 믹서를 통해 크기 및 분포를 정밀히 제어하여 Al_2O_3 원료 분말과 균일 혼합한 슬러리 제조 후 분무건조 공정을 통해 구형의 이종 혼합 과립으로 제작했다. 입자의 크기를 균일하게 제어하기 위한 공정 중 3D 믹서 밀링 방법은 볼을 3차원으로 회전시켜 큰 에너지로 분쇄할 수 있으며 한 번에 많은 양을 처리할 수 있는 장점으로 인해 적용하게 되었다. Al_2O_3와 크기 및 분포 형태가 제어된 B_2O_3 구형 과립은 열처리를 통해 최종적으로 $Al_{18}B_4O_{33}$ 구형 분말로 제작했다. 3D 믹서를 통한 입자 제어는 구형 분말의 치밀성을 향상시켰으며, 결과적으로 유동성을 높이는 효과를 발현했다. B_2O_3의 입자 크기는 3D 믹서 12시간 밀링 공정에서 가장 작았으며, Al_2O_3에 첨가 후 구형 과립으로 제작했을 때 가장 향상된 치밀성을 나타내며 결과적으로 12시간 밀링 공정을 통해 제작된 $Al_{18}B_4O_{33}$ 구형 분말은 밀링 전 대비 17 % 감소된 하우스너 비율 (1.041)과 29 %로 낮아진 안식각 (23.87 °)를 나타낸다. 본 연구를 통해 유동도가 향상된 $Al_{18}B_4O_{33}$ 구형 분말은 항공우주, 반도체 산업에서 고성능 세라믹 소재로 활용될 가능성을 내포하며, 다양한 이종 혼합 분말을 제조하는 공정으로 확장 가능할 것으로 기대된다.

2. Experimental

2.1 Al_2O_3/B_2O_3 혼합 슬러리 제작

Al_2O_3/B_2O_3 혼합 구형 분말을 제작하기 앞서, B_2O_3 (Boron oxide, Daejung Chemicals, Co. Ltd, South Korea)의 입자 크기를 제어하기 위해 3D 믹서 (KMC-T2 3D mixer)에 B_2O_3 분말을 넣고 고형분 대비 50 vol% 지르코니아 볼 (3 ϕ)을 함께 넣어 100 RPM에서 12시간 동안 밀링을 진행했다. Al_2O_3 (Aluminum oxide, Sumitomo Chemical, Co. Ltd, Japan) 1047 g과 B_2O_3 153g 혼합 후 증류수 (Deionized water) 1800 g을 첨가했으며, 분말을 분산시키기 위해 NH_4OH (Ammonium hydroxide, Daejung Chemicals, Co. Ltd, South Korea) 15.3 g을 첨가해 슬러리를 제작했다. 균일한 혼합을 위해 슬러리의 50 vol% 비율로 알루미나 볼 (5 ϕ)을 첨가하여 볼 밀링을 150 RPM으로 24 시간 동안 진행했다.

2.2 $Al_{18}B_4O_{33}$ 구형 분말 제작

제작된 슬러리에 바인더인 HS-BD 14.4 g을 첨가하였고, 모터 교반기 (Overhead Motor Stirrer)를 이용해 100 RPM으로 1 시간 동안 교반 진행했다. 완성된 슬러리는 분무 건조기 (Spray dryer, Dongjin Eng, Co. Ltd, South Korea)를 이용해 구형의 과립 형태로 제작했다. 분무 건조 후 제작된 Al_2O_3/B_2O_3 혼합 과립은 $Al_{18}B_4O_{33}$ 구형 분말로 제작하기 위해 박스 칸탈로 (Box furnace)에서 1 ˚C/min의 승온 속도로 600 ˚C까지 승온 후, 3시간 동안 유지하여 하소를 진행했다. 이후, 소결을 위해 3 ˚C/min의 속도로 1450 ˚C까지 승온 후, 3 시간 동안 유지하며 최종 $Al_{18}B_4O_{33}$ 구형 분말을 제작했다.

2.3 B_2O_3, Al_2O_3/B_2O_3 혼합 과립, $Al_{18}B_4O_{33}$ 구형 분말의 물성 분석

B_2O_3 입자 크기를 측정하기 위해 입도 분석기 (Particle size analyzer, BeVision D2, Bettersize, China)를 사용했다. 분말의 미세구조 분석은 전계 방출 주사 전자 현미경 (JSM 7610F, Jeol)을 통해 관찰했다. $Al_{18}B_4O_{33}$ 구형 분말의 결정 구조는 X-선 회절 분석기 (XRD, D/max 2500, Rigaku)를 통해 10 ˚/min의 속도로 10 ˚ ~ 80 ˚ 범위에서 측정했다. 구형 분말의 유동성을 측정하기 위해 자동 분체 특성 측정기 (BT-1001, Bettersize, China)을 이용하여 탭 밀도와 안식각을 측정했다.

3. Results and discussion

그림 1(a)는 균일한 구형의 $Al_{18}B_4O_{33}$분말을 제작하는 과정을 나타낸 전체적인 개략도를 보여준다. B_2O_3의 입자 크기를 균일하게 감소시켜 Al_2O_3와 혼합하여 슬러리를 제조했으며 균일한 형태의 과립으로 제작 후 열 처리를 통해 최종적으로 $Al_{18}B_4O_{33}$분말을 제작하는 과정이다. 본 연구에서 B_2O_3의 입자를 균일하고 정밀하게 제어하며 크기를 줄이기 위해 3D믹서를 이용한 밀링 방법을 고안했다. 일반적으로 사용되는 밀링 방법으로는 볼밀 (ball mill) 공정과 플레너터리 밀 (planetary mill) 공정이 있지만 볼밀 공정은 단방향으로 회전하여 상대적으로 낮은 에너지로 미세한 입자로의 분쇄에는 제한이 있으며, 플레너터리 밀 공정은 고속으로 회전하여 상대적으로 짧은 시간에 공정이 진행되지만 한번의 공정으로 분쇄 가능한 분말의 양이 적다는 단점이 있다[25, 26]. 그에 반해 3D 믹서를 이용한 공정은 입자를 3차원으로 회전시켜 볼이 떨어지는 중력 에너지와 회전하는 통의 원심력 에너지가 더해져 큰 에너지로 미세하게 분말을 분쇄할 수 있으며, 한 번에 많은 양을 처리할 수 있는 장점이 있다(그림 1b) [27]. 이렇게 입자 크기를 감소시킨 B_2O_3 와 Al_2O_3원료 분말을 혼합하여 슬러리를 제작한 후 분무건조 공정을 통해 구형의 이종 혼합 과립으로 제작한다(그림 1c). 분무건조 공정은 혼합 슬러리를 고속으로 회전하는 디스크에 의해 미세한 물방울 형태로 고온 챔버에 분사되면 용액들이 일정한 크기로 고온의 챔버 내에서 회전하며 건조되어 구형의 과립형태로 제작되는 공정이다. 이때 슬러리 내부의 바인더에 의해 B_2O_3와 Al_2O_3 가

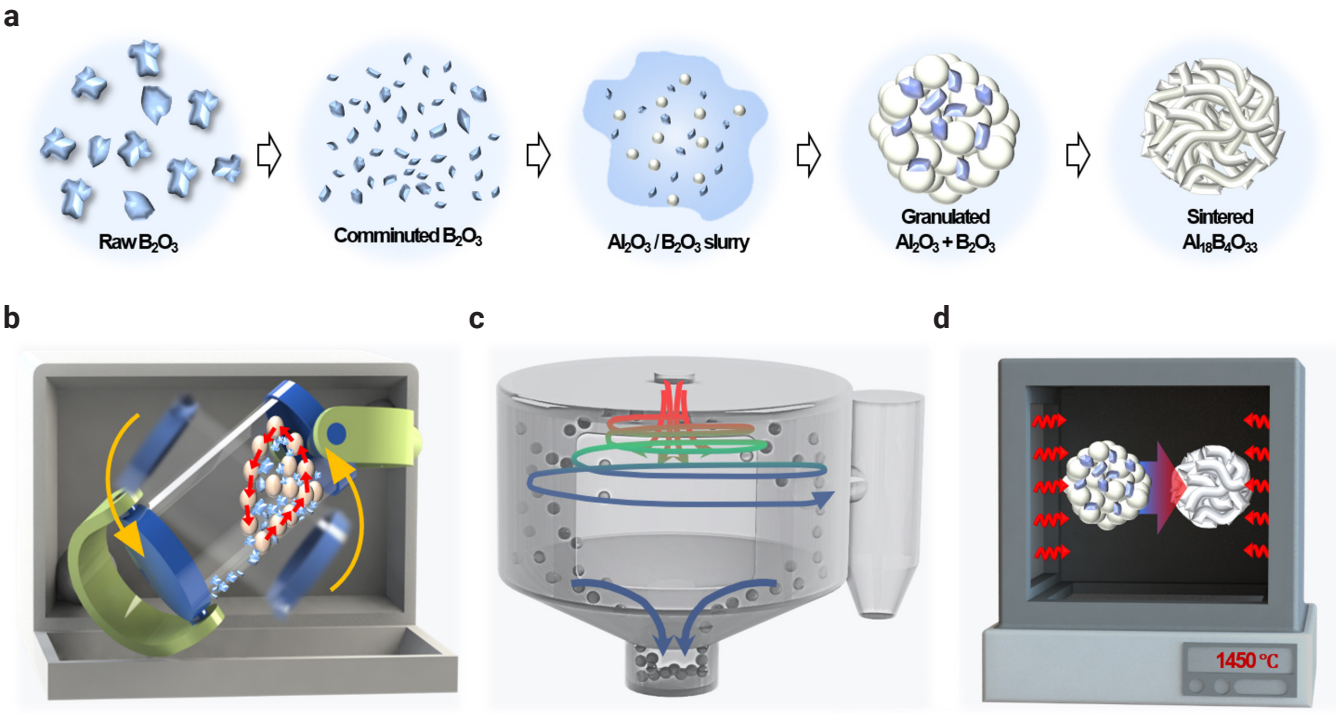

Fig. 1. (a) Schematic diagram of the formation of $Al_{18}B_4O_{33}$ spherical powders. (b) A 3D mixer used to reduce the particle size of B_2O_3; (c) A spray dryer used for granule formation; (d) A heat treatment process at 1450 °C for granule sintering.

혼합되어 응집해 과립으로 형성 이후 최종적으로 1450 ˚C 에서 열처리를 통해 $Al_{18}B_4O_{33}$ 구형 분말을 제작한다(그림 1d).

B_2O_3의 입자 크기 및 분포를 제어하기 위해 3D 믹서를 통해 시간 변수로 나눠서 실험을 진행했다. 그림 2(a)의 밀링 전 원소재인 B_2O_3 입자 형태는 등방성 보단 이방성에 가까운 복잡한 형태이다. 이러한 B_2O_3 입자를 4시간부터 16시간까지 4시간 단위로 밀링 했을 때, 4시간 밀링 과정에서 일부B_2O_3 입자는 분쇄되어 크기가 감소했지만 전체 영역에 균일한 에너지를 전달하기에 부족한 시간으로 인해 분쇄되지 못한 큰 입자들이 많이 분포했다. 밀링 전 B_2O_3 원소재와 크기 차이가 많이 나지 않는 것을 확인할 수 있다(그림 2b). 그림 2(c)와 그림 2(d)에서 8시간과 12시간 밀링 후 입자의 형상은 등방성의 일정한 형상을 띄고 있으며, 1μm보다 작은 입자 분포가 증가한 것을 확인할 수 있다. 하지만 그림 2(e)의 16시간 밀링 후 B_2O_3 입자는 오히려 이방성의 모난 형상을 띄며 입자 평균 크기가 1.14 μm로 커진 것을 확인할 수 있는데 이는 과도한 밀링으로 인해 열이 발생하였고 열에 민감한 B_2O_3 입자가 응집된 것을 의미한다[28]. 그림 2(f)에서 볼 수 있듯, 3D 믹서로 12시간 밀링을 진행했을 때 입자의 평균 크기는 0.77 μm로 가장 작은 크기를 나타냈다. 누적 백분율 50 %에 해당하는 입도 분포인 D_{50} 값이 밀링 전 B_2O_3 대비 52 % 감소하여 가장 작고 균일하게 분쇄된 것을 확인할 수 있다.

분무건조 공정에서 혼합물이 회전하며 건조될 때 비슷한 입자 크기를 가지면 구형 과립 내 입자의 분포가 균일해지지만, 입자의 크기가 다를 때 밀도 차이로 인해 다른 관성 에너지를 가져 큰 입자가 표면에 위치하게 되면서 층을 이루게 된다[29, 30]. 따라서 본 연구에서 분무건조 공정 후 제작된 과립에 균일하게 B_2O_3 와 Al_2O_3 가 분포해 있어야 열처리 후 구형화율이 높은 $Al_{18}B_4O_{33}$가 형성될 수 있을 것으로 예상했으며, 정확한 $Al_{18}B_4O_{33}$의 형상을 제작하고자 B_2O_3의 크기 변수에 따라 Al_2O_3와 혼합해 각각의 슬러리를 분무건조 공정을 통해 구형 과립으로 제작했다. 그림 3(a)는 시간 변수에 따라 제작된 B_2O_3/Al_2O_3 슬러리를 분무 건조 공정 후 제작한 과립의 이미지이며, B_2O_3의 입자크기가 클수록 구형 분말의 표면에 위치하는 것을 볼 수 있다. Al_2O_3와 가장 유사한입자 크기를 갖는 12시간 조건의 구형 과립 표면 B_2O_3 입자 분포가 줄어든 것을 확인할 수 있다. 과립 내부에 B_2O_3 입자 분포를 확인하기 위해 과립의 단면을 확인해보았을 때, 4시간 밀링 공정을 진행한 B_2O_3 분말을 이용한 B_2O_3/Al_2O_3 혼합 과립 내부보다 표면에 B_2O_3 입자가 대부분 분포한 것을 확인할 수 있다(그림 3b). 그림 3(e)의 EDS mapping 이미지를 통해서도 4시간 밀링 공정을 진행한 구형 과립의 표면에 B_2O_3 가 분포해 있는 것을 확인할 수 있다. 반면 상대적으로 작은 B_2O_3일수록 제작된 과립의 단면은 내부에 균일하게 분포하고 있는 것을 확인할 수 있으며, 이는 Al_2O와 B_2O_3가 크기가 비슷할 때 균일하게 분포된다는 것을 의미한다. 그림 3(c)는 제작된 구형 과립을 열처리하여 최종적으로 제작한 $Al_{18}B_4O_{33}$ 구형

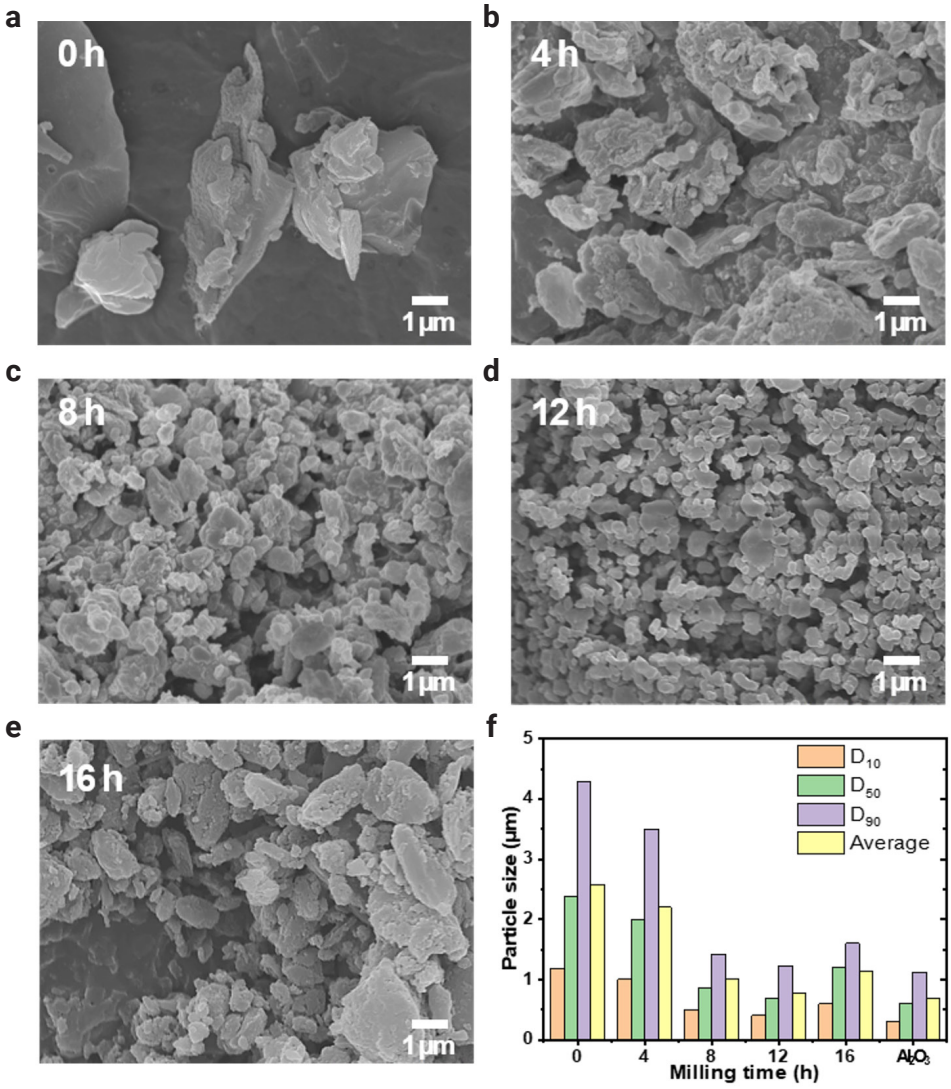

Fig. 2. Scanning electron microscopy images of milled B_2O_3 with milling times of (a) 0 h, (b) 4 h, (c) 8 h, (d) 12 h, and (e) 16 h. (f) Graph of particle size of B_2O_3 as a function of milling time.

분말의 표면 이미지이다. 0시간과 4시간, 16시간으로 밀링 공정을 진행한 상대적으로 입자 크기가 큰 B_2O_3로 제작된 구형 과립은 열처리 후 표면에 많은 기공이 발생했다. 이는 표면에 많이 응집되어 있는B_2O_3입자가 열처리 시 $Al_{18}B_4O_{33}$로 결합되지 못해 B_2O_3입자 탈락이 발생해 빈 공간이 생긴 것을 의미한다. 그에 반해 상대적으로 작은 입자인 8시간과 12 시간 밀링 공정을 진행한 B_2O_3 분말을 이용한 과립은 열처리 후에도 표면이 매끄럽고 균일하게 소결된 것을 확인할 수 있다. 또한 열처리 후 구형 분말의 단면을 확인해 보았을 때, 0시간과 4시간, 8시간, 16시간 밀링 공정에서 내부에 빈공간이 확인할 수 있는데, 이는 단면으로 표면 연마 과정에서 내부에 존재하는 반응하지 못한 B_2O_3의 입자가 탈락되어 내부 기공처럼 보이게 된다(그림 3d). 이러한 빈 공간의 크기는 B_2O_3의 입자 크기에 비례해서 각각 2.11 μm, 1.98 μm, 1.60 μm, 1.73 μm으로 측정이 되었다. 반면 12시간 밀링 공정을 진행한 B_2O_3를 이용한 구형 분말의 단면에서 가장 작고 (1.23 μm), 적은 기공이 발생한 것을 통해 크기가 작고 입자 분포도가 좁은 B_2O_3의 입자가 Al_2O_3와 가장 균일하게 분포하여 우수한 구형화가 가능했음을 확인하였다.

본 연구에서 가장 중요한 것은 분말의 구형을 유지하며 균일한 $Al_{18}B_4O_{33}$ 결정 구조를 갖는 것이다. 밀링 공정 변수에 따라 제작된 과립을 열처리한 구형 분말의 XRD 결정구조를 분석한 결과 공통적으로 $Al_{18}B_4O_{33}$ 구조에 잔류 Al_2O_3가 존재하는 것을 확인할 수 있다(그림 4a). 이는 12시간 밀링 공정을 제외한 표면에 상대적으로 큰 B_2O_3 입자가 분포한 구형 이종 분말에서 열처리 시 주변 Al_2O_3 입자와 충분히 반응하지 않고 B_2O_3 입자가 탈락되어 균일한

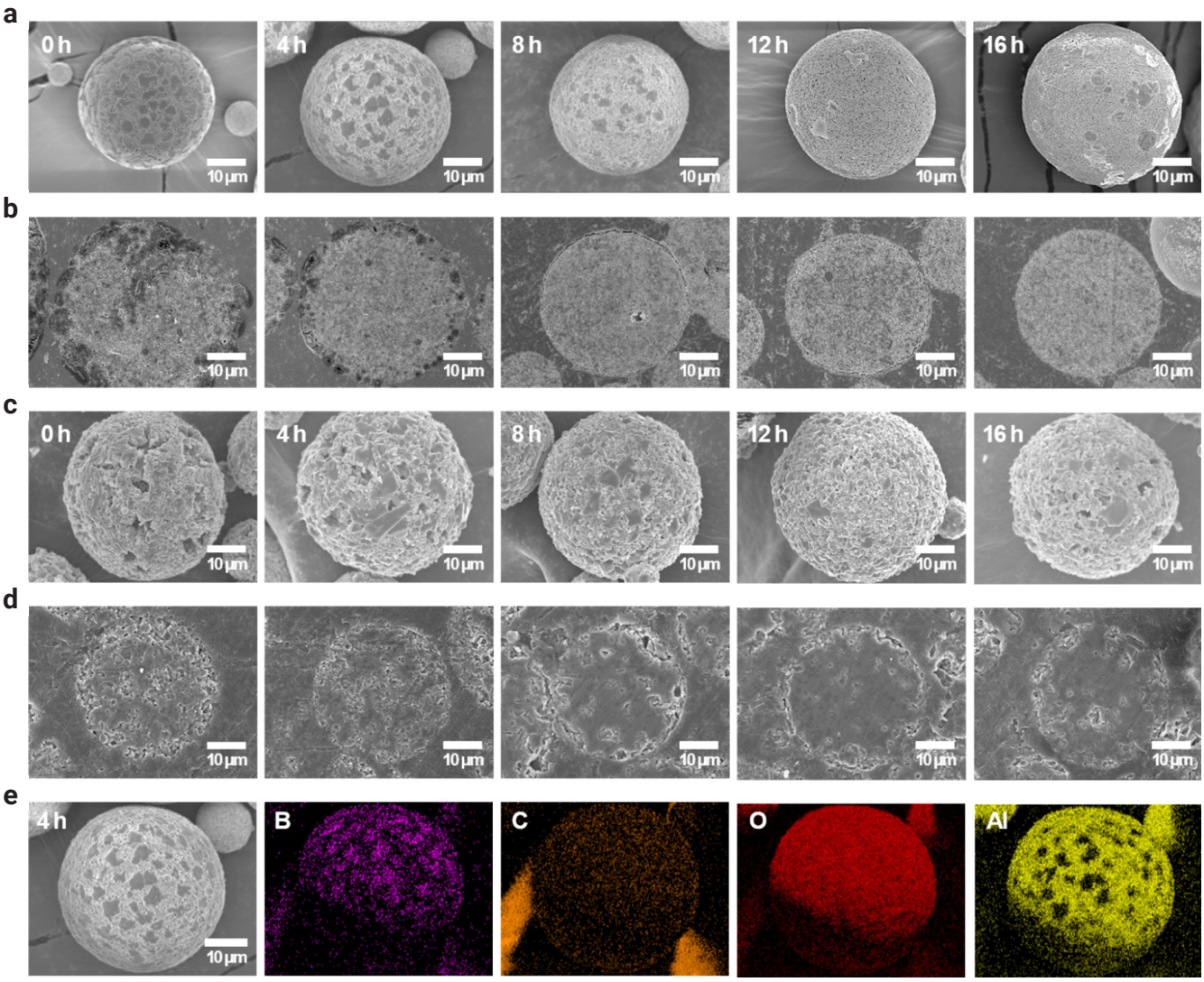

Fig. 3. Scanning electron microscopy images of (a) the surface and (b) the cross-section of synthesized granules, as well as (c) the sintered granules and (d) cross-section of the sintered granules with different milling times. Energy-dispersive X-ray spectroscopy mapping images of granules after 4 hours of milling.

합성이 이루어지지 못해 잔류 Al_2O_3가 존재하는 것을 의미한다. 그에 반해 비교적 B_2O_3 입자가 Al_2O_3 입자와 균일하게 혼합된 12시간 밀링 공정 후 제작한 구형 분말에서 가장 낮은 Al_2O_3피크를 나타내었다. 균일한 $Al_{18}B_4O_{33}$제조 정도를 정량화하기 위해 잔류 Al_2O_3의 가장 높은 intensity를 나타내는 (113)면 피크의 intensity를 측정해 비교했다(그림 4b). 밀링을 진행하지 않은 B_2O_3를 이용해 제작한 구형 분말의 Al_2O_3 (113) 면 피크를 기준 (100 %)으로 설정 후, 상대비를 정리한 결과 B_2O_3 입자의 크기가 가장 작고 균일했던 B_2O_3를 12 시간 밀링 진행 후 제작한 구형 분말에서의 Al_2O_3비율이 5.7 %로 가장 낮게 나타났다. 이는 Al_2O_3와 가장 유사한 입자크기를 갖는 B_2O_3 입자의 탈락이 가장 적어 대부분 $Al_{18}B_4O_{33}$ 형성으로 반응이 진행된 것을 의미한다. 하지만 16시간 밀링 후 열 응집으로 오히려 B_2O_3의 크기가 커졌기 때문에 반응하지 못한 Al_2O_3로 인해 Al_2O_3 비율이 증가한 결과를 보였다.

그림 5(a)의 그래프는 B_2O_3 밀링 공정 시간에 따라 제작된 $Al_{18}B_4O_{33}$ 구형 분말의 크기 (D_{10}, D_{50}, D_{90})를 나타낸다. D_X분말 재료의 평균 입도를 나타내는 데 사용되는 누적 백분율이다. 예를 들어 D_{50} 100 μm는 100 μm보다 큰 50 % 입자와 100 μm보다 작은 50 % 입자가 있음을 의미합니다. 16시간까지 B_2O_3 밀링 공정 시간 변화에도 구형 분말 크기는 일정한 것을 확인할 수 있다. 이는 밀링 공정을 통해 B_2O_3의 입자 크기와 분포를 조절하는 것은 소결 균일성에 영향을 미치지만 구형 분말 크기에는 영향을 주지 않는 것을 의미한다. 열처리한 구형 분말의 유동성을 확인하기 위해 자동 분체 특성 측정기를 통해 겉보기 밀도 및 탭 밀도를 측정하여 하우스

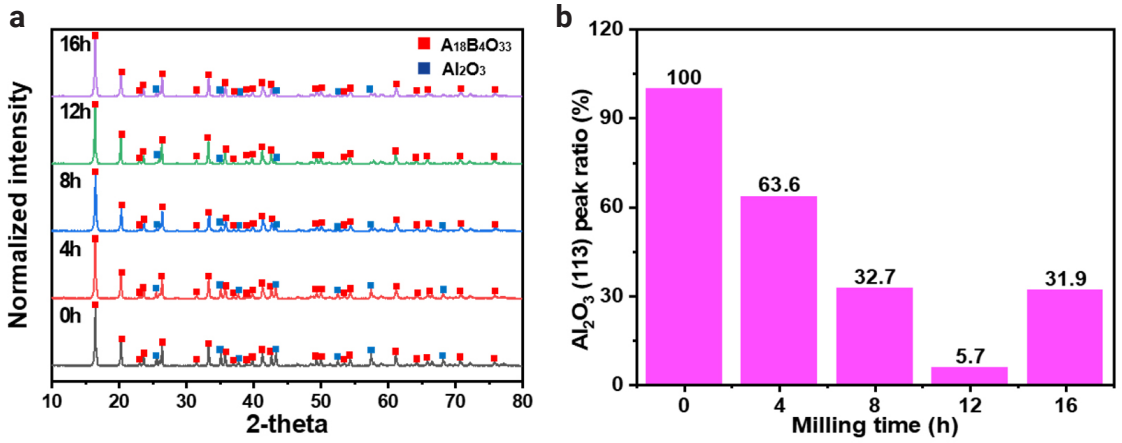

Fig. 4. (a) X-ray diffraction patterns of $Al_{18}B_4O_{33}$ spherical powder according to milling times. (b) Normalized ratio of Al_2O_3 (113) peaks according to milling times.

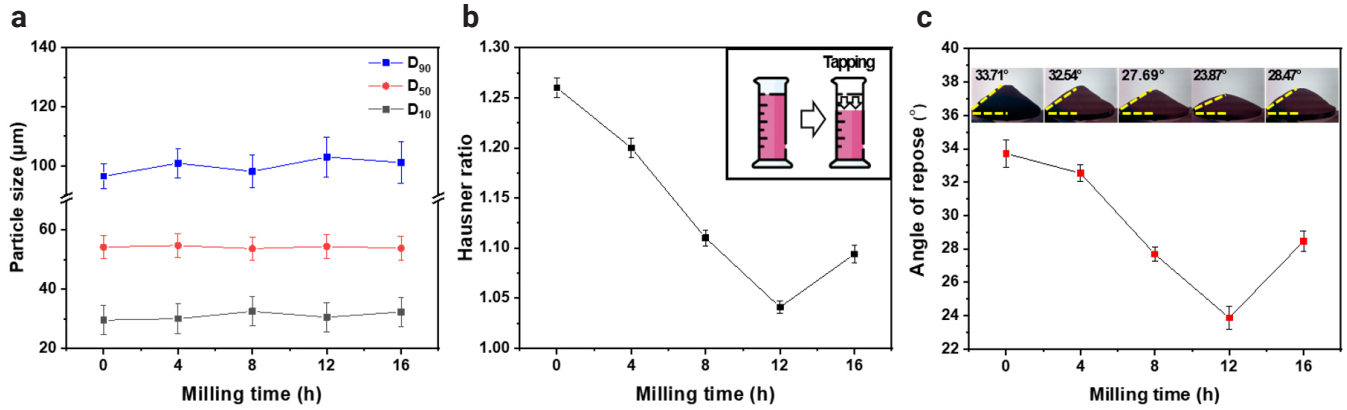

Fig. 5. Graphs of (a) particle size, (b) the Hausner ratio, and (c) the angle of repose (inset: optical image of the angle of repose) of $Al_{18}B_4O_{33}$ powders according to milling times.

너 비율 (Hausner ratio)을 분석했다(그림 5b) [31]. 하우스너 비율은 탭 밀도를 겉보기 밀도로 나눈 값으로, 1에 가까울수록 구형 분말의 유동성이 높은 것을 의미한다. 겉보기 밀도는 구형 분말을 용기에 채운 후 공극을 포함한 전체 부피를 기준으로 측정한 밀도이며, 탭 밀도는 구형 분말을 용기에 채운 후 일정 시간 동안 진동으로 분말이 충진 시킨 후 부피가 최소화될 때의 밀도이다[32]. 따라서 충진 되는 비율은 구형 분말의 유동성과 연관이 있으며, 비교적으로 큰 B_2O_3 입자로 제작된 구형 분말일수록 하우스너비가 큰 결과를 나타낸다. 0시간부터 4시간, 8시간, 12시간, 16시간 밀링 공정에 따라 탭밀도는 1.56 g/cm^3, 1.59 g/cm^3, 1.68 g/cm^3, 1.73 g/cm^3, 1.67 g/cm^{3}의 결과를 나타냈으며, 12시간 밀링 공정에서 가장 높은 밀도를 확인할 수 있다. 결과적으로 12 시간 밀링 공정을 통해 균일한 B_2O_3를 이용하여 제작된 이종 과립을 열처리한 구형 분말의 하우스너비가 1.04로 밀링을 진행하지 않은 B_2O_3를 이용했을 때보다 17 % 감소되어 향상된 유동성의 결과를 나타낸다. 또한 분말의 유동 특성은 수평면 위에 분말을 수직방향으로 자유낙하 시켰을 때 원뿔 형태로 유지되는 기울기 경사각인 안식각으로도 분석 가능하다[33]. 유동성이 높을수록 원뿔 형태의 높이는 낮게 유지된다. 밀링을 하지 않은 B_2O_3를 사용한 구형 분말의 안식각은 33.7도인 반면, 12 시간 밀링 공정으로 제작된 구형 분말은 23.9도로 29 % 낮아진 안식각을 통해 높은 유동성을 나타낸다. 결과적으로 3D 믹서를 이용한 B_2O_3의 밀링 공정을 통해 입자를 Al_2O_3와 유사한 크기로 감소시키면 내부까지 균일 혼합된 이종 과립이 형성되며, 열처리 후 매끈한 구형 형태와 균일한 $Al_{18}B_4O_{33}$ 결정상을 가짐에 따라 향상된 유동성을 구현할 수 있다는 것을 확인할 수 있다. 본 연구를 통해 제시한 고 유동성의 $Al_{18}B_4O_{33}$ 세라믹 소재는 우수한 내구성이 필요한 반도체, 우주항공 산업 분야에서 활용 가능할 것으로 기대된다.

4. Conclusion

본 연구에서는 반도체, 우주항공을 포함한 다양한 산업에 적용 가능한 고 유동성 특성의 $Al_{18}B_4O_{33}$ 구형 분말의 제작 방법을 개발했다. 3D 믹서를 통해 B_2O_3의 입자의 크기를 균일하게 제어할 수 있으며 B_2O_3의 밀링 공정을 통해 입자를 Al_2O_3와 동일하게 크기로 감소시켰을 때 내부까지 치밀한 이종 혼합 과립을 형성할 수 있다는 것을 증명했다. 열처리 후 향상된 $Al_{18}B_4O_{33}$ 결정상을 나타냈다. 이러한 밀링 공정을 통해 치밀화 된 $Al_{18}B_4O_{33}$ 구형 분말은 밀링을 진행하지 않은 B_2O_3 분말을 사용한 구형 분말에 비해 18 % 감소한 하우스너비 (1.04)와 29% 감소한 안식각 (23.9)을 가짐으로 향상된 유동성 특성을 나타낸다. 본 연구에서 개발한 $Al_{18}B_4O_{33}$의 고유동화 기술은 높은 유동 특성을 요구하는 반도체, 이차전지, 항공우주 등의 차세대 산업에서 세라믹 코팅 공정 및 고밀도 소결체 제조 공정에 다양하게 적용될 수 있을 것이라 기대된다.

Funding

This research was supported by the National Research Foundation of Korea (NRF) grant funded by the Korean government (MSIT) (grant number 2022R1F1A1069574).

Conflict of Interest

The authors declare no competing financial interests or personal relationships.

Data Availability Statement

The original contributions presented in the study are included in the article, further inquiries can be directed to the corresponding authors.

Author Information and Contribution

송기호: **위촉 연구원**; conceptualization, writing–original draft, data curation. **이상인**: **석사과정 학생**; conceptualization, data curation. **송현승**: **석사과정 학생**; data curation. **안창의**: **선임연구원**; conceptualization, writing–review & editing, supervision

Acknowledgement

None.

References

[1] J. C. Williams, E. A and J. A. m. Starke Jr: Acta Mater., **51** (2003) 5775.
[2] E. Bakan, D. E. Mack, G. Mauer, R. Vaßen, J. Lamon and N. P. Padture: Advanced Ceramics for Energy Conversion and Storage, (2020) 3.
[3] E. P. Simonenko, D. V. Sevast'yanov, N. P. Simonenko, V. G. Sevast'yanov and N. T. Kuznetsov: Russ. J. Inorg. Chem., **58** (2013) 1669.
[4] A. S. Okada: Mater. Sci. Eng. B, **161** (2009) 182.
[5] S. Zhang, J. Wang, M. Zhang, L. Ding, H. Chan, X. Liu, F. Wu, Z. Tu, L. Shao and N. Ye: Coatings, **13** (2023) 956.
[6] X. Guo, Q. Xun, Z. Li and S. Du: Micromachines, **10** (2019) 406.
[7] K. Sun, W. Zhong, S. Qiu, W. Cai, X. Xie, H. Wang, S. Zhang and W. Li: Coatings, **14** (2024) 377.
[8] T. Ma, T. List and V. M. Donnelly: J. Vac. Sci. Technol. A, **36** (2018) 031305.
[9] M. F. Hernández, G. Suárez, M. Cipollone, M. S. Conconi, E. F. Aglietti and N. M. Rendtorff: Ceram. Int., **43** (2017) 2188.
[10] D. Lao, Y. Zhang, L. Huang, X. Liang and W. Jia: J. Aust. Ceram. Soc., **30** (2024) 905.
[11] J. Choi, S. Lee, K. Song, T. Kim and C. Ahn: J. Powder Mater., **30** (2023) 356.
[12] M. Yoshida, S. Takeuchi, J. Pan, G. Sasaki, N. Fuyama, T. Fuj and H. M. Fukunaga: Adv. Compos., **8** (1999) 259.
[13] S. Yu, Y. Zhao, G. Zhao, Q. Liu, B. Yao and H. Liu: Int. J. Adv. Manuf. Technol., **132** (2024) 1053.
[14] J. Wei, J. Li, X. Song, Y. Feng and T. Qiu: J. Alloys Compd., **768** (2018) 503.
[15] M. Shi, Z. Xue, Z. Zhang, X. Ji, E. Byon and S. Zhang: Surf. Coat. Technol., **395** (2020) 125913.
[16] R. Sobhanverdi and A. Akbari: Ceram. Int., **41** (2015) 14517
[17] M. Yang, Z. Li, X. Wang, Y. Li, F. Chen, M. Li, Y. Chen and W. Chen: Ceram. Int., **48** (2022) 1125.
[18] M. Yu, J. Lin and J. Fang: Chem. Mater., **17** (2005) 1783.
[19] C. Ramachandran, V. Balasubramanian and P. Anantha-padmanabhan: Surf. Coat. Technol., **206** (2012) 3017.
[20] R. Li, M. Qin, C. Liu, H. Huang, H. Lu, P. Chen and X. Qu: Int. J. Refract. Met. Hard Mater., **62** (2017) 42.
[21] T. Wong and P. John, Handbook of Nanoparticles, (2016) 329.
[22] B. Özgür, O. Bilaç and C. Duran: Ceram. Int., **50** (2024) 14987.

[23] W. J. Walker Jr, J. S. Reed and S. K. Verma: J. Am. Ceram. Soc., **82** (1999) 1711.
[24] G. Bertrand, P. Roy, C. Filiatre and C. Coddet: Chem. Eng. Sci., **60** (2005) 95.
[25] M. Gasgnier, H. Szwarc and A. Ronez: J. Mater. Sci., **35** (2000) 3003.
[26] C. F. Burmeister and A. Kwade: Chemical. Soc. Rev., **42** (2013) 7660.
[27] K. Bhoite, G. Kakandikar and V. Nandedkar: Mater. Today: Proceed., **2** (2015) 1700.
[28] Y. Zhao, Q. Zhang, J. Chen, Y. Yi, M. Zhou and J. Cui: J. J. Mater. Sci.: Mater. Electron., **35** (2024) 225.
[29] S. Wintzheimer, L. Luthardt, K. L. A. Cao, I. Imaz, D. Maspoch, T. Ogi, A. Bück, D. P. Debecker, M. Faustini and K. Mandel: Adv Mater., **35** (2023) 2306648.
[30] A. B. D. Nandiyanto, T. Ogi, W.-N. Wang, L. Gradon and K. Okuyama: Adv. Powder Technol., **30** (2019) 2908.
[31] H. A. Murtaza, A. Mukhangaliyeva, B. Golman, A. Perveen, and D. Talamona: J. Mater. Eng. Perform., **33** (2024) 10853.
[32] J. S. e Silva, D. Splendor, I. Gonçalves, P. Costa and J. Sousa Lobo: Aaps Pharmscitech., **14** (2013) 1098.
[33] S. Duverger, V. Angelidakis, S. Nadimi, S. Utili, S. Bonelli, P. Philippe and J. Duriez: Granular Matter, **26** (2024) 20.

Research Article

pISSN 2799-8525 · eISSN 2799-8681
J Powder Mater 2024;31(6):521-529

Journal of Powder Materials

재사용 열보호시스템용 경량 단열소재 및 코팅제조와 고온 성능평가

남민수[1,2], 김종일[1], 신재성[3], 김현준[3], 오범석[4], 김성원[1,*]

[1]한국세라믹기술원 이천분원 엔지니어링소재센터
[2]고려대학교 신소재공학과
[3]한국항공우주연구원 소형발사체연구부
[4]한국항공우주연구원 발사체기술연구1부

Fabrication and High-Temperature Performance Evaluation of Light-Weight Insulation Materials and Coatings for Reusable Thermal Protection Systems

Min-Soo Nam[1,2], Jong-Il Kim[1], Jaesung Shin[3], Hyeonjun Kim[3], Bum-Seok Oh[4], Seongwon Kim[1,*]

[1]Engineering Materials Center, Korea Institute of Ceramic Engineering and Technology, Icheon, Gyeonggi-do, 17303, Republic of Korea
[2]Department of Materials Science and Engineering, Korea University, Anam-dong, Seongbuk-gu, Seoul, 02841, Republic of Korea
[3]Small Launch Vehicle Research Division, Korea Aerospace Research Institute, 169-84 Gwahak-ro, Yuseong-Gu, Daejeon, 34133, Republic of Korea
[4]Launch Vehicle Technology Research Division (1), Korea Aerospace Research Institute, 169-84 Gwahak-ro, Yuseong-Gu, Daejeon, 34133, Republic of Korea

Light-weight ceramic insulation materials and high-emissivity coatings were fabricated for reusable thermal protection systems (TPS). Alumina-silica fibers and boric acid were used to fabricate the insulation, which was heat treated at 1250 °C. High-emissivity coating of borosilicate glass modified with $TaSi_2$, $MoSi_2$, and SiB_6 was applied via dip-and-spray coating methods and heat-treated at 1100°C. Testing in a high-velocity oxygen fuel environment at temperatures over 1100 °C for 120 seconds showed that the rigid structures withstood the flame robustly. The coating effectively infiltrated into the fibers, confirmed by scanning electron microscopy, energy-dispersive X-ray spectroscopy, and X-ray diffraction analyses. Although some oxidation of $TaSi_2$ occurred, thereby increasing the Ta_2O_5 and SiO_2 phases, no significant phase changes or performance degradation were observed. These results demonstrate the potential of these materials for reusable TPS applications in extreme thermal environments.

Keywords: Thermal Protection System(TPS); Ceramic insulation; Glass former; Fibrous materials; Glass coatings

Received: September 30, 2024
Revised: November 11, 2024
Accepted: November 11, 2024

***Corresponding author:**
Seongwon Kim
TEL: +82-31-645-1452
FAX: +82-31-645-1492
E-mail: woods3@kicet.re.kr

1. Introduction

열보호시스템(Thermal Protection System, TPS)은 우주비행체의 재진입(Re-entry) 환경 혹은 극초음속(Hypersonic) 비행체에서 발생하는 공력가열(Aerodynamic heating)로부터 비행체와 내부를 보호하는 필수적인 요소이다[1]. 비행체와 공기의 마찰로 인해 발생하는 공력가열은 대류현상에 의해 발생되고 이를 효과적으로 보호하기 위한 TPS에는 시스템적인 전도, 복사 열전달과 소재의 화학반응이 중요하게 작용한다. 공력가열의 양상은 재진입궤도, 속도나 선단부(Leading edge) 형상에 따라 달라지며 따라서 TPS 또한 적용되는 온도와 형상에 따라 그 소재와 특성이 결정된다[2]. TPS는 공력가열로 발생하는 열유속 환경에 따라 재사용과 삭마형 TPS로 구분된다. 재진입의 열유속이 1 MW/m^2 이하인 지구 저궤도(Low Earth Orbit, LEO) 임무를 수행하는 우주비행체가 재진입하는 경우 낮은 열전도도를 갖는 단열소재(Insulation)와 표면의 열

https://doi.org/10.4150/jpm.2024.00318

을 견디는 내열소재(Refractory materials)로 구성된 재사용(Reusable) TPS로 비행체를 보호할 수 있다. 반면 그 이상의 열유속 환경에서 재진입하는 경우에는 열분해(pyrolysis)를 통해 기체상을 형성하는 삭마형(Ablative) TPS를 통해 비행체를 보호해야 한다[1].

재사용 TPS가 적용되는 우주비행체의 선단부는 열분산 구조를 갖는 무딘 선단부(Blunt edge)와 고속 비행시의 열집중 구조를 갖는 예리한 선단부(Sharp edge) 두 가지 형상으로 크게 나뉜다[3]. 우주왕복선 등에 적용된 무딘 선단부는 공력가열로 발생하는 열의 대부분을 복사를 통해 방출하고 내부로의 열전달은 단열소재를 통해 최소화시킨다. 반면 극초음속 비행체는 예리한 선단부를 갖는데 비행체의 기동이나 안정성을 향상시키며 공력가열로 발생하는 열을 집중시킨다. 따라서 녹는점이 높고 내열 특성이 좋은 초고온세라믹스(Ultra-high Temperature Ceramics, UHTC) 등의 소재가 TPS로 적용된다[4, 5].

우주비행체 선단부를 통해 기체 내부로 전달되는 열을 막기 위해 다양한 소재와 형상의 재사용 TPS가 NASA ARC(Ames Research Center)와 GRC(Glenn Research Center)에서 개발되었다[6]. RCC(Reinforced Carbon-Carbon)를 제외한 RSI(Reusable Surface Insulation)는 세라믹 섬유를 활용한 다공체로 제조되었으며 LI(Lockheed Insulation) 등의 실리카(SiO_2) 섬유를 활용한 단열소재와 FRCI(Fibrous Refractory Composite Insulation), AETB(Alumina Enhanced Thermal Barrier), BRI(Boeing Rigid Insulation)등의 실리카와 알루미나(Al_2O_3) 섬유가 혼합된 단열소재 등 그 제조 방식, 소재, 사용온도 측면에서 다양한 종류의 TPS가 개발되었다[6-8]. 초기에 개발된 LI 단열소재는 실리카 섬유를 실리카 나노분말과 열처리하여 결합한 소재로 낮은 밀도와 열전도도를 갖지만 강도가 낮고 고온안정성이 떨어지는 단점을 지닌다. 이를 보완하기 위해 알루미나 섬유를 첨가하여 강도와 고온안정성을 높인 FRCI 나 AETB 등의 단열소재가 개발되었고, Boro-aluminosilicate섬유를 결합재로 사용하는 방식으로 제조되었다. 이후에 BRI로 제조방식이 개선되어 흡습성이 높은 B_2O_3 대신 B_4C 분말과 각각의 실리카, 알루미나 섬유를 혼합하여 단열소재를 제조하였다. 이러한 산화물계 세라믹 섬유 단열소재는 후술될 다층구조 TPS인 TUFROC(Toughened Uni-piece Fibrous Reinforced Oxidation-resistant Composite)의 단열소재 파트로 응용될 수 있다[9, 10].

TUFROC은 NASA에서 개발되어 X-37B 우주비행기에 처음 적용된 다층구조 재사용 TPS의 명칭이다. TUFROC은 표면에서 내부까지 내열온도가 다른 3층의 소재가 하나의 부품(Uni-piece)으로 물리, 화학적으로 결합된 TPS다. TUFROC이 적용된 X-37B는 현재 여러 번의 지구 저궤도 임무와 재진입을 수행하며 재사용 TPS의 성공적인 사례를 보여주고 있다. 이러한 TUFROC을 벤치마킹하여 한국세라믹기술원과 한국항공우주연구원이 함께 국내에서 확보가능한 소재를 활용하여 한국형 TPS 소재 및 시스템의 개발을 진행하고 있다.

본 연구에서는 선행 연구를 통해 개발한 한국형 재사용 TPS의 산화물 경량 고온 단열소재의 품질 향상을 위해 유리형성제 변경과 열처리 온도 변경을 통해 공정을 개선하였다. 또한 HETC(High Efficiency Tantalum-based Ceramic Composite)[11] 코팅을 벤치마킹하여 제조한 고방사율 코팅을 적용하여 시편을 제조하였고, 이를 HVOF(High Velocity Oxygen Fuel)를 이용한 모사환경 평가를 진행하여 재사용 가능성을 평가하였다. 평가된 소재는 미세구조, 결정구조 등의 분석을 통해 모사환경 평가 이후 미세구조적 파손, 박리, 균열 등의 흔적이나 결정구조적 변화를 분석하여 재사용 TPS 적용 가능성을 제시하였다.

2. Experimental procedure

경량 단열소재의 제조는 Al_2O_3-SiO_2 조성의 세라믹 섬유인 세라크울(Cerak Wool, 1300 Bulk, KCC Corp., Korea)을 사용한다. 섬유간 결합을 위한 유리형성제는 붕산(Boric acid, Daejung Chemicals & Metals co., ltd., Korea)분말을 사용하였다. 섬유와 유리형성제는 표 1의 조성에 따라 증류수 용매 내에서 overhead mixer와 metal impeller를 이용하여 2 시간 동안 400 rpm으로 분쇄, 혼합, 분산된다. 제조된 슬러리는 60Ø 아크릴 몰드 내에 장입되어 증류수를 제거하며 일정 크기로 성형하는 탈수성형 공정을 통해 일정 형태로 성형된다. 성형된 섬유는 대기 분위기의 박스로 내에 장입하고 1250˚C 온도에서 1.5 h 동안 열처리하여 단열소재로 제조된다.

고방사율 유리 코팅층의 원료는 분쇄된 붕규산 유리(Borosilicate glass, low form, Duran®, Schott, Germany)를 사용한다. 이에 HETC를 벤치마킹하여 내열성과 방사율을 향상시킨 원료로 $TaSi_2$(KOJUNDO KOREA co., ltd., Korea), $MoSi_2$(KOJUNDO KOREA co., ltd., Korea), 그리고 SiB_6(KOJUNDO KOREA co., ltd., Korea)를 함께 사용하였다. 코팅을 위한 슬러리는 표 2의 조성에 따라 가소제인 methylcellulose(Methocel®, A4M, Sigma-Aldrich, USA)를 일정 비율 첨가하여 10 Ø ZrO_2 볼과 함께 무수에탄올 용매에서 24 시간 동안 습식혼합 및 분쇄공정을 거쳐 제조된다.

제조된 유리코팅 슬러리는 내부 침투 코팅을 위한 딥(Dip) 코팅과 표면 코팅을 위한 스프레이(Spray) 코팅법을 통해 단열소재에 코팅한다. 딥 코팅은 ZrO_2 볼을 걸러낸 코팅 슬러리에 단열소재를 담가 15 초 동안 코팅 소재의 단열재 내부로 함침한다. 단열재를 80˚C 오븐에서 10 분 동안 건조하여 에탄올을 증발시킨 후 0.5 MPa 압력의 공압에 연결된 스프레이 건에 담아 단열재에 각 면당 10 초

Table 1. Light-weight insulation batch compositions used in this study

Process	B4C	Boric acid
Fiber (wt.%)	4.2	5.8
Glass former (wt.%)	0.4	1.9
DIW (wt.%)	95.4	92.3

Table 2. HETC-like high emissivity coating batch compositions used in this study

Materials	Weight ratio (%)
Anhydrous ethanol	57.5
Glass frit	15.9
$TaSi_2$	10.6
$MoSi_2$	6.2
SiB_6	0.9
Thickener	8.9

Table 3. HVOF conditions tested in this study

HVOF test conditions	
Gun distance	180 mm
Calculated heat flux	1.8MW/m^2
Exposure time	120 s
Max surface temperature	1153.5°C

HVOF, high-velocity oxygen fuel.

동안 분사하여 스프레이 코팅을 진행하고 건조하는 과정을 5회 반복한다. 코팅을 완료한 단열소재는 대기 분위기의 박스로 내에 장입하고 1100˚C 온도에서 1 h 동안 열처리하여 코팅층을 제조한다.

고온내구성 평가는 HVOF용사 장비를 이용하여 제조된 시편에 직접적으로 고온 고속 화염을 분사하여 평가를 진행하였다. 평가는 대기 분위기에서 진행되었으며 180 mm 분사 거리에서 총 120 초 동안 평가를 진행하였다. 평가 진행 중 IR pyrometer를 통해 분사 표면 온도를 측정하였다. 자세한 HVOF 평가 조건을 표 3에 나타내었다.

HVOF 평가 이후 코팅소재의 결정구조는 Cu(λ = 1.5406 Å) 타겟을 사용한 X-선 회절 분석기(D/MAX-2500-PC, Rigaku Corp., Japan)를 통해 1°/min 스캔 속도로 2θ = 10–60° 범위에서 40 kV, 100 mA 조건으로 측정하여 평가하였다.

단열소재의 미세구조 및 조성분석은 전계방출형 주사 전자 현미경(FE-SEM, JSM-7610F+, JEOL Ltd., Japan)과 에너지 분산형 분광분석법(EDS, Ultim Max 100, Oxford Instruments, UK)을 통해 평가되었다. 단열소재의 단면과 표면에 대한 미세구조와 조성분석을 통해 재사용 TPS로의 활용 가능성을 평가하였다.

3. Results and discussion

3-1. 경량 고온 세라믹 단열소재의 제조 및 공정개선

그림 1(a), (b)는 선행연구[12]의 공정을 통해 제조된 세라믹 단열소재를 보여주며 그림 1(c), (d)는 공정 개선을 통해 본 연구에서 제조된 세라믹 단열소재의 형상을 보여준다. 좌측에 위치한 백색 시편은 열처리 직후의 단열소재 형상이며, 우측에 위치한 흑색 시편은 코팅 공정이 적용된 이후의 단열소재 형상이다. 그림 1(a), (c)는 각 공정에 따른 시편의 평면도를 나타내며, 그림 1(b), (d)는 정면도를 나타낸다. 본 연구를 통해 개선된 공정은 유리형성제 변경과 열처리 온도 변경 2가지 개선점을 갖는다. 기존 공정은 boron source인 유리형성제로 B_4C를 사용하여 섬유 내에 입자 분산 형태의 슬러리를 제조하였다. 반면 개선된 공정은 유리형성제로 수용성을 갖는 붕산을 사용하여 용액 형태의 분산 방식을 사용하여 더 균질한(Homogeneous) 유리형성제 분산 슬러리를 제조하였다. 또한 과도한 소결 방지를 위하여 열처리 공정을 1400˚C, 1 h 에서 1250˚C, 1.5 h 로 변경하였다.

그림 1(a), (b)에서 관찰되는 B_4C를 이용해 제조한 단열소재는 측면이 휘어지는(bending) 형상을 보인다. 이는 유리형성제로 사용된 입자 분산 형태인 B_4C의 불균질(Heterogeneous) 분산의 결과로 보인다. 성형 공정을 통해 원기둥(Cylinder) 형태로 성형된 단열소재는 열처리 공정을 통해 유리형성제의 산화를 통한 B_2O_3 형성과, 유리질 형성을 통한 섬유간 결합을 통해 제조된다. 반면 그림상에서 관찰되는 휘어지는 형상은 치밀화와 수축을 동반하는 소결의 결과로 보이며, 등방성 수축이 아닌 이방성 수축을 보이며 과소결의 결과로 관찰된다.

반면에 그림 1(c), (d)에 붕산을 유리형성제로 사용하여 제조된 시편은 B_4C를 사용해 제조한 시편과 달리 휘어지는 현상이 관찰되지 않는다. 이는 유리형성제의 용매 및 섬유 내 분산 차이로 인해 발생하는 결과로 보인다. B_4C는 용매와 섬유 내에 입자 형태의 분산을 통해 유리형성제로 작용하며 고온 산화 분위기에서 B_2O_3로 산화되어 섬유간 결합을 해주는 역할을 한다. 결합 정도와 유리질 분포는 B_4C 입자의 분산 정도에 따라 큰 영향을 받게 된다. 표 1에 나타난 공정 배치에서는 분산제 첨가나 극성 조절을 통한 화학적 분산 방법 없이 혼합에 의한 물리적인 분산 방법만 사용하기 때문에 균질한 B_4C 입자의 분산을 기대하기 어렵다. 반면 붕산은 용매에 완전히 용해되어 입자상 분산이 아닌 용액상태로 균질하게 분산되고, 고온에서 마찬가지로 B_2O_3 로 분해되어 유리형성제로 작용한다. 용액 상태의 분산이기 때문에 모든 섬유에 동일하게 분산되며 시편 내에서 균일한 분포를 갖게 된다. 따라서 그림 1(c), (d)에 나타난 시편의 형상에서 휘어지는 현상 없이 모든 방향에서 균일한 시편이 제조되었다.

그림 2(a), (b)에 나타난 미세구조는 각각 B_4C 와 붕산 분말을 유리형성제로 사용해 제조한 시편의 미세구조를 보여준다. 서로 다른 유리 형성제를 이용하였지만 섬유 각각의 결합 형태는 큰 차이를 보이지 않는다. 일반적으로 동일한 몰수의 붕산보다 B_4C 가 4배 더 많은 boron source를 갖기 때문에 이를 맞추기 위해 배치 공정 상에서 B_4C 대비 붕산 분말을 4배 더 많이 사용하였다. 따라서 유리형성제로 사용된 boron 원소 총량은 두 공정에서 같으며 미세구조적 특징에서 이 차이가 크게 관찰되지 않는다. 섬유간 끝단을 유리상이 발생하며 결합해주는 유사한 미세구조가 관찰되고 있으며, 미세구조적으로 유사한 구조 내에서도 붕산 분말을 사용한 시편이 외관적인 측면에서 더 나은 균일성을 보임을 그림 1, 2를 통해 확인하였다.

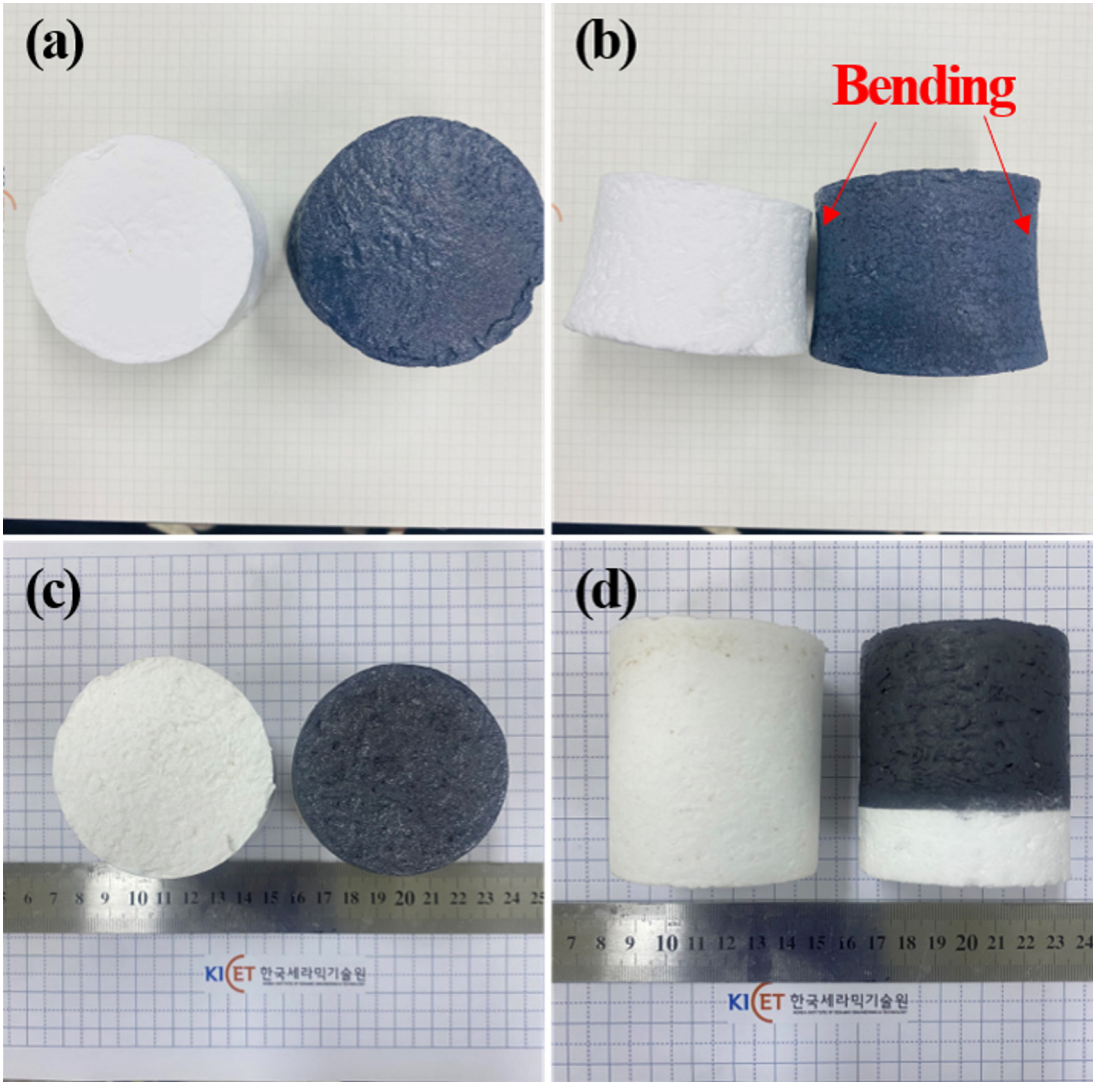

Fig. 1. Sample pictures of light-weight high-temperature insulation and high-emissivity coated samples: (a) and (b) B4C is used as the glass former. (c) and (d) Boric acid is used as the glass former.

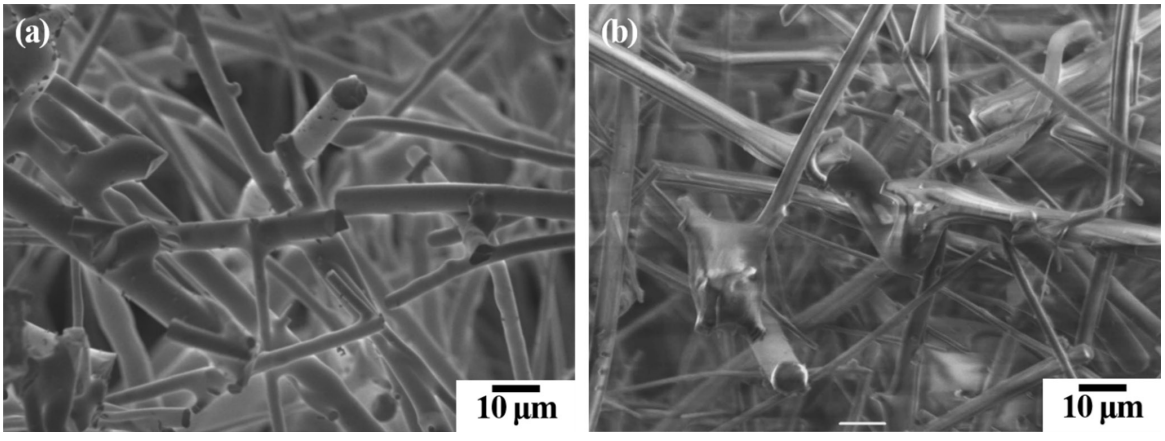

Fig. 2. Scanning electron microscopy micrographs of light-weight high-temperature insulations used in this study: (a) B4C powder is used as glass former. (b) Boric acid is used as glass former.

3-2. 고방사율 코팅소재의 제조

재사용 TPS 개발 초기 NASA ARC에서 개발된 표면 코팅인 RCG(Reaction-Cured Glass)[13] 코팅은 다공성 단열재가 습윤환경에 노출되어 생기는 문제를 막기 위해 불투수성(waterproof)을 위한 유리 코팅에 추가적으로 공력가열에 의한 열을 복사로 방출하는 높은 방사율(emissivity)을 갖는 소재(SiB_4)를 첨가하여 스프레이 코팅을 통해 표면에 적용한다[12, 14]. 이때 적용된 코팅은 단열재 표면 위로 적용되는 코팅이며 개기공이 없는 표면 상태로 FOD(Foreign Object Damage)등에 의한 파손 및 탈락에 취약한 특징을 갖는다. 이를 보완하기 위한 코팅 방법이 TUFI(Toughened Uni-piece Fibrous Insulation)[1, 15]나 HETC 등에 적용된 침투 코팅(penetration coating) 방식이다. 코팅 슬러리를 딥 코팅을 통해 단열재에 직접적으로 함침하여 침투된 코팅소재가 단열재 섬유와 직접적인 결합을 유도하고, 후술될 기공형성제로 인한 표면 기공이 균열전파를 막아 FOD 에도 쉽게 탈락되지 않도록 하는 원리로 적용된다[1].

단열재에 적용되는 고방사율 코팅의 원료로 사용되는 다양한 소재는 고온에서 유리 기지와 반응하여 2차상을 생성하거나, 결정화를 일으키지 않는 붕화물(Boride) 이나 규화물(Silicide) 계열의 소재들이 선정되었다. 초기의 표면 코팅인 RCG 코팅에는 기지(matrix) 역할을 하는 붕규산 유리와 방사율을 높이는 emittance agent로 사용되는 SiB_4 가 원료로 사용되었다[13]. 이후 침투 코팅인 TUFI 코팅에는 붕규산 유리 기지 내에 온도수용성과 방사율을 높이는 소재로 $MoSi_2$ 가 사용되었고, 그에 따라서 높아진 열처리 공정 온도를 낮추기 위한 processing aid 와 기공형성제 로 SiB_6 소재가 함께 사용되었다[15]. SiB_6 첨가로 인해 발생한 표면의 기공은 FOD로 인한 파손시 균열의 전파를 막아 코팅의 수명 연장의 역할을 수행한다. 본 연구에서 벤치마킹한 HETC 코팅은 TUFI 원료에 보다 높은 사용온도를 위해 $TaSi_2$ 원료가 추가되었다. HETC 코팅에서 각각의 원료는 $TaSi_2$: 1차 emittance agent, 조성에 따른 기지, $MoSi_2$: 2차 emittance agent, 산소 게터(Oxygen getter), SiB_6: processing aid, 기공형성제, 붕규산유리: 기지, boron source의 역할을 수행한다[11].

그림 3은 고방사율 코팅소재를 표면에 적용한 단열재 시편의 단면 미세구조를 나타낸다. HETC 코팅을 벤치마킹하여 제조한 코팅은 단열재 내부로 침투하는 타입의 코팅 구조를 갖는다. 그림 3에서 관찰되는 단면의 미세구조와 EDS map 상에서도 Mo map과 Ta map 결과를 통해 표면에 형성된 유리 코팅층이 관찰되며 단열재 내부로 침투하여 섬유와 결합한 침투 코팅층도 함께 관찰된다. 따라서 본 연구를 통해 제조된 시편의 코팅은 충분히 단열재 내부로 침투하여 코팅을 형성하였으며 이에 FOD 등의 요인으로 인한 파손으로부터 우수한 내구성을 갖는 코팅층으로 제조되었다.

3-3. 고온내구성 평가

코팅까지 완료하여 제조된 단열소재 시편은 HVOF 시험을 통해 고온내구성 평가가 진행되었다. 시편의 형상은 그림 4(a)에서 관찰되는 형상처럼 고정용 흑연 지그에 장착되어 고정되었고, 시편의 정중앙에 HVOF 화염을 노출시켰다. 평가는 180 mm 거리에서

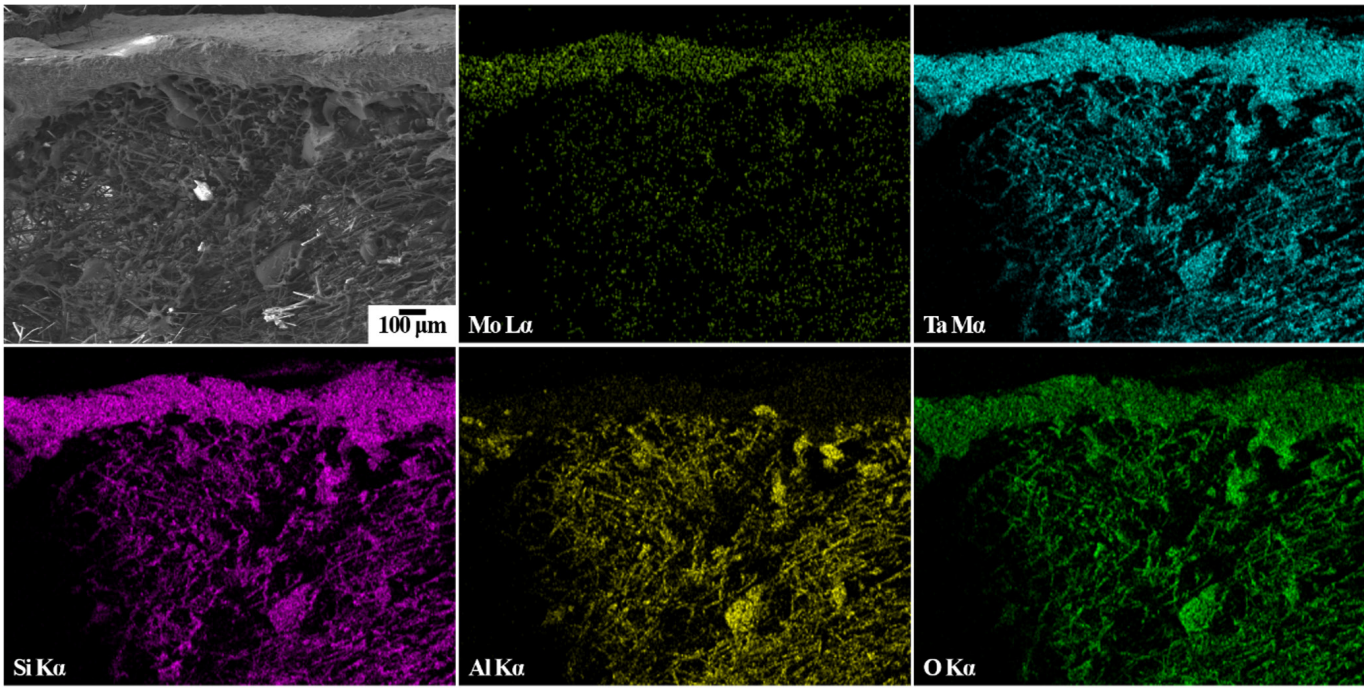

Fig. 3. Cross-sectional scanning electron microscopy–energy-dispersive X-ray spectroscopy results of manufactured light-weight high-temperature insulation samples coated by high emissivity glass composite coating.

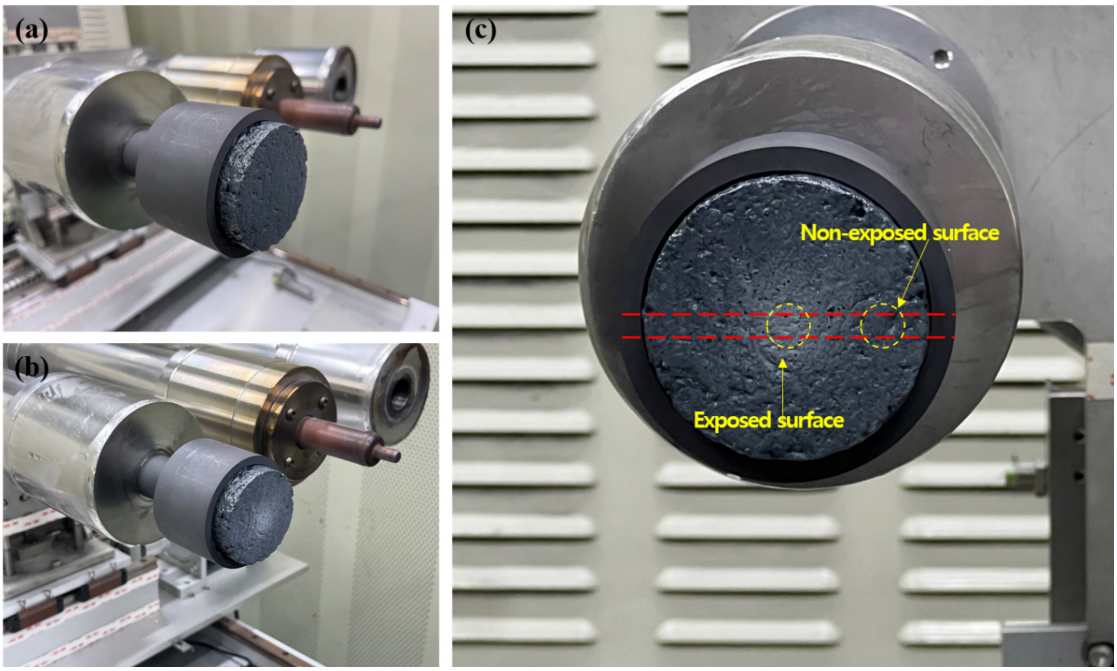

Fig. 4. Before and after test photographs of the mounted sample for high-velocity oxygen fuel testing. (a) Before testing, (b) after testing, and (c) identification of the flame-exposed surface for subsequent analysis.

120 초 동안 진행되었고 평가기관을 통해 계산된 모사환경의 열 유속은 1.8 MW/m^2 로 계산되었다. 평가 중 IR pyrometer를 통해 측정된 표면의 최고 온도는 1153.5˚C 로 측정되었다. 그림 5에 HVOF 화염 노출 시간에 따른 표면 온도 변화 그래프가 나타나 있으며 모든 시간에서 평균적으로 1100˚C 이상의 고온에 노출되었음을 확인할 수 있다. 그림 4(b)에 나타난 평가 이후 시편 표면의 형상에서 직접적으로 HVOF 화염 분사에 노출되어 코팅 표면의 색상이 변한 부분이 관찰되며 시편의 가장자리 부분은 색상이 변하지 않았음이 관찰된다. 코팅층 색상 변화에 대한 평가를 위해 그림 4(c)에 나타낸 방식으로 HVOF 화염 분사에 직접적으로 노출된 노출 표면과 비노출 표면으로 시편을 구분하였으며 해당 두 부분에 대한 분석을 진행하였다.

그림 6은 HVOF 평가 이후 시편의 단면 미세구조를 보여주며 그림 6(a)는 노출 단면 그림 6(b)는 비노출 단면이다. 직접적인 화염 노출 단면과 비노출 단면 모두 미세구조적으로 비교되는 특별한 차이를 보이지 않는다. 그림 6(a), (b)에 나타난 코팅층의 두께는 미세구조 내에서 위치별로 10 회 측정하여 평균값을 사용하였으며 각각 185 μm, 199 μm 으로 비슷한 코팅 두께를 보이고 있다. 노출 단면에서 관찰되는 코팅층과 섬유 단열소재 층 모두 화염 분사 노출에 의한 파손의 흔적이 관찰되지 않으며 120 초 동안의 HVOF 시험이 코팅층과 단열소재에 영향을 미치지 않음을 확인하였다.

그림 7은 HVOF 평가 이후 시편의 표면 코팅층의 미세구조와 EDS 분석 결과를 보여주며 그림 7(a)는 노출 표면 그림 7(b)는 비노출 표면이다. EDS map 결과에서 노출 표면과 비노출 표면은 큰

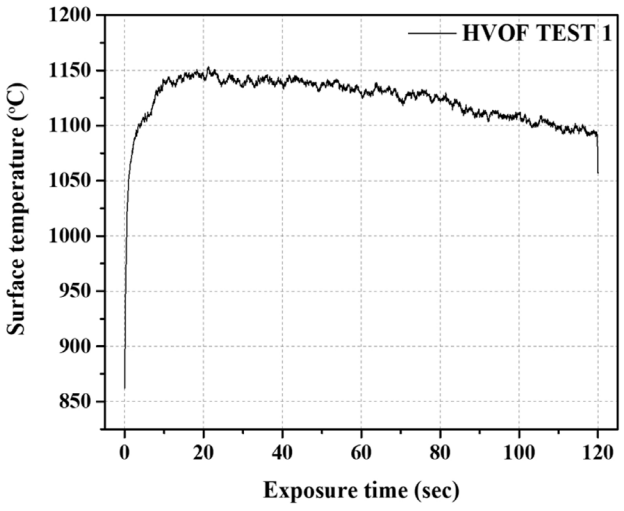

Fig. 5. Time-temperature graph of surfaces exposed to high-velocity oxygen fuel flame recorded by an infrared pyrometer.

차이가 나타나지 않으며 구성 원소들의 비슷한 분포를 보이고 있다. 표 4에 나타난 EDS point 분석 결과 또한 두 표면의 성분이 큰 차이를 보이지 않으며 HVOF 화염 분사에 직접적으로 노출되어도 구성 성분의 큰 변화가 없음을 보이고 있다. 표면 미세구조 특징은 그림 7(a)의 노출 표면에서 보이는 기공의 크기가 그림 7(b)의 비노출 표면에서 보이는 기공보다 작은 크기를 갖는다. 앞서 서술한 것

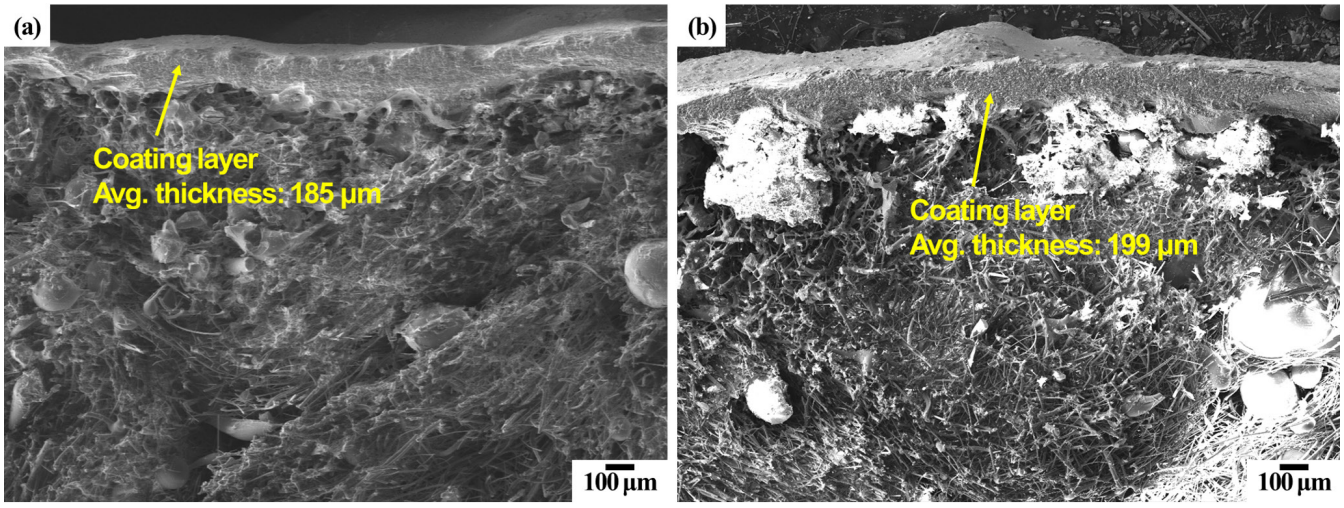

Fig. 6. Cross-section scanning electron microscopy micrographs of a high-velocity oxygen fuel–tested specimens. (a) High-velocity oxygen fuel flame–exposed cross-section, and (b) non-exposed cross-section.

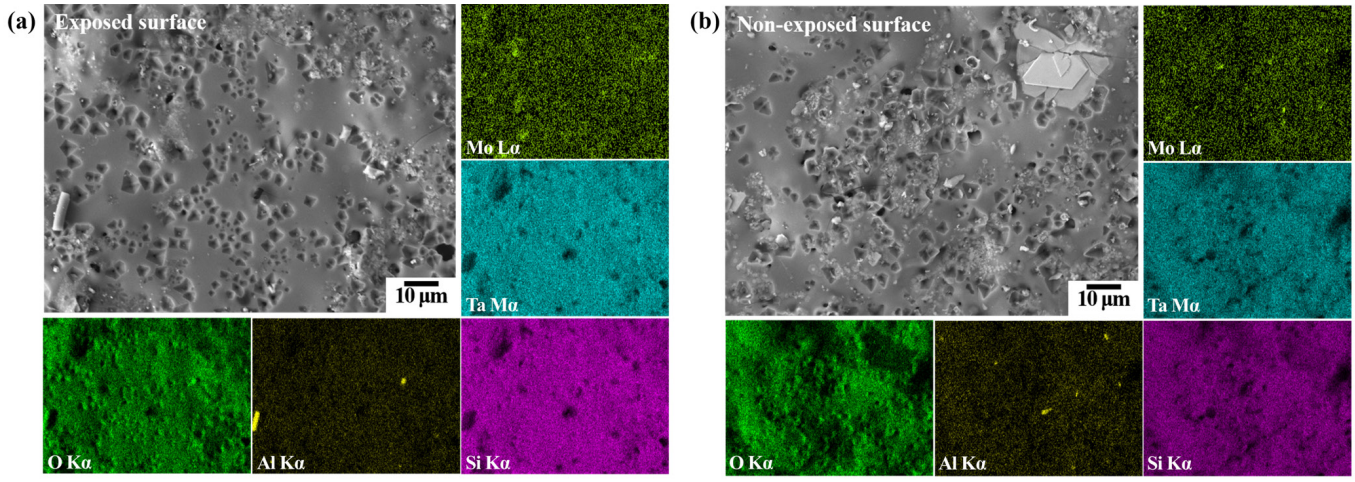

Fig. 7. Scanning electron microscopy–energy-dispersive X-ray spectroscopy results of coating surfaces of tested specimens. (a) High-velocity oxygen fuel flame–exposed surface, and (b) non-exposed surface.

Table 4. EDS point analysis results as average of five measurements of the coating surface shown in Figure 7

Elements	Exposed surface (wt.%)	Non-exposed surface (wt.%)
Mo	6.1	6.4
Ta	10.7	11.2
Si	33.8	31.3
Al	1.3	1.1
O	48.0	50.0

EDS, energy-dispersive X-ray spectroscopy.

처럼 HETC나 TUFI같은 표면과 침투 코팅 개념이 복합적으로 적용된 코팅층은 기존의 RCG와 달리 FOD로부터 취약한 문제를 해결하기 위해 개기공을 포함한 표면 미세구조를 갖도록 설계되었다[1, 11, 15]. 따라서 본 연구에 적용된 코팅 또한 표면에 개기공을 포함한 구조로 관찰되며 이는 추가로 노출되는 온도에 따라 치밀화 현상을 보일 수 있다. HVOF 시험 중 노출 표면은 화염 분사를 통한 직접적인 가열로 인해 가장 높은 온도에 노출되었고 비노출 표면은 화염에 직접적인 노출보단 표면 온도 상승에 따른 전도열에 의한 가열이 더 큰 영향을 미쳤을 것이며 더 낮은 온도에 도달했을 것이다. 이러한 온도 차이로 인해 표면에서 관찰되는 기공의 크기가 다르며 그림 7(a)의 표면이 더 높은 온도에 노출되어 치밀화 현상으로 인해 기공 크기가 감소하는 결과가 관찰된다.

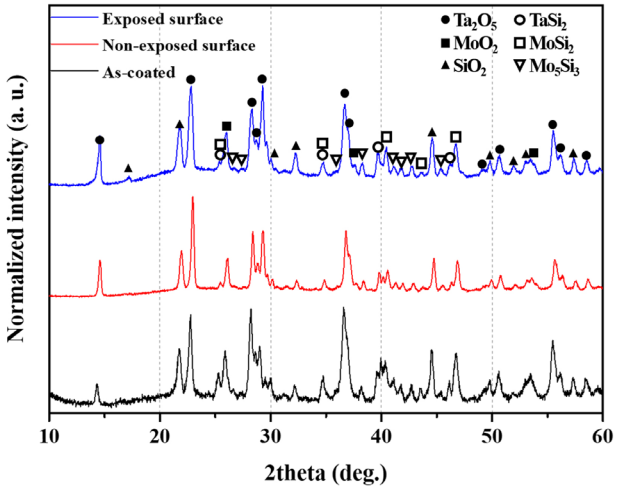

Fig. 8. X-ray diffraction patterns of as-coated and high-velocity oxygen fuel–tested specimens measured by the different locations of the coating surface.

그림 8은 평가 전후 시편 표면 코팅층의 평가전과 평가후 서로 다른 위치에 따른 XRD 측정 결과 그래프를 나타낸다. 평가전 표면과 평가후 노출 표면과 비노출 표면 모두 공통적인 산화물(Ta_2O_5, MoO_2, SiO_2)과 규화물($TaSi_2$, $MoSi_2$, Mo_5Si_3) 결정상이 관찰되며 화염 노출로 인해 특별히 다른 결정상이 나타나지 않음을 보이고 있다. 원료로 사용된 규화물 원료 대비 산화물 결정상이 관찰되는 현상은 코팅 직후 표면 XRD 결과에서도 비슷한 강도로 관찰된다. 특히 Tao et. al.에 따르면 $TaSi_2$ 결정상은 코팅 소재 내의 산소나 붕소 원료와 쉽게 반응하여 산화되기 때문에[16] 본 연구 결과에서 Ta_2O_5 결정상이 등장하는 산화 반응은 코팅 공정 중 대부분 발생하는 것으로 확인된다. 평가후 코팅층은 상대적으로 노출 표면에서 더 높은 산화물 결정상의 강도가 나타나고 있으며 특히 Ta_2O_5 와 SiO_2 결정상의 강도가 높게 증가한다. 화염 노출에 의한 고온 산화 분위기가 형성됨에 따라 코팅층에 포함된 $TaSi_2$ 결정상의 산화로 인하여 Ta_2O_5 와 SiO_2 결정상이 추가로 형성되어 더 높은 회절강도를 보이게 된다. 따라서 그림 4(b), (c)에서 관찰되는 노출 표면의 코팅층 색상 변화는 산화의 영향으로 확인된다. 하지만 그림 5에 나타난 시편의 표면 온도 변화는 동일한 열유속 환경의 지속적인 화염 노출에도 온도가 더 증가하지 않고 유지되거나 감소하는 경향을 보인다. 이로 인해 표면 코팅층의 일부 산화는 코팅의 방사율과 성능저하에 큰 영향을 미치지 않는 것으로 관찰된다. 따라서 제조한 시편은 진행된 모사환경 평가의 열유속 환경과 120 초 동안의 평가 진행 시간 동안 치명적인 성능 저하나 파손 없이 재사용 TPS로의 사용 가능성을 확인하였다.

4. Conclusion

본 연구에서는 재사용 TPS 개발을 위해 세라믹 섬유를 이용한 경량 고온 단열소재와 표면의 고방사율 유리 코팅을 제조하였다. 국내에서 수급 가능한 Al_2O_3-SiO_2 계 상용 세라믹 섬유와 유리형성제인 붕산을 이용하여 타일 형태로 제조하였고 균일한 형상을 갖는 단열소재 제조가 가능하였다. 제조된 단열소재는 표면에 고방사율 유리 코팅을 적용하여 마무리되었고 HVOF 모사 환경 평가에 노출되어 성능을 평가하였다. 모사 환경 평가는 HVOF 화염에 시편을 120 초 동안 노출시켜 진행되었고 IR pyrometer로 측정된 시편의 표면 온도는 평균 1100˚C 이상으로 나타났다. 평가 후 시편은 미세구조, EDS, XRD를 통해 분석하였고 HVOF 평가를 통한 높은 열유속 환경에 노출된 이후에도 시편의 파손이나 변형 등 품질 저하 없이 재사용 TPS로의 사용 가능성을 확인하였다.

Funding

본 연구는 한국항공우주연구원 2024년도 기본사업(출연금)과제 “극초음속 미래비행체 핵심기술 연구(1711170889)”로부터 연구비를 지원받아 수행되었으며 이에 감사드립니다.

Conflict of Interest

저자들은 이해상충관련 해당사항 없음을 선언합니다.

Data Availability Statement

Data will be made available on request.

Author Information and Contribution

남민수 : 박사과정 학생/논문 초안 작성, 실험디자인, 결과해석, 조사, 김종일 : 선임연구원/결과 해석, 조사, 논문 리뷰 및 편집, 신재성 : 선임연구원/결과 해석, 조사 김현준: 책임연구원/결과 해석, 조사 오범석 : 책임연구원/결과 해석, 조사, 김성원 : 수석연구원/실험 디자인, 결과 해석, 조사, 논문리뷰 및 편집, 연구책임자

Acknowledgement

None.

References

[1] S. M. Johnson: Thermal Protection Materials and Systems: An Overview in Engineered Ceramics (T. Ohji and M. Singh, eds.), John Wiley & Sons, Inc., Hoboken, New Jersey, USA, (2016) 224.
[2] D. W. Richerson: The Magic of Ceramics, (2nd ed.), John Wiley & Sons, Inc., Hoboken, New Jersey, (2012).

[3] M. J. Gasch, D. T. Ellerby and S, M. JohnsonL: Ultra High Temperature Ceramic Composites in Handbook of Ceramic Composites (N. P. Bansal, eds.), Springer, New York, (2005).
[4] S. Kim, J.-M. Chae, S.-M. Lee, Y.-S. Oh, H.-T. Kim, K.-J. Kim and S. Nahm: J. Powder Mater., **16** (2009) 442.
[5] J.-M. Chae, S.-M. Lee, Y.-S. Oh, H.-T. Kim, K.-J. Kim, S. Nahm and S. Kim: J. Korean Ceram. Soc., **47** (2010) 578.
[6] H. E. Goldstein: Fibrous Ceramic Insulation in Advanced Materials Technology, NASA Conference Publication, **2251** (1983).
[7] R. A. Frosch, D. B. Leiser, H. E. Goldstein and M. Smith: US Patent 4,148,962, (1979).
[8] V. Heng, B. Park, K. A. Hinkle, A. Viejo and M. A. Santos: US patent 2004/0033881 A1, (2004).
[9] D. A. Stewart and D. B. Leiser: US patent 7,314,648 B1, (2008).
[10] D. A. Stewart and D. B. Leiser: US patent, US patent 7,381,459 B1, (2008).
[11] D. A. Stewart, D. B. Leiser, R. R. DiFiore and V. W. Katvala: US patent 7,767,305 B1, (2010).
[12] S. Kim, M. S. Nam, Y. S. Oh, S. Nahm, J. S. Shin, H. J. Kim and B. S. Oh: J. Powder Mater., **29** (2022) 477.
[13] J. C. Fletcher, H. E. Goldstein, D. B. Leiser and V. W. Katvala: US Patent 4,093,771, (1978).
[14] H. E. Goldstein, D. B. Leiser and V. Katvala: Reaction Cured Borosilicate Glass Coating for Low Density Fibrous Silica Insulation in Borate Glasses: Structure, Properties, Applications, Plenum Publishing Corp., (1978) 623.
[15] D. B. Leiser, M. Smith, R. A. Churchward and V. W. Katvala: US patent 5,079,082, (1992).
[16] X. Tao, Z. Liang, J. Li, J. Zhang, X. Guo and M. Wang: Ceram. Int., **48** (2022) 37333.

Research Article

pISSN 2799-8525 · eISSN 2799-8681
J Powder Mater 2024;31(6):530-536

Journal of Powder Materials

습식법으로 제조된 BN 계면을 가진 SiC_f/SiC 복합재의 제조

김경호, 한윤수*

한국세라믹기술원 이천분원

Fabrication of SiC_f/SiC Composites with a BN Interphase Prepared by the Wet Method

Kyung Ho Kim, Yoonsoo Han*

Korea Institute of Ceramic Engineering and Technology (Icheon), Gyeonggi-do 17303, Republic of Korea

This study presents a cost-effective wet chemical coating process for fabricating a boron nitride (BN) interphase on silicon carbide (SiC) fibers, increasing the oxidation resistance and performance of SiC_f/SiC ceramic matrix composites. Using urea as a precursor, optimal nitriding conditions were determined by adjusting the composition, concentration, and immersion time. X-ray diffraction analysis revealed distinct BN phase formation at 1300°C and 1500°C, while a mixture of BN and B_2O_3 was observed at 1200°C. HF treatment improved coating uniformity by removing SiO_2 layers formed during the de-sizing process. Optimization of the boric acid-to-urea molar ratio resulted in a uniform, 130-nm-thick BN layer. This study demonstrates that the wet coating process offers a viable and economical alternative to chemical vapor deposition for fabricating high-performance BN interphases in SiC_f/SiC composites that are suitable for high-temperature applications.

Keywords: BN; interphase; Wet chemical coating; Composites

Received: October 29, 2024
Revised: December 4, 2024
Accepted: December 4, 2024

***Corresponding author:**
Yoonsoo Han
E-mail: corundum69@kicet.re.kr

1. Introduction

첨단 산업 분야에서의 기술 발전은 고온, 고압 등의 극한 환경에서도 성능을 유지할 수 있는 새로운 소재의 필요성을 지속적으로 증가시키고 있다. Ceramic Matrix Composites (CMCs)는 이러한 요구를 충족하기 위한 핵심 소재로 주목받고 있다. 특히 CMCs는 초내열 합금에 비해 30%정도로 경량성이 뛰어나며, 우수한 내열성, 내산화성, 내크립성을 제공하여, 가스터빈, 항공 엔진, 자동차 부품과 같은 고온 작업 환경에서 높은 성능을 발휘한다. 이로 인해 항공우주, 에너지, 방위산업 등에서 CMCs의 응용 가능성이 급격히 확대되고 있다[1-3]. CMCs의 성능을 결정짓는 중요한 요소 중 하나는 섬유상(fiber)과 기지상(matrix) 사이의 계면(interphase)이다. CMCs는 본질적으로 섬유상 재료와 기지상 재료가 복합적으로 결합된 구조를 가지며, 섬유는 높은 인장강도를 통해 복합재의 기계적 성능을 보강한다[4, 5]. 하지만 섬유상과 기지상 간의 결합력이 지나치게 강하면, 기지에서 발생한 균열이 섬유로 직접적으로 전파되어 섬유 손상을 유발하고, 결과적으로 복합재의 파괴로 이어질 수 있다[6, 7]. 따라서, 섬유상과 기지상 사이에 약한 계면을 형성하여 균열이 섬유로 직접 전달되지 않도록 하는 계면(interphase)의 buffer 역할이 매우 중요하다. 계면은 섬유가 파괴되지 않고 효과적으로 기능할 수 있도록 보호하며, 섬유상과 기지상 간의 결합 강도를 적절히 조절하여 균열의 우회를 유도한다 [8-11]. 이로 인해 CMCs의 내구성이 크게 향상되며, 계면은 열충격, 산화, 기계적 응력 등 다양한 외부 환경으로부터 섬유를 보호하는 중요한 역할을 한다. 현재 CMCs 제조에 사용되는 대표적인 계면의 재료로는 Pyrolytic carbon (PyC)와 Boron nitride (BN)가 있다[12-14]. 특히 BN은 높은 내열성과 산화 저항성을 바탕으로 항공우주와 같은 고온 환경에서의 적용에 매우 적합한 재료로 알려져 있다. BN 계면은 주로 Chemical vapor deposition (CVD)법을 통해 제

https://doi.org/10.4150/jpm.2024.00339

조된다[15, 16]. CVD법은 고온에서 전구체 가스를 사용해 균일한 BN 코팅층을 형성할 수 있지만, 고가의 장비와 전구체 사용, 그리고 복잡한 공정으로 인해 상업적 적용에는 한계가 있다. 이를 극복하기 위해 최근에는 보다 저렴하고 간단한 습식 화학 코팅법이 주목받고 있으며, 이는 기존의 CVD 방식보다 비용 효율적이며 안전한 공정을 제공한다. 그러나 습식 코팅법의 경우, 코팅층의 균일성과 두께 조절이 중요한 도전 과제로 남아 있으며, 이러한 문제를 해결하기 위한 다양한 연구가 진행 중이다[17–20].

본 연구에서는 비용 효율적이고 공정이 간단한 습식 화학 코팅법을 이용해 SiC_f/SiC 복합재에 BN 계면을 형성하는 기술을 개발하고자 하였다. CVD 방식에 비해 상대적으로 저비용의 공정임에도 불구하고, 고성능의 계면을 구현할 수 있는 방법을 모색하는 데 중점을 두었다. 특히, 습식법을 통해 BN계면을 형성할 경우 코팅층의 균일성과 두께 제어가 중요한 과제로 제기되므로, 이를 해결하기 위해 다양한 공정 조건을 설정하고 평가하였다. BN 계면을 형성하기 위해 Boric acid와 Urea를 전구체로 사용하였으며, 이를 기반으로 최적의 질화 조건을 도출하였다. 구체적으로, Boric acid와 Urea의 비율, 전구체 용액의 농도, 침지 시간 등 주요 변수를 체계적으로 조절하여, 최적의 코팅 성능을 확보하고자 하였다.

2. Experimental Section

코팅 작업에 앞서, SiC fabric에 포함된 sizing agent를 제거하는 탈사이징(de-sizing) 처리를 진행하였다. 이 과정은 약 1000˚C에서 2시간 동안 진행되었으며, 열처리 과정에서 SiC 섬유 표면에 SiO_2막이 형성되었다. 이 SiO_2막은 hydrogen fluoride (HF) 용액을 사용하여 제거하였다. HF는 0.1 mol/L 농도로 준비되었으며, SiC fabric을 30초간 담가 산화막을 제거하였다. SiO_2 막을 제거한 후, SiC fabric에 BN 계면 코팅을 적용하기 위한 습식 코팅 공정을 진행하였다. 전구체 용액은 Boric acid (H_3BO_3, ≥99.5%, Sigma-Aldrich, USA)와 Urea (CH_4N_2O, 99.0-100.5%, Sigma-Aldrich, USA)를 혼합하여 제조하였으며, 메탄올과 증류수를 3:1의 부피비로 혼합한 용매를 사용하였다. 전구체로 사용된 Boric acid와 Urea의 몰비는 2:1, 3:1, 4:1로 각각 설정하였으며, 전구체 용액의 농도는 0.5 mol/L와 2 mol/L로 준비하였다. (표1) 이를 위해 Boric acid 와 Urea를 50˚C에서 가열하면서 교반기로 용매에 완전히 용해시키는 과정을 거쳤다.

코팅 공정은 SiC fabric을 준비된 전구체 용액에 약 10분간 담가 균일하게 코팅이 이루어지도록 하였다. 이 과정에서 코팅층의 두께와 균일성을 확보하기 위해, 용액 내에서 SiC fabric을 일정한 시간 동안 담그고 서서히 꺼내는 방식을 사용하였다. 코팅이 완료된 SiC fabric은 80˚C의 오븐에서 2시간 이상 건조시켜 남아 있는 용매를 제거하고, 전구체가 섬유 표면에 안정적으로 부착되도록 하였다. 질화처리는 알루미나 튜브로에서 H_2 4%-N_2 96% 혼합가스가 1 L/min의 유량으로 공급되었다. BN상 합성을 위해 5˚C /min의 승온 속도로 1200˚C, 1300˚C, 1500˚C에서 진행되었으며, 이후 1300˚C에서 10, 15, 20시간으로 유지 시간의 변화를 주어 XRD (D/MAX2500VL/PC, Rigaku, Japan, at 40 kV, 100 Ma from 10-80˚)분석을 이용하여 BN상 합성을 확인하였다. 이후 최적 조건을 선택하여 질화 처리를 완료하였다. 마지막으로, BN 코팅층의 균일도와 두께를 확인하기 위해 FE-SEM (JSM6701F, JEOL, Japan)을 사용하여 SiC 섬유의 표면 미세구조를 분석하였다.

3. Results and Discussion

BN 상 합성이 이루어지는 최적의 온도를 확인하기 위해 1200˚C, 1300˚C, 1500˚C에서 실험을 진행하였다. 그림 1에 나타난 XRD 분석 결과에 따르면, 1500˚C와 1300˚C에서 BN 상이 명확하게 형성된 반면, 1200˚C에서는 BN과 B_2O_3가 혼합된 상이 관찰되었다. 이는 1200˚C에서는 열처리 온도가 낮아 BN 상이 완전히 형성되지 못하고, B_2O_3가 잔존함을 의미한다. 이와 같은 결과는 BN 상의 형성을 위해 최소한 1300˚C 이상의 고온이 필요함을 시사한다.

또한, 열처리 시간에 따른 BN 상 형성의 영향을 조사하기 위해, 1300˚C에서 10시간, 15시간, 20시간의 열처리 조건을 적용한 결과, 10시간과 15시간 동안의 열처리에서는 BN 상의 형성된 것으로 나타났다(그림 2). 그러나 1300˚C 이상의 온도에서도 여전히 B_2O_3 상이 주로 관찰되었으며, 이는 22˚의 회절 각(2θ)에서 나타난 넓은 피크에 의해 확인되었다. 이는 비정질 형태의 B_2O_3가 존재함을 시사하며, BN으로 완전히 합성되지 않은 중간 상의 B_2O_3가 비정질 상태로 존재하고 있으며, 동시에 BN 결정 상이 일부 형성되었음을 의미하기도 한다. 이와 같은 결과는 열처리 시간이 길어질수록 BN 상이 보다 명확하게 형성되지만, 1300˚C 이상의 고온에서도 B_2O_3가 완전히 제거되지 않고 일부 남아있을 수 있음을 시사한다. 이를 통해 BN 상 합성을 위해서는 적절한 열처리 시간과 온도를 동시에 최적화해야 할 필요성이 있음을 알 수 있다.

실제 복합재 제조 공정에서 전구체를 섬유 표면에 코팅한 경우, 코팅 두께는 일반적으로 수십 나노미터 수준에 불과하므로 B_2O_3가 BN으로 완전히 변환될 가능성이 크다[21]. 이러한 결과는 복합재의 성능을 극대화하기 위해 BN 상 형성과 중간 상 변환이 열처리 온도 및 시간에 크게 의존함을 보여주며, 향후 복합재 제조 공정에

Table 1. Ratio of boric acid to urea in the precursor and the precursor concentration

Condition	Composition (Boric acid : Urea)	Concentration
1	2:1	0.5 mol/L
2	2:1	2 mol/L
3	3:1	0.5 mol/L
4	3:1	2 mol/L
5	4:1	0.5 mol/L
6	4:1	2 mol/L

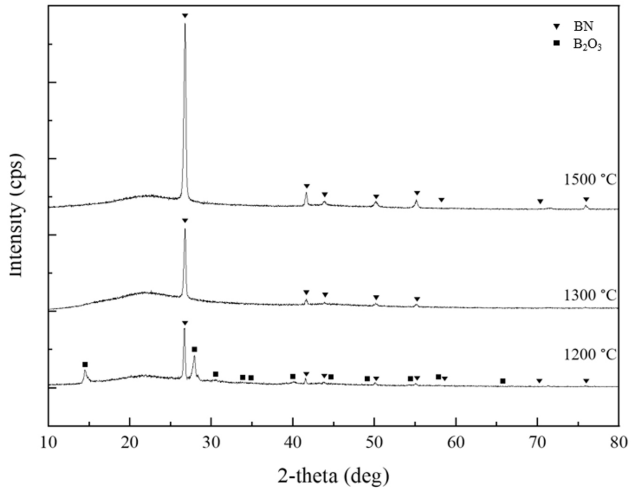

Fig. 1. X-ray diffraction peak of BN phase formation according to the temperature of heat treatment.

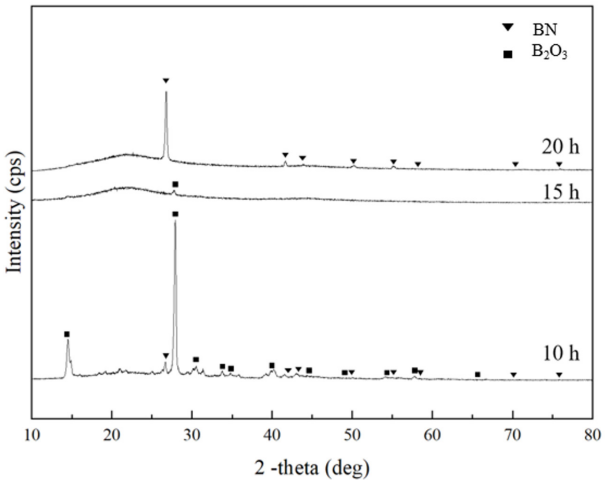

Fig. 2. X-ray diffraction peak of BN phase formation according to the holding time of heat treatment.

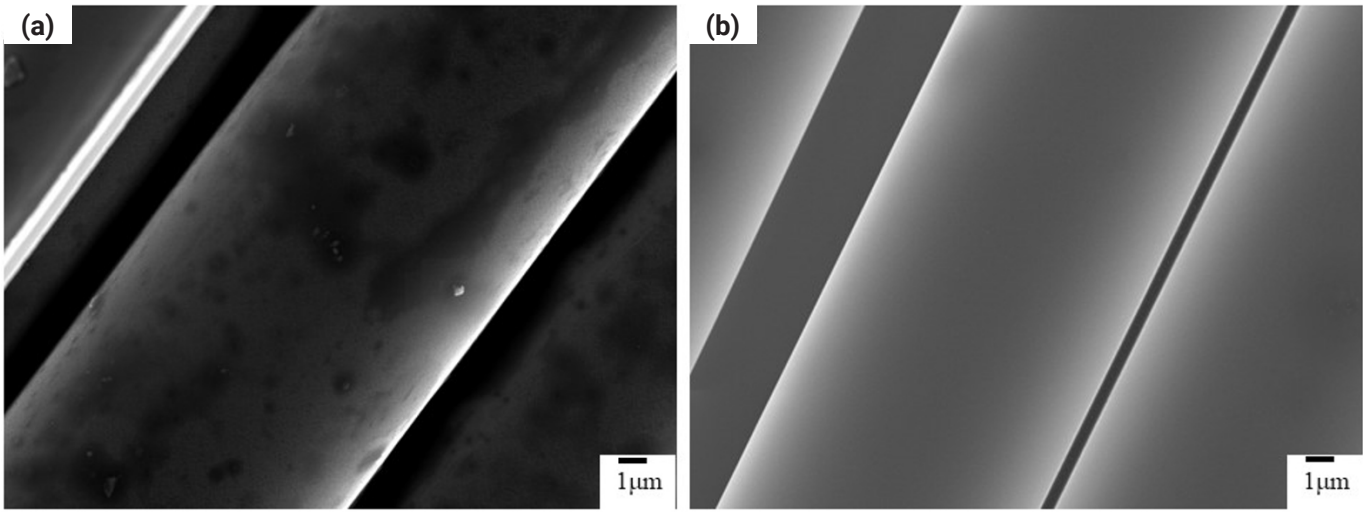

Fig. 3. Surface image of a silicon carbide fiber: (a) before de-sizing, (b) after de-sizing.

서 최적의 조건을 도출하는 데 중요한 기준을 제공한다.

SiC 섬유는 섬유 간의 결합력과 접착력을 강화하기 위해 제조 과정에서 sizing agent 가 도포되어 있다(그림 3(a)). 이러한 sizing agent 로 인해 다양한 불순물과 불필요한 물질들이 섬유 표면에 존재하게 된다. 이 불순물들은 코팅 공정에 영향을 미칠 수 있기 때문에, 코팅을 진행하기 전에 불순물을 제거하는 de-sizing 공정이 필수적이다. 그림 3(b)는 de-sizing이 진행된 후 불순물과 불필요한 물질이 제거된 깨끗한 표면을 보여준다. 그러나 SiC 섬유는 de-sizing 공정 중 산화 분위기에서 열처리를 받는 동안 공기 중에 노출되어 SiO_2 산화막이 쉽게 형성되는 경향이 있다. 이처럼 SiO_2 막이 표면에 존재할 경우 균일한 코팅 형성을 저해하여, 코팅막이 불 균일하게 형성될 수 있는 문제를 야기한다(그림 4). 이를 해결하기 위해, de-sizing 공정 후 HF용액을 사용하여 SiO_2 막을 제거하는 추가적인 표면 처리를 진행하였다. HF 처리는 0.1 mol/L 농도의 용액을 사용하여 30초간 SiC 섬유를 담그는 방식으로 수행되었으며, 이를 통해 SiO_2 막을 효과적으로 제거할 수 있었다. 이후 HF 처리된 SiC 섬유는 미리 준비된 Boric acid : Urea 용액에 담가 10분간 습식 코팅을 진행하였다.

그림 5는 HF 처리 후 SiC fabric에 전구체를 적용한 후의 BN 계면 코팅 결과를 보여준다. Boric acid 와 Urea의 비율에 따른 코팅 특성을 관찰하기 위해, 표 1에 정리된 바와 같이 Boric acid 와 Urea의 몰비를 2:1, 3:1, 4:1로 설정하였다. 모든 전구체 용액의 농도는 2 mol/L로 고정하여 제조하였으며, 코팅 후 질화처리를 진행하였다. Boric acid의 비율이 증가함에 따라(2:1, 3:1, 4:1) 그림 5

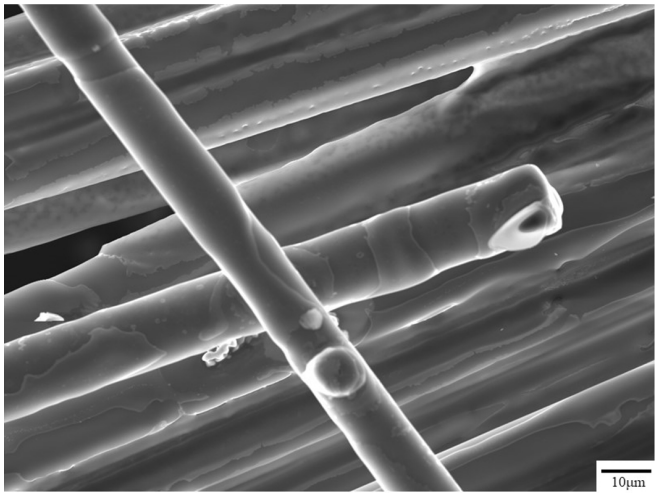

Fig. 4. SiC_f/BN interphase without removing the SiO_2 oxide film; boric acid-to-urea ratio 3:1, concentration 2 mol/L.

에서 확인할 수 있듯이, 세 가지 조건 모두에서 과도한 코팅 층이 형성되고 유사한 코팅 구조가 관찰되었다. 이는 전구체 용액의 농도(2 mol/L)와 깊은 관련이 있는 결과로 보인다. 2 mol/L라는 높은 농도는 Boric acid와 Urea 간의 반응을 섬유 표면에서 과도하게 촉진시켜, BN 코팅 두께가 일정 수준 이상으로 성장하게 만든 것으로 해석된다. 또한, 높은 농도는 전구체 용액 내에서 과포화 상태를 유발해 섬유 표면에서 BN 입자가 고르게 분산되지 못하고 응집되는 원인이 되었다. 특히, 2 mol/L 농도에서는 섬유 간 결합 부위와 표면에서 국소적으로 과도한 반응이 유발되며, 균일한 코팅 대신 불균일한 두께와 아일랜드 형태의 입자 응집이 발생하였다. 일부 영역에서는 과도한 액상이 잔존하였으며, 섬유 표면에서 균일하지 않은 두께와 함께 아일랜드 형태의 입자 성장이 뚜렷하게 관찰되었다. 이는 2 mol/L 농도의 전구체 용액이 과도한 농도로 인해 균일한 코팅층을 형성한 이후에도 잔류 반응물이 고르게 분산되지 못하고 응집되어 추가적인 입자 성장이 유발된 결과로 해석된다.

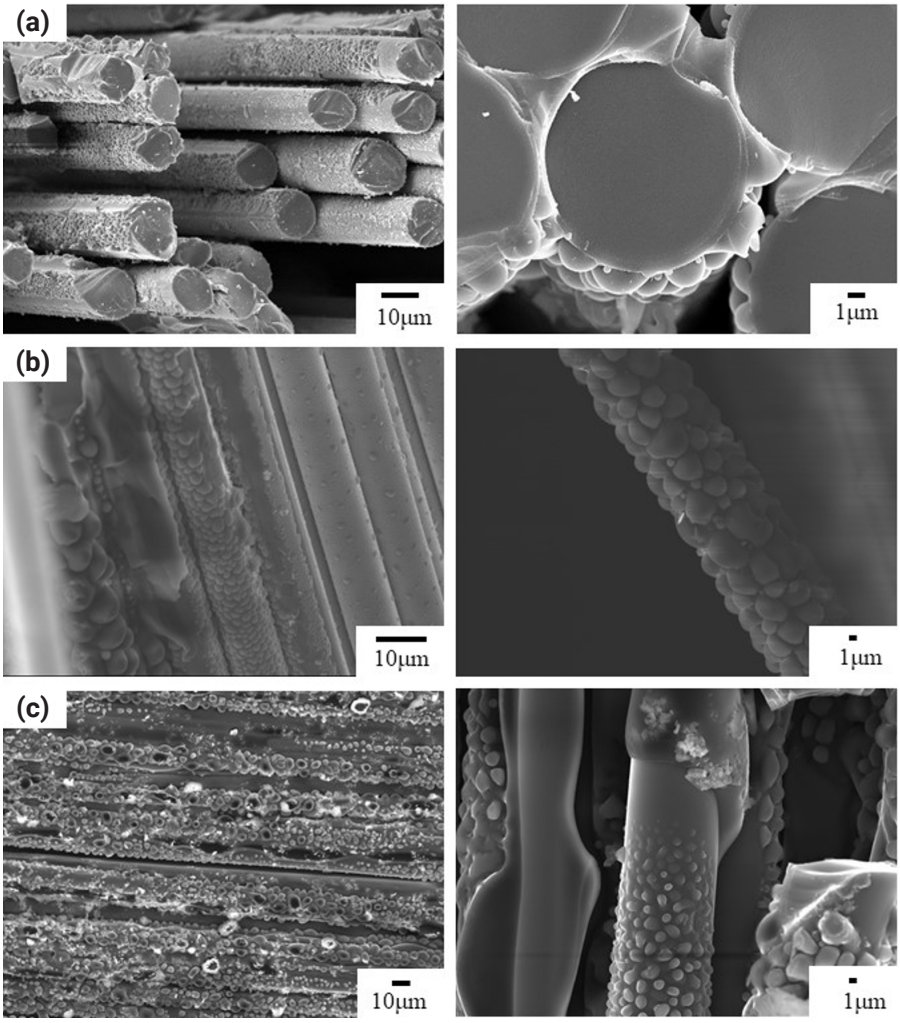

Fig. 5. Coating changes of BN on silicon carbide fibers as a function of the ratio of boric acid to urea in the precursor solution (a) condition 2, 2:1, 2 mol/L; (b) condition 4, 3:1, 2 mol/L; (c) condition 6, 4:1, 2 mol/L.

따라서 전구체 농도가 코팅 반응의 균일성과 두께 제어에 중요한 역할을 하며, 2 mol/L 이상의 높은 농도는 오히려 비효율적인 코팅 구조를 초래할 수 있음을 보여준다.

반면, 그림 4와 동일한 조건에서 진행된 그림 5(b)와 비교해 보면, 그림 4에서는 부분적으로 코팅이 진행된 반면, 그림 5(b)에서는 전체적으로 코팅층이 형성된 것을 확인할 수 있다. 이러한 차이는 HF 처리를 통해 SiO_2 산화막을 제거한 결과, SiC 섬유 표면의 젖음성(wettability)이 개선되었기 때문으로 해석된다. SiO_2 산화막은 전구체 용액의 확산과 섬유 표면에서의 반응성을 저하시켜 불균일한 코팅을 초래할 수 있지만 HF 처리를 통해 산화막이 제거되면서 전구체 용액이 섬유 표면에 고르게 분산되고 균일한 코팅이 유도된 것으로 보인다. 이러한 결과는 HF를 이용한 SiO_2 산화막 제거가 SiC 섬유 코팅 공정에서 균일성과 품질을 확보하는 데 매우 효과적인 방법임을 보여준다.

그림 6은 BN 계면 코팅 공정에서 Boric acid와 Urea의 비율을 2:1, 3:1, 4:1로 설정하고, 전구체 농도를 0.5 mol/L로 조절한 후 SiC fabric의 미세구조를 관찰한 결과를 보여준다. 그림 6(c)에 나타난 바와 같이, 전구체 농도를 0.5 mol/L로 낮췄음에도 불구하고, 표 1의 condition 5에 해당하는 경우, 여전히 2 mol/L 농도에서 관찰된 것과 유사한 형태의 두꺼운 코팅 층과 비정상적으로 성장한 입자 구조가 확인되었다. 이는 전구체 농도를 낮추는 것만으로는 과도한 코팅 형성을 효과적으로 억제하기 어렵다는 것을 보여준다. 반면, 표 1의 condition 1에서는 condition 5와는 완전히 다른 결과가 관찰되었다. 섬유 표면 전체에 균일한 코팅이 형성되지 않고, 국부적으로 물방울 형태의 비균일한 코팅이 분포하였다(그림 6(a)). 이는 전구체 용액이 섬유 표면에 충분히 퍼지지 못하고, 특정 위치에서만 코팅 반응이 진행되었음을 나타낸다. 이는 전구체 용액의 점도, 표면 장력, 또는 코팅 공정 조건이 섬유 표면과의 상호작용에 영향을 미친 결과로 해석된다. 마지막으로 표 1의 condition 3에서는 condition 1과 condition 5에서 나타난 비균일한 양상과

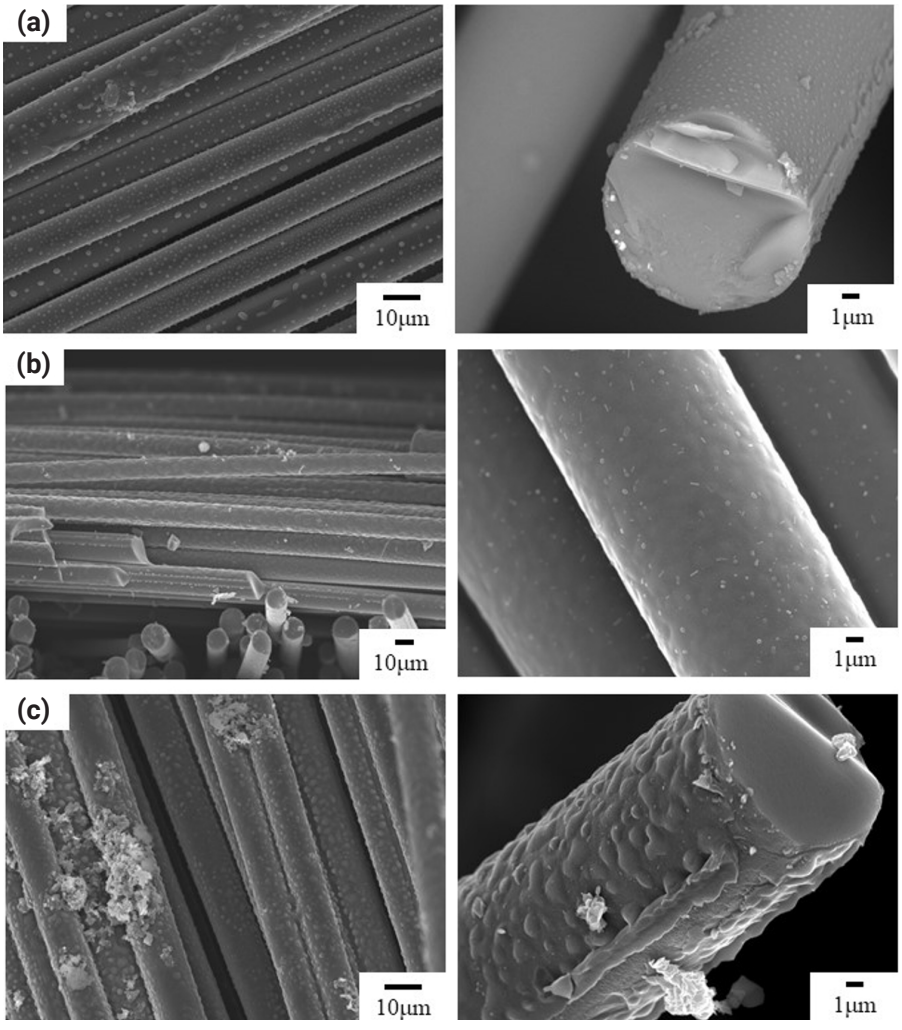

Fig. 6. Coating changes of BN on silicon carbide fibers as a function of the ratio of boric acid to urea in the precursor solution (a) condition 1, 2:1, 0.5 mol/L; (b) condition 3, 3:1, 0.5 mol/L; (c) condition 5, 4:1, 0.5 mol/L.

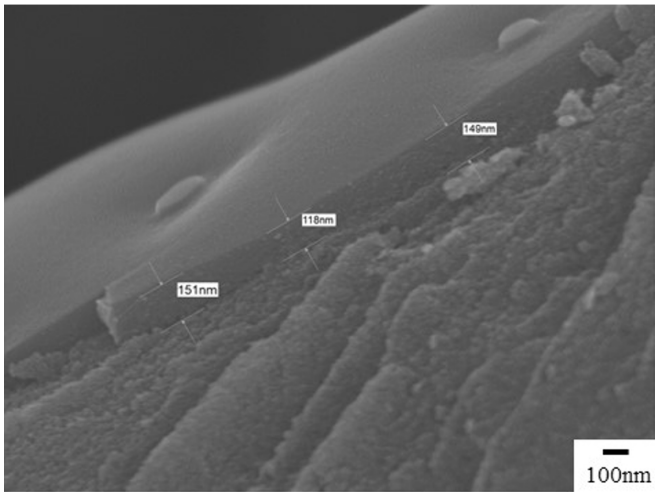

Fig. 7. Coating thickness of BN on silicon carbide fibers according to the precursor composition and concentration: boric acid-to-urea ratio 3:1, concentration 0.5 mol/L.

달리, 섬유 표면 전체에 걸쳐 비교적 균일하고 매끄러운 코팅이 형성되었다(그림 6(b)). 이러한 결과는 Boric acid와 Urea의 비율을 조정함으로써 전구체의 확산성과 반응 균일성을 개선할 수 있음을 보여준다.

기존 carbon 섬유에 BN 계면 코팅을 진행한 연구와는 다르게 본 연구에서는 Boric acid 와 Urea의 비율을 조절하고 전구체의 농도를 줄였음에도 불구하고, 한 번의 Dip 코팅 공정만으로도 탄소 섬유에 비해 더 두꺼운 약 130 nm의 BN코팅층을 형성할 수 있었다(그림 7). 이는 기존 CVD 방식보다 상대적으로 간단한 습식 코팅 공정을 통해 두꺼운 BN 계면 코팅층을 형성할 수 있음을 보여준다. 이러한 결과는, BN 계면 코팅을 형성하는 새로운 방법으로 습식 공정이 충분히 실용적일 수 있음을 보여주며, 고온 산화 환경에서의 성능 향상을 위한 신규 코팅 기술의 가능성을 제시한다.

4. Conclusion

본 연구에서는 SiC 섬유에 BN 계면 코팅을 적용하여 고온 산화 저항성을 개선하고, 복합재의 성능을 극대화하기 위한 습식 코팅 공정을 제안하였다. 실험을 통해 Boric acid 과 Urea를 전구체로 사용하여 다양한 농도와 몰비를 조절한 코팅 조건을 평가하였다.

BN 상의 합성 온도 최적화 실험을 통해 1300˚C 이상의 온도에서 BN 상이 명확하게 형성됨을 확인하였며, 1200˚C에서는 BN 상과 함께 B_2O_3가 혼합된 상이 관찰되었다. BN 상을 안정적으로 형성하기 위해서는 1500˚C에서 가장 좋은 결과를 얻을 수 있었다. 이는 BN 상의 형성을 위해 적절한 열처리 온도가 필요함을 시사한다. 또한, 질화처리 시간과 온도에 따른 상 변화 실험에서 1300˚C에서 10시간, 15시간, 20시간의 질화처리 조건을 적용한 결과, 15시간 이상의 처리 시간에서 안정적인 BN 상이 형성되었음을 확인하였다. 하지만 여전히 일부 B_2O_3 상이 잔존하였으며, 이는 질화처리 시간이 열처리 결과에 중요한 변수임을 의미한다.

SiC 섬유 표면의 SiO_2 산화막을 제거하기 위해 HF 처리를 적용한 결과, 코팅층의 균일성이 크게 개선되었다. SiO_2 산화막을 제거함으로써 SiC 섬유 표면의 젖음성이 향상되었고, 이를 통해 균일한 BN 코팅층을 형성할 수 있었다. 이는 SiO_2 산화막 제거가 습식 코팅 공정의 필수적인 단계임을 확인시켜 주었다.

Boric acid와 Urea의 몰비 및 전구체 농도를 조절한 결과, 전구체 농도를 0.5 mol/L로 낮추는 것이 균일한 코팅층을 형성하는 데 유리하였다. 특히, 2:1, 3:1, 4:1의 Boric acid 와Urea 몰비를 조절한 실험에서, 전구체 농도와 몰비가 과도하지 않으면 아일랜드 형태의 입자 성장 없이 균일한 코팅층을 형성할 수 있음을 확인하였다. 이를 통해 기존 본 연구에서 제시한 습식 코팅 공정은 상대적으로 간단한 공정으로도 약 130 nm의 BN 계면 코팅층을 형성할 수 있었다.

결론적으로, 본 연구에서는 CVD에 비해 공정이 간단한 습식 화학 코팅법을 통해 SiC 섬유에 BN 계면을 성공적으로 형성할 수 있음을 확인하였다. 특히, 전구체 농도와 Boric acid 와Urea 몰비 조절, SiO_2 산화막 제거 등의 변수를 최적화함으로써 균일하고 두꺼운 BN 코팅층을 형성할 수 있었으며, 이는 복합재의 고온 성능을 크게 향상시킬 수 있는 기술적 가능성을 제시하였다. 향후 연구에서는 이 공정을 다양한 고온 환경에 적용하여 실질적인 성능 향상 효과를 검증하는 것이 필요하다.

Funding

이 연구는 2024년도 산업통상자원부 및 산업기술평가관리원(KEIT) 연구비 지원에 의한 연구임(RS-2023-00259942).

Conflict of Interest

The authors declare no conflicts of interest relevant to this article.

Data Availability Statement

The datasets generated and/or analyzed during the current study are not publicly available due to [reason, e.g., privacy, confidentiality] but are available from the corresponding author upon reasonable request.

Author Information and Contribution

김경호: 박사; conceptualization, writing–original draft
한윤수: 박사; writing–original draft, funding acquisition, supervision

Acknowledgement

None.

References

[1] R. Naslain: Compos. Sci. Technol., **64** (2004) 155.
[2] W. Krenkel and F. Berndt: Mat. Sci. Eng. A, **412** (2005) 177.
[3] K. Wei, R. He, X. Cheng, R. Zhang, Y. Pei and D. Fang: Mater. Des., **66** (2015) 552.
[4] N. A. Nasiri, N. Patra, N. Ni, D. D. Jayaseelan and W. E. Lee: J. Eur. Ceram. Soc., **36** (2016) 3293.
[5] L. Longbiao: Theor. Appl. Fract. Mech., **92** (2017) 24.
[6] N. P. Bansal and J. Lamon, Ceramic Matrix Composites: Materials, Modeling and Technology, John Wiley & Sons, (2014).
[7] V. Bheemreddy, K. Chandrashekhara, L. R. Dharani and G. E. Hilmas: Comput. Mater. Sci., **79** (2013) 663.
[8] N. Chandra: Composites, Part A, **33** (2002) 1433.
[9] S. Bahl: Mater. Today Proc., **39** (2021) 317.
[10] J.-K. Kim and Y.W. Mai: Engineered Interfaces in Fiber Reinforced Composites, (1998) 401.
[11] H. Ohnabe, S. Masaki, M. Onozuka, K. Miyahara and T. Sasa: Composites, Part A, **30** (1999) 489.
[12] M. Ghanbarian, E. Taheri Nassaj and A. Kariminejad: Surf. Coat. Technol., **288** (2016) 185.
[13] L. Li, Interface of Ceramic-Matrix Composites: Design, Characterization, and Damage Effects, John Wiley & Sons, (2020).
[14] D. Mandelli, I. Leven, O. Hod and M. Urbakh: Sci. Rep., **7** (2017) 10851.
[15] R. R. Naslain: Kompozyty(Composites), **5** (2005) 3.
[16] M. B. Ruggles-Wrenn, D. T. Christensen, A. L. Chamberlain, J. E. Lane and T. S. Cook: Compos. Sci. Technol., **71** (2011) 190.
[17] J. Liu, S. Wang, P. Li, M. Feng and X. Yang: Surf. Coat. Technol., **286** (2016) 57.
[18] H. Liu and H. Tian: J. Eur. Ceram. Soc., **32** (2012) 2505.
[19] D. Ding, W. Zhou, F. Luo, M. Chen and D. Zhu: Mater. Sci. Eng. A, **543** (2012) 1.
[20] Y. Mu, W. Zhou, F. Luo and D. Zhu: Ceram. Int., **40** (2014) 3411.
[21] N. S. Jacobson, D. S. Fox and E. J. Opilab: Pure Appl. Chem., **70** (1998) 493.

Research Article

pISSN 2799-8525 · eISSN 2799-8681
J Powder Mater 2024;31(6):537-545

Journal of Powder Materials

Hot-Cracking Behaviors in $(CoNi)_{85}Mo_{15}$ Medium-Entropy Alloys Manufactured via Powder Bed Fusion

Seungjin Nam[1], Heechan Jung[1], Haeum Park[2,3], Chahee Jung[1], Jeong Min Park[3], Hyoung Seop Kim[4,5,6,7,8], Seok Su Sohn[1,2,*]

[1]Department of Materials Science and Engineering, Korea University, Seoul 02841, Republic of Korea
[2]Department of Advanced Future Convergence Materials, Korea University, Seoul 02841, Republic of Korea
[3]Department of 3D Printing Materials, Korea Institute of Materials Science (KIMS), Changwon 51508, Republic of Korea
[4]Department of Materials Science and Engineering, Pohang University of Science and Technology, Pohang 37673, Republic of Korea
[5]Graduate Institute of Ferrous and Eco Materials Technology, Pohang University of Science and Technology, Pohang 37673, Republic of Korea
[6]Center for Heterogenic Metal Additive Manufacturing, Pohang University of Science and Technology, Pohang 37673, Republic of Korea
[7]Advanced Institute for Materials Research (WPI-AIMR), Tohoku University, Sendai 980-8577, Japan
[8]Institute for Convergence Research and Education in Advanced Technology, Yonsei University, Seoul 03722, Republic of Korea

Additive manufacturing makes it possible to improve the mechanical properties of alloys through segregation engineering of specific alloying elements into the dislocation cell structure. In this study, we investigated the mechanical and microstructural characteristics of CoNi-based medium-entropy alloys (MEAs), including the refractory alloying element Mo with a large atomic radius, manufactured via laser-powder bed fusion (L-PBF). In an analysis of the printability depending on the processing parameters, we achieved a high compressive yield strength up to 653 MPa in L-PBF for $(CoNi)_{85}Mo_{15}$ MEAs. However, severe residual stress remained at high-angle grain boundaries, and a brittle μ phase was precipitated at Mo-segregated dislocation cells. These resulted in hot-cracking behaviors in $(CoNi)_{85}Mo_{15}$ MEAs during L-PBF. These findings highlight the need for further research to adjust the Mo content and processing techniques to mitigate cracking behaviors in L-PBF-manufactured $(CoNi)_{85}Mo_{15}$ MEAs.

Keywords: Powder bed fusion; Medium-entropy alloys; Hot-cracking; Dislocation cells; Mo segregation

Received: August 20, 2024
Revised: November 6, 2024
Accepted: November 21, 2024

***Corresponding author:**
Seok Su Sohn
TEL: +82-2-3290-3271
FAX: +82-2-928-3584
E-mail: sssohn@korea.ac.kr

1. Introduction

Since the concept of high-/medium-entropy alloys (H/MEAs) has been suggested, metallic materials have been allowed to open a new chapter with the freedom in compositional tailoring from multiple principal alloying elements [1, 2]. Based on CrCoFeNiMn [3] and CrCoNi [4] alloys, which exhibit a single solid-solution phase with a face-centered cubic (FCC) structure, various alloy systems have been explored through compositional tailoring and adding alloying elements, such as Al, Ti, and Si. This approach overcomes the limitation in mechanical properties of conventional alloys by strengthening the contribution of second-phase precipitation (i.e., $L1_2$, Sigma, Laves phases) [5–7]. Furthermore, understanding the specific roles of each alloying element enables a more systematic selection and addition of alloying elements to improve material properties. In this aspect, the addition of alloying elements with larger atomic radius has been proposed to induce severe lattice distortion into alloys, resulting in the significant effects of not only solid-solution hardening but also grain-boundaries strengthening due to increasing atomic size differences [8–10]. For instance, VCoNi MEAs have been reported to exhibit yield strength of near 1 GPa with exceptional ductility of 38% through the increase in atomic bond distance fluctuation caused by V addition [8]. Recent research has investigated the impact of adding the refractory element Mo [9]; Mo atom tended to segregate at grain boundaries in CoNi-Mo-based MEAs owing to the large difference in atomic radius, leading to the excellent properties due to the high Hall-

https://doi.org/10.4150/jpm.2024.00262

Petch coefficient [11].

On the other hand, HEAs and MEAs have inherent cost issues because of the high prices of alloying elements. In order to reduce the losses caused by subtractive manufacturing, research has focused on laser-based additive manufacturing (AM), including laser-powder bed fusion (L-PBF) and laser-direct energy deposition (L-DED). AM offers significant advancements in near-net shape production as well as microstructural aspects and resultant mechanical properties [12–16]. For instance, AMed CrCoNi MEAs [17, 18] and CrCoFeNiMn HEAs [19–22] have overcome their inherent weakness of relatively low yield strengths through the formation of refined dislocation cells. Moreover, adding Si into CrCoNi MEAs successfully enhanced the strength by introducing multiscale defects induced by AM processing [23]. Adding C to CrCoFeNiMn has also improved strengths by inducing back stress at the dislocation cells through C atom segregation within the cell structure [24, 25]. Consequently, the segregation of specific elements into the dislocation cell structure formed during AM can be utilized as a strengthening strategy, which is not feasible through conventional processing approaches. Given that the strengthening mechanism of CoNiMo MEAs primarily relies on the Hall-Petch effect, adopting AM processes, particularly L-PBF, offers significant potential for enhancing mechanical properties, wherein the rapid cooling rates of L-PBF enable to accelerate the formation of Mo-segregated dislocation-cell boundaries.

Thus, we investigated the mechanical properties and microstructural characteristics of $(CoNi)_{85}Mo_{15}$ MEAs produced via L-PBF. After exploring their printability, optimal processing parameters were determined, and compressive tests were conducted on blocks printed under successful conditions. Although the specimens exhibited attractive mechanical peroperteis, the results of microstructural analysis revealed cracks in L-PBF $(CoNi)_{85}Mo_{15}$ MEAs. Therefore, this study focused on the underlying the cracking behavior.

2. Experimental procedure

$(CoNi)_{85}Mo_{15}$ powders were supplied by Eloi Materials Lab (EML) via gas atomization under argon atmosphere. Fig. 1(a) presents a scanning electron microscopy (SEM) image of the

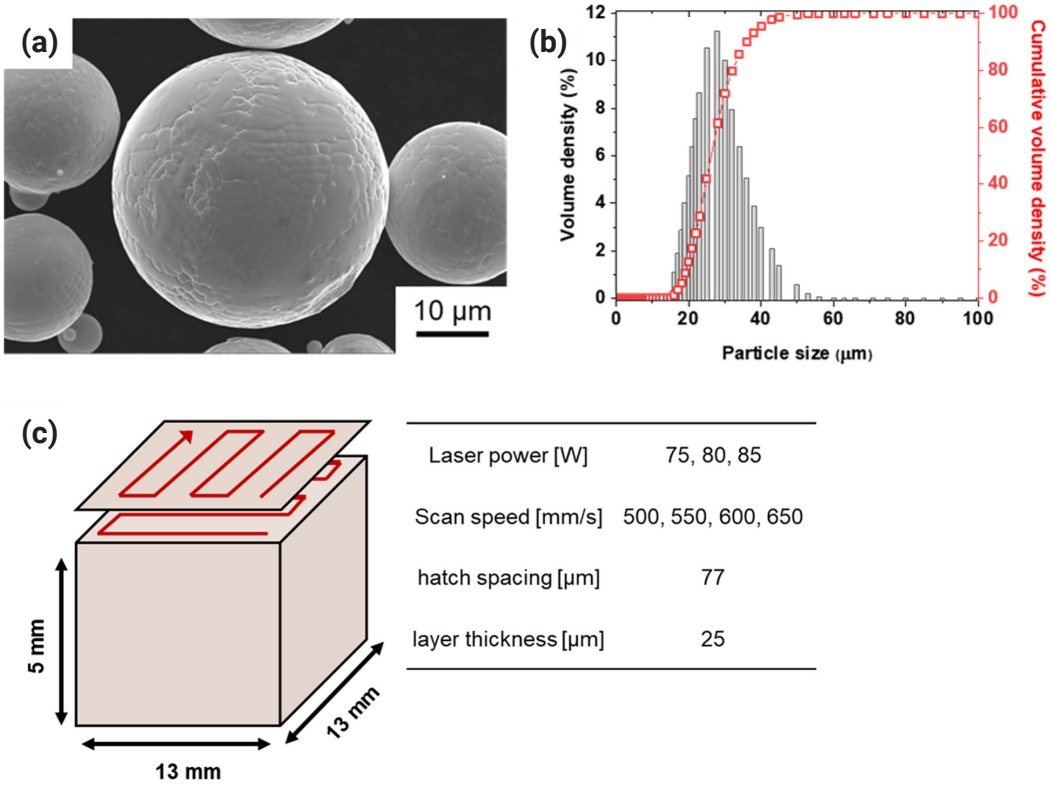

Fig. 1. (a) Scanning electron microscopy image and (b) powder size distribution of gas-atomized $Mo_{15}(CoNi)_{85}$ powders. Fig. 1(c) presents the schematic description of scanning strategy and processing parameters for laser-powder bed fusion.

powders, showing the spherical morphology with minor dendritic structures on the surface owing to the rapid cooling of the powder fabrication process. Moreover, when the powder size distribution measured by particle size analyzer (PSA 1090, Anton Paar), as shown in Fig. 1(b), the powder size was ranged between 15 and 53 μm, which falls within the optimized size for L-PBF. In detail, the powder shows d_{10} of 18.8 um, d_{50} of 26.3 um, and d_{90} of 40.0 um with a mean size volume of 28.1 um. The terms d_{10}, d_{50}, and d_{90} stand for the particle size value, when the cumulative distribution percentage from the smallest to largest, reach 10 %, 50 %, and 90 %, respectively [26, 27]. The powder was used to print blocks of 13 × 13 × 13 mm^3 on 316L stainless steel substrates through L-PBF machine of Mlab (GE additive). As described in Fig. 1(c), 90° rotation after each layer was applied to minimize the discrepancy according to the sample direction [28, 29]. The detailed processing parameters are also summarized in Fig. 1(c); the printability of L-PBF $(CoNi)_{85}Mo_{15}$ MEAs was investigated under the laser power of 75, 80, and 85 W, scan speed of 500, 550, 600, and 650 mm/s, and the fixed hatch spacing and layer thickness of 77 and 55 um, respectively.

After the removal of the printed blocks from the substrate, the cross-section was polished using SiC papers (to 4000 grit), a diamond suspension of 1 μm, and a colloidal silica for 0.5h. The cross-sectional surface of L-PBF $(CoNi)_{85}Mo_{15}$ MEAs was observed using optical microscopy (OM, Imager D1m, ZEISS). Phase identification was carried out by using X-ray diffractometer (XRD, D/max2500, Rigaku). SEM (Quanta FEG 250, FEI) and electron backscatter diffraction (EBSD, S-4300SE, Hitachi) were used to observe the microstructures. The nano-scale microstructures were carefully investigated using a high-resolution transmission electron microscopy (HR-TEM, Titan G3, FEI) system. The TEM specimen was prepared using a dual-beam focused ion beam-SEM (FIB-SEM, Helios NanoLab 650, FEI). Finally, compression tests were conducted at a strain rate of 10^{-4} s^{-1} using an Instron-type apparatus (RB 301 UNITECH-M, R&B) to measure the yield strength of L-PBF $(CoNi)_{85}Mo_{15}$ MEAs with dimensions of 2 × 2 × 3 mm^3 [30].

3. Results and Discussion

The printability of $(CoNi)_{85}Mo_{15}$ MEAs was investigated depending on the laser power and scan speed of the L-PBF system. Fig. 2 presents the optical images showing the cross-sec-

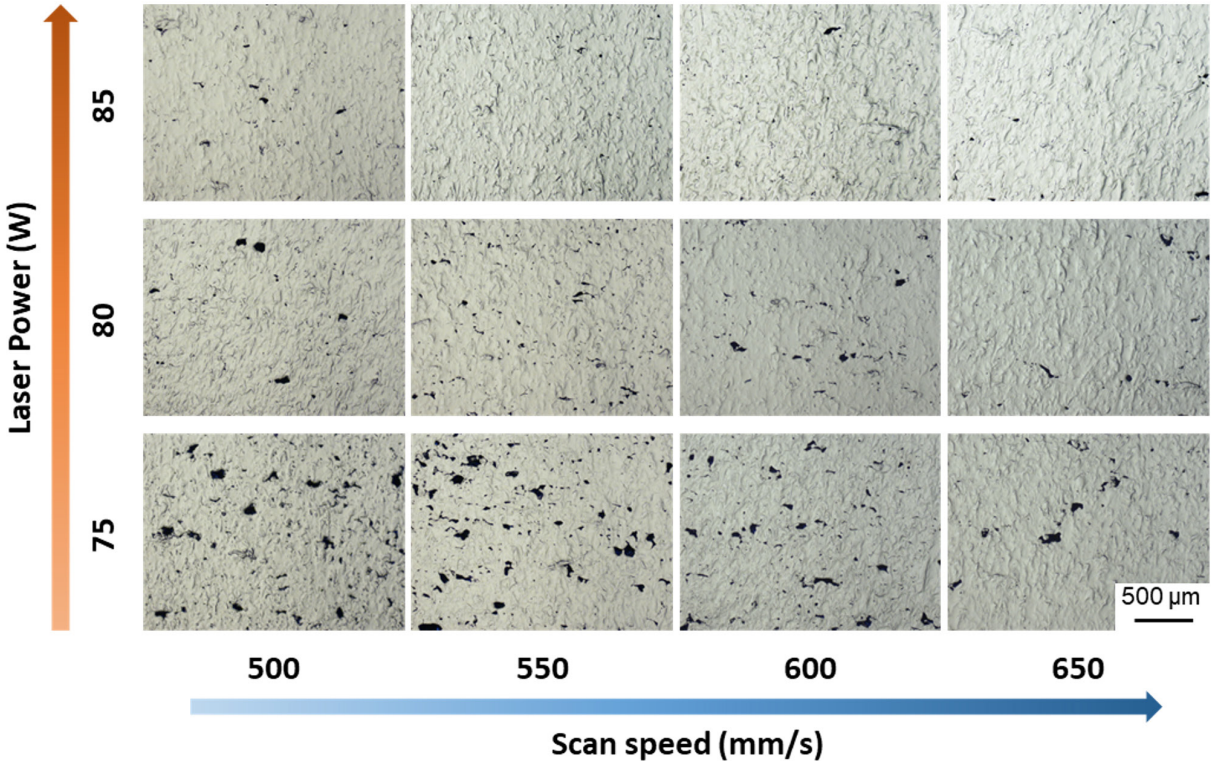

Fig. 2. Summary of optical images for laser-powder bed fusion–manufactured $(CoNi)_{85}Mo_{15}$ depending on processing parameters.

tion of L-PBF $(CoNi)_{85}Mo_{15}$ MEAs produced with varied processing parameters. While the printed blocks with the relatively low laser power of 75 W revealed a lack of fusion-based defects, the defects tended to disappear with increasing laser power. Furthermore, the porosity of the blocks was quantitatively calculated using Image J software from the images (Fig. 2) [31]. Fig. 3 shows the contour map of the porosity depending on the laser power and scan speed. While the highest value was measured in the block with the low laser power of 75 W and low scan speed of 500 mm/s, the porosity was reduced to under 1% with increasing laser power and scan speed. Thus, we determined the candidate for optimal processing parameters as 85 W in laser power and 550, 600, and 650 mm/s in scan speed.

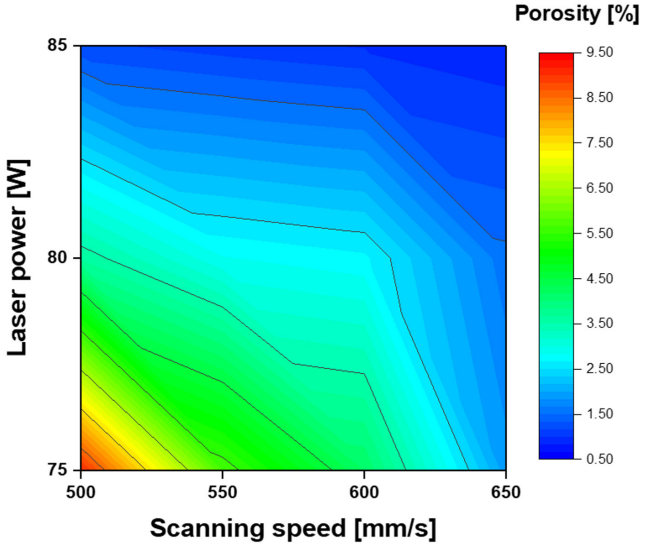

Fig. 3. Porosity contour map for laser-powder bed fusion–manufactured $(CoNi)_{85}Mo_{15}$ depending on processing parameters.

To evaluate the yield strength of L-PBF $(CoNi)_{85}Mo_{15}$ MEAs, we performed compressive tests on the blocks printed with scanning speeds of 550, 600, and 650 mm/s at the laser power of 85 W. Fig. 4(a) reveals their engineering strain-engineering stress curves, and the yield strength of the alloys was measured to be 620, 653, and 635 MPa, respectively. Moreover, the strength was compared to the values of AMed HEAs and MEAs reported in the literature. When DED CoCrFeMnNi was reported to have a yield strength of 346 MPa [21], DED $Al_{0.3}CoCrFeNi$ [32], DED $AlCoCrFeNi_{2.1}$ [33], and PBF $Fe_{40}Mn_{20}Co_{20}Cr_{15}Si_5$ [34] revealed higher values of 477, 508, and 530 MPa, respectively.

While the major strengthening mechanism of equiatomic CoCrFeMnNi HEAs can be considered solid-solution strengthening, the addition of alloying elements (i.e., Al, Si, or N) results in additional strengthening by second phases [35–37]. Furthermore, VCoNi MEA was reported to have the largest atomic size difference among equi-atomic HEAs and MEAs with a single solid-solution phase [8, 38]. The severe lattice distortion resulted in a high yield strength of 670 MPa in DED VCoNi [39]. Similarly, PBF CrCoNi presented a high value of 692 MPa because Cr atoms could increase the lattice distortion [40]. Additionally, despite the larger atomic radius of V (164 pm) compared to Cr (128 pm), the strength of PBF CrCoNi was slightly higher than that of DED VCoNi. It might be be-

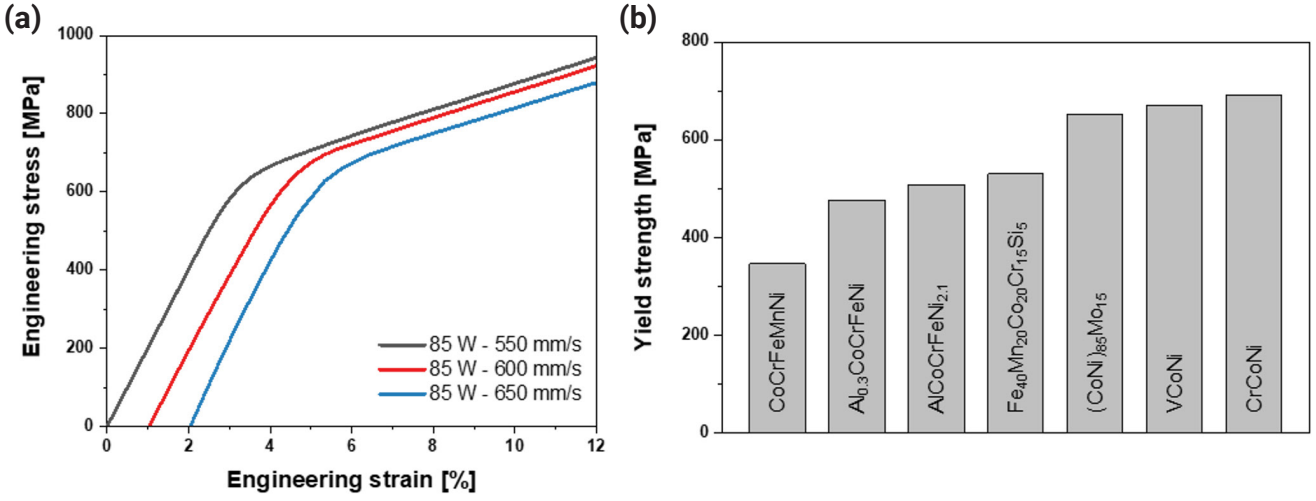

Fig. 4. (a) Engineering stress–strain curves of laser-powder bed fusion–manufactured $(CoNi)_{85}Mo_{15}$ and (b) comparison of yield strength among additive-manufacturing–produced high-entropy allows and medium-entropy allows [21, 32-34, 39, 40].

cause the cooling rate of PBF is faster, leading to a higher dislocation density and finer microstructure [41–43]. This indicates that dislocation strengthening could also be involved in PBF CrCoNi. Consequently, L-PBF $(CoNi)_{85}Mo_{15}$ MEAs (85 W – 600 mm/s) achieved a high yield strength value of 653 MPa in this study due to the Mo alloying element with a larger atomic radius (141 pm), even compared to V or Cr.The microstructural characteristics of L-PBF $(CoNi)_{85}Mo_{15}$ MEAs were investigated and summarized in Fig. 5. Fig. 5(a) exhibits the XRD pattern of the $(CoNi)_{85}Mo_{15}$, showing a single solid-solution FCC phase. One notable observation is that the peak intensity of (200) is relatively higher than (111), caused by the preferred orientation formation toward the direction of heat flux during the L-PBF. Moreover, Figure 5(b) reveals EBSD inverse pole figure (IPF) map observed at vertical direction to building direction, presenting the repeated melt pool formed during the L-PBF. The width of the melt pool was measured as approximately 75 μm. The elongated grains are aligned along the building direction from the centerline of the melt pool. The fine dislocation cell structures are presented in the cross-sectional backscattered electron (BSE) image of Fig. 5(c). The dislocation cells could be formed by the rapid solidification and aligned with a regular mean distance (~ 500 nm) and pattern in L-PBF $(CoNi)_{85}Mo_{15}$ MEAs.

Furthermore, the dislocation cell structure is closely observed by TEM analyses. Fig. 5(d) exhibits a scanning TEM high-angle annular dark-field (STEM-HAADF) image and the corresponding elemental chemical maps of Co (blue), Ni (green), and Mo (red). It clearly shows that Mo atoms are segregated at the dislocation cells, and Mo-rich particles are precipitated at the triple junctions, as marked by white arrows. Fig. 5(e) displays a HR-TEM image, showing the precipitate.

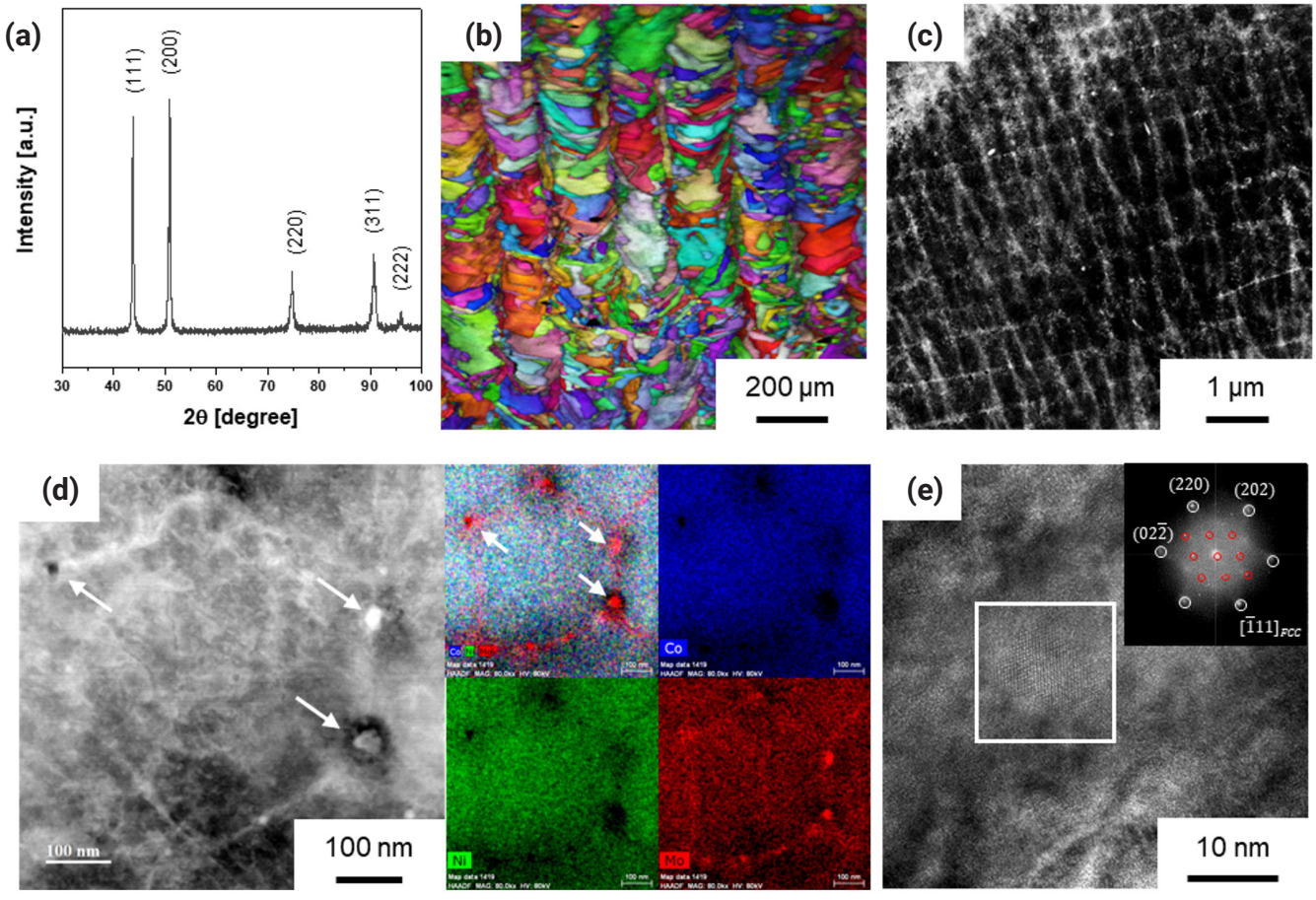

Fig. 5. (a) X-ray diffraction pattern, (b) electron backscatter diffraction-inverse pole figure map and (c) high-magnification scanning electron microscopy image of laser-powder bed fusion–manufactured $(CoNi)_{85}Mo_{15}$. Fig. 5(d) presents a scanning transmission electron microscopy high-angle annular dark-field image and the corresponding energy-dispersive X-ray spectroscopy chemical elemental maps, indicating Mo-segregation as marked by white arrows, and the transmission electron microscopy image is shown in Fig. 5(e).

To identify the particle, the inserted fast Fourier transformation (FFT) pattern was obtained from the area marked by a white square. When the spots marked by white and red circles correspond to the matrix and particle, respectively, it indicates that the image is the projection for the (111) plane of the matrix with an FCC structure. Moreover, Mo-rich particles are considered to be a topologically-closed-packed (TCP) μ phase, wherein spots corresponding to the particle represent a (011) plane of the rhombohedral lattice (R-3m space group). Thus, we can conclude that the Mo-rich μ phase was precipitated in L-PBF $(CoNi)_{85}Mo_{15}$ MEAs owing to the Mo segregation at the dislocation cells.

However, the enlarged EBSD analysis reveals that severe cracks are observed on the L-PBF $(CoNi)_{85}Mo_{15}$ MEAs, as shown in Fig. 6, which includes (a, d) EBSD-IPF and (b, e) Kernel average misorientation (KAM) maps obtained in the vertical and parallel directions to the building direction, respectively. Moreover, Fig. 6(c, f) presents the profile of misorientation degree along the traces as marked by yellow arrows in Fig. 6(a, d). The black squares and red circles represent the misorientation degrees between adjacent points (i.e., Point-to-point) and the initial point (i.e., Point-to-origin) at each location. According to the EBSD results, the cracks propagated through the high-angle boundaries, where severe residual stress remained. In general, hot cracking occurs along high-angle grain boundaries, where the solidification directions of adjacent dendrite regions belonging to different grains diverge. As solidification progresses, solute atoms are rejected, and the liquid remaining at the boundaries undergoes tensile stress owing to the varied solidification directions of the surrounding matrix. This tensile stress causes the vulnerable liquid to be pulled apart, resulting in the hot-cracking phenomenon [44–46]. The presence of severe residual stress at high-angle grain boundaries, as shown in the KAM maps in Fig. 6, plays a cru-

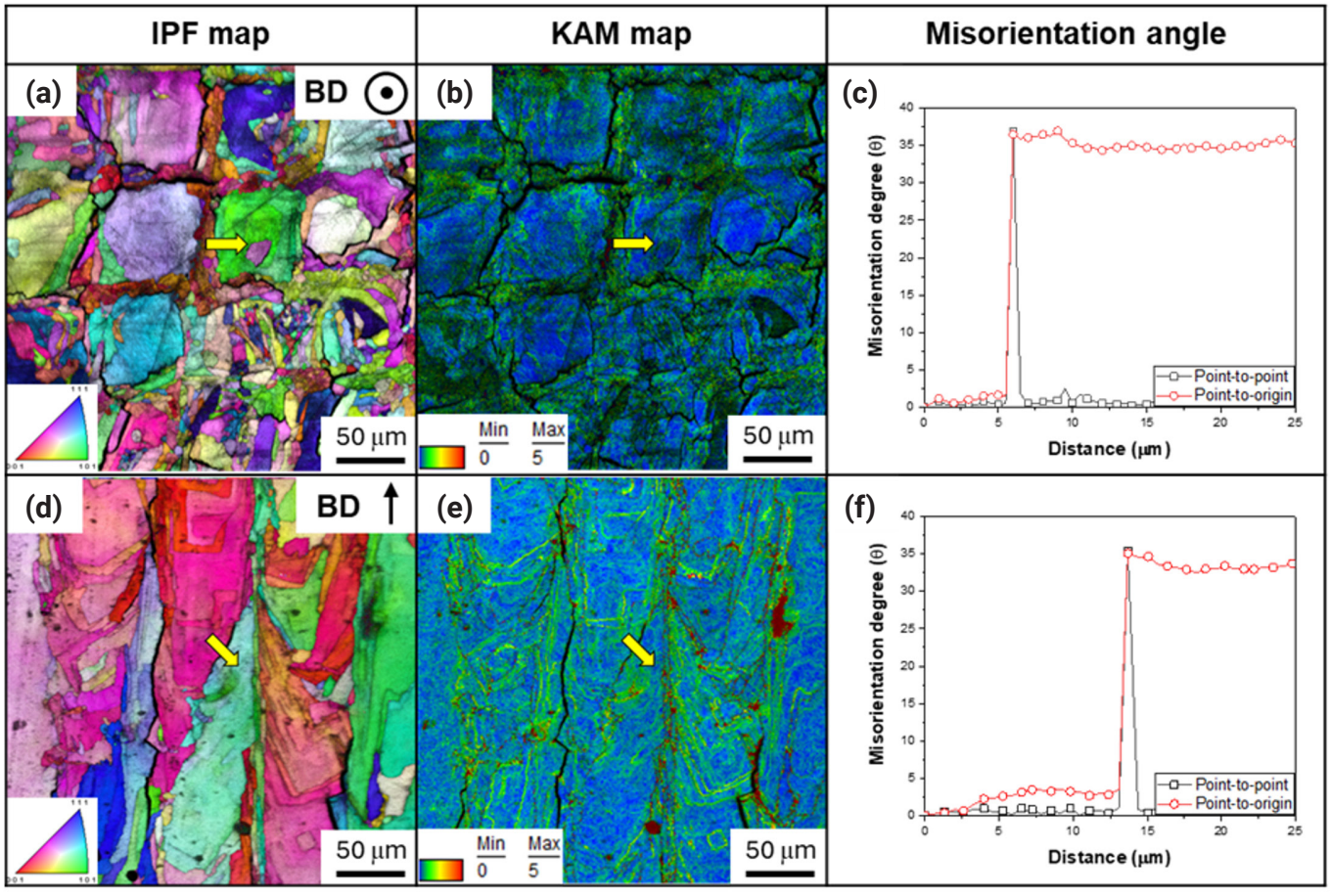

Fig. 6. High magnification (a,d) electron backscatter diffraction-inverse pole figure and (b,e) kernel average misorientation maps for laser-powder bed fusion–manufactured $(CoNi)_{85}Mo_{15}$ observed at parallel and vertical directions to the building direction. Fig. 6(c,f) presents the misorientation degree.

cial role in the initiation and propagation of hot cracks. Residual stress arises from the rapid thermal cycles inherent to the L-PBF process, accumulating at grain boundaries, particularly high-angle boundaries. Consequently, these high-angle boundaries become preferential sites for crack initiation under the rapid thermal cycles inherent to the L-PBF process.

On the other hand, the segregation of alloying elements, such as Mo, during the rapid solidification of the L-PBF process can lead to localized regions with different features [47, 48]. Fig. 7 exhibits a STEM-HAADF image and the corresponding EDS elemental maps near cracks, clearly showing that Mo-segregation and Mo-rich precipitates are observed along the crack. Similarly, several studies have indicated that hot-cracking behaviors in Mo-containing alloys, such as Ni-based superalloys, are attributable to the formation of Mo-rich carbides at grain boundaries during the L-PBF process [49, 50]. During the L-PBF of Mo-containing alloys, the segregation of Mo at dislocation cells could be driven by two key factors of the differences in atomic radius and diffusion rates between Mo and other alloying elements. The larger atomic radius of Mo enhances its compatibility with the strained lattice surrounding dislocation cells, energetically favoring its segregation. Additionally, the lower diffusivity of Mo compared to Co and Ni may restrict its redistribution from the dislocation cells during rapid solidification. At last, Mo segregation facilitates the formation of brittle μ phases at dislocation cells, which further diminishes resistance to cracking, especially at high-angle grain boundaries that overlap with one or more sides of the dislocation cells [45, 48]. Consequently, the presence of Mo segregation, combined with severe residual stress, significantly contributes to the initiation and propagation of hot cracks at high-angle boundaries overlapping with dislocations in L-PBF $(CoNi)_{85}Mo_{15}$ MEAs. To mitigate these issues, both the alloy design adjustment of controlling the Mo content and process modifications (e.g., base plate preheating) should be further considered [51].

4. Conclusion

This study investigated the printability, mechanical properties, and microstructural characteristics of $(CoNi)_{85}Mo_{15}$ MEAs manufactured via L-PBF. The optimal processing parameters were determined to be a laser power of 85 W and scan speeds of 550, 600, and 650 mm/s. L-PBF $(CoNi)_{85}Mo_{15}$ MEAs achieved a high compressive yield strength of 653 MPa, attributed to the strengthening effect of the Mo alloying element with a larger atomic radius and the refined dislocation cell structures. However, cracks were observed along the high-angle grain boundaries. This cracking is attributed to the accumulation of severe stress at the boundaries during the L-PBF process and the local

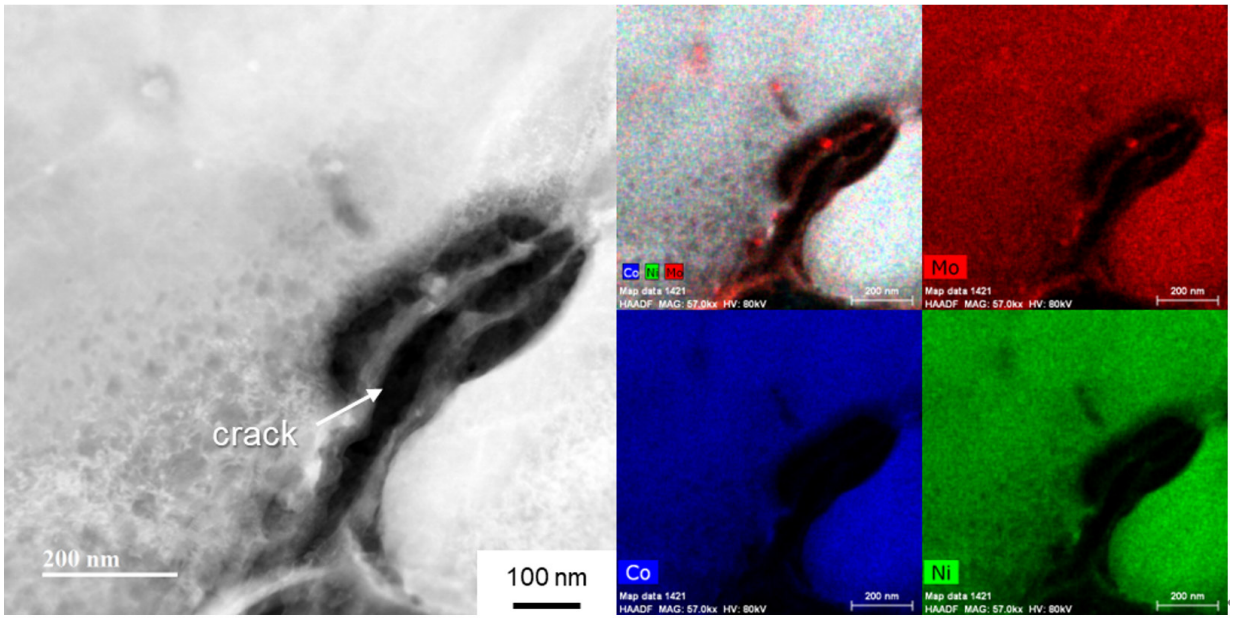

Fig. 7. Scanning transmission electron microscopy high-angle annular dark-field image and the corresponding energy-dispersive X-ray spectroscopy chemical elemental maps, showing the area near a crack in laser-powder bed fusion–manufactured $(CoNi)_{85}Mo_{15}$ medium-entropy alloys.

reduction in resistance to cracking owing to Mo segregation and μ phase precipitation. Therefore, further research is required to adjust the Mo content and modify processing techniques to mitigate cracking behaviors in L-PBF $(CoNi)_{85}Mo_{15}$ MEAs.

Funding

This study was supported by the National Research Foundation of Korea (NRF) grant funded by the Korea government (MSIT) [NRF-2022R1A5A1030054].

Conflict of Interest

The authors declare no competing financial interests or personal relationships.

Data Availability Statement

All data included in this study are available upon request by contact with the corresponding author.

Author Information and Contribution

S. Nam: Researcher, Investigation, Visualization, Writing – original draft, H. Jung: Ph.D candidate, Methodology, Investigation, H. Park: Ph.D candidate, Resources, C. Jung: Ph.D candidate, Formal analysis, J.M. Park: Senior Researcher, Methodology, Resources, H.S. Kim: Professor, Writing – review & editing, Project administration, S.S. Sohn: Professor, Conceptualization, Writing – review & editing, Funding acquisition, Supervision.

Acknowledgement

None.

References

[1] E.P. George, W.A. Curtin and C.C. Tasan: Acta Mater., **188** (2020) 435.
[2] Z. Li, S. Zhao, R.O. Ritchie and M.A. Meyers: Prog. Mater. Sci., **102** (2019) 296.
[3] B. Cantor, I. T. H. Chang, P. Knight and A. J. B. Vincent: Mater. Sci. Eng. A, **375–377** (2004) 213.
[4] B. Gludovatz, A. Hohenwarter, K. V. S. Thurston, H. Bei, Z. Wu, E. P. George and R. O. Ritchie: Nat. Commun., **7** (2016) 10602.
[5] H. Chang, T. W. Zhang, S. G. Ma, D. Zhao, R. L. Xiong, T. Wang, Z. Q. Li and Z. H. Wang: Mater. Des., **197** (2021) 109202.
[6] H. Jung, S. Lee, T. Kang, A. Zargaran, P.-P. Choi and S. S. Sohn: J. Mater. Sci. Technol., **181** (2023) 71.
[7] H. Chang, T. W. Zhang, S. G. Ma, D. Zhao, T. X. Bai, K. Wang, Z. Q. Li and Z. H. Wang: J. Alloys Compd., **896** (2022) 162962.
[8] S. S. Sohn, A. Kwiatkowski da Silva, Y. Ikeda, F. Körmann, W. Lu, W.S. Choi, B. Gault, D. Ponge, J. Neugebauer and D. Raabe: Adv. Mater., **31** (2019) 1807142.
[9] T. J. Jang, Y. N. Lee, Y. Ikeda, F. Körmann, J. H. Baek, H. S. Do, Y. T. Choi, H. Gwon, J. Y. Suh, H. S. Kim, B. J. Lee, A. Zargaran and S. S. Sohn: Acta Mater., **255** (2023) 119030.
[10] H. Jung, G. Lee, M. Koo, H. Song, W. S. Ko and S. S. Sohn: Steel Res. Int., **94** (2023) 202200240.
[11] J. Han, S. Nam, Y. T. Choi, T. J. Jang, C. Jung, S. S. Sohn, H. S. Kim and H. Choi: Int. J. Refract. Met. Hard Mater., **119** (2024) 106535.
[12] S. Chen, Y. Tong and P. K. Liaw: Entropy, **20** (2018) 937.
[13] A. O. Moghaddam, N. A. Shaburova, M. N. Samodurova, A. Abdollahzadeh and E. A. Trofimov: J. Mater. Sci. Technol., **77** (2021) 131.
[14] Y. M. Wang, T. Voisin, J. T. McKeown, J. Ye, N. P. Calta, Z. Li, Z. Zeng, Y. Zhang, W. Chen, T. T. Roehling, R. T. Ott, M. K. Santala, P. J. Depond, M. J. Matthews, A. V. Hamza and T. Zhu: Nat. Mater., **17** (2018) 63.
[15] C. Y. Yap, C. K. Chua, Z. L. Dong, Z. H. Liu, D. Q. Zhang, L. E. Loh and S. L. Sing: Appl. Phys. Rev., **2** (2015) 041101.
[16] S. P. Murray, K. M. Pusch, A. T. Polonsky, C. J. Torbet, G. G. E. Seward, N. Zhou, S. A. J. Forsik, P. Nandwana, M. M. Kirka, R. R. Dehoff, W. E. Slye and T. M. Pollock: Nat. Commun., **11** (2020) 4975.
[17] J. Ge, C. Chen, R. Zhao, Q. Liu, Y. Long, J. Wang, Z. Ren and S. Yin: Mater. Des., **219** (2022) 110774.
[18] B. Han, C. Zhang, K. Feng, Z. Li, X. Zhang, Y. Shen, X. Wang, H. Kokawa, R. Li, Z. Wang and P. K. Chu: Mater. Sci. Eng. A, **820** (2021) 141545.
[19] J. G. Kim, J. M. Park, J. B. Seol, J. Choe, J. H. Yu, S. Yang and H. S. Kim: Mater. Sci. Eng. A, **773** (2020) 138726.
[20] P. Wang, P. Huang, F. L. Ng, W. J. Sin, S. Lu, M. L. S. Nai, Z. L. Dong and J. Wei: Mater. Des., **168** (2019) 107576.
[21] Z. Tong, X. Ren, J. Jiao, W. Zhou, Y. Ren, Y. Ye, E. A. Larson and J. Gu: J. Alloys Compd., **785** (2019) 1144.
[22] R. Li, P. Niu, T. Yuan, P. Cao, C. Chen and K. Zhou: J. Alloys

Compd., **746** (2018) 125.
[23] H. Jung, J. Lee, G. H. Gu, H. Lee, S. M. Seo, A. Zargaran, H. S. Kim and S. S. Sohn: Addit. Manuf., **61** (2023) 103360.
[24] J. M. Park, E. S. Kim, H. Kwon, P. Sathiyamoorthi, K. T. Kim, J. H. Yu and H. S. Kim: Addit. Manuf., **47** (2021) 102283.
[25] H. Park, H. Kwon, K. T. Kim, J. H. Yu, J. Choe, H. Sung, H. S. Kim, J. G. Kim and J. M. Park: Addit. Manuf., **86** (2024) 104223.
[26] J. H. Park, G. B. Bang, K. A. Lee, Y. Son, Y. H. Song, B. S. Lee, W. R. Kim and H. G. Kim: Met. Mater. Int., **28** (2022) 2836.
[27] C. Garcia-Cabezon, M. A. Castro-Sastre, A. I. Fernandez-Abia, M. L. Rodriguez-Mendez and F. Martin-Pedrosa: Met. Mater. Int., **28** (2022) 2652.
[28] X. Zhang, H. Xu, Z. Li, A. Dong, D. Du, L. Lei, G. Zhang, D. Wang, G. Zhu and B. Sun: Mater. Charact., **173** (2021) 110951.
[29] J. Xu, Y. Ding, Y. Gao, H. Wang, Y. Hu and D. Zhang: Mater. Des., **209** (2021) 109940.
[30] S. Nam, M. J. Kim, J. Y. Hwang and H. Choi: J. Alloys Compd., **762** (2018) 29.
[31] C. A. Schneider, W. S. Rasband and K. W. Eliceiri: Nat. Methods, **9** (2012) 671.
[32] H. Peng, S. Xie, P. Niu, Z. Zhang, T. Yuan, Z. Ren, X. Wang, Y. Zhao and R. Li: J. Alloys Compd., **862** (2021) 158286.
[33] L. Huang, Y. Sun, N. Chen, H. Luan, G. Le, X. Liu, Y. Ji, Y. Lu, P. K. Liaw, X. Yang, Y. Zhou and J. Li: Mater. Sci. Eng. A, **830** (2022) 142327.
[34] P. Agrawal, S. Thapliyal, S. S. Nene, R. S. Mishra, B. A. McWilliams and K. C. Cho: Addit. Manuf., **32** (2020) 101098.
[35] X. Gao, Z. Yu, W. Hu, Y. Lu, Z. Zhu, Y. Ji, Y. Lu, Z. Qin and X. Lu: J. Alloys Compd., **847** (2020) 156563.
[36] Z. Li, C. C. Tasan, K. G. Pradeep and D. Raabe: Acta Mater., **131** (2017) 323.
[37] E. G. Astafurova, K. A. Reunova, M. Y. Panchenko, E. V. Melnikov and S. V. Astafurov: J. Alloys Compd., **925** (2022) 166616.
[38] B. Xu, H. Duan, X. Chen, J. Wang, Y. Ma, P. Jiang, F. Yuan, Y. Wang, Y. Ren, K. Du, Y. Wei and X. Wu: Nat. Mater., **23** (2024) 755.
[39] Y.L. A. Amar, M. Wang, L. Zhang, J. Li, L. Huang, H. Yan and Y. Zhang: Addit. Manuf., **68** (2023) 103522.
[40] P. Kumar, M. Michalek, D. H. Cook, H. Sheng, K. B. Lau, P. Wang, M. Zhang, A. M. Minor, U. Ramamurty and R. O. Ritchie: Acta Mater., **258** (2023) 119249.
[41] A. Bandyopadhyay and K. D. Traxel: Addit. Manuf., **22** (2018) 758.
[42] S. P. Yadav and R. S. Pawade: Metals (Basel)., **13** (2023) 287
[43] K. M. Bertsch, G. Meric de Bellefon, B. Kuehl and D. J. Thoma: Acta Mater., **199** (2020) 19.
[44] Z. Sun, X. P. Tan, M. Descoins, D. Mangelinck, S. B. Tor and C. S. Lim: Scr. Mater., **168** (2019) 129.
[45] E. Chauvet, P. Kontis, E. A. Jägle, B. Gault, D. Raabe, C. Tassin, J. J. Blandin, R. Dendievel, B. Vayre, S. Abed and G. Martin: Acta Mater., **142** (2018) 82.
[46] L. Guo, J. Gu, B. Gan, S. Ni, Z. Bi, Z. Wang and M. Song: J. Alloys Compd., **865** (2021) 158892.
[47] J. M. Park, H. Kwon, J. Choe, K. T. Kim, J. H. Yu, Y. U. Heo and H. S. Kim: Scr. Mater., **237** (2023) 115715.
[48] B. Guo, Y. Zhang, Z. Yang, D. Cui, F. He, J. Li, Z. Wang, X. Lin and J. Wang: Addit. Manuf., **55** (2022) 102792.
[49] J. Hu, Y. Hu, C. Lan, Q. Zhang, F. Jin, W. Li, X. Kin and W. Huang: J. Mater. Res. Technol., **21** (2022) 3526.
[50] G. Marchese, G. Basile, E. Massini, A. Aversa, M. Lombardi, D. Ugues, P. fino and S. Biamino: Materials, **11**(10):(2018) 106.
[51] K. Kempen, B. Vrancken, S. Buls, L. Thijs, J. Van Humbeeck and J. P. Kruth: J. Manuf. Sci. Eng. Trans. ASME, **136** (2014) 061026.

Research Article

pISSN 2799-8525 · eISSN 2799-8681
J Powder Mater 2024;31(6):546-555

Journal of Powder Materials

High-Temperature Steam Oxidation Behavior of Silicide- or Aluminide- Coated Mo and Nb Refractory Metals

Woojin Lim[1], Je-Kyun Baek[2], JaeJoon Kim[1], Hyun Gil Kim[1], Ho Jin Ryu[2,*]

[1]Korea Atomic Energy Research Institute, Daejeon 34057, Republic of Korea
[2]Department of Nuclear and Quantum Engineering, Korea Advanced Institute of Science and Technology, Daejeon 34141, Republic of Korea

Refractory materials, such as molybdenum and niobium, are potential candidates for cladding material due to their high melting temperatures and desirable mechanical properties at higher temperatures than those of zirconium alloys. However, refractory materials have low resistance to oxidation at elevated temperatures. Therefore, this study examined silicide or aluminide surface coatings as protection against rapid oxidation of refractory materials at elevated temperatures for a potential accident-tolerant fuel cladding. Silicide or aluminide layers were formed on refractory metal substrates by using the pack cementation method. The steam oxidation behavior of both coated and uncoated samples was compared by thermogravimetric analysis at 1200°C. The weight changes of the coated samples were greatly reduced than those of uncoated samples. Microstructural analyses demonstrated that the silicide and aluminide layers were oxidized to form a protective surface oxide that prevented rapid oxidation of the refractory substrate at elevated temperatures.

Keywords: Refractory metals; Silicide/aluminide coating; Pack cementation; Steam oxidation

Received: November 5, 2024
Revised: December 5, 2024
Accepted: December 6, 2024

***Corresponding author:**
Ho Jin Ryu
E-mail: hojinryu@kaist.ac.kr

1. Introduction

Zirconium-based alloys have been used in nuclear reactors as fuel cladding for decades. They have excellent technical properties in normal operation, such as low neutron cross-section, excellent irradiation resistance, and acceptable corrosion resistance. However, at high temperatures, contemporary zirconium-based alloys face several challenges, such as low strength, relatively high rates of oxidation, and poor thermal shock resistance. In case of a nuclear reactor accident, such as Loss of Coolant Accident (LOCA), zirconium alloys lose strength above 750°C and oxidation is accelerated with high-pressure steam with temperatures above 700°C, resulting in the generation of hydrogen gas [1]. Since the Fukushima nuclear power plant accident in 2011, researchers have examined the concept of accident-resistant fuel with desired traits such as high strength and oxidation resistance even in case of a severe accident. Extensive research has been conducted on fuel cladding with a low oxidation rate in a steam atmosphere and improved thermo-mechanical properties to develop accident-tolerant fuel cladding [2]. To improve the performance of contemporary cladding systems in case of accidents, new concepts of cladding have been suggested. Refractory metals, including niobium (Nb) and molybdenum (Mo), have been suggested as potential cladding materials because of their high-temperature strength than that of zirconium alloys. Refractory metals exhibit desirable mechanical strengths at elevated temperatures. In Table 1, the mechanical properties of metals and alloys currently under study, such as Mo, and Nb are compared with those of the currently used zirconium alloy. Compared with the zirconium alloy, refractory metals have higher melting points, Young's moduli, and thermal conductivities. Furthermore, refractory metals, have desirable high-temperature mechanical properties and acceptable neutron absorption cross-section properties because of which they can be considered as candidate materials for accident-resistant fuel-cladding.

https://doi.org/10.4150/jpm.2024.00381

Table 1. Mechanical properties data (Mo, Nb, zirconium alloy)

	Molybdenum	Niobium	Zirconium alloy
Melting point (°C)	2623	2477	1850
Density (g/cm^3)	10.28	8.57	6.56
Young's Modulus (GPa)	329	105	99.3
Thermal expansion coefficient ($\times 10^{-6}$/K)	5.35	7.3	6
Thermal conductivity (W/m K)	138	53.7	21.5
Neutron absorption cross-section (barns)	2.65	1.15	0.18

2. Materials and Methods

2.1. Refractory metals

To conduct an oxidation test, two representative refractory metals, Mo and Nb, were prepared. Mo has been suggested as a potential cladding material because of its high-temperature strength and high melting point, but it has relatively poor oxidation resistance. Furthermore, Mo shows very destructive oxidation behavior, commonly referred to as "pest oxidation," in the temperature range 650–750°C. In this range, molybdenum trioxide (MoO_3), which is volatile, is produced as an oxidation product. The need for coating or alloying methods has been suggested if Mo is to be used as a cladding material [3-5]. Nb is also a candidate for use as a cladding material because it retains its strength at high-temperatures and has a high melting point; however, it has weak oxidation resistance at high temperatures, similar to Mo [6-8].

Surface coatings are applied to mitigate the weak oxidation problem of Mo and Nb at elevated temperatures. The formation of continuous oxide layers has been considered an effective way to better oxidation resistance. The oxide layer on the specimen acts as a barrier for oxygen diffusion, thereby decreasing the oxidation rate. The silicon dioxide (SiO_2) on the surface of metallic silicide enhances oxidation resistance. Also, aluminide coatings have been applied in high-temperature industries to improve oxidation resistance. A stable Al_2O_3 oxide scale can protect the underlying substrate from aggressive oxygen penetration in an oxidizing environment. Consequently, a silicide or aluminide-coating method was proposed in this study to prevent oxidation of underlying metal substrates [9-11].

2.2. Surface coating

Pack cementation is a favorable coating method because it is simple, inexpensive, and produces strong bonds between the coating and substrate by inter-diffusion reactions during the process of coating. Furthermore, the method is suitable for uniformly coating materials that have complex shapes because the method uses gaseous diffusion [11-14]. The Al-rich or Si-rich coating on surfaces can form a protective oxide layer after exposure to a high-temperature oxidation environment. The substrate is buried with a powder mixture consisting of several depositional materials, called the master metal, such as Si and Al. The powder mixture also contains a halide salt and an inert filler, such as Al_2O_3 and SiO_2. The coating layers are formed by diffusion of the mixed elements, in their vapor form, toward the substrate. The metal halides decompose and release the depositional element on the surface.

Rod-shaped (8Φ × 100 mm) Mo and Nb substrates were provided by Phillip Trading Co., Ltd. The specimens were cut into a 2-mm thick disc using a diamond cutter and subsequently polished using SiC abrasive papers of different grits (800, 1200, 2000, and 4000 grades) to smooth the surface of the specimen. Polished specimens were then cleaned by sonicating in deionized water, and dried.

Several types of powders, namely Al_2O_3 (as filler), silicon (Si), aluminum (Al), ammonium chloride (NH_4Cl), and sodium fluoride (NaF) (activator), were prepared for the coating. The powder mixtures and substrates were each contained in an alumina crucible. Two mixtures, Al_2O_3, Si, and NH_4Cl (50:30:20 wt. %), and Al_2O_3, Al, and NaF (50:30:20 wt. %), were used for the silicide and aluminide coatings, respectively. The crucible was installed in a tube furnace, (Fig. 1) and heat treatment was applied at 1200°C for the silicide coating and at 950°C for the aluminide coating. During the heating process, silicide and aluminide underwent the chemical interactions listed in Table 2. The crucibles were heated to the target temperatures at a rate of 10°C/min in argon gas. Several heat treatment times for 1, 3, 5, 15, and 20 h were used to change the thickness of silicide and aluminide layers.

2.3. Oxidation test

Thermogravimetric analysis (TGA) is commonly adopted to

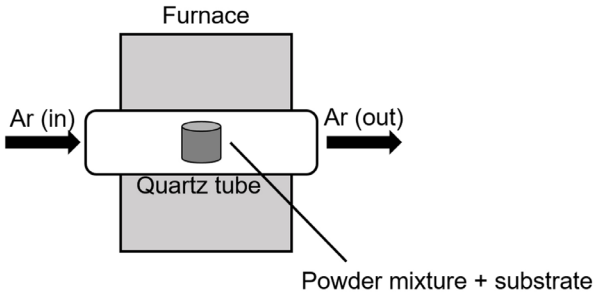

Fig. 1. A schematic illustration of the pack cementation method.

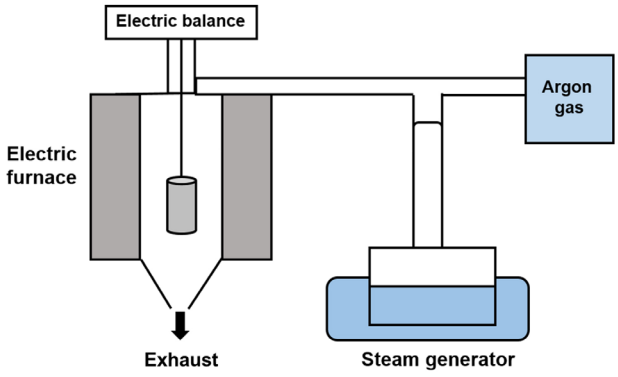

Fig. 2. A schematic illustration of thermogravimetric analysis.

analyze oxidation behavior because it provides information regarding the weight changes of samples as a function of time. Therefore, TGA was applied in this study to conduct the high-temperature oxidation tests. Figure 2 shows a schematic of the method used for conducting TGA.

The oxidation test for disc-shaped specimens was conducted in a steam environment at 1200°C, for up to 2000 s. The steam flowed with high purity argon gas at a flow rate of 0.5 ml/min. This process was conducted for coated specimens with different duration heat treatments and uncoated, (bare), specimens.

2.4. Microstructural analysis before and after oxidation

The microstructures before (as-coated specimens) and after (post-oxidized specimens) conducting the oxidation test were compared with each other. The cross sections of coated specimens were polished and the microstructures of silicide and aluminide coatings were examined. Similarly, the microstructures of samples were characterized after the TGA tests. Specimens were mounted with epoxy resin and then polished, in a direction perpendicular to the sample, with SiC abrasive paper, to observe the coating and the oxide layer after the TGA test. The morphologies of the coating and the oxide layer were examined by scanning electron microscopy (SEM). The chemical compositions of the coating and oxide layers were measured using energy dispersive X-ray spectroscopy (EDS). The crystalline structure of the coating and the oxide layers was identified using X-ray diffraction (XRD) with Cu Kα radiation (k = 1.5406Å), a voltage of 40 kV and a current of 300 mA. The scan speed was 4 degrees/min from 20 to 90 degrees with a step size of 0.01 degrees.

Table 2. Chemical reactions experienced during the pack cementation process [9, 15]

Siliconizing
$NH_4Cl(s) \rightarrow NH_3(g) + HCl(g)$
$2NH_3(g) \rightarrow N_2(g) + 3H_2(g)$
$4HCl(g) + Si(s) \rightarrow SiCl_4(g) + 4H$
$3SiCl_4(g) + Si(s) \rightarrow 4SiCl_3(g)$
$2SiCl_3(g) + Si(s) \rightarrow 3SiCl_2(g)$
$SiCl_2(g) + Si(s) \rightarrow 2SiCl(g)$
$Si(s) + Cl_2(g) + H_2(g) \rightarrow SiH_2Cl_2(g)$
Aluminizing
$NaF(g) + Al(s) \rightarrow AlF(g) + Na(g)$
$2NaF(g) + Al(s) \rightarrow AlF_2(g) + 2Na(g)$
$3NaF(g) + Al(s) \rightarrow AlF_3(g) + 3Na(g)$

3. Results

3.1. Microstructure

Table 3 summarizes the changes in coating thickness with time during the pack cementation heat treatment. The growth kinetics of the coated layer exhibited the following relationship between growth rate and time:

$x = kt^{0.5}$ where x is the coating thickness (μm), k is the kinetics parameter, and the t is time (h). As shown in Fig. 3, the k values obtained from the silicide coating for Mo and Nb samples were 18.4 and 10.6 μm/h$^{0.5}$, respectively. The k values calculated from growth kinetics of the aluminide coating, for Mo and Nb samples, were 19.0 and 20.3 μm/h$^{0.5}$, respectively.

SEM images demonstrated that the silicide coating deposited at 1200°C for 3 h was a double layer coating (Fig. 4a, 4c). The compositions of the silicide coating were measured as presented in Table 4. The Si concentration in the outer layer was approximately 67 at. %, which corresponds to stoichiometric $MoSi_2$ and $NbSi_2$. Stable molybdenum silicide and niobium silicides are Mo_3Si, Mo_5Si_3, and $MoSi_2$, and Nb_3Si, Nb_5Si_3, and

$NbSi_2$, respectively. Only two types of silicides of Mo and Nb, Mo_5Si_3 and $MoSi_2$, and Nb_5Si_3 and $NbSi_2$, respectively, were detected by microstructural analysis.

During the pack cementation process with Al, molybdenum aluminide or niobium aluminide intermetallic compounds were generated due to the diffusion of aluminum toward the substrate. The cross-sectional image of the specimen coated with aluminide at 950°C for 3 h was analyzed by SEM. The gray phase in Fig. 4b corresponded to the Mo_3Al_8 coating layer based on XRD characterization as shown in Fig. 5a. In the case of the Nb substrate (Fig. 4d), the $NbAl_3$ coating layer was identified as shown in Fig. 5b.

Table 3. Average silicide and aluminide coating thickness as a function of the duration of heat treatment

Heat treatment time (h)	Average thickness (μm)			
	Silicide		Aluminide	
	Mo	Nb	Mo	Nb
1	9	7	13	13
	11	8	11	14
3	35	17	36	31
	38	20	35	34
5	49	25	50	51
	57	29	54	53
15	60	35	66	75
	70	37	75	74
20	80	47	81	88
	88	51	87	87

3.2. Thermogravimetric analysis

To evaluate oxidation behavior, TGA tests were conducted at 1200°C for 2000 s. Table 5 summarizes the weight change of the uncoated and coated samples after the oxidation tests. In the case of the uncoated Mo specimens, the weight loss was very large, exceeding 120 mg/cm^2, due to the volatility of MoO_3. For both silicide and aluminide-coated samples, the weight change after the oxidation tests was much less. Both SiO_2 and Al_2O_3 oxide scales provided an oxidation resistant barrier to the substrate because of their low permeability to oxygen and metal ions. The presence of the $MoSi_2$ and Mo_3Al_8 coating generated the protective SiO_2 and Al_2O_3 layers during oxidation, respectively. The weight changes decreased with the thickness of the silicide or aluminide-coating layers as shown in Fig. 6. This tendency means that the protectiveness of the coated layers was enhanced with the heat treatment time as the average thickness of the coating layers increased.

Unlike the Mo substrate, the bare Nb substrate exhibited weight gain because niobium oxide is not volatile. Meanwhile, silicide- and aluminide-coated Nb exhibited a similar weight change compared with the Mo substrate sample. The protective mechanism was the same as that for the coated Mo substrate. The presence of the $NbSi_2$ and $NbAl_3$ coating generated a protective SiO_2 and Al_2O_3 layer during oxidation, respectively. The weight change also decreased with the thickness of silicide- and aluminide-coating layers as shown in Fig. 6. The minimum weight change of 1.12 mg/cm^2 after steam oxidation at 1200°C for 2000 s was obtained for the Nb specimen with an aluminide

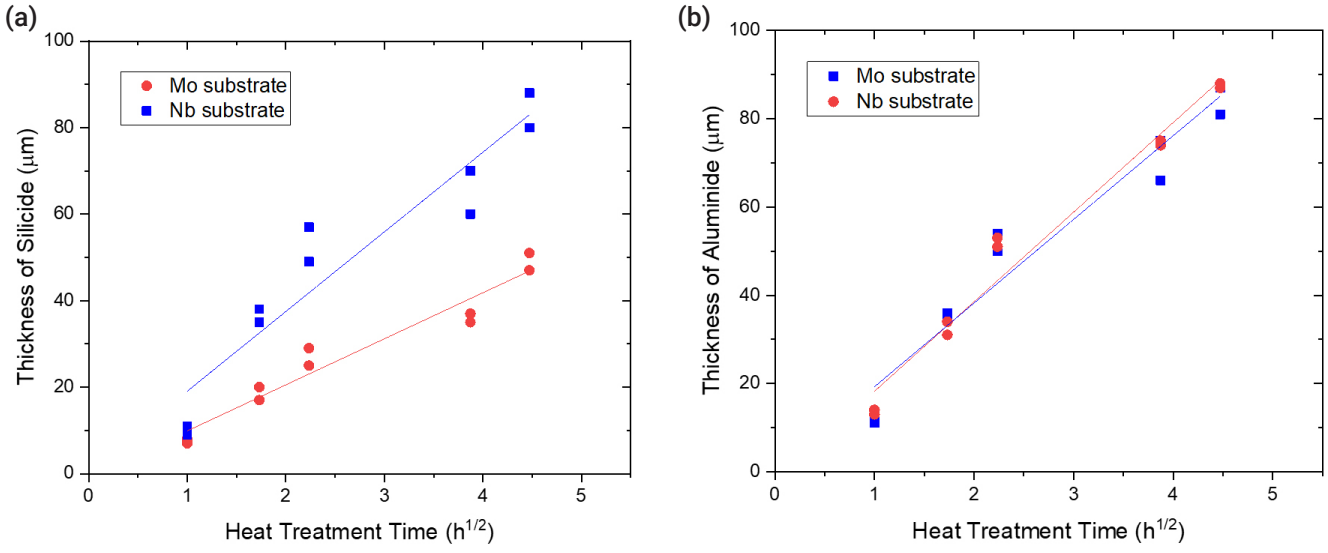

Fig. 3. The variation of the thicknesses of (a) silicide and (b) aluminide coatings after pack cementation of Mo and Nb substrates.

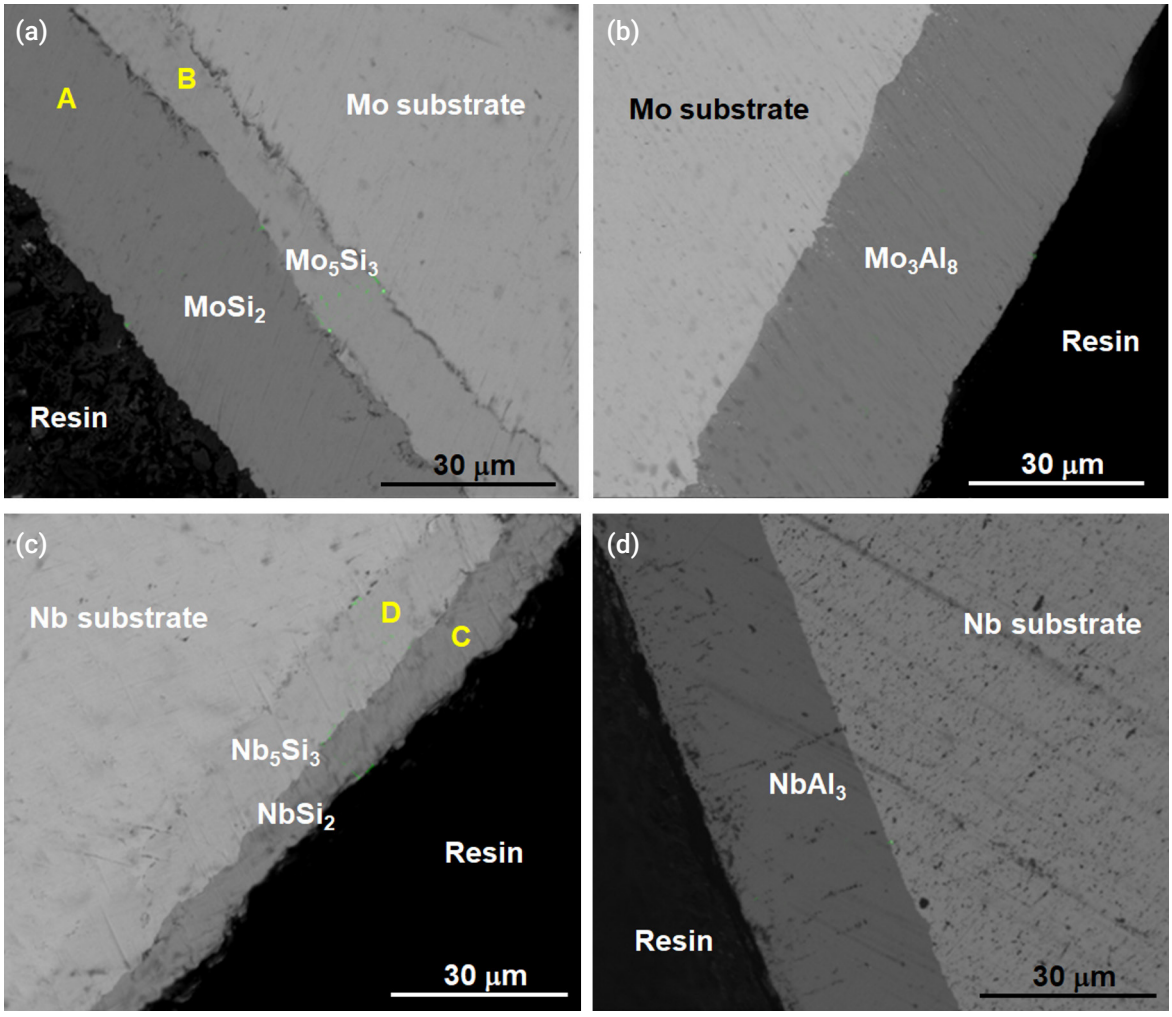

Fig. 4. Microstructures of (a) molybdenum silicide, (b) molybdenum aluminide, (c) niobium silicide, and (d) niobium aluminide coating on each specimen (heat treatment time: 3 h).

Table 4. Energy-dispersive X-ray spectroscopy measurement results of the silicide coating layers, as shown in Fig. 4

Point		Element composition (at. %)	
		Mo	Si
Mo substrate	A	32.8	67.2
	B	60.8	39.2
Nb substrate	C	32.0	68.0
	D	60.4	39.6

layer coated by the heat treatment of 15 h.

3.3. Sample morphology after oxidation test

The SEM image of the uncoated Mo specimen after the oxidation test demonstrates that the outermost oxide layer has peeled off (Fig. 7). The remaining outer layer corresponds to MoO_3, and it is hypothesized that the volatile MoO_3 that formed during oxidation at elevated temperature evaporated during cooling.

Figure 8 shows the oxide scales on the silicide coating of the specimen after it underwent oxidation at 1200°C for 2000 s under a steam environment. A thin oxide scale was formed on the surface of each coated specimen, with thicknesses ranging between 1 and 10 μm. Table 6 summarizes the point EDS results of the samples used in SEM; the outermost layers (G, H) were composed of SiO_2. Small cracks were observed in the Mo specimen and very large cracks were observed in the Nb specimen. Particularly, the delamination of the Nb_5Si_3 layer is remarkable as shown in Fig. 8b. Because the thermal expansion coefficients of the silicide layers and the substrate are different, this thermal

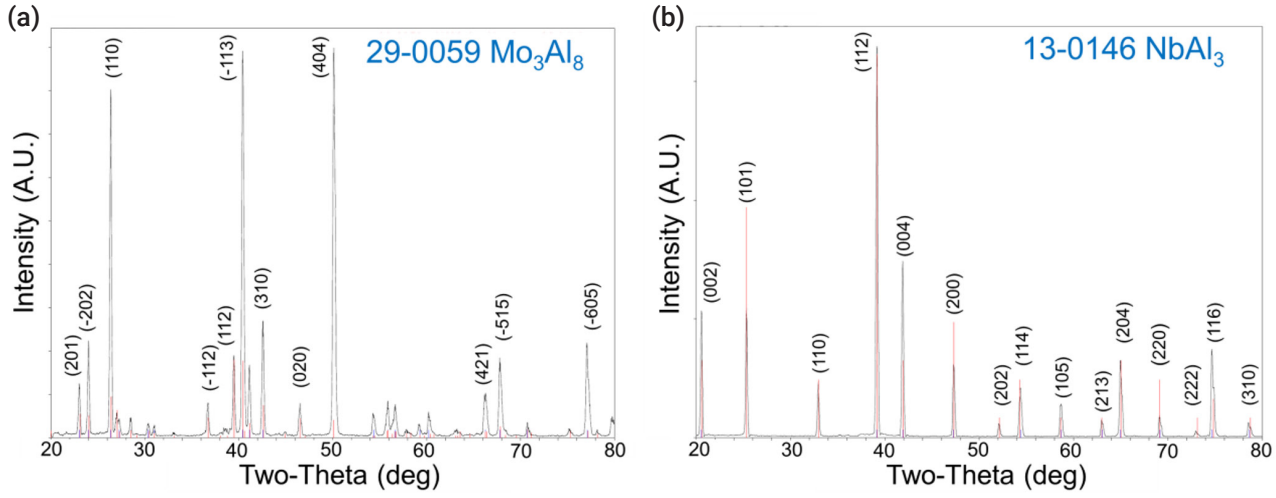

Fig. 5. X-ray diffraction patterns of (a) molybdenum aluminide (Mo_3Al_8) and (b) niobium aluminide ($NbAl_3$) coating on each specimen.

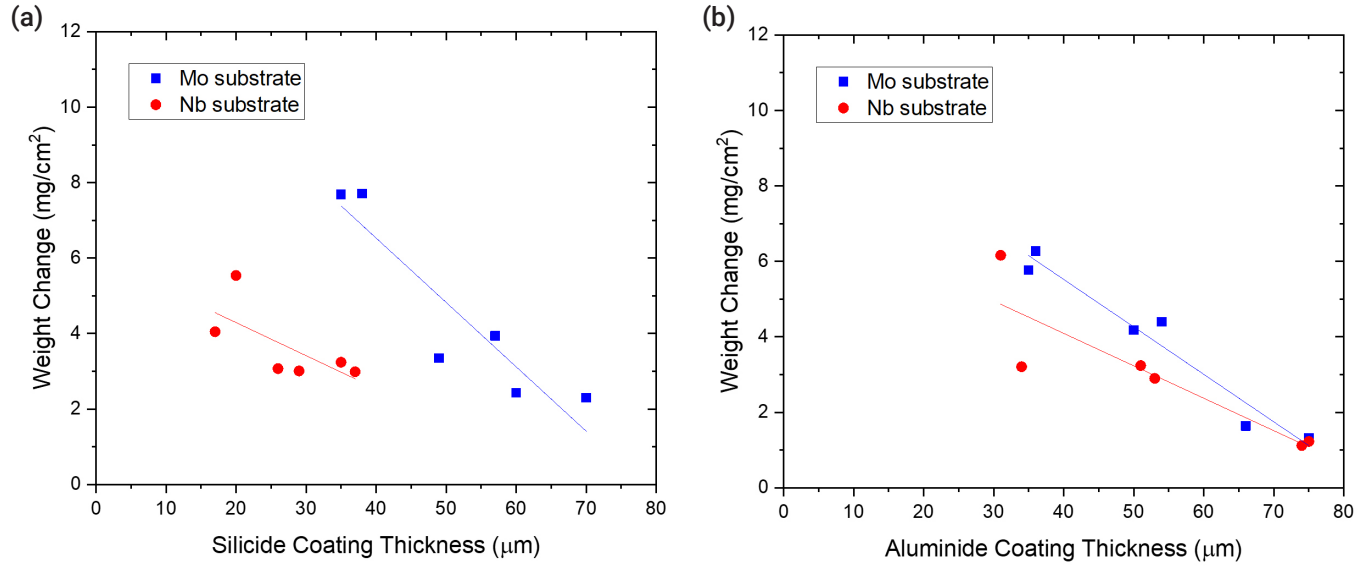

Fig. 6. Relationship between the coating thickness and weight change of (a) silicide-coated and (b) aluminide-coated Mo and Nb substrates after thermogravimetric analysis tests at 1200°C for 2000 s.

Table 5. Weight change of coated specimens after thermogravimetric analysis tests at 1200°C for 2000 s

Specimen			Weight change (mg/cm^2)			
			Silicide		Aluminide	
Mo	Bare		-121.7	-120.1	-100.7	-101.1
	Heat treatment time	3 h	7.69	7.71	6.27	5.77
		5 h	3.35	3.94	4.18	4.40
		15 h	2.43	2.30	1.64	1.32
Nb	Bare		19.7	21.3	19.7	21.3
	Heat treatment time	3 h	4.05	5.54	6.16	3.21
		5 h	3.07	3.01	3.24	2.90
		15 h	3.24	2.99	1.23	1.12

stress may have initiated the formation of cracks along the coating layers.

Figure 9 and Fig. 10 show the microstructure of oxidized aluminide-coated Mo and Nb specimens treated at 1200°C for 2000 s, respectively. When compared with the previous silicide-coated Mo specimen, the coating was not retained well as shown in Fig. 9, although the weight change in the silicide-coated specimens was similar to that in the aluminide-coated specimens after the oxidation test. It is hypothesized that the coating of the aluminide samples has poor resistance to thermal stress, low ductility, and a high thermal expansion mismatch between the substrates and the aluminide layer. Therefore, the coating became detached during the oxidation test and cooling. In the SEM image of the aluminide-coated Nb substrate, a very large area of Al_2O_3 and a mixture of oxides were observed along the cracks as shown in Fig. 10. In silicide-coated specimens, there was no oxide located along cracks, and this was interpreted as indicating that the crack in the silicide occurred during cooling because of the mismatch of the thermal expansion between the silicide coating and the Nb substrate. However, in aluminide-coated specimens where oxides were formed along the cracks, this was interpreted to mean that the cracks already existed during the oxidation experiment.

Table 7 shows the thermal expansion coefficients of the coatings and substrates. The difference in the thermal expansion coefficient between Mo-Mo_5Si_3-$MoSi_2$ was lower than the Nb-Nb_5Si_3-$NbSi_2$ layer. The thermal expansion coefficient of Nb_5Si_3

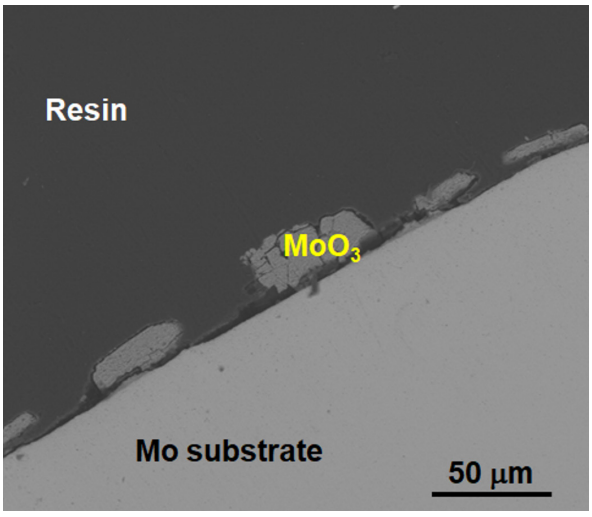

Fig. 7. A scanning electron microscopy image of a bare Mo specimen after steam oxidation.

Table 6. Energy-dispersive X-ray spectroscopy analysis results of silicide specimens after the oxidation test

Point	Element composition (at. %)			
	Mo	Nb	Si	O
E	60.8		39.2	
F	30.9		69.1	
G	1.4		30.2	68.3
H		1.7	32.1	66.2
I		31.3	68.7	
J		59.4	40.6	

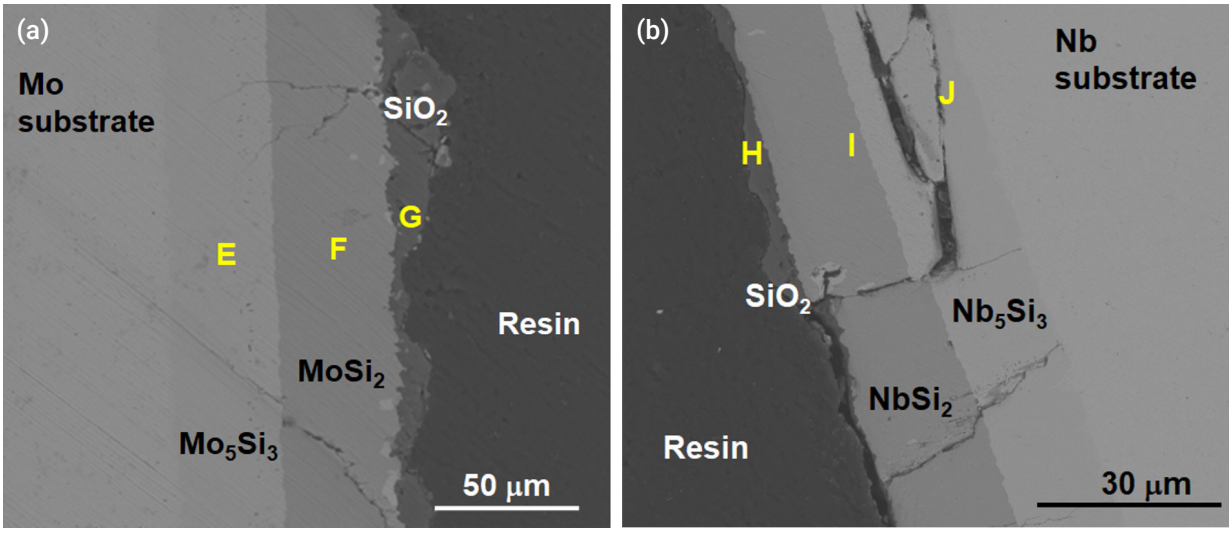

Fig. 8. Scanning electron microscopy images after the oxidation test (silicide-coated sample) (1200°C for 2000 s) (a) Mo substrate, (b) Nb substrate.

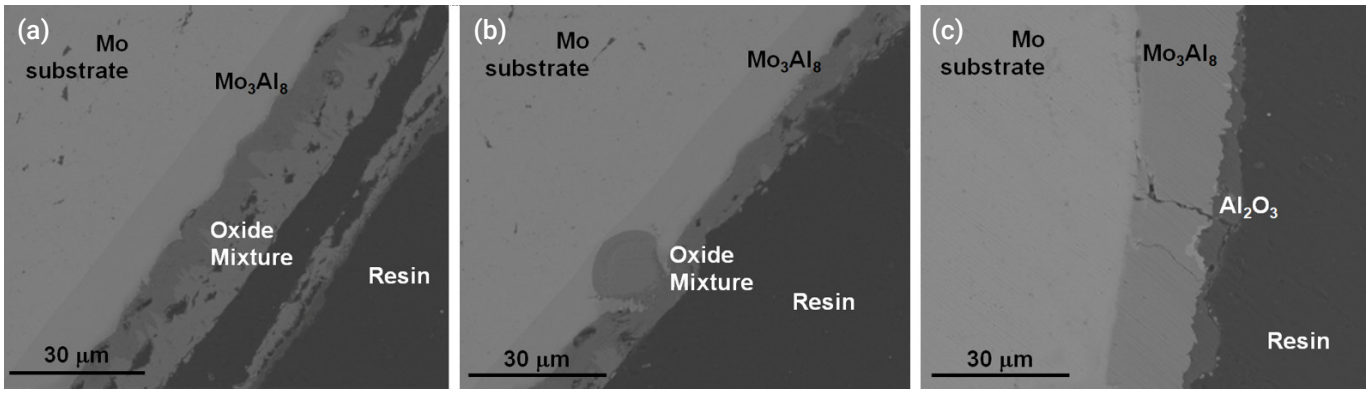

Fig. 9. Scanning electron microscopy images after oxidation test of aluminide-coated Mo samples (1200°C for 2000 s) (a) 3 h heat-treated Mo, (b) 5 h heat-treated Mo, (c) 15 h heat-treated Mo substrate.

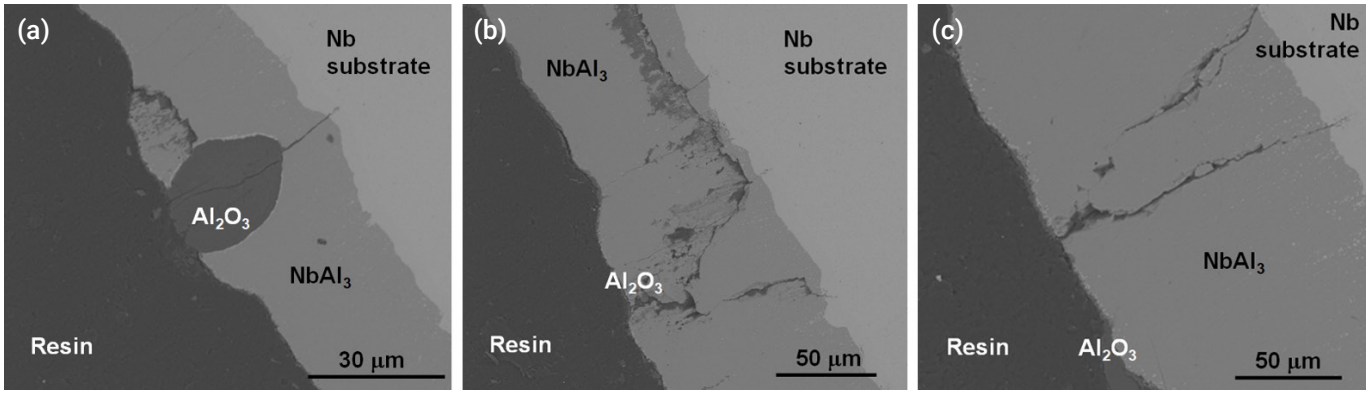

Fig. 10. Scanning electron microscopy images after oxidation test of aluminide-coated Nb samples (1200°C for 2000 s) (a) 3 h heat-treated Nb, (b) 5 h heat-treated Nb, (c) 15 h heat-treated Nb substrate.

Table 7. Thermal expansion coefficients of various materials for each layer [16-24]

Element	Thermal expansion coefficient ($\times 10^{-6}$/K)
Al_2O_3	8.2 (293-1273 K)
Mo	6.7 (293-1973 K)
Nb	8.9 (293-1973 K)
$MoSi_2$	9.2 (298-1723 K)
Mo_5Si_3	5.2 (a), 11.5 (c)
$NbSi_2$	11.7
Nb_5Si_3	8.638 (a), 12.359 (c) (RT-1273 K)
Nb_2O_5	5.9
Mo_3Al_8	6.7
$NbAl_3$	15

was twice that of $NbSi_2$ and three times larger than that of Nb. Therefore, large thermal mismatches occurred during cooling and this resulted in a large crack along the Nb_5Si_3 layer. Similarly, the difference between Nb-$NbAl_3$ resulted in cracks along the $NbAl_3$ layer.

Nb silicide and aluminide demonstrated superior oxidation resistance compared to Mo silicide and aluminide, respectively. However, for future applications, it is important to consider that the larger thermal expansion mismatch of Nb silicide and aluminide, compared to other coatings, may result in the development of thermal shock cracks.

4. Conclusions

Refractory materials have been considered promising materials as alloy claddings because of their high creep resistance and significantly higher melting points than those of contemporary zirconium alloy claddings. To mitigate the weak oxidation behavior of refractory metals at an elevated temperature, protection through the formation of a surface coating was pro-

posed. Silicide coating was selected to protect underlying metals against oxygen penetration because the SiO_2 on the surface of the silicide can enhance oxidation resistance. Aluminide coatings have also been tested to compare the oxidation behavior with that of silicide coatings.

Uncoated (bare) and coated specimens were exposed to an elevated temperature to analyze their oxidation resistance. Silicide- and aluminide-coated specimens showed improved oxidation resistance, exhibiting only a small weight change than that in bare specimens subjected to oxidation. Coated samples also exhibited lower weight gain than the current Zircaloy-4.

Microstructural analysis after oxidation demonstrated that a thin and continuous SiO_2 was formed on the silicide-coated specimens. The SiO_2 oxide scale provided an oxidation resistant barrier, preventing the penetration of oxygen toward the underlying substrate. The weight change following oxidation was dramatically decreased in aluminide-coated specimens; the morphologies of oxidized aluminide-coated specimens were poor due to the irregular formation of Al_2O_3 oxide in the aluminide layers. Large cracks were found in both Nb substrates after the oxidation test due to the thermal expansion mismatches during cooling.

Funding

None.

Conflict of Interest

The authors have no conflicts of interest to declare.

Data Availability Statement

The dataset files are available upon request.

Author Information and Contribution

WJ Lim: Researcher; investigation, visualization, writing–original draft

JK Baek: PhD student; investigation

JJ Kim: Senior Researcher; investigation

HG Kim: Principal Researcher; methodology, resources

HJ Ryu: Professor; conceptualization, writing–review & editing, supervision

Acknowledgement

Some parts of the preliminary study have been presented in 2017 Water Reactor Fuel Performance Meeting by the same authors. This paper is based on the first author's M.S. dissertation completed at KAIST.

References

[1] H. M. Chung: Nucl. Eng. Technol., **37** (2005) 327.
[2] K. A. Terrani, J. Nucl. Mater., **501** (2018) 13.
[3] A. T. Nelson, E. S. Sooby, Y. J. Kim, B. Cheng and S. A. Maloy: J. Nucl. Mater., **448** (2014) 441.
[4] R. O. Suzuki, M. Ishikawa and K. Ono: J. Alloys Compd., **306** (2000) 285.
[5] B. Cheng, P. Chou and Y.-J. Kim: EPJ Nuclear Sci. Technol., **2** (2016) 5.
[6] B. Vishwanadh, R. H. Naina, S. Majumdar, R. Tewari and G. K. Dey: Metall. Mater. Trans. A, **44** (2013) 2258.
[7] B. P. Bewlay, M. R. Jackson, J. Zhao and P. R. Subramanian: Metall. Mater. Trans., **34A** (2003) 2043.
[8] M. Steinhorst and H. J. Grabke: Mater. Sci. Eng. A, **120–121** (1989) 55.
[9] L. Tong, Y. Dengzun and Z. Chungen: Chinese J. Aeronaut., **23** (2010) 381.
[10] C. H. Koo and T. H. Yu: Surf. Coat. Technol., **126** (2000) 171.
[11] T. C. Munro and B. Gleeson: Metall. Mater. Trans. A, **27** (1996) 3761.
[12] N. Kandasamy and L. L. Seigle: Thin Solid Films, **84** (1981) 17.
[13] R. Sakidja, J. S. Park, J. Hamann and J. H. Perepezko: Scr. Mater., **53** (2005) 723.
[14] A. S. Khalil, F. Surfhvv, I. R. U. Wkh, L. Srzghu, F. Surfhvvlqj and W. Dqg: Microsc. Microanal., **19** (2013) 1896.
[15] S. P. Chakraborty, S. Banerjee, I. G. Sharma and A. K. Suri: Development of silicide coating over molybdenum based refractory alloy and its characterization. J. Nucl. Mater., **403**(1–3):(2010) 152.
[16] J.A. Lembertg and R.O. Ritchie: Adv. Mater., **24** (2012) 3445.
[17] I. L. Shabalin: Ultra-High Temperature Materials I, (2014) 451.
[18] I. L. Shabalin: Ultra-High Temperature Materials I, (2014) 531.
[19] S. L. Urtiga Filho, J. C. Earthman, I. Nieves, M. H. Roberts

and T. P.Waked: Mater. Sci. Forum, **498** (2005) 158.
[20] R. Mania, L. Stobierski, E. Godlewska, S. Koziński and K. Mars: ISMAN, **13** (2004) 49.
[21] F. Chu, D. J. Thoma, K. J. McClellan and P. Peralta: Mater. Sci. Eng. A, **A261** (1999) 44.
[22] M. L. Bauccio: ASM Engineered Materials Reference Book, Second Edition, (1994).
[23] T. Tabaru, K. Shobu, M. Sakamoto and S. Hanada: Intermetallics, **12** (2004) 33.
[24] L. Zhang and J. Wu: Scr. Mater., **38** (1997) 307.

학 회 소 식

2024년도 학회 행사(2024.10.21. ~ 2024.12.22.)

2024년도 추계학술대회
일　　시 : 2024년도 11월 7일(목) ~ 11월 8일(금)
장　　소 : 광주 김대중컨벤션센터

2024년도 제6차 편집위원회 회의
일　　시 : 2024년도 12월 11일(수) 13시 30분
장　　소 : 온라인(Zoom)
회의내용 : 2025년도 학회지 발전방안 외

2024년도 제6차 회장단 회의
일　　시 : 2024년도 12월 12일(목) 14시
장　　소 : 학회사무국
회의내용 : 추계학술대회 결과보고의 건 외

2024년도 제6차 이사회의
일　　시 : 20024년도 12월 12일(목) 16시
장　　소 : 과학기술회관 소회의실 1
회의내용 : 추계학술대회 결과보고의 건 외

– 학회동정 –

◆ 한국분말재료학회지는 한국연구재단의 등재학술지입니다. (사)한국분말재료학회에서는 항상 회원님들의 논문을 투고받고 있사오니 많은 참여 바랍니다.
◆ (사)한국분말재료학회 홈페이지에서는 한국분말재료학회지 원문 서비스를 시행하고 있습니다. 로그인 후 한국분말재료학회지를 열람하실 수 있사오니 많은 이용 바랍니다.
◆ (사)한국분말재료학회 회원가입과 한국분말재료학회지에 논문을 투고하시는 것은 학회 홈페이지를 통해 이용 가능합니다.
◆ (사)한국분말재료학회 홈페이지(http://www.kpmi.or.kr/)의 많은 이용 바랍니다. 기타 문의사항은 이메일(kpmi@kpmi.or.kr) 또는 전화(☎02-539-4603)로 연락바랍니다.

특 / 별 / 회 / 원

K회원

신한다이아몬드공업㈜
(21635) 인천광역시 남동구 남동동로 375 (남동인더스파크 36B-10L)
Tel (032) 814-2211 / Fax (032) 814-1190
http://www.shinhandia.co.kr
E-mail : webmaster@shinhan.co.kr

다이아몬드공구제조

㈜창성
(21628) 인천광역시 남동구 승기천로 320 남동공단 11-9
Tel (032) 420-8700 / Fax (032) 812-8779
http://www.changsung.com
E-mail : cscsale@changsung.com
Metal Powders (금속분말), Clad Metal (클래드메탈)
Magnetic Powder Core (분말자성코아),
Conductive Paste (도전성페이스트)

㈜풍산홀딩스 창원사업장
(51544) 경남 창원시 성산구 공단로 670(성주동)
Tel (055) 239-0700 / Fax (055) 239-0800
http://www.poongsanhc.co.kr
E-mail: Webmaster@poongsan.co.kr
동제품 외

㈜아스플로
(16648) 경기도 수원시 권선구 산업로156번길 7
아스플로 기술연구소
Tel (031) 352-2301 / Fax (031) 352-2309
http://www.asflow.com
반도체 배관 부품, 가스제어시스템

용인전자(주)
(17015) 경기 용인시 기흥구 동백중앙로 16번길 16-4,
에이스동백타워 1동 1101호
TEL: (031) 332-4402

전장용 자성체류

P회원

대구텍㈜
(42936) 대구광역시 달성군 가창면 가창로 1040
Tel (053) 760-7114 / Fax (053) 768-8055
http://www.taegutec.co.kr
E-mail : ct_d_sales@taegutec.co.kr
텅스텐, 중합금제품, 세라믹 제품

대신강업주식회사
(44252) 울산광역시 북구 책골길 45
Tel (052) 287-6162~4 / Fax (052)287- 6165
http://www.dsgu.co.kr
E-mail : nabormj@hanmail.net
자동차용 각종 플랜지류 및 너트류 생산
공구강 및 특수강 판매 대리점

대한소결금속㈜
(42983) 대구광역시 달성군 논공읍 논공로87길 43
Tel (053) 610-0700 / Fax (053) 610-0701
http://www.iksm.co.kr
E-mail : master@iksm.co.kr
철계 소결 기계부품

케이제이알로이㈜
(40046) 경상북도 성주군 선남면 명관로 337-7
Tel (054) 933-5578 / Fax (054) 933-5523
http://www.kjalloy.com
E-mail : kjalloy@kjalloy.com
정밀금형소재, 단조/분말금형, 절삭공구소재

특 / 별 / 회 / 원

(주)코스글로벌
(52057) 경상남도 함안군 법수면 윤외공단길 68
Tel (055) 570-8500 / Fax (055) 570-8599
http://http://www.koswire.com

스테인레스 와이어, 스테인레스 와이어로프, 금속분말

하나에이엠티㈜
(28126) 충북 청주시 청원군 오창읍 각리 1길 75
TEL: (043) 211-0046
http://www.hanaamt.com
E-mail : davidkim@hanaamt.com

가스아토마이징 금속분말, 3D프린팅, Mg, Al, SUS, Ti

신생금속공업(주)
(15078)경기도 시흥시 마유로 238번길 113
TEL: (031) 499-3671~8 / FAX: (031) 499-3680
http://www.shinsaeng.co.kr
E-mail : sales@shinsoeny.co.kr

귀금속 전기접점, 저온 특수 용접봉, Flux

월드인덕션
(22108) 인천광역시 남구 염전로 165번길 38-38 (도화동)
TEL: (032) 572-6100 / FAX: (032) 572-6101
https://induction.uriweb.kr/index
E-mail : worldhft@daum.net

고주파 산업 응용장치, 아토마이져, 진공 챔버, 합금제조 등

㈜씨이피테크
(07228) 서울특별시 영등포구 영신로 220,
케이엔케이디지털타워 208호
TEL: (02) 749-9346 / FAX: (02) 749-9347
http://www.ceptech.co.kr/

3D프린터, 3D 스캐너, 소프트웨어 등

(주)엠티아이지
(06058) 서울시 강남구 논현동 106-7 (언주로 712),
영진빌딩 5층 MTIG
TEL: (02) 540-3617 / FAX: (02) 540-3616

타이타늄, 플랜트(신소재)

아이에스시
(13217) 경기도 성남시 중원구 갈마치로 215, B동 6층
TEL: (031) 777-7675 / FAX : (031) 777-7699
https://kor.isc21.kr

반도체 테스트 솔루션

(주)코나솔
(31806) 충청남도 당진시 면천면 산업단지길 17-60
TEL : (041) 359-6600
http://www.millroll.com

분말야금 제품, 기계부품, 압연롤

(주)이엠엘
(16229) 경기도 수원시 영통구 창룡대로256번길 77, 4층 409호
(이의동, 에이스 광교타워3)
TEL : (031) 5186-6282 / FAX : (0504) 265-8507
http://www.eloiml.co.kr/

금속 분말, 증착용 타겟

이지캐스텍
(13595) 경기도 성남시 분당구 황새울로 224 청구블루빌 619호
TEL : (031) 726-2242
https://www.ezcastech.com

주조(열유동) 및 구조 해석

아토메탈테크코리아㈜
(10049) 경기도 김포시 양촌읍 황금4로 82
TEL : (031) 986-9988 / FAX : (031) 996-2456
http://www.attometal.com/
비정질 합금 파우더

(주)버추얼랩
(04773) 서울특별시 성동구 왕십리로 38, 홍성빌딩 6층
TEL : (02) 3293-0204
https://www.virtuallab.co.kr/

디지털 소재 연구개발 플랫폼

특 / 별 / 회 / 원

일진다이아몬드㈜

(27659) 충청북도 음성군 대소면 대금로 157
Tel (043) 877-6831 / Fax (043) 882-1040
http://www.iljindiamond.co.kr
E-mail : minho.ryoo@iljin.co.kr
공업용 합성다이아몬드, PCB, NCBN, 초경합금제품 등

(주)그린리소스

(22839) 인천광역시 서구 가정로37번길 39
http://www.greenresource.kr/
Tel: 070-4667-4646
희토류, 희소금속, 메탈, 세라믹파우더 등

케이피씨

(41081) 대구광역시 동구 안심로 59길 8
Tel: (053) 960-1574
http://www.kpccorp.co.kr/
제조 기계부품 및 밸브/기타 비철금속 제련, 정련 및 합금제

특 별 회 원

M회원

㈜강앤박메디컬
(28160) 충청북도 청주시 청원구 오창읍 중심상업2로 48(양청리) 중소기업청 T-팩토리 사무동 204호
Tel (070) 7702-9983
http://www.knpmedical.com

의료용 TiNi계 형상기억 소재

경원산업㈜
(15084) 경기도 시흥시 정왕동 희망공원로 241 (시화공단 2나 205호)
Tel (031) 498-3982 / Fax (031) 498-3987
http://www.kwfi.co.kr
E-mail : kwfi@kwfi.co.kr
K/SENSOR, 마그네트

로얄초경
(21690) 인천광역시 남동구 남동동로123번길 33 (공단95블럭 3롯트)
Tel (032) 814-3612 / Fax (032) 814-3616
http://www.royaltc.co.kr
E-mail : royaltc@royaltc.co.kr

초경합금, Heavy Alloy, W-Cu Alloy, 밀링인서트

㈜삼한
(51560) 경상남도 창원시 성산구 연덕로 84
Tel (055) 285-0041 / Fax (055) 282-0144
http://www.samhanltd.co.kr
E-mail : samhan@samhan.biz

자동차부품, Stainless 계열, 연자성 계열, 고강도 부품

알란텀㈜
(13229) 경기도 성남시 중원구 둔촌대로 400 (상대원동, 스타우드 프라자 8층)
Tel (031) 737-0991 / Fax (031) 737-0980
http://www.alantum.com/kr
E-mail : info@alantum.com
배기가스 후처리 기술, 화학 촉매 기술, 산업용 특수 제품

㈜에이피엠
(43013) 대구광역시 달성군 구지면 달성2차3로 60 (달성2차 산업단지 25B-3L)
Tel (053) 611-3101 / Fax (053) 611-3117
http://www.apmworld.co.kr
E-mail : administrator@apmworld.co.kr
오일리스베어링, 소결 기계 부품 , 금형

㈜엔젤
(46988) 부산광역시 사상구 새벽시장로 74 (감전동)
Tel (051) 326-3004 / Fax 051-322-7004
http://angel-juicer.com
E-mail : angeljuicer.web@gmail.com
전기녹즙기, 액추에이터, 모터

㈜유승
(50566) 경남 양산시 상북면 소토4길 34-1
Tel (055) 375-8856 / Fax (055) 375-8858
http://www.ysbiz.co.kr
E-mail : yuseung@ysbiz.co.kr
분말야금공정(자동화공정, 전자공정), 파이프공정

㈜이엔에프테크놀로지
(17084) 경기 용인시 기흥구 탑실로 35번길 14(공세동)
TEL: (031) 881-8200 / FAX: (031) 282-6855
http://www.enftech.com

Etchant, Stripper

이화다이아몬드공업㈜
(18145) 경기도 오산시 남부대로 374
Tel (031) 370-9000 / Fax (031) 370-9229
www.ehwadia.co.kr

다이아몬드공구제조

지멘스㈜
(37668) 경상북도 포항시 남구 지곡로 394 포항테크노파크 벤처3동 PLM XDCR
Tel (054) 223-2629
http://www.siemens.co.kr
E-mail : adscs.kr@siemens.com
의료기기, 터빈, 산업용 소프트웨어

㈜펨토바이오메드
(37673) 경상북도 포항시 남구 지곡동 청암로 77 포스텍 융합연구동 C5, 716
Tel (054) 221-6200 / Fax (054) 221-6209
http://www.smartdrop.co.kr
E-mail : office@femtobiomed.com
접촉각 측정기(Smart Drop)

특 / 별 / 회 / 원

한국분말야금㈜
(31435) 충청남도 아산시 인주면 인주산단로 111번지
Tel (041) 538-3800 / Fax (041) 538-3815
http://www.korpm.co.kr
E-mail : technical@korpm.co.kr
자동자 부품, 가전기기부품, 산업 기계용 부품 제조

한국야금㈜
(28589) 충청북도 청주시 흥덕구 산단로 55
Tel (043) 262-0141 / Fax (043) 262-0146
http://www.korloy.co.kr
E-mail : korloy@korloy.com
초경합금절삭공구(코팅, 써메트, 초경 등)

한국회가내스㈜
(06654) 서울특별시 서초구 서초중앙로 41 대성빌딩 13층
Tel (02) 511-4344 / Fax (02) 548-2592
http://www.hoganas.com/korea
E-mail : korea@hoganas.com

각종 분말야금용 철분말 등

존슨일렉트릭오퍼레이션스㈜
(28122) 충청북도 청주시 청원구 오창읍 과학산업5로 101
Tel (043) 241-7114 / Fax (043) 241-7119
http://www.hallastackpole.co.kr
E-mail : bkmoon@hallastackpole.co.kr
분말야금제품, 자동차부품

㈜KAMI
(08502) 서울특별시 금천구 가산디지털1로 196, 1005호 (가산동, 에이스테크노타워10차)
Tel (02) 6670-4114 / Fax (02) 6670-4110
http://kami.biz/kami/
E-mail : info@kami.biz
부품 개발 및 생산, 기술용역, 세라믹가공기, 다이아몬드 분말

KB오토시스㈜
(31443) 충남 아산시 음봉면 아산온천로 528-24
Tel (041) 537-5358 / Fax (041) 537-5110
https://www.kbautosys.com
E-mail : webmaster@kbautosys.com

자동차 브레이크 마찰재

승림전기(주)
(14569)경기도 부천시 조마루로385번길 72
Tel (031) 616-6336 / Fax (031) 616-6337
http://www.seunglimelec.com/
E-mail : sales@seunglimelec.com
전기차단기부품(전기접점) 제조, 전기회로 개폐, 보호 및 접속 장치

(주)MS가스
(18525) 경기도 화성시 비봉면 푸른들판로1010번길 127-32 (청요리428-39)
Tel (031) 8047-5051~3 / Fax (031) 8047-5055
http://www.msgas.co.kr
E-mail : inquiries@msgas.co.kr
고압가스 및 가스공급설비

㈜에너리치
(14353) 경기도 광명시 일직로 43, GIDC A 2207
TEL: (02) 898-7888
http://www.enerichs.com/
수소 제조 및 연료전지용 금속 다공체

㈜엠케이
(17794) 경기도 평택시 청북읍 고렴1길, 41-50
TEL : (031) 686-5490 / FAX : (031) 696-5490
https://www.mkmetal.co.kr

금속분말(분말야금용, 적층제조용, 기타)

(주)부강특수산업
(38899) 경상북도 영천시 본촌공단길 42
Tel : (054) 335-9996
http://www.bkcoalloy.co.kr/
내열/내마모/내부식 특수합금

(주)비에스지머티리얼즈
(14521) 경기도 부천시 옥산로214번길 21, 4층
Tel : (070)7537-2527

전기자동차 2차전지용 음극 활물질

Code of Ethics for the Journal of Powder

Journal of Powder Materials

Established: 2007. 10. 23

Full Text

First published in April 1994, with the purpose for the revitalization of technical exchange between Academics & Industry in Powder Metallurgy related advanced studies. Journal of Powder Materials is currently published on a bi-monthly basis.

The Korean Powder Metallurgy & Materials Institute has prepared a code of ethics for a qualitative improvement to its journal. We can therefore secure the ethics required for scientific research through this code of ethics; and we intend to raise the value of our journal through the addition of originality and integrity to our journal. Therefore, all authors of theses, review committee members and editorial committee members shall observe this code of ethics in order to reject any dishonesty in the publication of theses and secure the integrity of any research.

Chapter 1. Matters to be observed by the author of thesis

1. The criteria of the authorship

The Author of academic paper means a person who meets all of the following criteria for authorship (based on the criteria of International Committee of Medical Journal Editors). Those who are not satisfied with any of the following criteria shall be divided into “contributor”.

A. Substantial contributions to the conception or design of the work; or the acquisition, analysis, or interpretation of data for the work.
B. Drafting the work or revising it critically for important intellectual content.
C. Final approval of the version to be published.
D. Agreement to be accountable for all aspects of the work in ensuring that questions related to the accuracy or integrity of any part of the work are appropriately investigated and resolved.

2. The duty of the author

The author of thesis shall explain the results and discussions of the research which the author has performed in a concise and accurate manner. When submitting the research results to the Journal of Powder Materials, an author of a thesis shall observe the code of ethics of this institute and conform to the honesty, accuracy and integrity of the research result submitted as such.

A. When submitting a thesis to the Journal of Powder Materials, the author of a thesis shall abide to the code of ethics as outlined by the Journal of Powder Materials
B. The author of a thesis shall reject any fabrication or falsification of the results for conducting all activities including the proposal, planning and execution of the research activities.
C. Submittal or publishing the same result to more than one journal simultaneously shall be regarded as an act of cheating and as such shall be eradicated.
D. The author of a thesis shall not submit and publish research results which were already published to this Journal.
E. An act of submitting another researcher's results under his/her own name shall be deemed as unethical and unacceptable.
F. An author who has submitted a thesis shall obtain proper consent from all existing co-authors and shall not include any inappropriate authors to the thesis. Co-authors shall contribute to the research academically and share the responsibility and achievements for the results altogether, and in the case of administrative and financial support for research, such shall be advised to state details through an "Acknowledgement".
G. An author of thesis shall obtain approval from the person concerned in advance with regards to submission if required, and confirm that there will be no future disputes of agreements and ownership.
H. The author of the thesis shall observe the regulations as provided in relevant laws, norms and as stated in the code of ethics; and to internationally accepted principles of the entire process of research and submission. Also, the author of such thesis shall also secure universality including the respect of human rights, the observation of bioethics, and the preservation of biological diversity and protection

for environments.

I. In the case of an error discovered in a submitted thesis during the publication process, the author of such thesis shall be obligated to correct any mistakes or withdraw the thesis altogether.

Chapter 2. Matters to be observed by the reviewer

The journal reviewer shall review a submitted thesis in compliance with this code of ethics and provide advice in regards to the publication of such thesis to the editorial committee members.

A. The journal reviewer shall review a submitted thesis fairly and objectively under consistent standards regardless of ethnicity, gender, religion, educational environment or acquaintance of the author of thesis.

B. The journal reviewer shall be obligated to review a thesis requested for review faithfully within the set period as determined in the review regulations.

C. The journal reviewer shall not disclose the information of the research results acquired through the review process to any third party or misuse such information.

D. The journal reviewer shall respect the personality of the author of the thesis and value the independence of intellectual ability. The journal reviewer shall prepare an amicable and supplementary written opinion without making subjective evaluations and shall avoid hostile expressions.

E. The journal reviewer shall request the author of the thesis to modify any inappropriate quoted contents and lead the author to quote references correctly. Also, the journal reviewer shall strictly review the thesis to determine is such has any similarity with previous published manuscripts that were presented in other publications.

F. The journal reviewer shall be obligated to reject review in the case of having any connection with the submitted thesis. The journal reviewer shall promptly notify such fact to the editorial committee members to appoint another journal reviewer.

Chapter 3. Matters to be observed by the editorial committee member

The editorial committee member shall retain full responsibility and authority to carry out the procedures to approve or reject a submitted thesis for publication in the journal. Each editorial committee member shall cooperate with the journal reviewer and other editorial committee members shall observe and carry out the following items.

A. The editorial committee member shall fairly evaluate the intellectual level of a thesis as submitted by the author regardless of ethnicity, gender, religion, educational environment or acquaintance of the author of a thesis.

B. The editorial committee member shall not delay the screening of a submitted thesis intentionally and shall perform prompt measures accordingly.

C. The editorial committee member shall screen the submitted thesis objective based on consistent standards, and the editorial committee member shall assume full responsibility and obligation for the required procedures.

D. The editorial committee member shall not release information regarding the submitted thesis to the public and shall not use such information for his/her own research purposes.

E. The editorial committee member shall be obligated to supervise any unethical behavior in a thesis submitted to the journal, and take any necessary measures for any wrongful acts. In the case of an appeal for wrongful acts, the editorial committee member and the review committee shall be obligated to investigate such matters.

F. The editorial committee member shall be obligated to reject screening in the case where editorial committee has written the thesis, or such has any connection with the submitted thesis. Another editing committee member shall be appointed for the screening process.

Chapter 4. Activities of the review committee

A. Clarifying integrity and responsibility of the research results – In the case where cheating has occurred, including plagiarism, duplicated submission or inappropriate citation is suspected, an investigation shall be carried out based on the editorial committee members recommendation The author of such thesis shall be responsible for any cheating including plagiarism, fabrication and falsification and duplicated presentation of the result.

B. In the case where any cheating is suspected in the process of a thesis submission and review, the editorial committee member shall submit such to the review committee and

request the review committee to investigate such in private. The review committee shall then carry out an inspection in compliance with the following guidelines to ensure that no victim shall suffer in good faith.

1. The review committee shall observe "the principle of presumption of innocence" until such is proven to be a wrongful act.
2. The review committee shall begin and perform such inspection fairly and without discrimination in private circumstances.
3. The review committee shall prepare, arrange and store documents in regards to the investigation.
4. The review committee shall suspend all process in regards to the thesis publication.
5. The review committee shall carry out an investigation promptly to reduce any damages due to delay.

C. The review committee shall carry out an investigation promptly and fairly at the editorial committee member's request. The investigation shall notify, carry out and finish based on the following guidelines.

1. The review committee shall notify any beginning of an investigation to the person or organization concerned that is questionable for cheating and also inform such as to any postponing of the publication of such thesis until the investigation is complete.
2. The review committee shall provide an opportunity for explanation to the person or organization subject to investigation within 30 days of written notice.
3. The review committee shall acquire and investigate any internal records or other publications related with cheating.
4. In the case of unintended mistakes or errors, the review committee shall finish the investigation promptly.
5. In the case where cheating is discovered, the review committee shall supervise measures for such cheating. The review committee shall return the submitted thesis to the author, notify the Institute's guideline to the author, remove or publish the withdrawal of the thesis in the case where such was already published, and restrict the author's thesis publication for 3 years afterwards.
6. In the case of a duplicated submission and publication with a joint publisher, such actions shall be notified to the relevant publisher and handled in conjunction with the relevant publisher.
7. All cases and investigations carried out by the review committee shall be documented and stored. In cases where cheating is not apparent, the relevant document shall be sealed.

Supplementary Provision

1. This code of ethics shall be in effect from October 23, 2007.
2. This Revised code of ethics shall be in effect from March 6, 2020.
3. This Revised code of ethics shall be in effect from February 10, 2022.

Journal of Powder Materials Research Misconduct-Related Regulations

Journal of Powder Materials

Enacted: June 17, 2016

Chapter 1 General Provisions

1. Purpose

The purpose of this guide is to strengthen research ethics by setting the standards, operation, and discipline of research

2. Ethics Committee

① The ethics committee of The Korean Powder Metallurgy & Materials Institute will be formed to deliberate and decide on the regulations.

② The chair of the Research Ethics Committee shall be the Editor-in-chief of The Korean Powder Metallurgy & Materials Institute Committee. The chair convenes and presides over the Research Ethics Committee when the Editorial Committee proposes an issue as regards research misconduct.

③ The Research Ethics Committee shall consist of no more than five members. The committee members are appointed by the president of the society after the recommendation of the Editorial Committee.

Chapter 2 Research Misconduct

3. Subject of Research Misconduct

Research misconduct is directed to articles, documents, and data submitted or published to the Journal of Powder Materials.

4. Simultaneous Submission

Submitted papers may not be submitted to other domestic or foreign academic journals simultaneously, or as a duplicate, regardless of whether it is submitted beforehand or afterwards.

5. Duplicated Publication

① Dissertations published in other domestic or foreign academic journals may not be duplicated.

② When submitting a research report or a part of a doctoral or a master's thesis as it is, or if it is corrected or supplemented, the correct description must be clearly stated.

6. Plagiarism

① Plagiarism is the act of deliberate description of the content of academic ideas, opinions, expressions, and research results already published through all written media, including domestic or foreign journals, academic papers, research reports, master's or doctoral dissertations, books, magazines, and the internet without reference to the source.

② Plagiarism also applies when the researcher is the same as the author of the paper already published (self-plagiarism). However, it is not considered plagiarism if it describes widely used academic knowledge or research results without citation./td >

Forgery and Falsification Forgery or falsification involves the act of intentionally expressing, among others, numerical values and photographs of the data or results used in the research differently from the truth.

1. Forgery is the act of untruthful creation of false data or research results that do not exist.
2. Falsification refers to the act of artificial manipulation of research materials, equipment, processes, or distorting research contents or results by modifying or deleting data arbitrarily.

Chapter 3 Deliberation and Resolution Procedures

8. Judgment of Research Misconduct

① If there is a report on research misconduct within or outside the institute, the chair of the Editorial Committee must convene the committee to collect relevant data and confirm the credibility of the report.

② When the chair of the Editorial Committee confirms the authenticity of the report, he/she will submit the document of issue to the Research Ethics Committee.

③ The chair of the Research Ethics Committee gives the researcher an opportunity to document the proposed issues within two weeks in advance of the hearing..

④ The Research Ethics Committee shall make a unanimous

decision on whether there has been a case of research misconduct. If there is a disagreement between the two parties, it shall be decided by a vote of 3/5 of the attending committee members.

9. Discipline and Result Processing

① A person who violates research ethics shall be subject to and notified of a disciplinary action through the following measures:

1. Member expulsion
2. Prohibition of contributing to the Journal of Powder Metallurgy
3. If the article is published, the article will be deleted. Papers that are scheduled to be published cannot be published.
4. Relevant organizations will be notified of ethics violations.
5. Other disciplinary actions that are deemed necessary

② The content of the violated research ethics shall be posted on the homepage after a two-week protest period.

③ The contents of the disciplinary action in Items 2, 3, and 5 of Clause 1 shall be notified in the name of the editor-in-chief after the decision of the Research Ethics Committee. The contents of disciplinary action in Items

10. Objection

① A researcher who is judged for a research misconduct may file an objection only once within one month from the date of notification, if the decision of the Research Ethics Committee or the reason for misconduct is unreasonable.

② The Research Ethics Committee can review or revise the contents of the resolution by deliberating the validity of the objection.

Supplement

1. Amendment, Opening, and Closing of Regulations

This regulation may be amended, opened, or closed through the resolution of the Board of Directors.

2. Effective Date

1. This regulation shall be effective beginning on the date of the Board of Directors' approval (June 17, 2016).
2. This Revised code of ethics shall be in effect from February 10, 2022.

Written Oath of Observance of Research Ethics

Journal of Powder Materials

Article title: _____

_____

Author name: _____

To Editor-in-chief of the Journal of Powder Materials

I, as a contributor to the Journal of Powder Materials, hereby declare that I have abided by the following Code of Research Ethics of The Korean Powder Metallurgy & Materials Institute while writing this article.

1. I swear that I shall observe The Korean Powder Metallurgy & Materials Institute's Research Ethics Code and regulations related to research misconduct, and have written this article through honest and rigorous research.
2. I swear that I have not published this article elsewhere and have no plan to submit this article in other journals until the deliberation is over.
3. I swear that I have not committed any research misconducts that can be defined as a violation of Research Ethics, such as forgery (falsification), alteration, plagiarism, duplicate publication, etc., that compromises academic integrity.
4. I swear that I acknowledge the legitimate efforts of participating researchers and did not make unreasonable authorship of those who have not contributed to the research.
5. I swear that I shall take full responsibility for all problems and disadvantages that may arise from noncompliance with the Research Ethics if found guilty of any of the above-mentioned research misconducts.

All authors must sign this Written Oath of Observance of Research Ethics, but in case of necessity, the correspondent author can obtain the consent of other authors and replace them.

All Authors:

_____ _____

Signature Date Signature Date

_____ _____

Signature Date Signature Date

One author on behalf of all co-authors:
"I warrant that I am authorized to execute this copyright on behalf of all the authors of the article referred to above."

Instructions for authors

Journal of Powder Materials

The Korean Powder Metallurgy & Materials Institute, founded in 1994, is a research journal that primarily aims to publish original research papers on a bi-monthly basis.

1. Forms and contents of publication

- Original Papers: This form of publication represents original research articles on various aspects of powder metallurgy, namely fabrication, characterization, and forming of metal powders for advanced industrial applications.
- Letters or Rapid Communications: Short reports of original researches are accepted for publication.
- Critical Reviews or Reports : Invited or submitted review papers and technical reports are accepted.

The journal overall serves as a much-desired international platform for publications of wide researches in materials science. The emphasis, however, has been given on originality and quality of the paper rather than quantitative research. Short reports on material development, novel process or properties are also welcome. The following list of topics is of particular interest to the journal: (1) Powder fabrication techniques, (2) Characterization, (3) Compaction and sintering methods, (4) Heat treatment processes in powder metallurgy, (5) Industrial application of powders, (6) Powder process control, (7) Particle modification, (8) Particle motion and rheology, and (9) Particle growth.

2. Submission of papers

1) Manuscript should be submitted online at the KPMI homepage (http://www.kpmi.or.kr) or e-mail to the KPMI (journal@kpmi.or.kr)
2) File type: MS Word files according to instructions below. Pictures and photos should be submitted in JPG or TIFF format (300 dpi).
3) Prior to publications: Submitted manuscript must not previously been published in a journal and it is not being simultaneously considered for publication elsewhere.

3. Preparation of manuscripts

1) All papers should be written in English and SI units should be used throughout. Abbreviations should be defined the first time they occur in manuscript. Manuscripts should be typed on a paper of A4 format with 2.5 cm margins (right, left, top, bottom), and double-spaced, using Times Roman 11 font.

2) Structure of the manuscript:
The Title : The tile should be carefully chosen to indicate as clearly as possible the subject of the manuscript. The first letter of each word should begin with a capital letter except for articles, conjunctions, and preparations. The first word after a hyphen should also be capitalized such as "Variation of Magnetic Properties of Nd-Fe-B Sintered Magnets with Compaction Conditions".

Bylines should include all those who have made substantial contributions to the work. The first author should be the major contributor of the work. All authors' names should be written in full. At least one author should be designated with a sign as the corresponding author.

Affiliations should include the following information in the order of Institute, Department, City, Zip Code, and Country.

Abstract and Keywords : Each paper should include 120~200 words abstract and five key words for use in indexing.

3) Text: Description headings should be used to divide the paper into its component parts as below.

1. Introduction
2. Experimental
3. Results & Discussions
4. Conclusions

Acknowledgement (This is author's option.)
References
List of Table and Figure captions
Tables and Figures

4) References:
References should be indicated in the text by consecutive numbers in square parentheses, e.g. [1, 2, 5-7], as a part of the text, the full reference being cited at the end of the text. References should contain all the names of the authors together with their initials, the title of the journal, volume number (Bold type), year and the first page number as below. References to books should contain the names of the authors, the title (the names of

editors), the publisher name, location and year as below.

[1] J. D. James, B. Wilshire and D. Cleaver: Powder Metall., 33 (1990) 247.
[2] I. H. Moon: J. Korean Powder Metall. Inst., 1 (1991) 66.
[3] H. E. Exner and G. Petzow: Sintering and Catalysis, G. C. Kuczynski (Ed.), Plenum Press, New York (1976) 279.
[4] D. R. Dank and D. A. Koss: High Temperature Ordered Intermetallic Alloys, C. T. Liu (Ed.), MRS Symp. Proc. Vol. 133, Pittsburg, PA (1989) 561.
[5] Daido Steel: USA, US 5,193,607 (1993).
[6] M.G.Kim and J.H.Kim: Korea, KR 0041070 (2010).
[7] Germany: DIN EN ISO 11876N, Hardmetals.
[8] ASTM B213:03, Standard Test Method for Flow Rate of Metal Powders.
[9] J. C. Kim: M.S. Thesis, Title of Dissertation, Daehan University, Seoul (2011) 123.
[10] J. C. Kim: Ph. D. Dissertation, Title of Dissertation, Hankook University, Seoul (2011) 123.

5) Tables and Figures
Tables: type each table on the separate page, number consecutively in Arabic numerals and supply a heading. Figures for best results submit illustrations in the actual size (300 dpi) at which they should be published. The line drawings and the photographs should be originals and sharp images, with somewhat more contrast than is required in the printed version. Each figure should be typed on a separate page. The figure captions must be included.

6) Equations
Equations are placed must be clearly printed and numbered sequentially with Arabic numbers enclosed with round parentheses at the right-hand margin.

$$Ex)f = f\infty + (f0 - f\infty)\exp(-\gamma r/\gamma \tilde{} r) \quad (1)$$

4. Peer-review

All manuscripts are treated as confidential. They are peer-reviewed by at least 3 anonymous reviewers selected by the editor. Letters to the editor are reviewed and published on the decision of the editor. The corresponding author is notified as soon as possible of the editor's decision to accept, reject, or request revision of manuscripts. When the final revised manuscript is completely acceptable according to the KPMI format and criteria, it is scheduled for publication in the next available issue. Rejected papers will not be peer-reviewed again.

5. The accepted manuscript

1) Copyright:
Upon acceptance of a paper, the author(s) will be asked to transfer the copyright of the paper to the publisher, The Korean Powder Metallurgy & Materials Institute. This transfer will ensure the widest possible dissemination of the information.

2) Proofs:
Proofs will be sent to the corresponding author for checking before publication and will not be returned to the author, unless requested otherwise. Only typographical errors may be corrected. Any substantial alterations other than these may be charged to the author. All joint communications must indicate the name and full address of the author to whom proofs should be sent.

3) Reprints:
The authors are entitled to 50 reprints or a PDF file of the article without additional charge, but are charged for additional reprints exceeding 50 in addition to the nominal publication charge.

4) Publication charge:
The publication fee is US$200 up to 6 pages, and US$30 per additional page regardless of a member or a non-member. Additional fee for acknoledgement is US $100. For color printings, US$100 per color page is charged to authors regardless of the membership.

6. Code of ethics

We can secure the ethics required for scientific research through this code of ethics; and we intend to raise the value of our journal through the addition of originality and integrity to our journal. Therefore, all authors of theses, review committee members and editorial committee members shall observe this code of ethics in order to reject any dishonesty in the publication of theses and secure the integrity of any research. For the policies on the research and publication ethics not stated in this instructions, International standards for editors and authors (http://publicationethics.org/international-standards-editors-and-authors) can be applied.

Copyright transfer agreement

Journal of Powder Materials

Article No: _____

Article Title: _____

_____

By: _____

It is hereby agreed that the copyright of the above article is transferred to The Korean Powder Metallurgy & Materials Institute. However, the author(s) reserves the following:

1. All proprietary rights other than copyright, such as patent rights.
2. The right to reuse all or part of this article in other works.
3. The right to use the article for the author's personal use provided the copies are not offered for sale.

All Authors:

_____ _____

Signature Date Signature Date

_____ _____

Signature Date Signature Date

One author on behalf of all co-authors:

"I warrant that I am authorized to execute this copyright on behalf of all the authors of the article referred to above."

signaturedate signaturedate

_____ _____

Signature Date Signature Date

This document must be signed by author(s) and be received by the production office before the article can be processed for publication. Please mail this document to the following address:

The Korean Powder Metallurgy & Materials Institute

Unit 706, (635-4, Yeoksam-Dong) 22, 7Gil,Teheran-Ro, Gangnam-Gu, 135-703 Seoul, Korea

Checklist

Journal of
Powder Materials

☐ 제목과 저자명, 저자 소속을 정확하게 확인하였습니다.

☐ 교신저자를 기호로 구분되어 표기하였으며, E-mail 주소와 연락처를 정확하게 표기하였습니다.

☐ Keyword는 학회지에 규정한 Keyword list에서 선정하여 정확하게 확인하였습니다.

☐ 그림과 그림설명이 잘 매치 되었는지 정확하게 확인하였습니다.

☐ 참고문헌은 한국분말재료학회지 작성 규정에 따라 정확하게 작성되었습니다.

☐ The paper title, authors' names, and authors' affiliations have been confirmed to be accurate.

☐ The corresponding author has been distinguished using symbol(s), and e-mail address(es) and contact number(s) have been indicated accurately.

☐ The keywords have been selected from the keyword list determined by the Journal and confirmed to be accurate.

☐ The figures and their captions have been confirmed to be matched accurately.

☐ The reference materials have been drawn up accurately according to the paper guidelines of the Journal of Powder Materials.

2024년도 임원명단

Journal of Powder Materials

직 위	성 명	소 속
회장	김택수	한국생산기술연구원
수석부회장	김진천	울산대학교
대외협력부회장	이기안	인하대학교
학술부회장	이정구	한국재료연구원
기술부회장	홍순직	공주대학교
산업체부회장	이병윤	㈜창성
감사	김정곤	인천대학교
	장시영	한국항공대학교
편집위원장	김경태	한국재료연구원
편집이사	김정한	한밭대학교
	박귀일	경북대학교
	양민호	단국대학교
	이석재	전북대학교
	최현주	국민대학교
편집간사	강정신	서울대학교
	김정준	고등기술연구원
	박정민	한국재료연구원
	박태주	한양대학교
	배재웅	국립부경대학교
	변종민	서울과학기술대학교
	손석수	고려대학교
	신세은	순천대학교
	안창의	한국세라믹기술원
	양승민	한국생산기술연구원
	이 빈	경희대학교
	이동주	충북대학교
	조승기	한국재료연구원
	최병준	서울과학기술대학교
학술이사	강석훈	한국원자력연구원
	공만식	고등기술연구원
	노기민	한국지질자원연구원
	류호진	KAIST
	백연경	한국재료연구원
	이재범	충남대학교
	임효령	국립부경대학교
	채홍준	고등기술연구원
학술간사	김용주	국민대학교
	이지운	공주대학교
	정다운	한국생산기술연구원
	주수현	단국대학교

직 위	성 명	소 속
국제위원장	이창규	한국원자력연구원
국제이사	김범성	한국생산기술연구원
	류성수	한국세라믹기술원
	안병민	아주대학교
	이근재	단국대학교
	이정구	울산대학교
국제간사	성효경	국민대학교
기술이사	김세훈	한국자동차연구원
	김영무	국방과학연구소
	박지환	엠티아이지
	윤중열	한국재료연구원
	이성희	목포대학교
	최한신	지아이텍
	황병철	서울과학기술대학교
기술간사	김연철	이화다이아몬드공업㈜
	김지원	고등기술연구원
	김충수	한국생산기술연구원
	정효연	한국생산기술연구원
	차희령	한국재료연구원
대외협력이사	강민철	3D프린팅연구조합
	박만호	㈜아스플로
	박진경	LG이노텍
	송인혁	한국재료연구원
	이찬기	고등기술연구원
	천영범	한국원자력연구원
	홍현선	성신여자대학교
대외협력간사	김영균	한국재료연구원
	이동근	순천대학교
	한준희	한국생산기술연구원
지역이사 (지부장)	권세훈	경상지부장 : 부산대학교
	김경훈	강원지부장 : 한국생산기술연구원
	오익현	호남지부장 : 전남테크노파크
	이진규	충청지부장 : 공주대학교
	현승균	경인지부장 : 인하대학교
지역간사	고원석	경인지부 : 인하대학교
	김태훈	호남지부 : 전남대학교
	양승민	강원지부 : 한국생산기술연구원
	엄두승	제주지부 : 제주대학교
총무이사	박경태	한국생산기술연구원
	이영인	서울과학기술대학교
총무간사	김태훈	한국재료연구원
	이 빈	경희대학교
	최상훈	고등기술연구원
	최현주	국민대학교
재무이사	변종민	서울과학기술대학교
	양상선	한국재료연구원
재무간사	송명석	한국생산기술연구원
	정재원	한국재료연구원

제 16 대 평의원 명단

성 명	소 속	성 명	소 속	성 명	소 속
강 철	한라스택폴㈜	박귀일	경북대학교	이규수	MS가스
강두홍	(주)아스플로	박기봉	㈜엠케이	이근재	단국대학교
강민철	3D프린팅연구조합	박동규	경상대학교	이기안	인하대학교
강석중	KAIST	박만호	㈜아스플로	이동주	충북대학교
강석훈	한국원자력연구원	박성진	포스코홀딩스	이민하	한국생산기술연구원
고원석	인하대학교	박원욱	인제대학교	이민호	버추얼랩
공만식	고등기술연구원	박은수	서울대학교	이병윤	(주)창성
구용모	㈜창성	박은수	㈜이엠엘	이상관	한국재료연구원
권세훈	부산대학교	박정민	한국재료연구원	이석재	전북대학교
권영순	울산대학교	박정환	대광소결금속	이선영	한양대학교
권영태	한국재료연구원	박정효	국방과학연구소	이성모	HD현대중공업
김 폴	코오롱 미래기술원	박종관	㈜삼한	이성희	국립목포대학교
김경태	한국재료연구원	박지환	MTIG	이영인	서울과학기술대학교
김경훈	한국생산기술연구원	박진경	LG이노텍	이완재	한양대학교
김기범	세종대학교	박희동	이화다이아몬드공업㈜	이원식	한국생산기술연구원
김기한	용인전자(주)	백연경	한국재료연구원	이재범	충남대학교
김대현	(주)풍산홀딩스	백운형	한국전자재료	이재성	한양대학교
김덕주	하나테크	변종민	서울과학기술대학교	이정구	한국재료연구원
김동환	(주)성림첨단산업	석명진	강원대학교	이정구	울산대학교
김득중	성균관대학교	설재복	경상국립대학교	이지운	공주대학교
김범성	한국생산기술연구원	성효경	국민대학교	이진규	공주대학교
김병기	자화전자	손석수	고려대학교	이찬기	고등기술연구원
김상훈	산업연구원	손인진	전북대학교	이창규	한국원자력연구원
김세훈	한국자동차연구원	손현택	한국생산기술연구원	이학성	동아대학교
김신경	신한다이아몬드공업㈜	송광호	한국분말야금㈜	임경묵	한국생산기술연구원
김양도	부산대학교	송승철	한국회가내스㈜	임중경	대신강업주식회사
김영도	한양대학교	송용설	(주)아모그린텍	임효령	국립부경대학교
김영립	KAMI㈜	송인혁	한국재료연구원	장시영	한국항공대학교
김영무	국방과학연구소	신 훈	㈜아이피티	장태석	선문대학교
김용진	한국재료연구원	신광섭	일진다이아몬드공업㈜	정영근	부산대학교
김우종	(주)대건테크	신세은	순천대학교	정임두	울산과학기술원
김정곤	인천대학교	안동길	대구텍㈜	정재원	한국재료연구원
김정기	경상국립대학교	안병민	아주대학교	정형식	아주대학교
김정한	한밭대학교	안상호	포항산업과학연구원	조권구	경상국립대학교
김종렬	한양대학교	안인섭	경상국립대학교	조승기	한국재료연구원
김주용	리프로텍	안중호	안동대학교	조영철	현대자동차
김지순	울산대학교	안창의	한국세라믹기술원	좌용호	한양대학교
김진천	울산대학교	양동열	한국재료연구원	채홍준	고등기술연구원
김충수	한국생산기술연구원	양민호	단국대학교	천병선	충남대학교
김태규	한국원자력연구원	양상선	한국재료연구원	천영범	한국원자력연구원
김태훈	한국재료연구원	양승민	한국생산기술연구원	최병준	서울과학기술대학교

성 명	소 속	성 명	소 속	성 명	소 속
김택수	한국생산기술연구원	오승탁	서울과학기술대학교	최준필	한국기계연구원
김형섭	포항공과대학교	오왕근	(주)양우메탈	최한신	지아이텍
김홍물	하나에이엠티	오익현	전남테크노파크	최현규	현대제철
김효섭	한국생산기술연구원	유봉영	한양대학교	최현주	국민대학교
김휘준	한국생산기술연구원	유지훈	한국재료연구원	한유동	한국재료연구원
김희수	월드인덕션	윤덕용	KAIST	현승균	인하대학교
노기민	한국지질자원연구원	윤준철	현대제철	홍순직	공주대학교
류성수	한국세라믹기술원	윤중열	한국재료연구원	홍순형	KAIST
류시완	㈜풍산홀딩스	윤태식	대신강업㈜	홍현선	성신여자대학교
류호진	KAIST	은광용	㈜기술과가치	황득규	현대모비스㈜
박 준	제이피씨㈜	이 빈	경희대학교	황병철	서울과학기술대학교
박경태	한국생산기술연구원	이 성	국방과학연구소 민군협력진흥원		

본 학회지는 한국연구재단의 평가결과 등재학술지로 선정되었습니다.

"본 사업은 기획재정부의 복권기금 및 과학기술정보통신부의 과학기술진흥기금으로 추진되어 사회적 가치 실현과 국가 과학기술 발전에 기여합니다."